UNIVERSITÉ D'ORLÉANS

ÉCOLE DOCTORALE
Énergie, Matériaux, Sciences de la Terre et de l'Univers

Conditions Extrêmes et Matériaux : Haute Température et Irradiation
CEMHTI UPR 3079 CNRS

THÈSE présentée par :

Woei Jer NG

soutenue le : **30 juin 2026**

pour obtenir le grade de : **Docteur de l'Université d'Orléans**

Discipline/ Spécialité : Chimie

Structure–Property Coupling in Molten Chloride Fast Reactor Fuels: An Integrated Computational and Experimental Study of the NaCl–$MgCl_2$–$LaCl_3$ Surrogate System

THÈSE dirigée par :

M. Aydar RAKHMATULLIN	Ingénieur de Recherche, CEMHTI–CNRS, Orléans
M. Mathieu SALANNE	Professeur, PHENIX–CNRS, Sorbonne Université, Paris

RAPPORTEURS :

M. Thibault CHARPENTIER	Directeur de Recherche, CEA Saclay, Gif-sur-Yvette
Mme Anna Louise SMITH	Professeure Associée, TU Delft, Pays-Bas

---

JURY :

M. Thibault CHARPENTIER	Directeur de Recherche, CEA Saclay, Gif-sur-Yvette
Mme Anna Louise SMITH	Professeure Associée, TU Delft, Pays-Bas
M. Michaël DESCHAMPS	Professeur, CEMHTI–CNRS, Université d'Orléans, Orléans
M. Jérôme SERP	Ingénieur de Recherche, CEA Marcoule, Bagnols-sur-Cèze
Mme Virginie LAIR	Professeure, IRCP–CNRS, Chimie ParisTech – PSL, Paris, Présidente du Jury

INVITÉ :

Mme Catherine BESSADA	Directrice de Recherche, CEMHTI–CNRS, Orléans

Acknowledgements

With my PhD journey coming to an end, I would like to express my sincere gratitude to all those who have supported and contributed to this work.

First and foremost, I wish to acknowledge **Mme Catherine Bessada**, former director of CEMHTI–CNRS and my former principal thesis advisor, for opening this valuable research opportunity and enabling my academic journey in France. I am deeply thankful for the trust she placed in me and for allowing me to continue my MSc research in the field of molten salt chemistry.

I am profoundly indebted to **M. Aydar Rakhmatullin**, my principal thesis advisor and NMR specialist, for his patient guidance throughout my doctoral studies. His mentorship introduced me to the depth and versatility of NMR spectroscopy and shaped my understanding of molecular-level phenomena in molten salts.

I am equally grateful to **M. Mathieu Salanne**, my co-advisor and expert in computational materials science, for his invaluable instruction in molecular dynamics and DFT simulations. His guidance was instrumental in ensuring the structural accuracy and reliability of the computational modelling presented in this thesis.

I warmly thank all my collaborators whose expertise and support made my ambitious projects and publications possible. In particular, I wish to thank **Mme Kateryna Goloviznina** for her thorough introduction to molecular dynamics simulations and her rigorous review of my analyses and manuscripts. I extend my gratitude towards **M. Vincent Sarou-Kanian** for his assistance with PFG–NMR experiments that made diffusivity measurements possible. My thanks also go to **M. František Šimko** and **Mme Sandra Ory** for their assistance with phase transition measurements of molten salts. I am also grateful to **M. Emmanuel Veron** for his help on the XRD measurements. I acknowledge **M. Haruaki Matsuura** for coordinating the EXAFS experiments in the SPring-8 beamline in Japan, and recognise **Mme Marija Krštulovic** for her involvement in these experiments.

I gratefully acknowledge the members of the ISAC community and the MatRMag group for their constructive discussions and feedback. I would especially like to thank **M. Jérôme Serp** and **Mme Elisa Capelli** for their guidance throughout the project; **M. Franck Fayon** and **M. Didier Zanghi** for their insightful advice on first-principles NMR calculations; **M. Pierre Florian** for his pedagogical guidance in NMR spectroscopy.

I extend my sincere appreciation to **M. Thibault Charpentier** and **Mme Anna Louise Smith** for kindly agreeing to serve as rapporteurs and for their constructive comments, which significantly improved the quality of this manuscript. I also thank **M. Michaël Deschamps**, **Mme Virginie Lair**, and **M. Jérôme Serp** for agreeing to serve on the jury and adjudicate this work. I also express my gratitude towards **M. Hojin Ryu**, my BSc and MSc advisor at KAIST, who introduced me to the study of molten salt reactors and convinced me of the importance of molten salt chemistry for nuclear engineering.

Finally, I am deeply grateful to my parents and my younger brother for their unwavering support, patience, and encouragement throughout my academic journey. I also thank all members of the CEMHTI laboratory for welcoming me with open arms and helping me adapt to life in France throughout this PhD journey.

Merci, Thank you, Terima Kasih

感恩, 감사합니다

Table of Contents

Acknowledgements i

Table of Contents iii

Introduction (Français) 1

Introduction (English) 5

Chapter I: Réacteurs à Sels Fondus / Molten Salt Reactors 8

Résumé (Français) 10

I-1. The Demand for Nuclear Energy 12

I-2. The Evolution of Nuclear Power: From Shippingport to Generation IV Reactors 13

I-3. The Dilemma of Nuclear Energy: Spent Nuclear Fuel 15

I-4. The Evolution and Development of MSR Technology 17

I-5. The ARAMIS-A Reactor 20

I-6. Literature Review of MSR Fuel Chemistry 23

I-7. Thesis: Scope and Goals 26

Chapter II: Fondements Théoriques et Méthodologie de Recherche / Theoretical Background and Research Methodology 30

Résumé (Français) 32

II-1. Nuclear Magnetic Resonance 34

II-1.1. Fundamental Principles 34

II-1.2. Basic Pulse Sequences 38

II-1.3. Relaxation Times, T_1 and T_2 39

II-1.4. High-Temperature NMR 41

II-1.5. Solid-state NMR 44

II-1.6. Pulsed Field Gradient–NMR 46

II-1.7. Sample Preparation and Experimental Protocol 47

II-2. Classical Molecular Dynamics 49

II-2.1. Theoretical Background 49

II-2.2. Interaction Potential Parameters 52

II-2.3. MD Simulation Protocol 53

II-3. First-Principles NMR Calculations 59

II-3.1. Theoretical Background of DFT 59

II-3.2. NMR Calculations with DFT 64

II-3.3. Geometry Optimisation with DFT 66

Chapter III : Propriétés Structurelles / Structural Dynamics 68

Résumé (Français) 70

Introduction 73

III-1. High-Temperature NMR 73

III-1.1. Binary Systems 75
III-1.2. Ternary Systems 79
III-2. Solid-State NMR 81
III-3. Molecular Dynamics 87
III-3.1. Binary Systems 87
III-3.2. Ternary Systems 92
III-4. DFT Calculations of NMR Parameters 96
Conclusions 103
Chapter IV : Propriétés de Transport / Transport Properties 104
Résumé (Français) 106
Introduction 108
IV-1. Binary Mixtures: Transport Properties of the NaCl–$LaCl_3$ System 109
IV-1.1. Viscosity 109
IV-1.2. Self-diffusivity 110
IV-1.3. Limitations of PFG–NMR on $MgCl_2$-Containing Systems 113
IV-2. Ternary Mixtures: Influence of Mg^{2+} ions on Transport Properties in NaCl–$MgCl_2$–$LaCl_3$ 115
IV-2.1. Viscosity 115
IV-2.2. Self-diffusivity 116
IV-2.3. Effects of $MgCl_2$ on the Ion Transport Mechanism 117
Conclusions 119
Chapter V : Solubilité de l'Oxygène / Oxygen Solubility 122
Résumé (Français) 124
Introduction 127
V-1. Synthesis and Characterisation of LaOCl 128
V-2. Oxygen Dynamics in Molten Chlorides: A Molecular Dynamics Perspective 130
V-3. Oxygen Speciation in Molten Chlorides: An NMR Perspective 134
V-3.1. HT NMR Experiments 134
V-3.2. First-Principles NMR Calculations 139
V-4. Effects of Soluble Oxygen Concentration on Thermophysical Properties 148
Conclusions 149
Chapter VI : Perspectives et Conclusions / Perspectives and Conclusions 152
Conclusions et Perspectives (Français) 154
VI-1. Conclusions 155
VI-2. Future Work 156
Bibliography 158
Annexes 172
Annexe-A: Measured and Calculated Transport Properties 174

Annexe-B: Measured and Calculated Chemical Shifts in NaCl–$MgCl_2$–$LaCl_3$–LaOCl 176
Annexe-C: Scripts for First Principles NMR Calculations of Molten Salt Systems 179
Publications 186

Introduction (Français)

Les travaux présentés dans ce mémoire de thèse s'inscrivent dans le cadre du projet France 2030 intitulé *ISAC* « Innovative Systems for Actinides Conversion ». Ce projet a pour objectif d'évaluer la faisabilité de la transmutation des actinides mineurs dans des réacteurs à sels fondus (RSF), dans le but de réduire le stock de déchets de haute activité et à vie longue (HAVL) en France. Dans cette perspective, le projet ISAC fédère les principaux acteurs du secteur nucléaire français—CEA, CNRS, EDF, Orano et Framatome—autour de quatre grands axes techniques : (i) la conception, l'exploitation et la sûreté des réacteurs, (ii) le cycle du combustible et la chimie, (iii) la gestion des déchets, et (iv) les matériaux et la corrosion. Par ailleurs, le projet s'appuie sur des collaborations avec plusieurs institutions de recherche européennes, notamment le Centre commun de recherche de la Commission européenne (Karlsruhe, Allemagne) pour l'acquisition de données thermophysiques et thermochimiques relatives aux sels fondus, ainsi que le Nuclear Research & Consultancy Group (Petten, Pays-Bas) pour la réalisation d'expériences au sein du réacteur à haut flux.

Dans un contexte de croissance rapide de la demande énergétique mondiale, l'énergie nucléaire est largement reconnue comme une source d'énergie fiable et faiblement émettrice de carbone, capable de répondre aux besoins croissants de l'humanité. Toutefois, l'un des principaux inconvénients des réacteurs nucléaires conventionnels réside dans la radioactivité à long terme des combustibles nucléaires usés (CNU). En particulier, certains produits de fission (tels que le ^{99}Tc, le ^{129}I, le ^{135}Cs), ainsi que des éléments transuraniens (tels que le ^{237}Np et le ^{242}Pu), présentent des périodes radioactives pouvant atteindre plusieurs millions d'années, ce qui pose des défis majeurs en matière de gestion à long terme.

En France, le stockage des déchets radioactifs en couche géologique profonde a été retenu comme solution de référence afin d'isoler le CNU de la biosphère. Néanmoins, au-delà du caractère politiquement sensible de cette option, plusieurs verrous scientifiques et techniques doivent encore être levés avant sa mise en œuvre complète. En particulier, l'accumulation de la puissance résiduelle dégagée par le CNU est susceptible de compromettre l'intégrité structurelle des systèmes de confinement. Dans ce contexte, les radionucléides à vie moyenne, tels que le ^{137}Cs, le ^{90}Sr et le ^{241}Am, constituent les principaux contributeurs à cette production de chaleur résiduelle. Par conséquent, la séparation et la gestion sélectives de ces isotopes représentent une étape préalable essentielle pour garantir la sûreté et la fiabilité à long terme des stockages géologiques profonds.

La transmutation des actinides constitue une approche prometteuse pour le traitement des CNU. Dans un réacteur à eau pressurisée (REP) fonctionnant en cycle du combustible fermé, le plutonium et les autres actinides mineurs peuvent être séparés des stocks de CNU, puis transmutés par irradiation neutronique dans des réacteurs à spectre rapide en isotopes stables ou à vie plus courte. Parmi les concepts de réacteurs avancés envisagés à cette fin, les RSF à base de chlorures ont été identifiés comme des candidats particulièrement attractifs, en raison de la forte solubilité des actinides dans les sels de chlorures et de leur aptitude à maintenir un spectre neutronique rapide. Par ailleurs, les RSF fonctionnent à une pression proche de la pression atmosphérique et leur combustible liquide permet une configuration

homogène du cœur du réacteur, ce qui simplifie les opérations et renforce la sûreté intrinsèque par rapport aux systèmes REP à combustible solide.

L'objectif principal du projet ISAC est d'évaluer la faisabilité de la transmutation de l'américium à l'aide du réacteur ARAMIS-A, conçu spécifiquement pour la gestion des actinides dans le sel. Selon les spécifications de conception actuelles, ce réacteur devrait fonctionner à une puissance thermique de 300 MW_{th}, avec une température d'entrée de 570 °C et une température de sortie de 650 °C. La composition proposée pour le sel fissile frais est de 62 mol % de NaCl, 15 mol % de $MgCl_2$ et 23 mol % de $(Pu,Am)Cl_3$, avec un rapport massique d'actinides de 44,8 % de Pu et 55,2 % d'Am, reflétant une composition représentative des actinides présents dans l'inventaire français de CNU.

En tant que concept de réacteur innovant, le déploiement du réacteur ARAMIS-A soulève de nombreux verrous techniques et scientifiques. En particulier, le retour d'expérience sur les RSF à spectre rapide à base de chlorure demeure très limité, aucun réacteur de ce type n'ayant encore été construit. En conséquence, plusieurs aspects critiques restent insuffisamment explorés, notamment :

- le contrôle et la surveillance de la chimie des sels,
- le comportement en corrosion des matériaux de structure dans des environnements chlorures agressifs, à haute température et sous flux neutronique rapide,
- l'intégration de systèmes de manipulation et de maintenance à distance en environnements fortement irradiants,
- le développement d'un cadre complet d'analyse de sûreté adapté à ce concept de réacteur innovant.

Dans ce contexte, l'objectif principal de cette thèse est de contribuer à la levée des verrous liés à la chimie mentionnés ci-dessus. Plus précisément, ce travail porte sur la détermination de la structure locale du mélange fondu $NaCl–MgCl_2–PuCl_3–AmCl_3$ par l'examen de la composition du substitut $NaCl–MgCl_2–LaCl_3$, en mettant en évidence le rôle du $MgCl_2$ dans la spéciation des actinides/lanthanides ainsi que les mécanismes de formation de réseaux au sein des mélanges chlorurés fondus. L'influence de cette structure microscopique sur les comportements macroscopiques—tels que les propriétés thermophysiques et la solubilité de l'oxygène—est également analysée en détail.

L'étude des combustibles RSF constitue un défi expérimental majeur, en raison notamment de leurs températures de fonctionnement élevées (supérieures à 500 °C), de leur caractère hygroscopique et corrosif, de leur radiotoxicité ainsi que des risques potentiels de prolifération. Depuis les années 1990, le laboratoire CEMHTI (CNRS Orléans) a développé une plateforme complète de résonance magnétique nucléaire à haute température (RMN HT), permettant l'étude de la structure locale des oxydes, fluorures et chlorures fondus. Dans ce contexte, les variations du déplacement chimique en fonction de la composition et de la température fournissent des informations expérimentales directes sur les environnements de coordination des noyaux actifs en RMN. Parallèlement, le développement du modèle des ions polarisables (*Polarisable Ion Model*, PIM) dans les années 2000 a permis de décrire avec précision la structure atomistique des sels fondus au moyen de simulations de dynamique moléculaire (DM). Enfin, le calcul des paramètres RMN à partir de méthodes ab initio permet d'établir une validation croisée entre les simulations DM et les expériences RMN, assurant ainsi, de manière indépendante, la précision et la fiabilité des deux approches.

Dans ce travail, des mesures de RMN HT ont été couplées à des simulations DM (réalisées à l'aide du code *MetalWalls*), ainsi qu'à des calculs basés sur la théorie de la fonctionnelle de la densité (DFT, effectués avec le code *Vienna Ab-initio Simulation Package (VASP)*) afin d'étudier l'évolution de la structure des mélanges de chlorures fondus. L'utilisation du $PuCl_3$ et de l'$AmCl_3$ étant interdite au CEMHTI pour des raisons radiologiques et réglementaires, le $LaCl_3$ a été retenu comme substitut non radioactif des trichlorures d'actinides. Ce choix repose sur la similarité des structures cristallines, la présence de l'isotope ^{139}La actif en RMN, le caractère non paramagnétique de l'ion La^{3+}, ainsi que l'absence de risque de prolifération nucléaire. Les propriétés de transport des chlorures fondus—telles que les diffusivités ioniques et les viscosités—ont également été évaluées par simulations DM. Ces résultats ont ensuite été confrontés à nos propres mesures de RMN à gradient de champ pulsé (RMN–PFG), ainsi qu'aux valeurs de viscosité rapportées dans la littérature. Enfin, afin d'étudier la solubilité de l'oxygène, du LaOCl enrichi en ^{17}O a été introduit dans le mélange $NaCl–MgCl_2–LaCl_3$ en tant que contaminant oxyde, puis analysé au moyen d'une approche combinant RMN HT, simulations DM et calculs DFT.

Ce travail a été réalisé sous la direction d'Aydar Rakhmatullin et de Catherine Bessada (retraitée en 2025) au laboratoire CEMHTI–CNRS (Orléans) pour les études de RMN, ainsi que sous la direction de Mathieu Salanne du laboratoire PHENIX–CNRS, Sorbonne Université (Paris) pour les calculs atomistiques. Depuis janvier 2024, Mathieu Salanne est en poste au bureau du CNRS à Singapour.

***

Cette thèse est organisée de la manière suivante:

Le premier chapitre présente le concept des RSF dans le contexte plus large des transitions énergétiques mondiales et du regain d'intérêt pour l'énergie nucléaire. Il retrace l'évolution historique de la technologie RSF et décrit le développement du réacteur ARAMIS-A, retenu comme réacteur de référence pour ce travail. Ce chapitre aborde également ses paramètres de fonctionnement, les caractéristiques du combustible, le choix des matériaux, ainsi que les principaux défis techniques associés à sa conception. Une attention particulière est ensuite portée à la chimie du combustible RSF, à travers une revue approfondie de la littérature relative aux sels fondus à base de fluorures et de chlorures, suivie de la présentation de l'approche méthodologique et des compositions de sels retenues dans cette étude.

Le deuxième chapitre est consacré aux fondements théoriques et méthodologiques de la recherche. Il présente les principes de la spectroscopie RMN, le PIM utilisé pour les simulations classiques de DM, ainsi que le cadre DFT employé pour les calculs de mécanique quantique. Les procédures expérimentales, les protocoles de simulation et les paramètres des potentiels d'interaction y sont également détaillés.

Les chapitres suivants sont dédiés à la présentation et à la discussion des résultats obtenus dans le cadre de cette thèse :

- Le troisième chapitre analyse la dynamique structurelle du système $NaCl–MgCl_2–LaCl_3$ et examine l'influence de la composition et de la température sur sa structure locale;
- Le quatrième chapitre explore l'impact de la structure locale sur les diffusivités ioniques et les viscosités, en fonction de la composition, dans des conditions isothermes à 850 °C ;

- Le cinquième chapitre se concentre sur les mécanismes de solubilité de l'oxygène dans les chlorures fondus, à travers l'étude du système NaCl–$MgCl_2$–$LaCl_3$–LaOCl, avec une fraction cationique en La^{3+} fixée à 20 mol %, afin de simuler un cas idéalisé de contamination par des oxydes.

Enfin, le dernier chapitre synthétise les principales conclusions de ce travail, propose des perspectives pour les recherches futures et discute les enjeux et perspectives de développement des réacteurs à sels fondus en France et à l'échelle internationale.

Chaque chapitre comprend un résumé en français, suivi du texte principal en anglais.

Introduction (English)

The work presented in this thesis was carried out within the framework of the Innovative Systems for Actinides Conversion (ISAC) project, which is partially funded by the France 2030 investment plan. The ISAC project aims to evaluate the feasibility of transmuting minor actinides in molten salt reactors (MSRs) as a means to reduce the long-lived high-level waste (HLW) inventory in France. To assess the feasibility of a fully integrated MSR system, ISAC brings together the main stakeholders of the French nuclear sector— CEA, CNRS, EDF, Orano and Framatome—to address four main technical domains: (i) reactor design, operation and safety, (ii) fuel cycle and chemistry, (iii) waste management, and (iv) materials and corrosion. In parallel, the project also fosters collaborations with European research institutions, including the European Commission's Joint Research Centre (Karlsruhe, Germany) for the acquisition of molten salt thermophysical and thermochemical data, and the Nuclear Research & Consultancy Group (Petten, The Netherlands) for irradiation experiments on the High Flux Reactor.

With the global energy demand continuing to rise exponentially, nuclear power is widely regarded as a reliable and low-carbon energy source capable of meeting humanity's growing needs. However, a major drawback of conventional nuclear reactors lies in the long-lived radioactivity of spent nuclear fuel (SNF). Certain fission products (e.g., ^{99}Tc, ^{129}I, ^{135}Cs) and transuranic elements (e.g., ^{237}Np and ^{242}Pu) exhibit radioactive half-lives exceeding 10^6 years, posing significant long-term management challenges.

In France, deep geological disposal has been proposed as the reference solution to isolate SNF from the biosphere. Yet, beyond the politically sensitive nature of this option, several scientific and technical challenges must be resolved before its full implementation. Among these is the accumulation of residual decay heat within SNF repositories, which could compromise the structural integrity of the containment systems. In this regard, medium-lived radionuclides such as ^{137}Cs, ^{90}Sr, and ^{241}Am have been identified as the principal contributors to this residual heat generation. Consequently, the selective separation and management of these isotopes represent an essential first step towards ensuring the long-term safety and reliability of deep geological repositories.

Actinide transmutation offers a promising approach to addressing the long-term SNF radioactivity. In a conventional pressurised water reactor (PWR) operating within a closed fuel cycle, plutonium and other minor actinides can be separated from the SNF inventory and subsequently transmuted into shorter-lived or stable isotopes through neutron irradiation in fast-spectrum reactors. Among the advanced reactor concepts considered for this purpose, chloride-based MSRs stand out as particularly attractive candidates, owing to the high solubility of actinides in chloride salts and their ability to sustain fast neutron spectra. Furthermore, MSRs operate at near-atmospheric pressure and their liquid fuel form enables a homogeneous reactor core configuration, thereby simplifying operations and enhancing inherent safety compared to solid-fuelled PWR systems.

The main objective of the ISAC project is to assess the feasibility of americium transmutation using the Advanced Reactor for Actinides Management in Salt (ARAMIS-A) concept. According to the current design specifications, the reactor is expected to operate at a thermal power of 300 MW_{th}, with inlet and outlet temperatures of 570 and 650 °C, respectively. The proposed fresh fissile salt composition consists of 62 mol% NaCl–15 mol% $MgCl_2$–23 mol%

(Pu,Am)Cl_3, with an actinide ratio of 44.8 wt% Pu to 55.2 wt% Am, reflecting the representative actinide composition in the French SNF inventory.

As a first-of-its-kind design, the deployment of the ARAMIS-A reactor presents numerous technical and scientific challenges. Chief among these is the limited operational experience with chloride-based fast-spectrum MSRs, as no such reactor has yet been constructed. Consequently, several critical aspects remain insufficiently explored, including:

- the control and monitoring of salt chemistry,
- the corrosion behaviour of structural materials under corrosive chloride environments, high temperature, fast neutron irradiation,
- the integration of remote handling and maintenance systems in high radiation environments, and
- the development of a comprehensive safety analysis framework suited to this novel reactor concept.

In this context, the objective of this present thesis is to partially address the first challenge above. More specifically, this work focuses on determining the local structure of molten NaCl–$MgCl_2$–$PuCl_3$–$AmCl_3$ through examining the NaCl–$MgCl_2$–$LaCl_3$ surrogate composition, with particular attention to the role of $MgCl_2$ in lanthanide/actinide speciation and network formation behaviour in chloride melts. The influence of molecular-level structure on bulk thermophysical properties and oxygen solubility is also examined in detail.

The experimental investigation of chloride-based MSR fuels is particularly challenging, due to their high operating temperatures (> 500 °C), hygroscopic and corrosive nature, radiotoxicity, and potential proliferation risks. Since the 1990s, the CEMHTI laboratory (CNRS Orléans) has developed a comprehensive high-temperature nuclear magnetic resonance (HT NMR) platform enabling the study of the local structure of molten oxides, fluorides, and chlorides. Within this framework, chemical shift variations with composition and temperature provide direct experimental insight into the changes in coordination environments of NMR-active nuclei. In parallel, the development of the polarisable ion model (PIM) in the 2000s has made it possible to model the local dynamics of molten salts with high fidelity using classical molecular dynamics (MD) simulations at moderate computational cost. Furthermore, first-principles quantum mechanical calculations of NMR parameters enable cross-validation between MD simulations and NMR experiments, ensuring the accuracy and reliability of both approaches.

In this work, HT NMR measurements were coupled with PIM-based classical MD simulations (using the *MetalWalls* code) and density functional theory (DFT) calculations (using the *Vienna Ab-initio Simulation Package (VASP)* code) to study the structural dynamics of chlorinated mixtures in the molten state. Because the use of $PuCl_3$ and $AmCl_3$ is prohibited at CEMHTI for radiological and regulatory reasons, $LaCl_3$ was chosen as a non-radioactive surrogate for actinide trichlorides, owing to its analogous crystal structure, the NMR-active isotope of ^{139}La, non-paramagnetic nature of La^{3+}, and absence of nuclear proliferation risk. The transport properties of molten chlorides were also evaluated using pulsed-field gradient NMR (PFG–NMR) to measure ion diffusivities, which were then corroborated by MD simulations that additionally yielded viscosities. To investigate oxygen solubility, ^{17}O-enriched LaOCl was introduced into NaCl–$MgCl_2$–$LaCl_3$ as a surrogate oxide contaminant, and analysed through a combination of ^{17}O HT NMR, MD simulations, and DFT calculations.

This research was carried out under the supervision of Aydar Rakhmatullin and Catherine Bessada (retired 2025) at the CEMHTI–CNRS laboratory in Orléans for the NMR studies, and Mathieu Salanne from the PHENIX–CNRS laboratory, Sorbonne Université (Paris) for the computational work. Since January 2024, Mathieu Salanne has been based at the CNRS overseas office in Singapore.

***

The thesis is structured as follows:

Chapter I introduces the MSR concept within the broader context of global energy transitions and the renewed demand for nuclear power. It traces the historical evolution of MSR technology and provides an overview of the ARAMIS-A reactor, the reference system for this work. The chapter discusses its operational parameters, fuel characteristics, materials selection, and main technical challenges associated with its design. Emphasis is then placed on MSR fuel chemistry, with a comprehensive review of the literature on fluoride- and chloride-based molten salts, followed by a description of the methodological approach and the salt compositions adopted in this study.

Chapter II outlines the theoretical and methodological foundation of the research. It presents the principles of NMR spectroscopy, the PIM for classical MD simulations, and the DFT framework used for quantum-mechanical calculations. Details of the experimental procedures, simulation protocols, and interaction potential parameters are also provided here.

Chapters III, IV, and V present the results and discussions of the work conducted in the framework of this thesis:

- Chapter III investigates the structural dynamics of the NaCl–$MgCl_2$–$LaCl_3$ system and examines how composition and temperature affect its local structure.
- Chapter IV explores how local structure influences macroscopic transport properties, such as ionic diffusivities and viscosities, across the NaCl–$MgCl_2$–$LaCl_3$ ternary compositional space at 850 °C.
- Chapter V focuses on the mechanism of oxygen solubility in chlorinated molten mixtures, using the NaCl–$MgCl_2$–$LaCl_3$–LaOCl system with a fixed La^{3+} cationic fraction of 20 mol% to emulate realistic oxide contamination.

Finally, the concluding chapter summarises the main findings of this work, offers perspectives for future research, and reflects on the prospects of MSR development in France and worldwide.

Each chapter starts with a summary in French, followed by the main text in English.

Chapter I

Réacteurs à Sels Fondus/ Molten Salt Reactors

Résumé (Français)

Le chapitre I introduit le concept des réacteurs à sels fondus (RSF) dans le contexte plus large des transitions énergétiques mondiales et du regain d'intérêt pour l'énergie nucléaire. Il débute par une analyse de la croissance rapide de la consommation d'énergie civile, attribuée notamment à l'augmentation de la demande en électricité pour le refroidissement lié au réchauffement climatique, à l'expansion de l'activité industrielle, à l'électrification des transports et au développement des centres de données dédiés à l'intelligence artificielle. Face à cette demande énergétique croissante, l'énergie nucléaire est présentée comme une source d'énergie fiable et faiblement émettrice de carbone, susceptible de répondre aux besoins à long terme. Cette dynamique est illustrée par l'intérêt récent manifesté par de grandes entreprises technologiques — telles qu'Amazon (AWS), Google (Alphabet), Microsoft et Meta — pour les technologies nucléaires, en particulier les petits réacteurs modulaires.

Le chapitre se poursuit par une mise en perspective historique de l'évolution des réacteurs nucléaires civils, développés au fil des décennies pour répondre aux besoins changeants de la société et de l'industrie. Cette évolution est retracée depuis les premiers prototypes de la génération I, apparus dans les années 1950, jusqu'aux réacteurs de génération II, commercialement déployés et éprouvés sur le plan énergétique, puis aux modèles de génération III, intégrant des améliorations significatives en matière de sûreté passive et d'efficacité opérationnelle. L'analyse s'étend enfin aux concepts de génération IV, qui visent des objectifs élargis de durabilité, tels que le soutien à l'économie de l'hydrogène et une meilleure gestion du combustible nucléaire usé (CNU).

Dans ce contexte, les réacteurs à sels fondus ont été retenus comme l'un des six concepts de réacteurs de la génération IV. Le concept des RSF trouve son origine dans les années 1950, lorsqu'il a été initialement développé dans le cadre de programmes visant la conception de systèmes compacts à forte densité énergétique. Au cours des décennies suivantes, le programme MSRE (*Molten Salt Reactor Experiment*), conduit à l'Oak Ridge National Laboratory, a démontré la faisabilité des RSF pour une production d'énergie civile fiable.

Actuellement, les réacteurs à sels fondus sont principalement étudiés dans l'optique de l'atténuation de la radiotoxicité à long terme du CNU. Dans les RSF à base de fluorures, le spectre neutronique thermique permet le déploiement du cycle du combustible ^{232}Th/^{233}U limitant ainsi la production d'actinides mineurs plus lourds et caractérisés par des périodes radioactives longues. À ce jour, le TMSR (*Thorium Molten Salt Reactor*) développé en Chine constitue le seul RSF à base de fluorures en service, le réacteur ayant atteint la criticité en 2023. À l'inverse, les RSF à base de chlorures fonctionnent généralement avec un spectre neutronique rapide, plus adapté à la présence d'actinides lourds tels que le ^{238}U/^{239}Pu et le ^{240}Pu/^{241}Am. Cette caractéristique permet la transmutation des actinides mineurs issus du CNU des réacteurs conventionnels de générations II et III en isotopes à périodes radioactives plus courtes. Toutefois, à ce jour, aucun RSF à base de chlorures n'a encore été construit ni mis en service.

Dans ce contexte, le projet français ISAC (« Innovative Systems for Actinides Conversion ») vise le développement d'un réacteur rapide à chlorure fondu (*Molten Chloride Fast Reactor*, MCFR) afin de réduire l'inventaire d'actinides dans les stockages de CNU. Le déploiement du réacteur ARAMIS-A (« Advanced Reactor for Actinides Management

in Salts ») pourrait ainsi contribuer à une réduction significative de la durée de vie radiologique du combustible usé, renforçant la sûreté et la fiabilité à long terme des stockages en couche géologique profonde. Néanmoins, le retour d'expérience sur les MCFR demeurant très limité, plusieurs verrous scientifiques et techniques doivent encore être levés avant toute perspective de déploiement industriel. Dans ce cadre, la compréhension de la chimie des sels combustibles et de leurs interactions avec l'environnement constitue un enjeu central de cette thèse.

Le réacteur ARAMIS-A repose sur une composition de combustible de type $NaCl–MgCl_2–PuCl_3–AmCl_3$. Parmi les différents constituants du combustible, le $MgCl_2$ se distingue comme un choix particulièrement pertinent, offrant plusieurs avantages clés, tels que l'abaissement des températures de fusion, l'amélioration du transfert thermique, la réduction de la viscosité du sel fondu et l'atténuation des phénomènes de précipitation fissile — ces deux derniers points étant démontrés pour la première fois dans le cadre de cette thèse. Toutefois, l'utilisation du $MgCl_2$ présente également des défis, dans la mesure où ce composé est reconnu comme un vecteur d'impuretés oxygénées et d'humidité, susceptibles d'accélérer la corrosion des matériaux de structure environnants.

Afin de caractériser précisément le rôle du $MgCl_2$ dans les performances du combustible, une compréhension approfondie de la chimie du combustible des MCFR s'avère indispensable. À cette fin, une revue exhaustive de la littérature récente consacrée à la chimie des sels fondus a été menée. Celle-ci couvre à la fois les systèmes fluorés et chlorurés et intègre des approches expérimentales et de simulation.

Le chapitre I se conclut par la définition de la portée et des objectifs de cette thèse, qui visent à quantifier la dynamique structurelle des sels de chlorure fondus à l'échelle atomistique et à analyser son influence sur les propriétés macroscopiques du combustible. Plus précisément, l'impact du $MgCl_2$ sur l'ajustement de la structure locale et sur les propriétés macroscopiques du combustible est mis en évidence. Cette thèse aborde ainsi de manière systématique le couplage structure–propriété dans les combustibles MCFR, en s'articulant autour de trois axes principaux : *la structure*, *les propriétés de transport* et *la solubilité de l'oxygène*.

I-1. The Demand for Nuclear Energy

According to the *International Energy Agency* (IEA), global energy demand grew by 2.2% in 2024, significantly outpacing the decadal average of 1.3%. This surge was driven primarily by a 4.3% increase in electricity demand, reflecting rising consumption for cooling under extreme temperatures, expanding industrial activity, the electrification of transport, and the rapid growth of data centres [1].

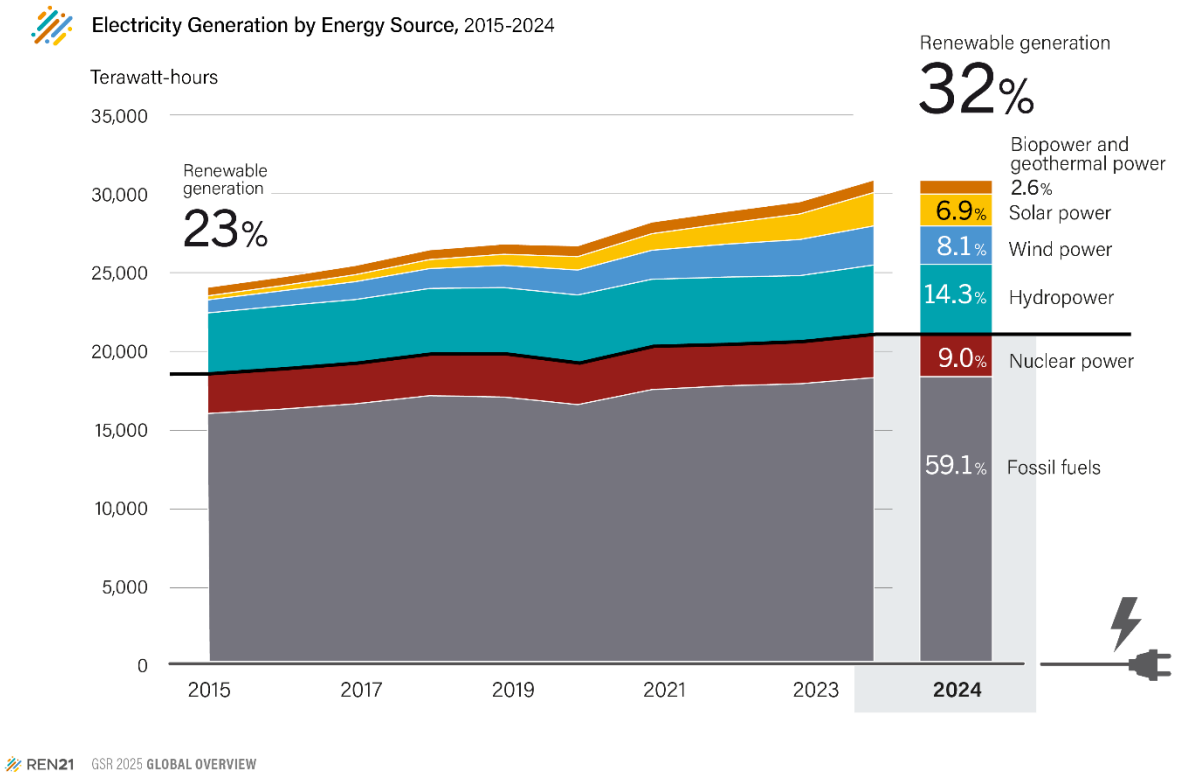

Figure I-1. Global electricity generation by energy source from 2015 to 2024. [2]

Amid this escalating demand, nuclear power is experiencing a global renaissance as a reliable and low-carbon energy source capable of meeting the world's growing electricity needs. In 2024, nuclear power supplied roughly 9% of global electricity generation (**Figure I-1**) [2], with over 7 GW capacity commissioned—representing a 33% increase from the previous year [1].

In the context of the Fourth Industrial Revolution, the accelerating deployment of artificial intelligence (AI) and large-scale data centres is expected to impose unprecedented strain on global electricity systems. Because nuclear power provides continuous, high-capacity baseload generation, major tech corporations—such as Amazon (AWS) [3], Google (Alphabet) [4,5], Microsoft [6], and Meta [7]—are increasingly turning to nuclear energy and small modular reactors (SMRs) to secure reliable, long-term energy supplies for their future AI and data-centre operations. Reflecting

this renewed interest, the *International Atomic Energy Agency* (IAEA) projects that the nuclear electrical generation capacity will increase by at least 50% by 2050 [8].

I-2. The Evolution of Nuclear Power: From Shippingport to Generation IV Reactors

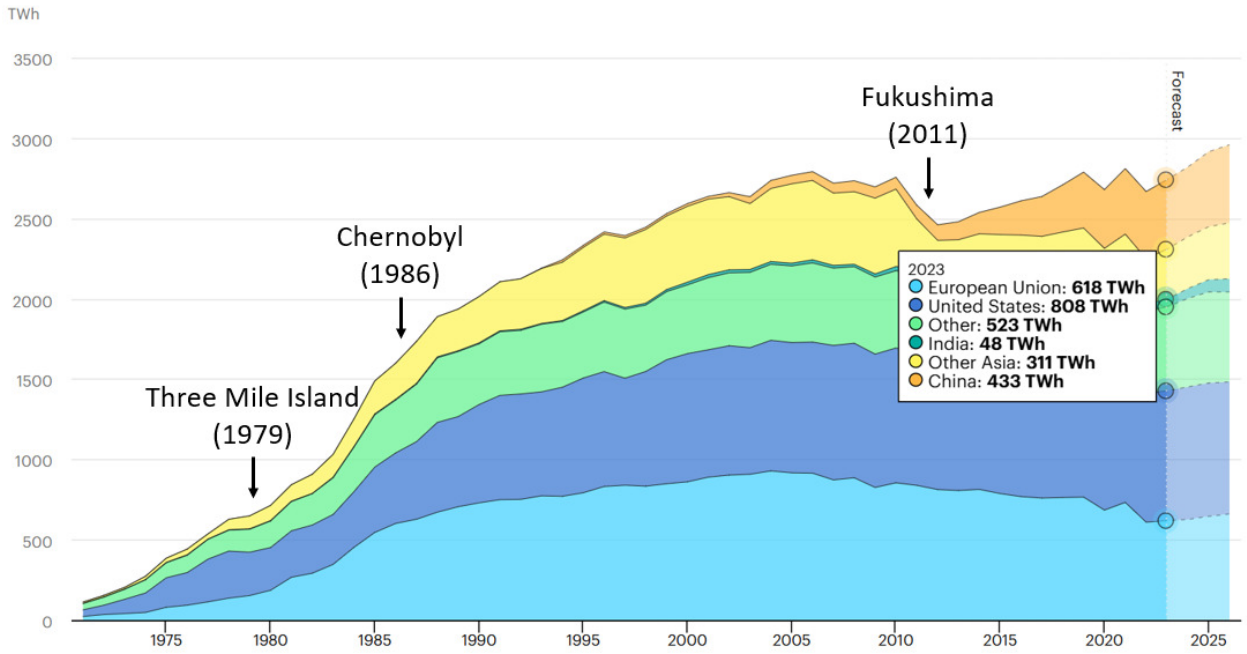

Figure I-2. Evolution of nuclear power generation by region from 1972 to 2026 (edited). [9]

Global nuclear power generation has expanded drastically since the 1973 oil crisis (**Figure I-2**) [9]. Over that period, nuclear reactor designs have also evolved to address changing societal and industrial requirements, including cost effectiveness, safety, security and non-proliferation, grid compatibility, commercialisation, and fuel cycle management. Within this context, nuclear reactor designs are commonly classified into "generations" according to their key technological and operational characteristics (**Figure I-3**) [10]:

- Generation I comprises the early prototype reactors of the 1950s and 1960s that initiated civilian nuclear programs. Notable reactors include Shippingport (Pennsylvania, 1957–1982), Dresden-1 (Illinois, 1960–1978), and Calder Hall-1 (United Kingdom, 1956–2011).
- Generation II refers to the first commercially deployed reactors, developed in the late 1960s, and they are still operational in many countries today. These systems were designed for economy and reliability, with a typical operational lifetime of around 40 years. Representative designs include the Pressurised Water Reactors (PWR), CANada Deuterium Uranium reactors (CANDU), Boiling Water Reactors (BWR), Advanced Gas-cooled Reactors (AGR), and Water-Water Energetic Reactor (VVER).

- Generation III reactors build upon Generation II designs, introducing key advances in fuel technology, thermal efficiency, modularised construction, passive safety, standardised design, and an extended design lifetime of up to 60 years. Notable examples include the Westinghouse Advanced PWR (AP-600) and General Electric's Advanced Boiling Water Reactor (ABWR).

- Generation III+ reactors represent an evolutionary step that enhances passive safety systems, often relying on gravity and natural circulation to ensure cooling and containment in the event of an abnormal condition. Prominent Generation III+ designs include the VVER-1200, Advanced CANDU Reactor (ACR-1000), AP1000, APR-1400, and European Pressurised Reactor (EPR). [11]

- Generation IV reactors embody the next stage in nuclear technology development, with design objectives encompassing enhanced sustainability, improved economics, superior safety and reliability, and inherent proliferation resistance. These systems are expected to operate at higher temperatures than current reactors, with complementary applications such as hydrogen production and actinide management in spent nuclear fuel. Six reference concepts have been selected: the Gas-cooled Fast Reactor (GFR), Lead-cooled Fast Reactor (LFR), Molten Salt Reactor (MSR), Sodium-cooled Fast Reactor (SFR), SuperCritical-Water-cooled Reactor (SCWR), and Very High-Temperature Reactor (VHTR) (**Figure I-4**) [12,13].

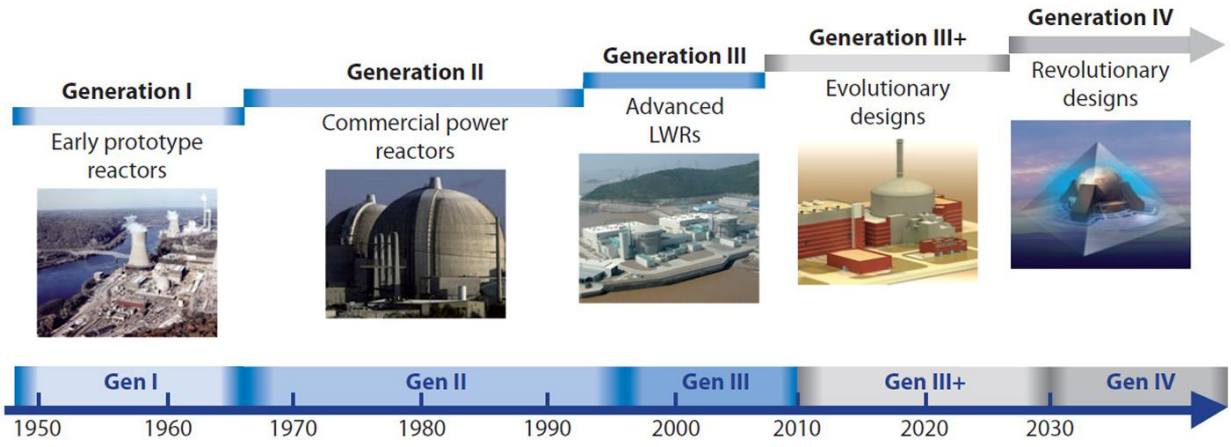

Figure I-3. Timeframe of nuclear reactor generations [10].

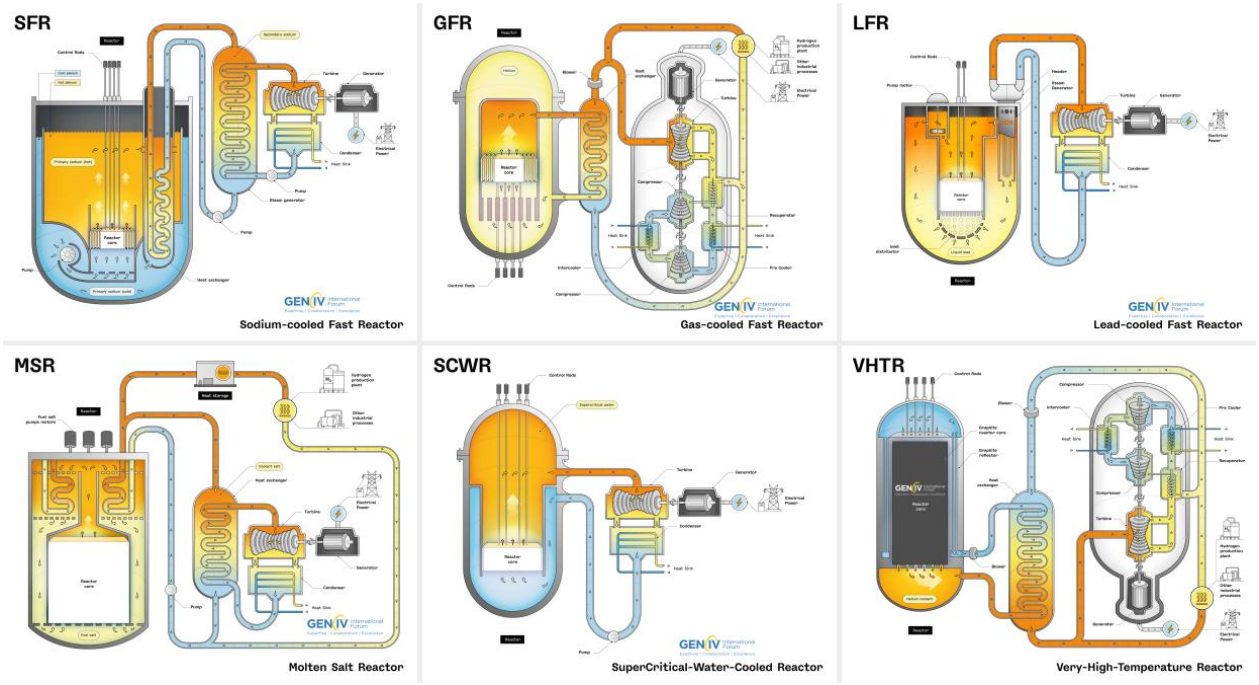

Figure I-4. Schematic of all six Generation IV reactor designs [13].

I-3. The Dilemma of Nuclear Energy: Spent Nuclear Fuel

Although nuclear power offers a low-carbon and reliable source of electricity, international opposition to its expansion persists. Much of this resistance arises from the absence of a universally accepted solution to the long-lived radiotoxicity of spent nuclear fuel (SNF). Certain fission products and transuranic isotopes—such as ^{99}Tc, ^{129}I, ^{135}Cs, ^{237}Np, and ^{242}Pu—exhibit long radioactive half-lives exceeding 10^6 years, presenting profound challenges for long-term management. In addition, radioisotopes with intermediate half-lives (5–100 years), such as ^{137}Cs, ^{90}Sr, and ^{241}Am, contribute substantially to residual heat generation for several decades after reactor discharge, complicating the design of interim storage systems.

A clear understanding of the nuclear fuel cycle (**Figure I-5**, [14]) is essential for addressing this challenge. In an open fuel cycle, SNF is initially cooled in spent fuel pools for several years before being transferred to dry cask storage for intermediate containment, typically lasting up to 40 years. The current long-term strategy involves the disposal of spent nuclear fuel in deep geological repositories, designed to ensure complete isolation from the biosphere. These repositories, constructed several kilometres below the Earth's surface, are intended to contain radionuclides safely for more than 10^5 years. Nonetheless, accurately modelling radiological dispersion phenomena over such an extensive timescale remains a formidable scientific and engineering challenge.

A closed fuel cycle is implemented in several countries to mitigate some of the limitations associated with the open fuel cycle. In this approach, spent fuel containing appreciable quantities of fissile (e.g., ^{235}U and ^{239}Pu) and fertile (e.g., ^{238}U and ^{240}Pu) isotopes is chemically reprocessed and recycled into mixed oxide (MOX) fuel—a composite of UO_2

and PuO_2—for a subsequent irradiation cycle in LWRs. In France, plutonium separation is carried out at the La Hague reprocessing facility, while MOX fabrication is performed at the Marcoule nuclear site.

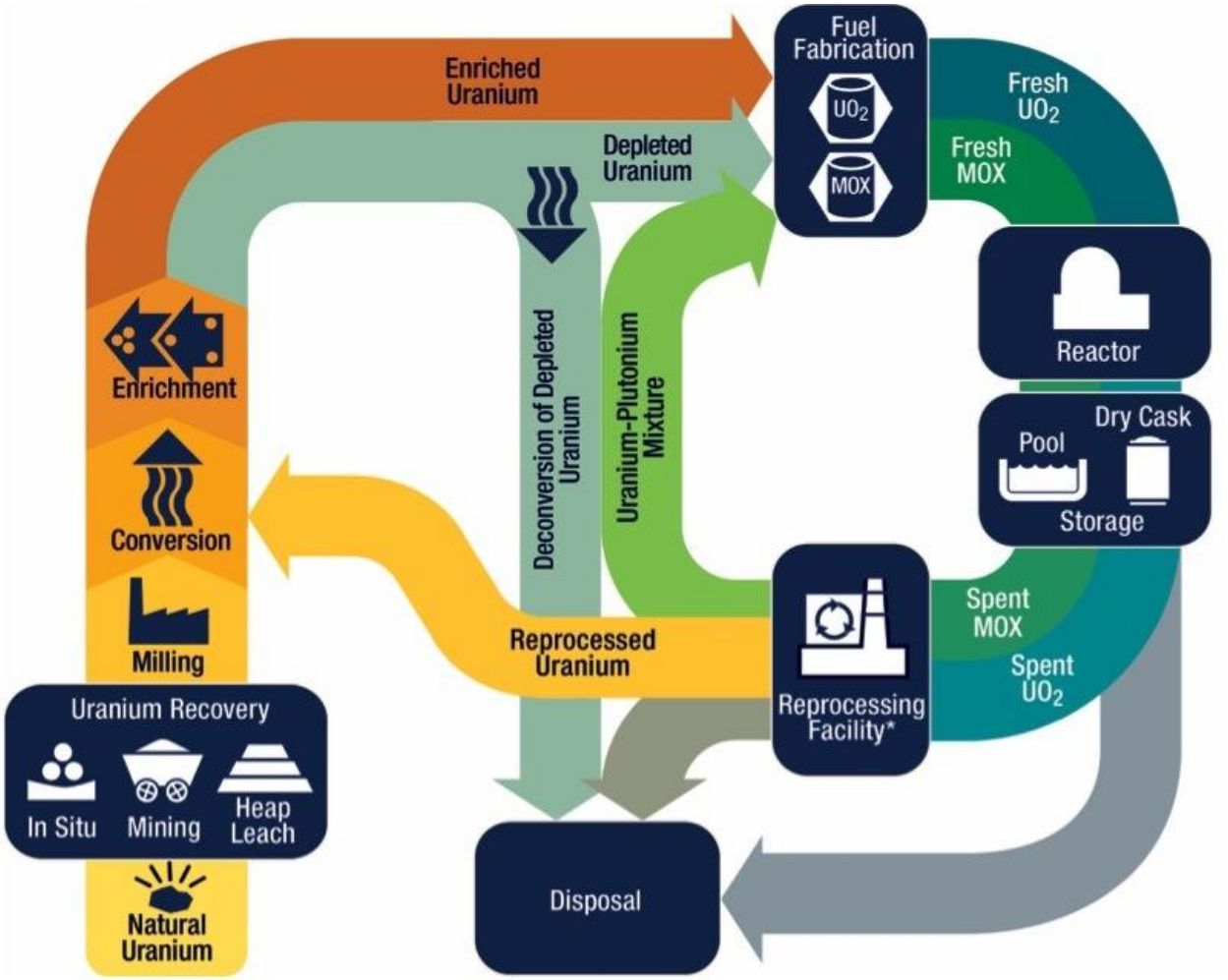

Figure I-5. The nuclear fuel cycle, as illustrated by the United States Nuclear Regulatory Commission in January 2019 [14].

Building on its long-standing expertise in spent fuel reprocessing, France has expressed a strategic intent to integrate Generation IV reactor technologies into its closed fuel cycle [15]. Within this framework, SFRs are envisaged to utilise MOX fuel, whereas MSRs are proposed for the transmutation of minor actinides into isotopes with shorter half-lives or stable end-products.

In this thesis, and in accordance with the objective of the ISAC project, emphasis is placed exclusively on the role of MSRs within the French spent fuel management strategy.

I-4. The Evolution and Development of MSR Technology

Research into MSRs originated in the United States during the early 1950s, driven by the Aircraft Nuclear Propulsion (ANP) program, which sought to develop compact, high-energy-density reactors for nuclear-powered bombers. The Aircraft Reactor Experiment (ARE), conducted at *Oak Ridge National Laboratory* (ORNL) in 1954, represented the first experimental MSR to reach criticality. It employed a fuel mixture of 53 mol% NaF–41 mol% ZrF_4–6 mol% UF_4 (enriched to 93.4 wt% ^{235}U), beryllium oxide (BeO) as the moderator, liquid sodium as the secondary coolant, and Inconel-600 as the structural material. The thermal reactor achieved a maximum steady-state fuel temperature of 860 °C and produced 96 MWh of energy over a 74-hour operation period [16,17].

In the 1960s, ORNL launched the Molten Salt Reactor Experiment (MSRE) program to evaluate the feasibility of an epithermal thorium-based breeder system, commonly referred to as the liquid fluoride thorium reactor concept. The MSRE utilised a fuel salt of 65.0 mol% LiF–29.1 mol% BeF_2–5.0 mol% ZrF_4–0.9 mol% $^{233}UF_4$, omitting the high-cost ThF_4 breeding blanket originally envisioned for the design. Instead, the reactor was loaded with ^{233}U, obtained from thorium breeding in other reactors. Molten FLiBe (67 mol% LiF–33 mol% BeF_2) served as the secondary coolant, pyrolytic graphite acted as the moderator, and Hastelloy-N was employed as the structural alloy. The MSRE achieved criticality in 1965 and operated successfully until 1969, reaching 7.4 MW_{th} and fuel temperatures of up to 650 °C [18].

Following the MSRE, ORNL developed the conceptual design of the Molten Salt Breeder Reactor (MSBR), intended to use 72 mol% LiF–16 mol% BeF_2–12 mol% ThF_4–0.4 mol% UF_4 as fuel and moderated by graphite. However, by the mid-1970s, MSR research was curtailed due to growing interest in the Liquid Metal Fast Breeder Reactor (LMFBR) program. The redirection of federal funding toward fast breeder development led to the stagnation of MSR research in the United States [19].

Outside the U.S., progress in MSR technology was comparatively limited. In the United Kingdom, the Atomic Energy Research Establishment (AERE) explored concepts for chloride-based molten salt fast reactors (MSFRs), employing liquid lead as a coolant, with the aim of utilising the nation's substantial plutonium stockpile. The program was halted in 1974, following the redirection of resources toward the fast breeder reactor at Dounreay [20]. In the USSR, the Kurchatov Institute initiated MSR research in the late 1970s, focusing primarily on theoretical and experimental investigations into the mechanical, corrosion, and radiation behaviour of structural materials in MSR environments. Their findings indicated no fundamental physical or technological barriers to the practical implementation of MSRs [21].

In 2002, MSRs regained significant attention within the scientific and engineering community following their selection by the Gen IV International Forum as one of the six reactor concepts for fourth-generation nuclear systems [22].

Compared to conventional water-cooled reactors, MSRs present a range of potential advantages. Operating at near-atmospheric pressure, they reduce the need for costly reactor pressure vessels, greatly diminish the possibility of core meltdown or hydrogen generation, and minimise the pressure-driven release of radioisotopes during accident scenarios. Their higher operating temperatures improve the thermodynamic efficiency of power conversion systems.

Unlike solid-fuelled systems, MSRs typically employ a homogeneous liquid fuel–coolant mixture, thereby eliminating issues associated with heterogeneous fuel–coolant interfaces, such as fuel swelling and cracking, fission gas bubble nucleation, and departure from nucleate boiling. The isotropic thermal expansion of molten salt fuels results in a strongly negative fuel temperature coefficient of reactivity, reinforcing inherent safety characteristics. Furthermore, MSFRs can sustain a fast neutron spectrum, enabling the transmutation of transuranic elements and long-lived fission product inventories.

Worldwide, there is now a growing momentum to advance MSRs to technological readiness.

In Canada, Terrestrial Energy is developing the Integrated Molten Salt Reactor (IMSR)—a 400 MW_{th} small modular system fuelled by low-enriched uranium (LEU) and moderated by graphite [23]. Moltex Energy Canada is developing the Stable Salt Reactor – Wasteburner (SSR–W) concept, which employs actinide trichloride fuel salts contained within fuel assemblies analogous to those of LWRs, cooled by a surrounding pool of liquid salt [24].

In Denmark, Copenhagen Atomics is developing an autonomously controlled, fluoride-based, thermal-spectrum MSR moderated by heavy water [25], while Saltfoss Energy is developing the Compact Molten Salt Reactor (CMSR)—a modular LEU-fuelled system moderated using NaOH [26].

In France, collaborative initiatives such as EVOL, SAMOFAR, SAMOSAFER, ISAC, and MOSARWASTE unite academic and industrial partners in evaluating MSR designs for actinide management within the national closed fuel cycle. These efforts have culminated in the ARAMIS (Advanced Reactor for Actinides Management In Salts) reactor concept, which serves as the reference system for the present work [15]. Additionally, local startups such as NAAREA (liquidated in 2026 [27]), Stellaria, and Thorizon (Dutch–French) are pursuing chloride-based modular MSFRs designed to recycle uranium and plutonium from spent nuclear fuel, thereby supporting a circular, closed fuel cycle economy [28].

In the United States, Flibe Energy is developing the Lithium Fluoride Thorium Reactor (LFTR) and Lithium Fluoride Low Enriched Uranium Reactor (LFLEUR) [29]; TerraPower and Southern Company are advancing the Molten Chloride Fast Reactor (MCFR) [30]; Kairos Power is constructing a fluoride salt-cooled research reactor employing TRISO particle fuel [31].

Despite these numerous developments, China remains the only country to have achieved MSR criticality in the 21st century, with a 2 MW_{th} experimental thorium-fuelled MSR reaching criticality in 2023 and successfully undergoing on-line refuelling while continuing operation in late 2024 [32].

Historically, only fluoride-based MSRs have achieved criticality, and operational experience with chloride-based systems remains limited. Nevertheless, chloride salts exhibit several potential advantages over their fluoride counterparts:

- *Lower melting temperatures*, which allow for greater thermal operating margins while maintaining the integrity of structural alloys.

- *Higher actinide solubility*, enabling operation with natural or low-enriched uranium and facilitating designs aimed at reducing the actinide inventory in SNF.
- *Compatibility with fast neutron spectra* due to the higher atomic mass of chlorine, which promotes fast fission of non-fissile actinide isotopes and enhances the breeding ratio in systems employing the U/Pu fuel cycle.
- *Greater chemical flexibility*, allowing the application of a broader range of established nuclear and metallurgical separation techniques—such as electrorefining, electrowinning, and solvent extraction—for salt purification and clean-up, in contrast to the more chemically inert fluoride systems.

However, chloride salts also present several notable challenges compared with fluorides:

- *Isotopic composition*. Natural chlorine comprises 75.8 at% ^{35}Cl and 24.2 at% ^{37}Cl. To mitigate the formation of long-lived radioactive ^{36}Cl (β^- decay, $T_{1/2} \approx 3\times10^5$ y) via neutron capture on ^{35}Cl, isotopic enrichment to ≥99 at% ^{37}Cl is required.
- *Dehydration difficulty*. Chloride salts are more challenging to dehydrate, increasing the risk of impurity-induced corrosion of structural alloys during MSR operation.
- *Radiation damage*. The harder neutron spectrum in chloride media accelerates radiation-induced corrosion and embrittlement of structural materials.
- *Fuel cycle compatibility*. Chloride systems are less well-suited to Th/U breeding cycles, which prefer a thermal or epithermal neutron spectrum.
- *Limited chemical data*. The thermochemical and redox properties of chloride salts for nuclear applications are comparatively less characterised, necessitating extensive experimental R&D to establish reliable databases. [33]

At the moment, the major technical challenges limiting the deployment of MSRs for widespread civilian energy generation can be summarised as follows:

- Precise control and monitoring of fuel salt chemistry;
- Comprehensive understanding and prediction of corrosion phenomena affecting structural materials under extreme MSR conditions;
- Integration of remote handling, inspection, and maintenance systems capable of operating reliably in high radiation environments;
- Development of a robust and MSR-specific safety analysis framework;
- Qualification of structural and functional materials;
- Establishment of appropriate regulatory standards and licensing pathways.

I-5. The ARAMIS-A Reactor

With its long-standing expertise in closed fuel cycle technologies, France is strategically positioned to advance the recycling of transuranic elements from SNF into MSR fuel salts. In this context, the ARAMIS-A was conceived as an actinide burner reactor designed to transmute long-lived actinides into short-lived isotopes, thereby reducing the long-term radiotoxicity of high-level nuclear waste.

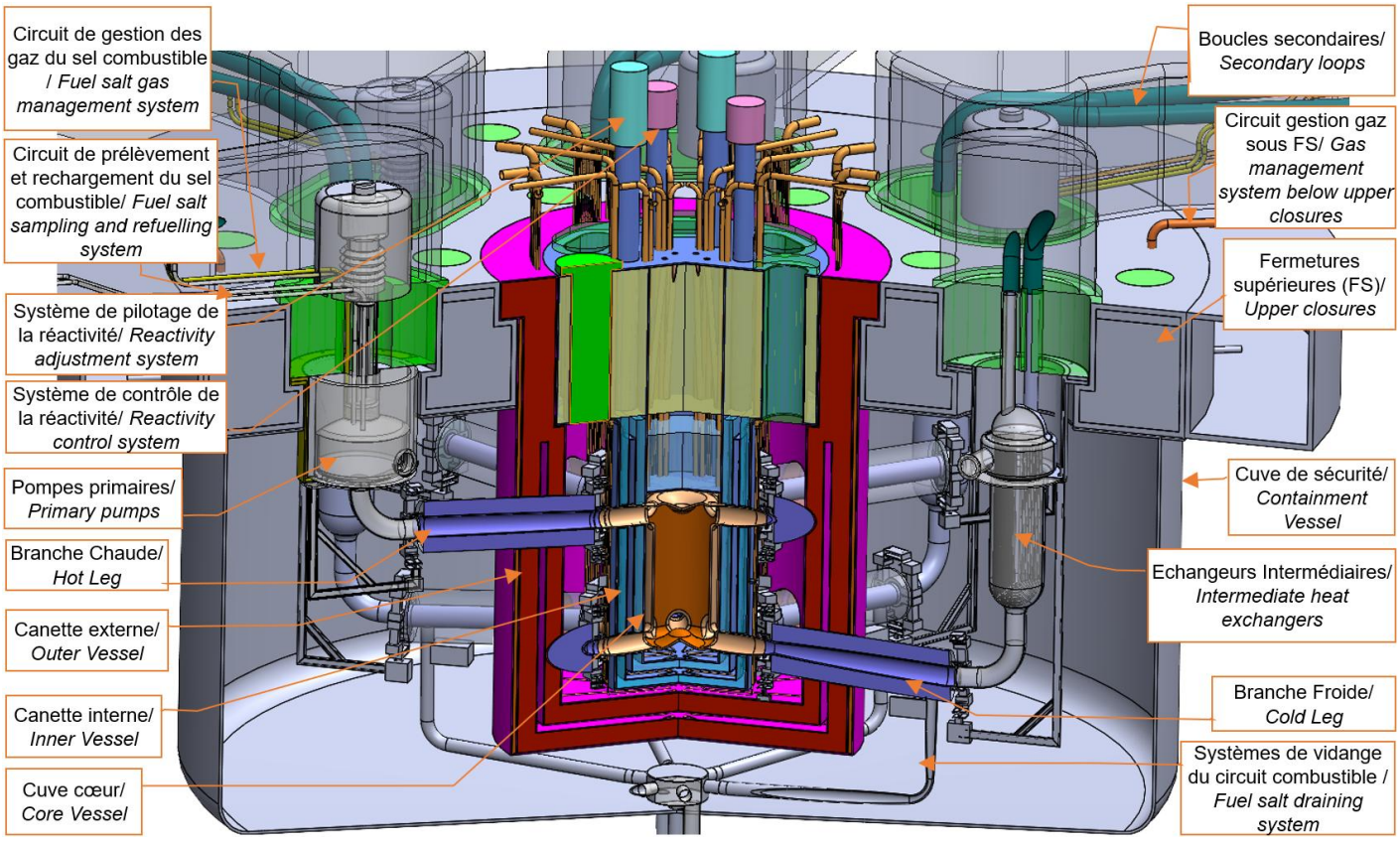

Figure I-6. Schematic view of the ARAMIS-A design (Version 2.0, Mid-2025). All reactor components are originally labelled in French, and translated into English by the author. [34]

Figure I-6 illustrates the latest sketch of ARAMIS-A (*Version 2.0, Mid-2025*) [34]. In the primary fuel circuit, the fuel mixture, composed of NaCl–$MgCl_2$–$PuCl_3$–$AmCl_3$, circulates through the reactor core and six connected sections, each comprising an intermediate heat exchanger (IHX), a fuel pump, and connecting piping. Through the IHX, fission-generated heat from the primary circuit is transferred to three intermediate loops, where a non-radioactive NaCl–$MgCl_2$ salt circulates. Thermal energy from the intermediate circuits is subsequently transferred via salt-gas heat exchangers (SGHX) to a Brayton power conversion system employing pressurised N_2 gas (180 bar) as the working fluid. A schematic representation of the ARAMIS circulation model is shown in **Figure I-7**, and the proposed operation parameters are given in **Table I-1** [35–37].

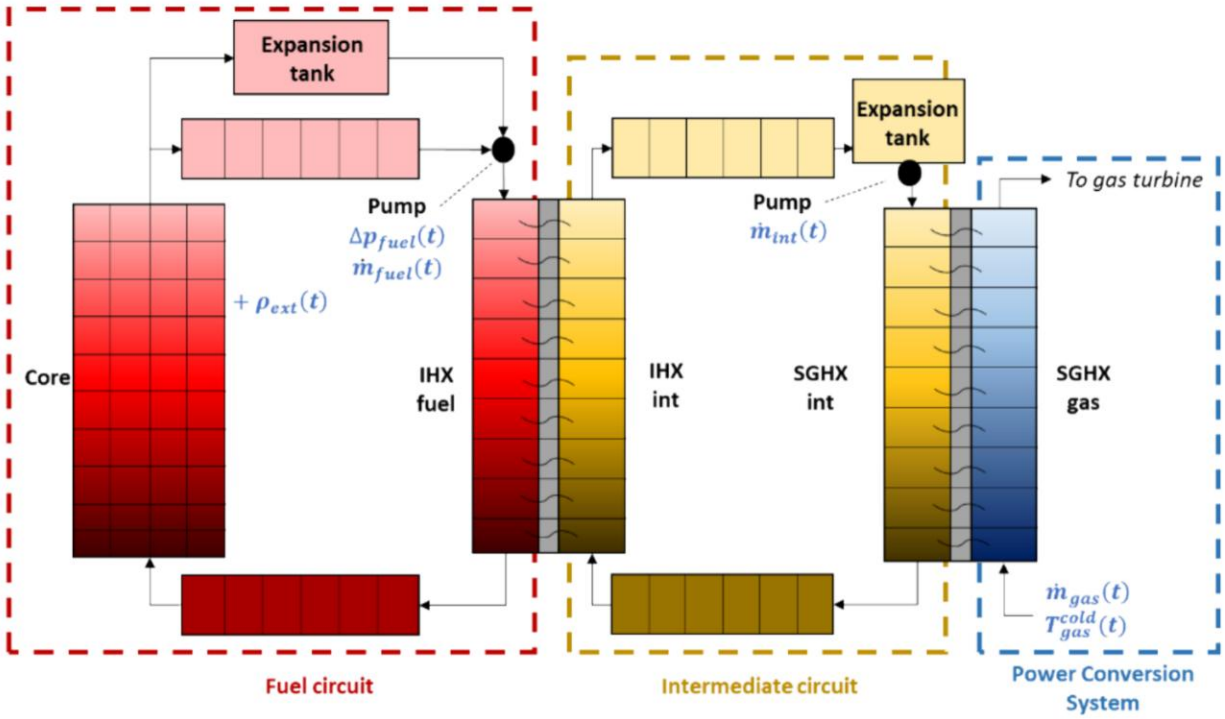

Figure I-7. Sketch of the ARAMIS-A heat circulation model. [36]

Table I-1. Proposed operation parameters of ARAMIS-A [35–37]

Parameter	Value
Thermal Power	300 MW_{th}
Core Volumic Power	250 MW/m^3
Core Volume (Critical Zone)	1.2 m^3
Core Diameter	0.91 m
Core Height	1.82 m
Core Circulation Time	0.6 s
Excore Volume	4.45 m^3
Excore Circulation Time	2.2 s
Composition of Fresh Fissile Salt	62.0 NaCl–14.95 $MgCl_2$–23.05 $(Pu,Am)Cl_3$ [in mol%]
Actinides Ratio in Fresh Fissile Salt	44.8 wt% Pu – 55.2 wt% Am
Initial Mass of Pu/Am	2827 kg/ 3485 kg
Minor Actinides Transmutation	78.9 kg/TWh_e (31.6 kg/TW_{th})
Fuel Salt Hot Temperature	650 °C
Margin to Materials Limit Temperature	50 °C
Fuel Salt Cold Temperature	570 °C

Margin to Fuel Salt Freezing	75 °C
Intermediate Salt Hot Temperature	550 °C
Intermediate Salt Cold Temperature	490 °C
Margin to Intermediate Salt Freezing	40 °C
Delayed Neutron Fraction	300 pcm
Delayed Neutron Fraction with Fuel Motion	70 pcm
Reactivity Coefficient of Density	16 pcm/kg·m^{-3}
Cycle Length/ Reactivity Loss	6 months/ 650 pcm

In chloride-based MSRs, NaCl is typically employed as the primary solvent or carrier salt to accommodate actinide trichlorides, which have intrinsically high melting temperatures. This is because NaCl is naturally abundant, inexpensive, and possesses well-characterised thermophysical and physicochemical properties. LiCl is generally avoided due to the low atomic mass of Li, which moderates neutrons and complicates the maintenance of a fast spectrum. In contrast, KCl is sometimes considered as an alternative carrier salt to maximise the actinide trichloride fraction in MSR fuels [38], given the high actinide solubility observed in the eutectic compositions of KCl–$AnCl_3$ mixtures [39].

The ARAMIS-A reactor, however, adopts a NaCl–$MgCl_2$ mixture as its carrier salt—a design choice motivated by several key advantages conferred by $MgCl_2$:

- *Lower melting temperatures*: NaCl–$MgCl_2$–$AnCl_3$ mixtures generally exhibit lower liquidus temperatures than the corresponding NaCl–$AnCl_3$ systems at the same actinide concentration [40]. This enables wider operational temperature margins between the cold-leg and hot-leg conditions, thereby enhancing safety and thermal stability.
- *Improved heat transfer*: $MgCl_2$ has a higher molar heat capacity and thermal conductivity than NaCl, contributing to improved thermal efficiency [41].
- *Reduced viscosity*: $MgCl_2$ is expected to reduce fuel viscosity, which can enhance heat transfer and support natural circulation, reducing dependence on active pumping systems. The effect of $MgCl_2$ on fuel viscosities will be demonstrated later in this thesis.
- *Mitigation of fissile precipitation*: $MgCl_2$ is projected to act as an "oxygen getter", sequestering residual oxygen impurities in the fuel and thereby limiting the formation and deposition of actinide-rich oxide phases on structural surfaces—a factor that can influence corrosion. This property will also be examined in detail in this thesis.

Despite these advantages, the use of $MgCl_2$ introduces one significant challenge: its strong affinity for oxygen and moisture. $MgCl_2$ is notoriously difficult to purify, and residual impurities originating from insufficiently purified $MgCl_2$ in the fresh fissile fuel may compromise the long-term corrosion resistance of structural alloys within the reactor.

I-6. Literature Review of MSR Fuel Chemistry

The scope of this thesis encompasses only the chemistry of the molten fuel salt in MSRs. As a preface to this study, a comprehensive review of contemporary research on MSR fuel chemistry was conducted. The works discussed here include studies on both fluoride- and chloride-based systems and are categorised based on the principal method of investigation—namely the Calculation of Phase Diagrams (CALPHAD) approach, MD simulations, and experimental studies.

Structural alloys in MSRs are exposed to extremely harsh conditions involving high temperatures, corrosive salt environments, and radiation damage. Owing to limited operational experience, Hastelloy-N remains the only alloy proven to endure these harsh conditions, as demonstrated in the MSRE at a maximum operating temperature of 650 °C [42]. Given this temperature constraint, many studies have focused on optimising actinide concentrations in fluorides and chlorides through phase diagram assessments. Commonly referred to as the CALPHAD method, these approaches employ thermodynamic modelling, typically supported by experimental data (e.g., differential scanning calorimetry and activity measurements), to construct phase diagrams at low computational cost.

The most prominent CALPHAD studies on fluoride fuel salts originate from collaboration between the European Commission Joint Research Centre (Karlsruhe, Germany) and TU Delft (The Netherlands). Beneš and Konings evaluated the potential actinide burner fuel system of LiF–NaF–BeF_2–PuF_3 and concluded that a quaternary fuel composition is necessary to satisfy MSR temperature constraints [43]. Capelli *et al.* examined the quinary LiF–NaF–ThF_4–UF_4 system, finding that BeF_2 had limited effect in lowering the liquidus temperature [44]. Further thermodynamic assessments of a fluoride-based fast reactor fuel mixture of LiF–ThF_4–PuF_3–UF_4 employed CeF_3 as a surrogate for PuF_3 to successfully reproduce PuF_3 solubility in LiF–ThF_4 [45]. Preliminary assessment of fission product solubility in fluoride-based MSR fuels was also conducted through the modelling of CsF–ThF_4, supported by vapour pressure measurements via Knudsen effusion mass spectrometry (KEMS) [46]. A broader investigation into volatile fission product stability (e.g., CsI) was performed through the thermodynamic assessment of all binary and ternary subsystems of LiF–ThF_4–CsF–LiI–ThF_4–CsI [47]. Alternatives to LiF-based fuel salts were also explored through the thermodynamic evaluation of the NaF–KF–UF_4 fuel system [48].

Historically, CALPHAD studies on actinide-containing chloride systems have centred on electrochemical separation applications, including the thermodynamic assessments of LiCl–KCl–UCl_3 [49], LiCl–KCl–$PuCl_3$ [50], and LiCl/RbCl/$CaCl_2$–NaCl–UCl_3–$PuCl_3$ [51] mixtures. More recently, studies on chloride-based fuel salts have garnered momentum. Beneš and Konings evaluated the NaCl–$MgCl_2$–UCl_3–$PuCl_3$ system and reported that $MgCl_2$ did not lower the melting temperature of the REBUS fast breeder reference fuel (55 mol% NaCl–38 mol% UCl_3–7 mol% $PuCl_3$) [40]. Another study examined NaCl–KCl–UCl_3–$PuCl_3$ mixtures as potential high-actinide-fraction fuels [52]. Thermodynamic evaluation of NaCl–KCl/$MgCl_2$/$CaCl_2$–UCl_3–$PuCl_3$ mixtures containing small amounts of soluble fission products (e.g., CsCl) revealed that the absence of intermediate compound/solid solution formation between $MgCl_2$ and actinide trichlorides helps lower liquidus temperatures with increasing fission product concentration [39]. Phase diagrams of thorium-based chloride fuels have also been reported [53].

In recent years, researchers at the University of South Carolina, in collaboration with U.S. national laboratories, have established the Molten Salt Thermodynamic Database (MSTDB), which compiles critically evaluated thermodynamic models and thermochemical parameters for fluoride and chloride salts [54,55]. The NaCl–$MgCl_2$–$PuCl_3$ ternary phase diagram constructed using the MSTDB is shown in **Figure I-8**.

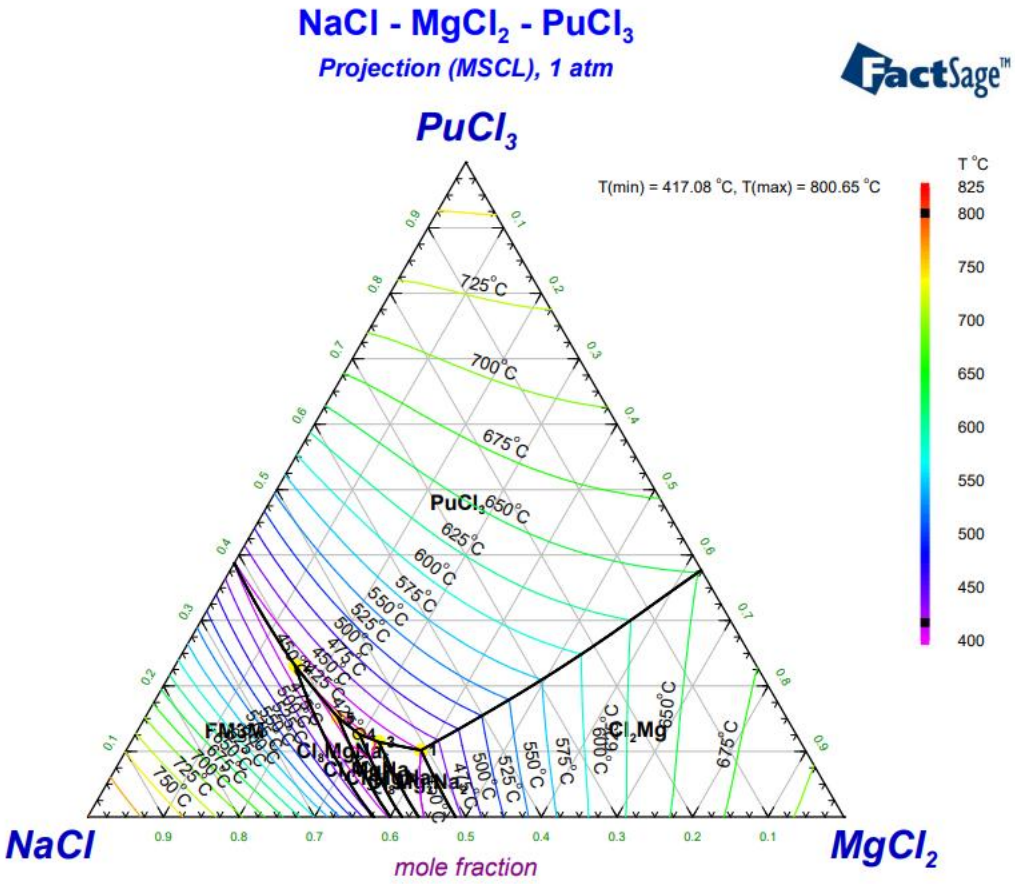

Figure I-8. Liquidus projection of the NaCl–$MgCl_2$–$PuCl_3$ ternary system, constructed using MSTDB.

Beyond phase diagram construction, the CALPHAD methodology has also been extended to predict thermophysical properties—such as density and viscosity—and validated against systems including NaCl–UCl_3, LiF–ThF_4, and LiF–ThF_4–UF_4 [33]. However, modern CALPHAD approaches, which rely on the quasichemical model with quadruplet approximation, do not fully capture the local structure of molten salts. This limitation affects the accurate quantification of thermophysical properties, particularly in multicomponent systems [56].

Consequently, MD simulations, which capture the local structure and dynamics of molten salts, are increasingly employed to predict their thermophysical properties. MD simulations can be broadly classified into two categories—*ab initio* MD (AIMD) and *classical* MD (CMD)—depending on how interatomic forces are computed. In AIMD, the forces are obtained directly from quantum mechanical calculations, allowing the explicit treatment of electronic structure and excited-state behaviour. AIMD has been applied to investigate the structure, dynamics and

thermophysical properties in MSR fuels, such as LiF–NaF–ThF_4–UF_4 [57], LiF–BeF_2–ThF_4 [58], NaCl–$MgCl_2$–UCl_3/UCl_4 [59], NaCl–$PuCl_3$ [60], NaCl–$ThCl_4$–UCl_3 [61]. A key advantage of AIMD is its ability to model the effects of chemically diverse, trace-level species in bulk fuel, such as the influence of transmutation products on the thermophysical properties of NaCl–UCl_3 [62]. However, because explicit treatment of electronic degrees of freedom is computationally expensive, AIMD simulations are typically restricted to relatively small systems (hundreds of atoms) and shorter timescales (on the order of tens of picoseconds). This finite-size effect may, in turn, limit the ability of AIMD to accurately predict bulk thermophysical properties, such as viscosity and thermal diffusivity.

In contrast, CMD is more widely employed for the simulation of molten salts. Early CMD studies commonly used the rigid ion model (RIM), which treated ions as point charges with fixed charge distributions. This model reproduced the dynamics of simple molten salts, such as LiCl–KCl, with reasonable accuracy [63,64]. However, RIM proved inadequate for more complicated melts, such as $ZnCl_2$, where local structures were dominated by corner-sharing tetrahedral units [65]. To overcome this limitation, the polarisable ion model (PIM) was introduced to account for the deformation of an ion's electron cloud in response to its electrostatic environment [66].

Initially, PIM interatomic potential parameters were empirically fitted to experimental data, such as structural factors and thermophysical properties [67]. However, these empirically derived parameters often lacked transferability, with prediction errors growing significantly when the melt composition deviated from the calibration dataset. To address this shortcoming, ab initio calculations were used to parametrise the PIM directly, yielding more physically realistic, accurate, and transferable interaction potentials [68]. Today, ab initio-parametrised PIM has been extensively employed for the CMD simulations of MSR fuel salts, including LiF–ThF_4 [69,70], LiF–BeF_2–ThF_4, LiF–NaF–KF–ThF_4 [71], NaCl–UCl_3 [72], KCl–UCl_3 [73], NaCl–KCl–UCl_3 [74], focusing primarily on local structure and transport properties. Apart from that, PIM-based CMD has also been used to evaluate density and local coordination structure for the CALPHAD modelling of NaF–ThF_4 [75] and to assess the suitability of lanthanide trichlorides as simulants for $PuCl_3$ in the NaCl–$PuCl_3$ eutectic composition [76].

More recently, advances in graph neural networks have enabled the development of machine-learned interatomic potentials (MLIPs) for CMD simulations, offering a balance between the high accuracy of ab initio methods and the computational efficiency of empirical potentials [77]. To date, MLIPs have only been applied to a handful of actinide-bearing MSR fuel systems, such as NaCl–$ThCl_4$, NaCl–UCl_3 [78], and NaCl–$PuCl_3$ [79]. Other MLIP studies of MSR fuels focus primarily on their carrier salts or secondary coolant mixtures, such as LiF–BeF_2 [80], LiF–NaF–ZrF_4, LiF–NaF–KF [81], NaF–BeF_2 [82], and NaF–BeF_2–ZrF_4 [83]. A key advantage of MLIPs lies in their ability to handle multicomponent systems—such as Cr–Ni speciation in LiF–BeF_2 [84]—that are prohibitively expensive for ab initio methods and insufficiently accurate for conventional interatomic potentials.

Experimental studies on the structure and thermophysical properties of actinide-bearing molten salts are inherently limited by their radiotoxicity, hygroscopicity, and corrosivity at elevated temperatures. Beyond the historical ARE and MSRE programs, such experiments have become exceedingly challenging in the 21st century due to stringent safety regulations and reinforced safeguards against nuclear proliferation.

For fluoride systems, Bessada *et al.* developed an airtight double-barrier cell enabling extended X-ray absorption fine structure (EXAFS) measurements of actinide-bearing fluoride melts at high temperatures. This apparatus was used to verify the local coordination environments in systems such as $KF–ThF_4$, $KF–UF_4$ [85], and $LiF–ThF_4–UF_4$ [86]. Smith *et al.* subsequently designed an alternative in situ high-temperature EXAFS setup suitable for radioactive and air-sensitive molten salts [87], applying it to examine the short-range structure of $AlkF–AnF_4$ (Alk = Li, Na, K, Cs; An = Th, U) [88]. Bobrova *et al.* introduced a steady-state coaxial cylinder to measure the thermal conductivity of $LiF–BeF_2–UF_4$, reporting a marked decrease in thermal conductivity with a 2 mol% addition of UF_4, indicative of strong complexation effects [89].

For chloride systems, more recent and extensive experimental work has been conducted primarily at ORNL. Rose *et al.* measured melting temperatures, heat capacities, and thermal diffusivities of the binary $NaCl–UCl_3$ and ternary $NaCl–KCl–UCl_3$ eutectic salts using differential scanning calorimetry (DSC) and laser flash analysis (LFA) [90]. Karlsson *et al.* synthesised high-purity $NaCl–PuCl_3$ and characterised its density and heat capacity, demonstrating good agreement with AIMD simulations. Nguyen *et al.* investigated the density and phase transition temperatures of the ternary 61 mol% NaCl–30 mol% UCl_3–9 mol% $PuCl_3$ mixture, comparing experimental data with CALPHAD, AIMD, and MLIP-CMD predictions [91]. Termini *et al.* measured the viscosity and thermal conductivity of high-purity 63 mol% NaCl–37 mol% UCl_3 using rolling ball viscometry and a variable gap apparatus, respectively, obtaining results consistent with AIMD simulations [92].

I-7. Thesis: Scope and Goals

This thesis is conducted within the framework of the ISAC project, partially funded by the France 2030 investment plan. ISAC aims to assess the feasibility of transmuting minor actinides in chloride-based fast reactors as a strategy to reduce France's long-lived HLW inventory. Achieving this objective requires a quantitative understanding of the chemistry of the proposed $NaCl–MgCl_2–PuCl_3–AmCl_3$ fuel mixture. In particular, elucidating the speciation behaviour of actinides in the chloride melts—and its dependence on composition and temperature—is essential for accurately predicting the thermophysical properties and oxygen solubility characteristics of high-temperature chloride fuels.

As discussed in the previous section, numerous theoretical studies on chloride-based MSR fuel systems have examined local coordination structures and predicted various thermophysical properties. Yet, most of these studies remain experimentally unvalidated, leaving their accuracy uncertain. This highlights a need for an integrated approach—combining experimental measurements and computer simulations—to achieve a more holistic and reliable molecular-level understanding of actinide-bearing chloride melts.

Since the 1990s, the CEMHTI–CNRS laboratory in Orléans has operated a comprehensive HT NMR platform, enabling detailed studies of the local structure of molten oxides, fluorides, and chlorides. Within this framework, chemical shift variations with composition and temperature provide direct experimental insight into the changes in coordination environments of NMR-active nuclei. However, the use of $PuCl_3$ and $AmCl_3$ is heavily regulated and not

permissible at CEMHTI. For that reason, the NMR-active and non-radioactive $LaCl_3$ was selected as a surrogate for the actinide trichlorides, and the NaCl–$MgCl_2$–$LaCl_3$ system was studied in this thesis. In particular, motivated by the potential advantages of $MgCl_2$ (outlined in Chapter I-5), special attention is given to the role of $MgCl_2$ in shaping the local coordination and its resulting influence on the bulk fuel properties.

It should be noted that while La^{3+} shares the +3 oxidation state relevant to MSR fuel conditions, the chemical analogy is imperfect: the empty 4*f* configuration of La^{3+} differs fundamentally from the partially occupied 5*f* shells of Pu and Am, and the latter elements exhibit a broader range of accessible oxidation states that may give rise to redox-dependent speciation absent in the lanthanum system.

The work presented in this thesis is divided into three main parts:

1. *Structural dynamics*. The local coordination structure of the ternary NaCl–$MgCl_2$–$LaCl_3$ system and its binary subsystems was examined as a function of composition and temperature. HT NMR served as the primary technique for probing the evolution of the ^{139}La and ^{35}Cl chemical shifts. Several complementary approaches were used to suport the interpretation of HT NMR data: solid-state NMR was employed to establish the relationship between chemical shifts and coordination numbers; PIM-based classical MD simulations were performed to quantify radial distribution functions, coordination structures, and lanthanide speciation networks; and first-principles NMR calculations were carried out on static MD snapshots to simulate NMR chemical shifts, providing a multimodal verification framework that ensures the consistency between experiment and simulation.

2. *Transport Properties.* The ion diffusivity and viscosity of NaCl–$MgCl_2$–$LaCl_3$ were investigated. PFG–NMR was employed as the primary experimental method to measure the diffusion of Na^+ ions in the NaCl–$LaCl_3$ binary mixture, while capillary viscometry data of the same binary system were obtained from the literature. These measurements were compared with transport properties calculated from PIM-based CMD simulations. Due to experimental constraints, the transport properties of ternary systems were only evaluated exclusively through simulation. Using computational metrics such as hydrodynamic radii and the potential of mean force, the multiscale influence of Mg^{2+} ions on the macroscopic transport behaviour was characterised for the first time.

3. *Oxygen Solubility*. In the ARAMIS-A design, $MgCl_2$ was selected as a fuel component for its presumed ability to sequester oxygen impurities—a hypothesis that had not been experimentally verified. To investigate this mechanism, ^{17}O-enriched LaOCl was used as a proxy for oxygen contamination in NaCl–$MgCl_2$–$LaCl_3$. High-temperature ^{17}O NMR served as the primary probe of oxygen behaviour in the melt, supported by PIM-based CMD and first principles NMR calculations. The pronounced ^{17}O chemical shift variations with NaCl:$MgCl_2$ composition provided—for the first time—direct molecular-level evidence and atomistic insight of $MgCl_2$-mediated oxygen solubility in chloride melts.

Before going into the main results, Chapter II provides the theoretical and methodological foundation of this work. It outlines the principles of NMR spectroscopy, the PIM used for classical MD simulations, and the DFT framework employed for quantum-mechanical calculations. The experimental procedures, simulation protocols, and interaction potential parameters are also detailed in this chapter.

The overarching goal of this thesis is to develop a comprehensive understanding of the chemistry and structure–property relationships governing chloride-based fuels for fast reactors. The data and analyses presented herein aim to sharpen the predictive capabilities of chloride fuel models and contribute to the qualification of chloride fuels for MSR applications. This thesis focuses exclusively on the chemistry of fresh fissile MSR fuels and does not address topics such as reactor neutronics, safety analysis, corrosion of structural alloys, or fission product behaviour.

Chapter II

Fondements Théoriques et Méthodologie de Recherche / Theoretical Background and Research Methodology

Résumé (Français)

Le chapitre II présente les fondements théoriques et méthodologiques mobilisés dans le cadre de ce travail, en s'appuyant sur trois approches complémentaires : la spectroscopie RMN, les simulations DM et les calculs de paramètres RMN basés sur des méthodes de premiers principes. Ces outils constituent le socle conceptuel et expérimental de l'analyse menée tout au long de la thèse.

Le chapitre II-1 est consacré à la spectroscopie RMN, une technique non destructive largement employée pour la caractérisation structurale et chimique des matériaux. Grâce à sa sensibilité aux variations de l'environnement atomique local et à sa sélectivité isotopique, la RMN permet d'accéder de manière fine à la structure et à l'environnement chimique de noyaux spécifiques. Le chapitre II-1 est structuré comme suit :

- le chapitre II-1.1 présente les principes fondamentaux de la spectroscopie RMN, y compris des notions telles que le moment magnétique nucléaire, l'effet Zeeman, la précession de Larmor, l'alignement des spins nucléaires dans un champ magnétique externe, la notion de magnétisation nette, les excitations par radiofréquence, ainsi que les concepts de masquage et de décalage chimique ;
- le chapitre II-1.2 décrit les séquences d'impulsions RMN les plus simples, telles que l'excitation à impulsion unique et l'écho de spin, qui constituent la base de la majorité des expériences RMN réalisées dans ce travail ;
- le chapitre II-1.3 est dédié aux temps de relaxation longitudinale (T_1) et transversale (T_2), essentiels à la compréhension de la dynamique des spins nucléaires, ainsi qu'aux procédures expérimentales mises en œuvre pour leur détermination;
- le chapitre II-1.4 est consacré à la RMN HT, qui constitue la principale technique expérimentale utilisée dans ce travail pour l'étude de la structure locale des chlorures fondus. Il propose une description détaillée du dispositif de RMN HT développé au laboratoire CEMHTI, incluant les caractéristiques de l'aimant RMN, du système de chauffage laser, de la sonde RMN et des creusets en nitrure de bore. Les évolutions marquées de la morphologie des signaux RMN entre les états solide et fondu sont également mises en évidence;
- le chapitre II-1.5 porte sur la RMN à l'état solide (RMN ES), utilisée comme technique expérimentale complémentaire afin d'établir des corrélations entre les nombres de coordination et les déplacements chimiques, ainsi que pour le *benchmarking* des calculs de paramètres RMN. Les expériences de RMN ES ont été réalisées à la fois en mode statique et en rotation à l'angle magique (*magic-angle spinning*, MAS), ces deux approches étant complémentaires pour l'étude de l'anisotropie du déplacement chimique et de l'élargissement quadripolaire dans les spectres RMN ES. La réduction des largeurs de raies et l'apparition des bandes de rotation caractéristiques du mode MAS sont notamment discutées;
- le chapitre II-1.6 présente la RMN–PFG, en utilisant un dispositif spécifiquement développé au CEMHTI pour la mesure des diffusivités ioniques dans les sels fondus. La séquence de type *Stimulated Gradient Echo*

(STGE) employée pour les mesures RMN–PFG est décrite, ainsi que sa dépendance vis-à-vis des temps T_1 et T_2.

- Enfin, le chapitre II-1.7 détaille les procédures de préparation des échantillons ainsi que les protocoles expérimentaux mis en œuvre pour l'ensemble des expériences RMN réalisées dans le cadre de cette thèse.

Le chapitre II-2 est consacré aux simulations classiques de DM, une approche de calcul relativement peu coûteuse permettant d'accéder à la structure locale et aux propriétés thermophysiques de matériaux complexes et dangereux, tels que les sels fondus. Le chapitre II-2 est structuré comme suit :

- le chapitre II-2.1 établit les bases théoriques des simulations classiques de DM dans le cadre du PIM ;
- le chapitre II-2.2 présente l'ensemble des paramètres des potentiels d'interaction utilisés dans cette étude, incluant les polarisabilités atomiques, les potentiels interatomiques de type Born–Mayer, ainsi que les paramètres d'amortissement de Tang–Toennies associés aux interactions charge–dipôle ;
- le chapitre II-2.3 détaille le protocole de simulation mis en œuvre, comprenant le nombre d'atomes considérés, la génération des configurations initiales, le traitement algorithmique des interactions électrostatiques, le choix des ensembles statistiques, les procédures d'équilibrage, ainsi que les étapes de post-traitement des données.

Le chapitre II-3 est consacré aux calculs de paramètres RMN basés sur des méthodes de premiers principes. Cette étape constitue un élément clé de la démarche de validation multimodale mise en œuvre dans ce travail, en permettant de vérifier la cohérence des structures locales obtenues à partir des expériences RMN et des simulations DM. Le chapitre II-3 est structuré comme suit :

- le chapitre II-3.1 présente les bases théoriques des calculs RMN de premiers principes dans le cadre de la DFT ;
- le chapitre II-3.2 détaille le protocole des calculs RMN réalisés à l'aide du code VASP, incluant le choix des pseudopotentiels, l'échantillonnage de la zone de Brillouin des points *k*, la sélection de l'énergie de coupure, ainsi que les procédures d'étalonnage des blindages chimiques calculés pour l'obtention des déplacements chimiques. Les paramètres d'entrée spécifiques aux calculs RMN sur des structures cristallines et désordonnées y sont également discutés ;
- le chapitre II-3.3 décrit le protocole employé pour les calculs d'optimisation géométrique réalisés avec le code VASP, permettant de détendre les positions ioniques et d'accéder à la configuration de l'état fondamental au niveau DFT.

II-1. Nuclear Magnetic Resonance

NMR spectroscopy is a non-destructive method widely used for materials characterisation. It exploits the response nuclei with non-zero spin when subjected to radio-frequency excitation pulses in a strong, uniform magnetic field. Because NMR signals are sensitive to variations in the local atomic environment and are isotope-selective, the technique provides nanoscale information on the structural and chemical surroundings of specific nuclei. In this work, NMR spectroscopy is used to investigate the local structure of solid and molten chloride systems.

II-1.1. Fundamental Principles

NMR measurements are enabled by the intrinsic nuclear spin, $\vec{\boldsymbol{I}}$, which originates from the combined magnetic moments of protons and neutrons (i.e., nucleons) comprising the atomic nucleus. In general, nuclei with an even total number of nucleons have zero spin, although notable exceptions such as ^{2}H, ^{6}Li, and ^{14}N exhibit spin $I = 1$. Conversely, nuclei with an odd mass number, *Z*, typically possess non-zero nuclear spin, $|\vec{\boldsymbol{I}}| \geq ½$. The corresponding nuclear magnetic moment, $\vec{\boldsymbol{\mu}}$, is defined as:

$$\vec{\boldsymbol{\mu}} = \gamma \frac{h}{2\pi} \vec{\boldsymbol{I}},$$

(Eq. II-1)

where γ is the isotope-specific gyromagnetic ratio and h=6.6626×10^{-34} J·s is Planck's constant.

The magnetic quantum number, m_I, is quantised. For a nucleus with intrinsic spin *I*, the magnetic quantum number can only take discrete values, i.e., $m_I = -I, -I+1, -I+2, \ldots, I-2, I-1, I$.

In the absence of an external magnetic field, nuclei exist in the ground state, yielding a degeneracy of *2I+1*. When a magnetic field $\vec{\boldsymbol{B}}$ is applied, this degeneracy is lifted: the nuclear levels split into *2I+1* distinct Zeeman states. The energy of each particular state is given by:

$$E = -\vec{\boldsymbol{\mu}} \cdot \vec{\boldsymbol{B}}.$$

(Eq. II-2)

For a static field magnetic field B_0 applied along the *z*-axis, the energy of each Zeeman level becomes:

$$E = -\mu_z B_0 = -m_I \gamma \frac{h}{2\pi} B_0,$$

(Eq. II-3)

showing that the energy separation between levels increases linearly with the applied field strength, B_0. Moreover, states with magnetic moments aligned with the external field correspond to lower energy, whereas states aligned against the field lie at higher energy. A schematic illustration of this Zeeman splitting is given in **Figure II-1**.

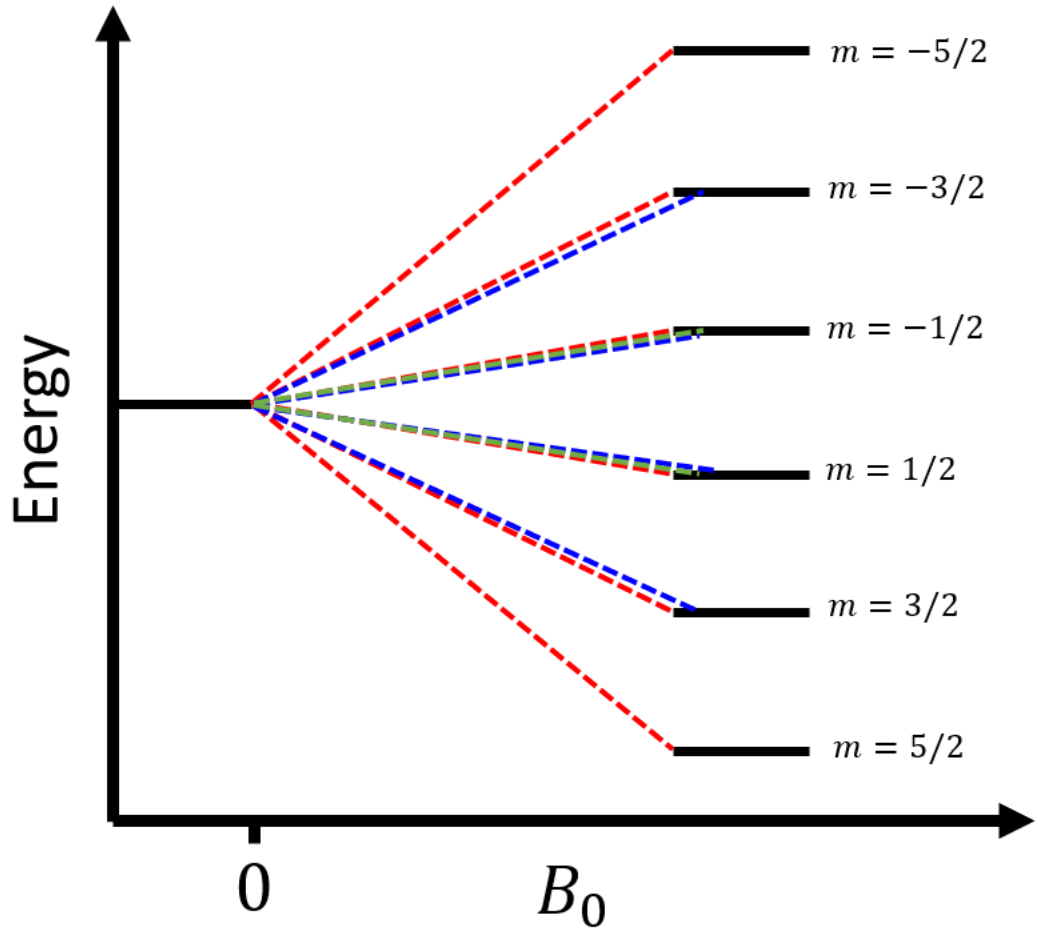

Figure II-1. Energy level splitting for nuclei with I=1/2 (Green dashed lines), I=3/2 (Blue dashed lines), I=5/2 (Red dashed lines), assuming the same gyromagnetic ratio. The slightly offset blue and green lines are for illustrative purposes only.

Figure II-2 illustrates the effects of an external magnetic field on the net magnetic moment of an ensemble of nuclei from a classical viewpoint. In the absence of a field, the individual nuclear magnetic moments are oriented randomly, and there is no net magnetisation as a result. When an external magnetic field is applied, it exerts a torque, $\vec{\boldsymbol{\tau}} = \vec{\boldsymbol{\mu}} \times \vec{\boldsymbol{B}}$, on each magnetic moment, causing the associated angular momentum vector to precess about the external field axis at the Larmor frequency, ν_0, given by:

$$\nu_0 = \frac{\gamma}{2\pi} B_0$$

(Eq. II-4)

Because the applied field also lifts the degeneracy of nuclear spin states, a Boltzmann distribution that slightly favours the lower-energy Zeeman levels is also produced. This population imbalance creates a net macroscopic nuclear magnetisation, M_0, along the direction of B_0, which scales with the number of contributing nuclei and forms the basis of NMR signal detection.

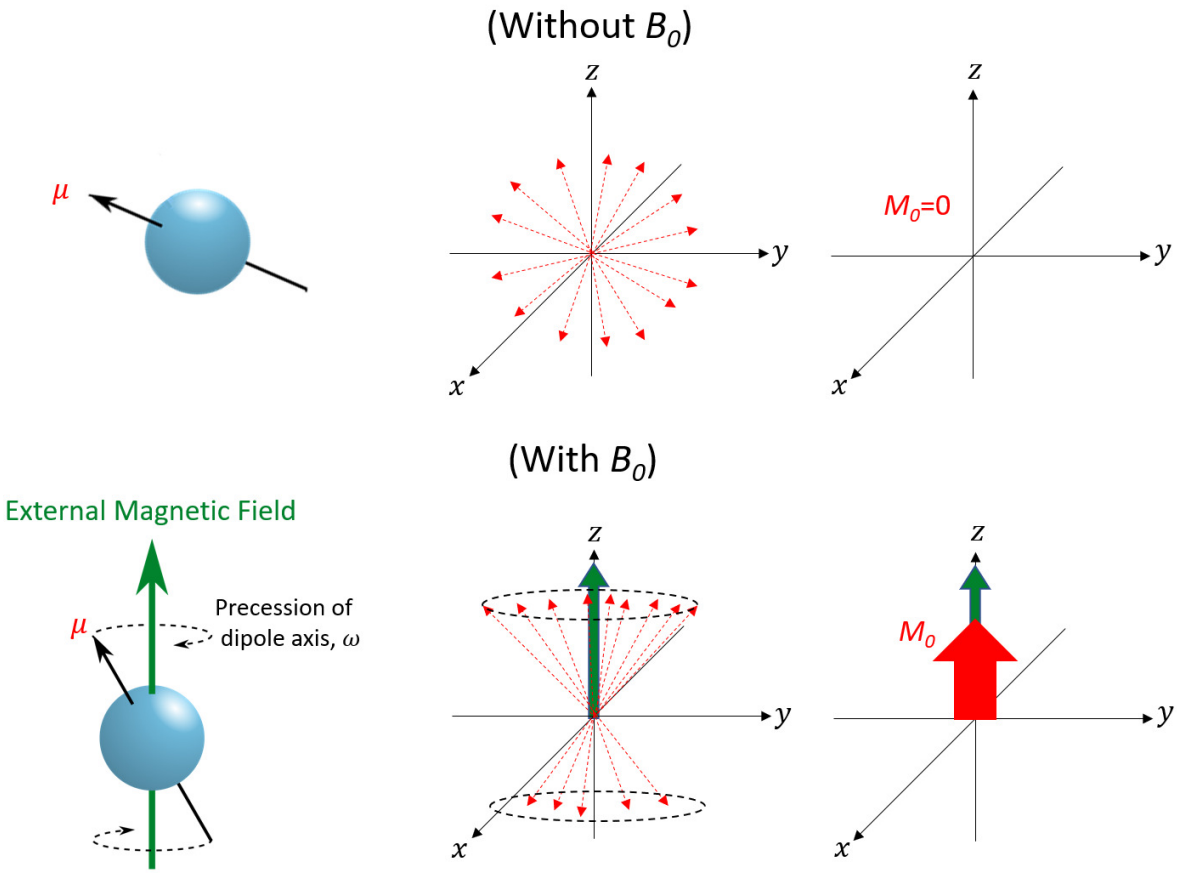

Figure II-2. Classical interpretation of the effects of external magnetic field on individual nuclei (left), an ensemble of nuclei (middle), net magnetisation vector (right).

In NMR, a second magnetic field, B_1, oscillating perpendicularly to the static B_0 field, is used to excite the nuclear spins. Excitation occurs only when the B_1 field oscillates at the Larmor frequency (i.e., under resonance conditions), which lies in the radiofrequency (RF) range in practice. An RF pulse typically lasts from a few microseconds to milliseconds. Under RF irradiation, the RF field appears as a static transverse field in the rotating frame of nuclei and drives transitions between adjacent Zeeman levels ($\Delta m = \pm 1$). As a result, the RF pulse tips the macroscopic magnetisation M_0 from the z-axis into the transverse plane, creating a measurable transverse component M_{xy}. After turning off the RF pulse, M_{xy} precesses about the z-axis as it gradually decays back toward the equilibrium magnetisation M_0, inducing a voltage in the receiver coil known as the free induction decay (FID). Applying a Fourier transform to the FID yields the NMR spectrum.

The principal observable in NMR spectroscopy is the chemical shift, which originates from the interaction between the applied magnetic field $\vec{\boldsymbol{B}}$ and the electron cloud surrounding the nucleus. When $\vec{\boldsymbol{B}}$ is applied, the surrounding electrons respond by circulating, generating an induced field $\vec{\boldsymbol{B}}_{\boldsymbol{i}}$ that typically opposes the applied field. The effective field experienced by the nucleus is therefore:

$$\vec{\boldsymbol{B}}_{eff} = \vec{\boldsymbol{B}} - \vec{\boldsymbol{B}}_i = (\mathbf{1} - \boldsymbol{\sigma})\vec{\boldsymbol{B}},$$

(Eq. II-5)

where $\boldsymbol{\sigma}$ is the magnetic shielding tensor, reflecting the dependence of the induced field on the molecular orientation relative to $\vec{\boldsymbol{B}}$. Since the Larmor frequency is directly proportional to the magnetic field (Eq. II–4), the nuclear precession frequency is shifted by the same tensor:

$$\boldsymbol{\nu} = (\mathbf{1} - \boldsymbol{\sigma})\nu_0.$$

(Eq. II-6)

In practice, this results in small frequency shifts—typically on the order of Hz to kHz—in the FID, which gives rise to chemical shift dispersion observed in NMR spectra.

In solids, where molecular orientations are usually fixed or only partially averaged, the anisotropy of $\boldsymbol{\sigma}$ leads to chemical shift anisotropy (CSA), resulting in broadened or orientation-dependent spectral features. In contrast, in liquids and molten systems, rapid molecular tumbling averages the tensor to its isotropic value:

$$\sigma_{iso} = \frac{1}{3}\left(\sigma_{xx} + \sigma_{yy} + \sigma_{zz}\right),$$

(Eq. II-7)

yielding a single resonance frequency for each chemically distinct site.

To express frequency shifts in a magnetic-field-independent manner, NMR spectra are always referenced to a reference compound. The chemical shift, δ, reported in parts per million or ppm, is defined as:

$$\delta = \frac{\nu - \nu_{ref}}{\nu_{ref}}.$$

(Eq. II-8)

It is important to note that the chemical shift is also a tensor quantity in the general case. In solids, the full chemical shift tensor determines the anisotropic lineshape, and the isotropic chemical shift, δ_{iso}, is defined analogously to the isotropic chemical shielding:

$$\delta_{iso} = \frac{1}{3}\left(\delta_{xx} + \delta_{yy} + \delta_{zz}\right).$$

(Eq. II-9)

II-1.2. Basic Pulse Sequences

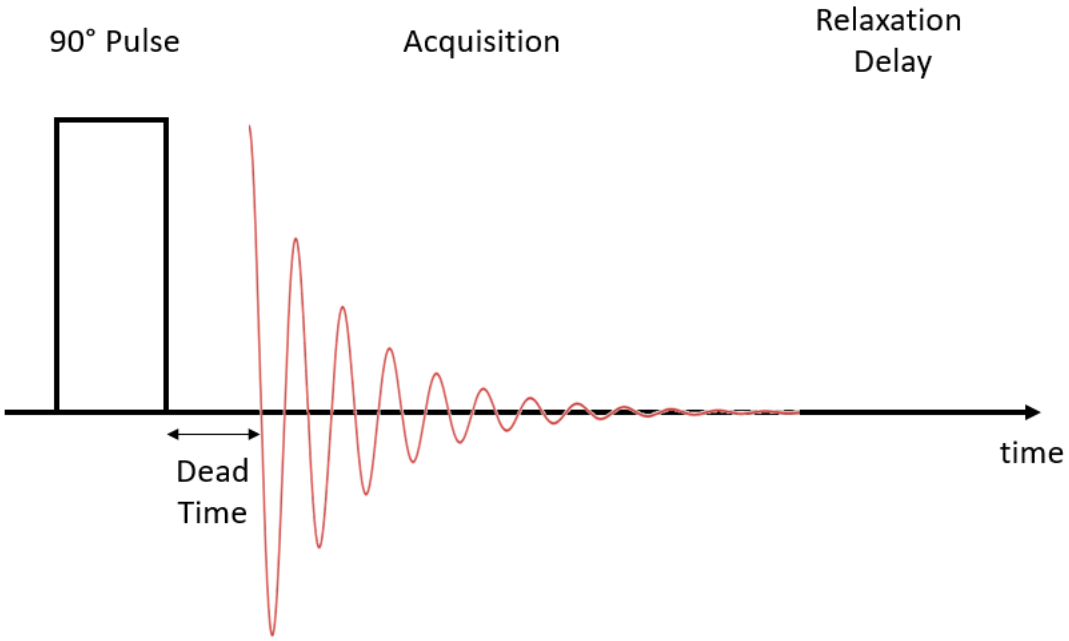

Figure II-3. Schematic representation of the single-pulse NMR experiment.

The single-pulse excitation (**Figure II-3**) lays the foundations of most NMR experiments. In its simplest form, a short 90° RF pulse is applied at the Larmor frequency, producing a transverse magnetic field that tips the equilibrium magnetisation M_0 away from the *z*-axis into the *xy*-plane. The pulse duration required to generate a 90° rotation is typically determined from nutation-frequency calibration experiments using a reference solution.

Once the pulse is switched off, the transverse magnetisation M_{xy} precesses about B_0 while relaxing back toward equilibrium, generating the FID. After a relaxation delay—long enough for most nuclei to return to their equilibrium state—the experiment is repeated and successive FIDs are accumulated to improve signal-to-noise ratio. The resulting FID is subsequently Fourier transformed to yield the NMR spectrum. Because liquid and molten samples typically exhibit rapid dynamics and short relaxation times, the single-pulse experiment remains the most robust and commonly used approach for acquiring their NMR spectra.

While the single-pulse excitation is straightforward to perform, it may at times be inadequate for obtaining coherent NMR signals. Due to inhomogeneities in B_0 and local variations in chemical environment, individual nuclear spins begin to dephase immediately after the 90° pulse, causing the transverse magnetisation M_{xy} to decay more rapidly than predicted by intrinsic relaxation alone.

The spin echo (**Figure II-4** [93]) is a fundamental pulse sequence designed to mitigate these effects by refocusing dephasing magnetisation and recovering coherent signals that would otherwise be lost. The sequence begins with a 90° pulse that tips the equilibrium magnetisation into the transverse plane. During the subsequent delay t, the transverse

magnetisation dephases. A 180° pulse is then applied, inverting the phases of the individual spin packets: spins that had been leading now lag, while those that had been lagging now lead. After an additional delay t, the spins rephase and form a spin echo at time $2t$, producing a restored signal that is detected as the Hahn echo. As the echo amplitude still decays according to the transverse relaxation time T_2, the Fourier transform of the echo signal can still be used to obtain an NMR spectrum with reduced contributions from field inhomogeneity, enhancing the signal resolution.

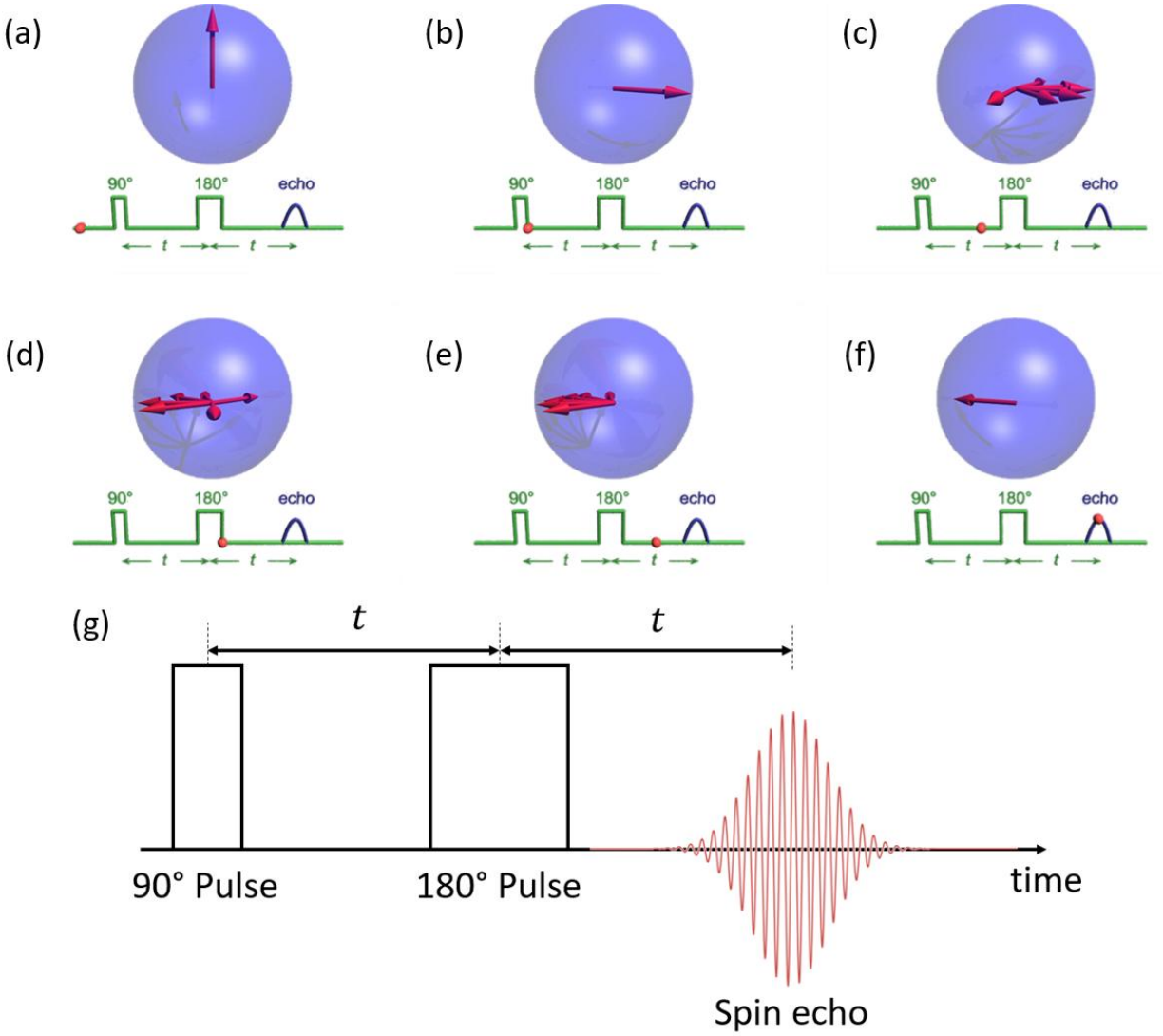

Figure II-4. Schematic representation of the spin echo, showing the response of spins in every stage of the pulse sequence (a–f) and the echo signal (g). [93]

II-1.3. Relaxation Times, T_1 and T_2

In NMR, the return of nuclear spin magnetisation to equilibrium after RF excitation is governed by two distinct relaxation processes, each described by its own characteristic time constant:

- T_1, the *longitudinal* or *spin-lattice relaxation* time, determines the recovery of the magnetisation component $\overrightarrow{\boldsymbol{M}_{\boldsymbol{z}}}$ along the direction of the applied magnetic field $\overrightarrow{\boldsymbol{B}}$ (conventionally taken as the z-axis). In practice, T_1 limits the pulse repetition rate of many experiments, as delays of approximately five to seven times T_1 are typically required for complete recovery of equilibrium magnetisation.

- T_2, the *transverse* or *spin-spin relaxation* process, characterises the decay of phase coherence of magnetisation components in the *xy*-plane. Short T_2 values lead to rapid FID decay and consequently poorer spectral resolution.

T_1 and T_2 relaxation times can be measured using relatively simple pulse sequences. The inversion-recovery experiment is the most common method to measure T_1 (**Figure II-5a**). A 180° pulse is first applied to invert the magnetisation from $+M_0$ to $-M_0$. The magnetisation is allowed to relax toward equilibrium during a variable delay t. At the end of this delay, a 90° pulse rotates the partially recovered longitudinal magnetisation M_z into the transverse plane, where it generates an FID that is recorded and Fourier transformed. As t increases, the longitudinal magnetisation recovers toward $+M_0$, and the measured signal amplitude increases accordingly. Plotting the signal intensity (or integrated peak area) versus t yields an exponential recovery curve described by:

$$M_z(t) = M_0(1 - 2\mathrm{e}^{-t/T_1}).$$

(Eq. II-10)

Ideally, this expression fits well, but in practice, slight miscalibrations of the 90° or 180° pulse lengths can distort the inversion efficiency. To account for imperfect inversion, an additional coefficient, c_0, is introduced:

$$M_z(t) = M_0(1 - c_0\mathrm{e}^{-t/T_1}),$$

(Eq. II-11)

Although the prefactor changes, the exponential term remains unchanged, and the extracted T_1 value remains reliable.

The most straightforward method to determine T_2 is the variable-delay Hahn echo experiment (**Figure II-5b**). In this sequence, the delay t between the initial 90° pulse and subsequent 180° pulse is systematically varied. As t increases, dephasing of the transverse magnetisation component increases, and the amplitude of the refocused spin echo diminishes correspondingly, resulting in weaker NMR signals. Plotting the signal amplitude versus t yields an exponential decay that follows:

$$M_z(t) = M_0\mathrm{e}^{-2t/T_2}.$$

(Eq. II-12)

Here, the factor of 2 arises because the total evolution time contributing to the transverse dephasing is $2t$.

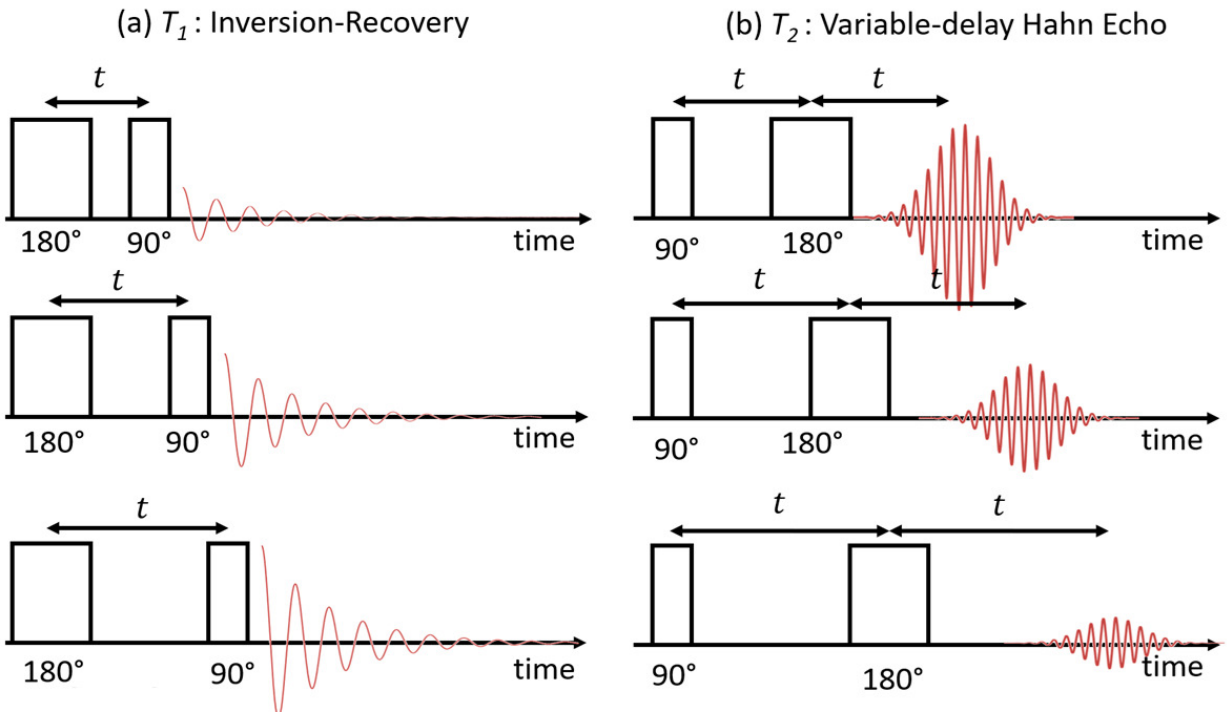

Figure II-5. Schematic representation of (a) the inversion-recovery experiment for T_1 measurements and (b) the variable-delay Hahn echo experiment for T_2 measurements.

II-1.4. High-Temperature NMR

HT NMR is the primary technique employed in this work to investigate the local structure of molten chlorides. Such measurements require specialised instrumentation capable of maintaining and probing materials at extreme temperatures while preserving NMR sensitivity. At the CEMHTI–CNRS laboratory in Orléans, a unique HT NMR experimental platform has been operated since the 1990s, enabling in-situ NMR studies of samples heated well into the molten regime. A schematic overview of the HT NMR system is provided in **Figure II-6**.

All HT NMR measurements in this study were performed on a Bruker AVANCE I spectrometer operating at 9.4 T. Sample heating is achieved using two axial CO_2 lasers, each delivering 250 W at a wavelength of 10.6 µm. The laser beams are reflected at right angles and focused onto the sample, allowing continuous radiative heating up to temperatures as high as 2500 °C. The heated region is enclosed by a ceramic heat shield, which protects the RF coil from thermal damage during operation.

Different sample environments are used depending on the physical and chemical nature of the materials investigated. For oxide glasses, small spherical beads (about 3 mm in diameter) are levitated inside the NMR probe with the aid of an aerodynamic levitation system. In contrast, molten salts are typically hygroscopic, volatile, and corrosive at high temperatures, necessitating the use of sealed containers. In this study, the samples were contained in high-purity boron nitride (BN) crucibles and enclosed with screw caps machined from the same material. These BN crucibles offer several advantages for the studies on molten salts, such as excellent thermal conductivity (20–300 W/m·K at 20 °C),

chemical and thermal stability up to ~2600 °C in reducing atmospheres, and minimal oxygen contamination due to the absence of oxide binders in their fabrication. The aerodynamic levitation system allows heating up to 2500 °C, while the crucible design can achieve a maximum temperature of 1500 °C. [94]

The NMR probe used in this study is the UHT 9mm crucible axial probe. Originally designed for liquid-state NMR, this probe was custom-modified in collaboration with Bruker for high-temperature operation. It is a static, multinuclear probe with two independently tunable RF channels: one for the high-Larmor-frequency nuclei (^{1}H and ^{19}F) and one for other nuclei (X). To ensure stable operation under extreme conditions, the probe incorporates a dual air-cooling system operating at ambient temperature and pressure. This cooling preserves the integrity of the RF coil, tuning elements, and other electronic components during laser-induced heating. Additionally, the probe includes a dedicated argon gas line, which delivers a continuous flow of dried argon (1.9 cm^3/s) through the laser pathway during high-temperature experiments. This inert gas stream maintains an oxygen-free environment around the sample and prevents oxidation of the BN crucibles during laser heating.

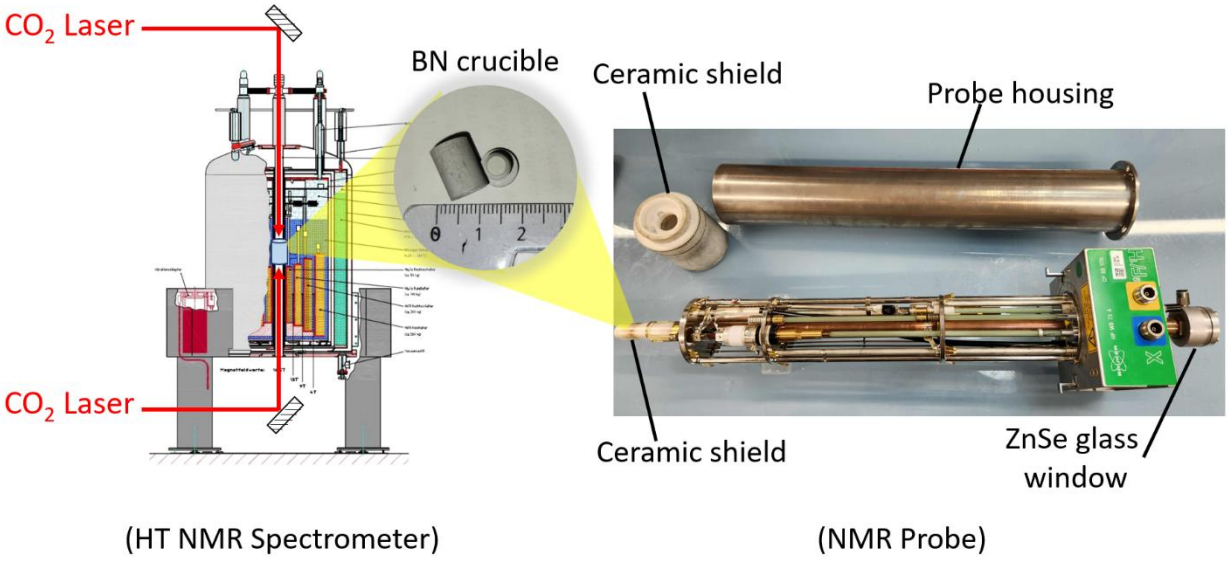

Figure II-6. Schematic diagram of the heating setup, high-purity BN crucible, and NMR probe for HT NMR at CEMHTI.

NMR signals of chloride salts differ markedly between the solid and molten states. For example, **Figure II-7** compares the static ^{139}La spectra of pure $LaCl_3$ at room temperature and at 1000 °C (beyond its melting point of 860 °C). In the solid state, the ^{139}La resonance is broad and anisotropic, reflecting strong quadrupolar interactions characteristic of the crystalline environment. Upon melting, this spectrum collapses into a sharp, isotropic Lorentzian peak. The isotropic chemical shift also changes significantly—from 305 ppm in the solid state to 570 ppm in the melt—revealing a substantial transformation of the local coordination environment.

The sharp, isotropic lines observed in molten-state NMR arise from the rapid ionic motion in the melt. The characteristic timescale of ionic exchange in molten salts (~ps) is several orders of magnitude faster than the temporal

resolution of NMR spectroscopy (~ns). As a result, anisotropic interactions—such as quadrupolar coupling and chemical shift anisotropy—are motionally averaged to zero, yielding a narrow, isotropic resonance. The resulting isotropic chemical shift can thus be interpreted as the temporal average of the chemical shifts of all possible local ionic configurations in the melt. This provides a meaningful link between experiment and simulation: ion dynamics from MD simulations combined with first-principles NMR calculations can be statistically averaged to reproduce this isotropic chemical shift.

Beyond their structural interpretation, the pronounced changes in spectral features across the solid–liquid phase transition also enable temperature calibration of the HT NMR setup. For this purpose, the ^{19}F signal of simple alkali fluorides—such as LiF, NaF, KF and their mixtures—is well suited, owing to their availability, the non-quadrupolar nature of ^{19}F, the low viscosity of the melt, and their well-defined melting temperatures. During a real-time ^{19}F scan, the laser power is gradually adjusted; a precipitous transition in the line shape and isotropic chemical shift marks the melting point of the salt. The resulting calibration curves relating laser power to temperature for the UHT 9mm Crucible probe and UHT 400 Gradient probe (used for PFG–NMR) are presented in **Figure II-8**.

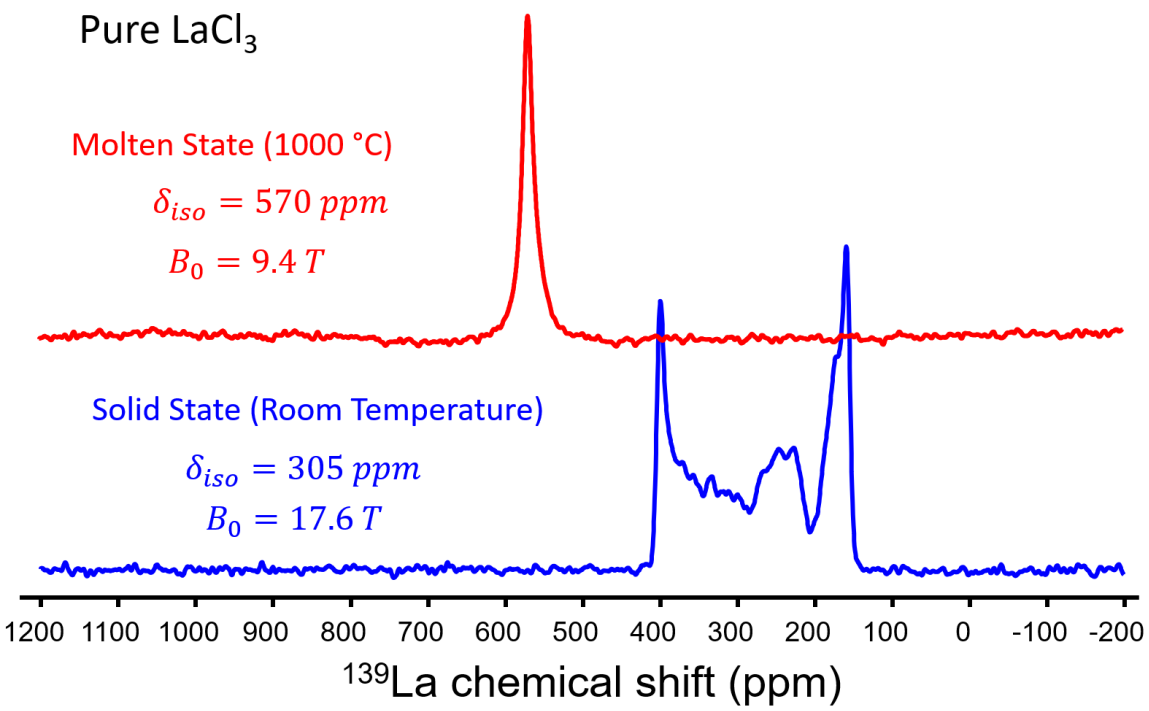

Figure II-7. Comparison of ^{139}La spectra of pure $LaCl_3$ in the molten state (top, red solid line) and in the solid state (bottom, blue solid line). The molten-state spectrum was obtained using the HT NMR spectrometer operating at 9.6 T, while the static solid-state spectrum was acquired using a separate NMR spectrometer operating at 17.6 T.

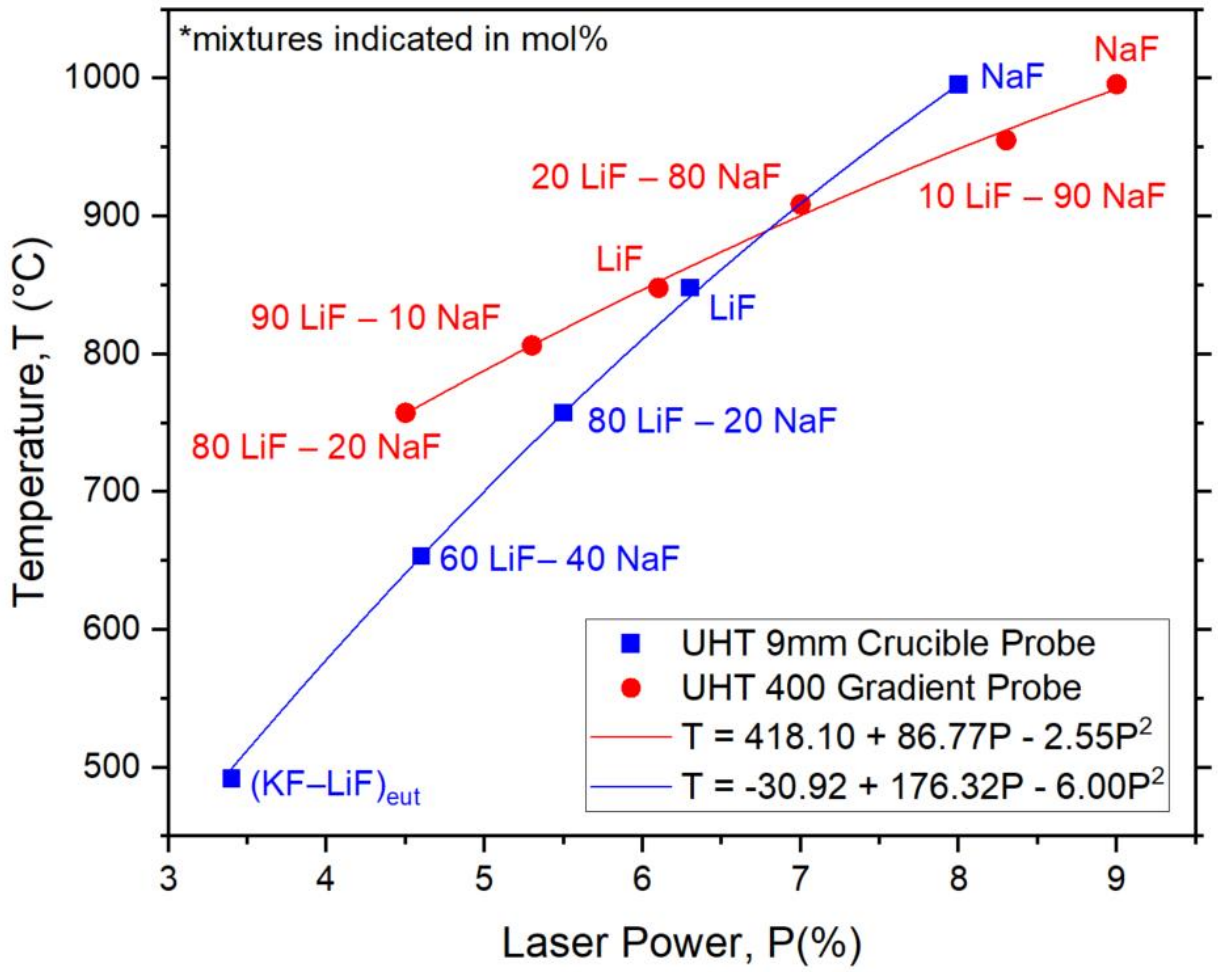

Figure II-8. Laser-power–temperature calibration curves relating laser power for the UHT 9mm Crucible probe (solid blue line and squares) and UHT 400 Gradient probe (solid red line and circles). The temperature calibration probe is valid from 500 to 1000 °C for the UHT 9mm Crucible and from 750 to 1000 °C for the UHT 400 Gradient probe in the HT NMR spectrometer operating at 9.4 T.

II-1.5. Solid-state NMR

While HT NMR is the principal method of investigation in this study, solid-state NMR (SS NMR) was employed as a complementary technique to support the interpretation of the molten-state results—for example, in verifying sample purity, establishing relationships between coordination numbers and chemical shifts, and benchmarking DFT-based NMR calculations.

SS NMR spectra in this work were obtained primarily using single-pulse and spin-echo experiments, which have been described in earlier sections. In crystalline solids, most static NMR spectra are inherently broadened due to orientation-dependent interactions, including CSA, dipolar coupling, and quadrupolar interactions. Because ions in a solid lattice adopt fixed orientations with respect to the external magnetic field B_0, each crystallite contributes a slightly different resonance frequency, resulting in broad powder patterns.

The chloride salts examined in this work contain only quadrupolar nuclei ($I > 1/2$), for which the interaction between the nuclear quadrupole moment and the local electric field gradient (EFG) produces substantial quadrupolar broadening. The orientation of the EFG tensor with respect to B_0 defines the magnitude of this effect. In static solids, the first-order quadrupolar interaction is typically the dominant contributor to the broad linewidth. Static powder patterns were analysed using the *Q-stat ½* and QUASAR modules in the DMFit software [95] , allowing extraction of key NMR parameters, such as the isotropic chemical shift (δ_{iso}), the quadrupolar coupling constant (C_Q), and the asymmetry parameter (η).

An effective method to reduce linewidth in SS NMR is magic-angle spinning (MAS). In MAS, rotors containing powdered samples are rapidly spun (kHz regime) at the magic angle of 54.74 ° relative to B_0. This condition averages out the first-order CSA interactions, resulting in significantly narrower lines. For quadrupolar nuclei, MAS does not remove the first-order quadrupolar interaction, but it does partially average the second-order quadrupolar interaction at sufficiently high spinning frequencies—especially at high magnetic fields—leading to notable narrowing of the central transition for moderately quadrupolar nuclei.

Additionally, spinning sidebands (SSBs) appear whenever the MAS rate is insufficient to average an anisotropic term fully. This phenomenon is general and can arise from CSA, dipolar coupling, or second-order quadrupolar effects; therefore, SSBs may be observed for both spin-½ and quadrupolar nuclei. In effect, MAS produces a spectrum that is qualitatively different from the broad static powder pattern, yet it encodes the same underlying NMR parameters. Using the *Q-MAS ½* and *QUASAR* modules in DMFit, δ_{iso}, C_Q, and η can be extracted in a manner directly comparable to the static case. **Figure II-9** compares the static and MAS ^{139}La spectra of pure $LaCl_3$, highlighting the improvement in resolution achieved under MAS.

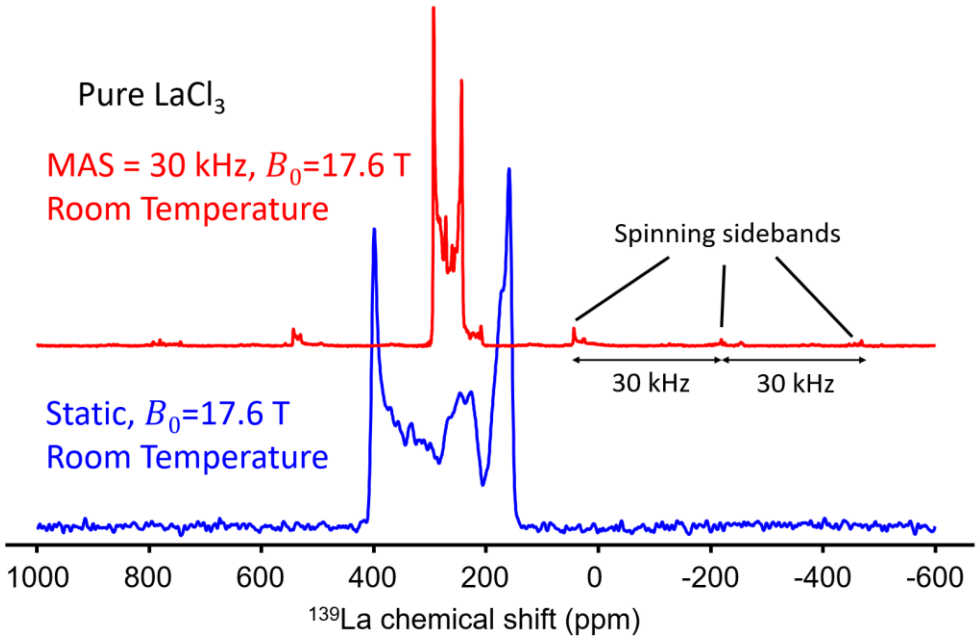

Figure II-9. Comparison of room-temperature ^{139}La spectra of pure $LaCl_3$ under MAS conditions (top, solid red line) and under static conditions (bottom, solid blue line). The occurrence of SSBs is highlighted, and the distance between adjacent SSBs is always equal to the MAS rate.

II-1.6. Pulsed Field Gradient–NMR

In addition to probing the local structure of molten chlorides, the effects of structure on transport properties are also investigated in this thesis. In this regard, PFG–NMR serves as a powerful method for measuring self-diffusion coefficients in liquids and molten salts. This technique exploits the fact that nuclear spins precess at slightly different Larmor frequencies when subjected to a magnetic field gradient along the z-axis. Under such a gradient, nuclear spins located at different positions along z accumulate different phases. Between two gradient pulses, if the spins are longitudinally displaced, the accumulated phases no longer perfectly refocus, resulting in a measurable attenuation of the observed NMR signal.

In this work, diffusion measurements were performed using the stimulated gradient echo (STGE) pulse sequence (**Figure II-10**), which is particularly well-suited for high-temperature molten salt systems with short T_2 relaxation times. The STGE sequence consists of three 90° pulses separated by two gradient pulses. The first 90° pulse tips the longitudinal magnetisation M_z into the transverse plane M_{xy}. A first gradient pulse is then applied, creating a magnetic field gradient along the z-axis for a duration δ. Consequently, nuclear spins at different z-positions accumulate different phases. A second 90° pulse is applied at time τ after the first 90° pulse, rotating the magnetisation along the negative z-axis, storing the phase-encoded magnetisation from the first gradient pulse and also protecting it from T_2 decay. Subsequently, the nuclear spins are allowed to mix for a period of T (the mixing time). After that, a third 90° pulse returns the encoded magnetisation to the transverse plane, producing a stimulated echo. At a time Δ after the first gradient pulse, an identical second gradient pulse is applied. Spins that have not diffused are perfectly refocused, whereas those that have been displaced are incompletely refocused, leading to an attenuation of the echo. The attenuation in the STGE sequence can be analysed using the modified Stejskal–Tanner equation, given by:

$$S(g,\delta,\Delta) = \frac{1}{2}S_0 \exp(-\mathrm{T}/T_1) \exp(-2\tau/T_2) \exp\left(-\gamma^2\delta^2 g^2 D\left(\Delta - \frac{\delta}{3}\right)\right),$$

(Eq. II- 13)

where g is the magnetic field gradient, D is the diffusion coefficient, and γ is the gyromagnetic ratio.

Typically, diffusion measurements rely only on the last exponential term. The first two exponential terms describe signal attenuation due to relaxation processes, and highlight the dependence of PFG–NMR on the relaxation times. Specifically, during the mixing time T, the encoded magnetisation resides along the z-axis, so $T_1 \gg \mathrm{T}$ is required to ensure that the echo attenuation arises from diffusion, rather than T_1 relaxation. Similarly, the transverse magnetisation must survive the short intervals around the gradient pulses, therefore requiring $T_2 \gg \tau > \delta$. In practice, a minimum threshold of ~5 ms for both T_1 and T_2 is generally required to perform PFG–NMR.

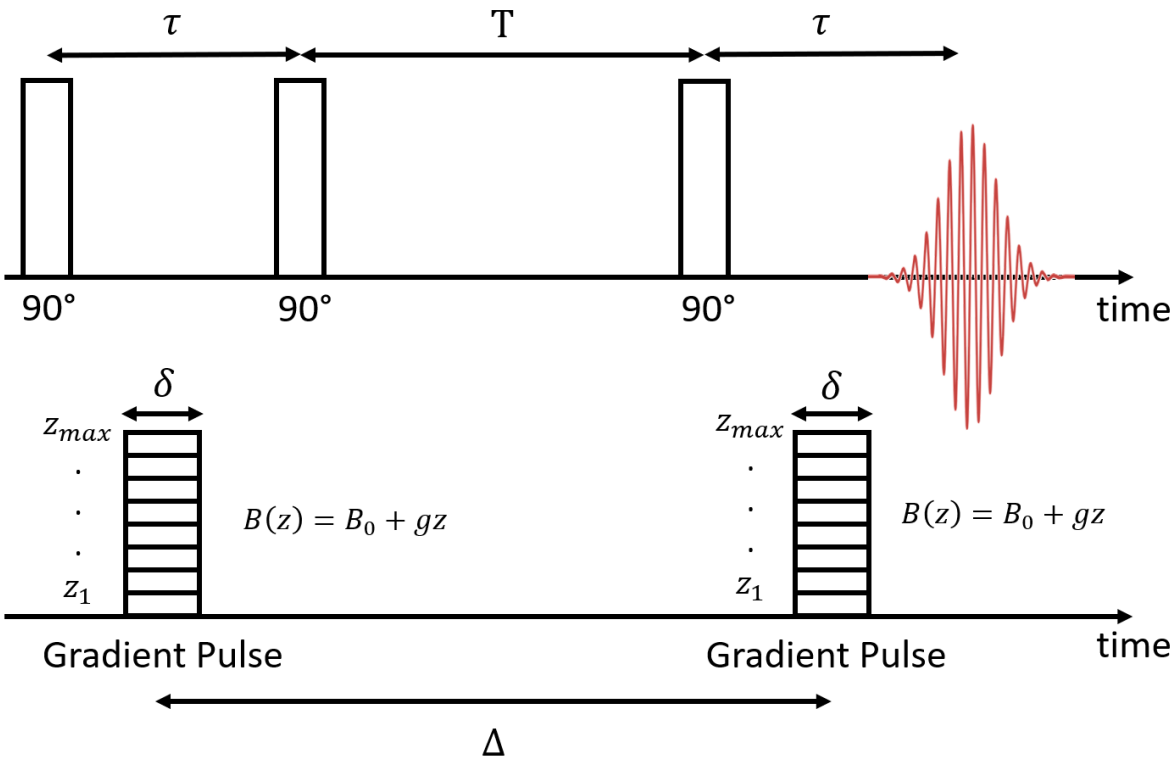

Figure II-10. Schematic illustration of the STGE sequence.

II-1.7. Sample Preparation and Experimental Protocol

Because chloride salts are extremely hygroscopic, they must be stored and handled under an inert atmosphere. In this work, all chloride samples were prepared inside an argon-filled glovebox, with moisture and oxygen levels maintained below 0.3 ppm and 1.0 ppm, respectively.

For HT NMR experiments (including PFG–NMR), most starting materials were used as received without further purification: NaCl (≥99.5%, Merck Suprapur), $MgCl_2$ (≥98%, Thermo Scientific Chemicals), $LaCl_3$ (anhydrous, ≥99.99%, AnhydroBeads). Only LaOCl required synthesis. It was obtained by reacting commercial $LaCl_3$ and 90 at% ^{17}O-enriched water (CortecNet). The synthesis and characterisation of LaOCl will be described in Chapter V.

The molten salt systems in this work consisted of mixtures of NaCl, $MgCl_2$, $LaCl_3$, and LaOCl. Inside the glove box, the salts were weighed to the desired compositions using an electronic balance and thoroughly homogenised using a mortar and pestle. For structural studies (Chapters III and V), samples were loaded into high-purity BN crucibles measuring 9 mm in diameter and 14 mm in height. For PFG–NMR experiments (Chapter IV), smaller BN crucibles (6 mm diameter × 14 mm height) were used to accommodate the smaller borehole of the UHT 400 Gradient probe. Additionally, three small fragments of BN (measuring <3 mm on each dimension) were inserted alongside the salt samples for PFG–NMR measurements. These BN inserts serve to suppress the convection currents of molten salts,

ensuring that the measured transport phenomena arise solely from ion diffusion [96]. All crucibles were tightly enclosed with their high-purity BN screw caps before removal from the glove box.

All HT NMR measurements were performed on the Bruker AVANCE I spectrometer operating at 9.4 T, as described in earlier sections. With the sample positioned in the probe and the RF circuit tuned to the resonance frequency of the nucleus of interest, the laser power was gradually adjusted to reach the desired temperature using the temperature calibration curves shown in **Figure II-8**. Before acquisition, the sample was irradiated at constant laser power for at least 3 minutes to ensure thermal equilibration. During this period, the RF coil frequency was monitored and manually adjusted if heating caused detuning.

Single-pulse experiments were used for structural studies, while the STGE sequence was used for PFG–NMR measurements [96]. For each experiment, the acquisition parameters were adjusted to achieve a sufficient signal-to-noise ratio. However, the duration of laser heating—and thus, the maximum acquisition time—was limited to 30 minutes to minimise volatilisation of the molten chlorides and prevent overheating of the shim coils, which preserve the spatial homogeneity of the static magnetic field B_0.

For SS NMR, sample preparation consisted of packing the chloride salts into MAS rotors of various diameters (1.3, 2.5, 4.0 mm) inside the glovebox. Only four salts were examined using SS NMR in this work: $LaCl_3$, K_2LaCl_5, Cs_3LaCl_6, and LaOCl. Among them, K_2LaCl_5 and Cs_3LaCl_6 were synthesised via a solid-state reaction; their synthesis and characterisation are presented in Chapter III-2.

All SS NMR experiments were conducted on the Bruker Avance NEO 17.6 T and 20 T spectrometers at CEMHTI–CNRS. Measurements were performed both under static conditions and under MAS, with spinning rates set to the maximum stable frequencies permitted by each rotor type: 14 kHz for 4.0 mm rotors, 30 kHz for 2.5 mm rotors, and 60 kHz for 1.3 mm rotors. Single-pulse excitation was used for nuclei exhibiting very short T_2 relaxation times, whereas a spin echo sequence was employed for nuclei with sufficiently long T_2 to refocus the transverse magnetisation. All SS NMR acquisitions were carried out at ambient temperature. Additionally, for NMR spectra exhibiting quadrupolar broadening larger than the RF excitation bandwidth, the variable-offset cumulative spectra (VOCS) technique [97] was used to stitch together multiple subspectra acquired at different transmitter offsets, thereby constructing a continuous spectrum over a wider frequency range.

For all NMR experiments, standard liquid solutions were used to reference the chemical shifts: 1.0 M NaCl solution for ^{23}Na and ^{35}Cl, 0.1 M $LaCl_3$ solution for ^{139}La, and tap water for ^{17}O. The same reference solutions were also used to calibrate the pulse lengths. For molten-state NMR, the 90° pulse length was determined from nutation-frequency experiments. For SS NMR, shorter pulses are required to uniformly excite all satellite transitions of quadrupolar nuclei with spin I. The corresponding 90° pulse length for SS NMR can be estimated from the relation:

$$\tau_{90,solid} = \frac{\tau_{90,liquid}}{I + 1/2}$$

(Eq. II-14)

II-2. Classical Molecular Dynamics

In contemporary materials chemistry, experimental observations alone are often insufficient to uncover the fundamental mechanisms governing molecular-level behaviour. Computational techniques have therefore become increasingly indispensable, not only for interpreting experimental results but also for predicting properties that are difficult to access experimentally. This is especially true for molten salts, in which their hygroscopicity, volatility, corrosivity, and radioactivity (in actinide-bearing systems) present significant challenges for high-temperature experimentation.

In this regard, classical MD simulations offer a hazard-free and cost-effective complementary approach for investigating molten salt behaviour. In this work, classical MD simulations were employed to model the local structure and thermophysical properties of the NaCl–$MgCl_2$–$LaCl_3$–LaOCl molten chloride system. Using the PIM, the collective dynamics of molten salt systems containing thousands of ions over the nanosecond timescales can be realistically reproduced. Statistical analyses of the resulting ion trajectories provide detailed insights into local structure, including radial distribution functions, coordination environments, and network formation. Furthermore, appropriate thermodynamic formalisms can be applied to extract key macroscopic properties, such as density, viscosity, heat capacity, and thermal expansion. Together, the combination of NMR spectroscopy and MD simulations enables a more rigorous and comprehensive understanding of the molecular-level interactions that govern molten chloride behaviour.

II-2.1. Theoretical Background

Interatomic potentials form the foundation of reliable classical MD simulations. In the case of molten salts, the RIM provides the simplest description of ion–ion interactions. The pairwise potential is expressed as:

$$V_{RIM} = \sum_{i<j}\left[\frac{q_i q_j}{4\pi\epsilon_0 r_{ij}} + B^{ij}\exp\left(-\alpha^{ij} r_{ij}\right) - \frac{C_6^{ij}}{r_{ij}^6} f_6^{ij}\left(r_{ij}\right) - \frac{C_8^{ij}}{r_{ij}^8} f_8^{ij}\left(r_{ij}\right)\right],$$

(Eq. II-15)

where ϵ_0 is the permeability of free space, r_{ij} is the separation between ions *i* and *j* ($\vec{\boldsymbol{r}}_{ij} = \vec{\boldsymbol{r}}_i - \vec{\boldsymbol{r}}_j$), q_i and q_j are their formal charges. The parameters B^{ij} and α^{ij} define short-range Born–Mayer repulsion, while C_6^{ij} and C_8^{ij} are attractive dispersion coefficients corresponding to the dipole–dipole and dipole–quadrupole interactions, respectively. The factors $f_6^{ij}(r)$ and $f_8^{ij}(r)$ are Tang–Toennies damping functions that correct the divergence of dispersion terms at short range. In this representation, the first term describes the long-range Coulomb interactions, the second term captures the short-range Pauli repulsions, whereas the third and fourth terms account for van de Waal's dispersion forces. Although useful for simple systems, the RIM potential treats ions as rigid point charges and therefore neglects any polarisation response, such as charge deformation under local electric fields. Consequently, it cannot adequately describe many-body effects or the strong charge-polarisation interactions that are characteristic of molten salts.

To overcome this limitation, the PIM introduces electronic polarisability explicitly. The central feature of the PIM is the induced dipole moment, which arises from the local electric field generated by all surrounding charges and induced dipoles. For an ion *i*, the induced dipole moment, $\vec{\boldsymbol{\mu}}_i$, is given as:

$$\vec{\boldsymbol{\mu}}_i = \alpha_i \vec{\mathbf{E}}_i,$$

(Eq. II- 16)

where α_i is the isotropic polarisability of ion *i*, and $\vec{\mathbf{E}}_i$ is the total electric field experienced by that ion.

If two ions approach too closely, their electron clouds overlap, causing the bare electric field to become unphysically large. To remedy this, the electric field is damped using Tang–Toennies functions, leading to the working PIM expression for the induced dipole:

$$\vec{\boldsymbol{\mu}}_i = \alpha_i \left(\sum_{j \neq i} q_j f_4^{ij}(r_{ij}) \mathbf{T}_{ij}^{(0)} + \sum_{j \neq i} f_6^{ij}(r_{ij}) \mathbf{T}_{ij}^{(1)} \vec{\boldsymbol{\mu}}_j \right),$$

(Eq. II- 17)

where $\mathbf{T}_{ij}^{(0)}$ is the charge–dipole interaction tensor, and $\mathbf{T}_{ij}^{(1)}$ is the dipole–dipole interaction tensor.

The charge–dipole interaction tensor is:

$$\mathbf{T}_{ij}^{(0)} = -\nabla \left(\frac{1}{r_{ij}} \right) = \frac{\vec{\boldsymbol{r}}_{ij}}{\left| \vec{\boldsymbol{r}}_{ij} \right|^3},$$

(Eq. II- 18)

The dipole field tensor is given by the equation:

$$\mathbf{T}_{ij}^{(1)} = \frac{1}{\left| \vec{\boldsymbol{r}}_{ij} \right|^3} \left(3\, \hat{\boldsymbol{r}}_{ij} \hat{\boldsymbol{r}}_{ij}^T - \mathbf{I} \right),$$

(Eq. II- 19)

where $\hat{\boldsymbol{r}}_{ij} = \vec{\boldsymbol{r}}_{ij} / \left| \vec{\boldsymbol{r}}_{ij} \right|$, $\hat{\boldsymbol{r}}_{ij} \hat{\boldsymbol{r}}_{ij}^T$ is its outer product, and $\mathbf{I}$ is the 3×3 identity matrix.

In its general form, the Tang–Toennies damping function is written as:

$$f_n^{ij}(r) = 1 - c_n^{ij} \exp\left(-b_n^{ij} r\right) \sum_{k=0}^{n} \frac{\left(b_n^{ij} r\right)^k}{k!}.$$

(Eq. II- 20)

In this work, $f_6^{ij}(r)$ and $f_8^{ij}(r)$ are damping functions applied to the dispersion terms, where b_6^{ij} and b_8^{ij} are their respective damping parameters, and the prefactors c_6^{ij} and c_8^{ij} are taken to be unity. Meanwhile, $f_4^{ij}(r)$ is the damping function for charge–dipole interaction, b_4^{ij} is its corresponding damping parameter, and the prefactor c_4^{ij} is generally non-unit, as it is adjusted to correct for short-range overpolarisation.

The total polarisation is then given by:

$$V_{pol} = -\sum_i \sum_{j \neq i} \vec{\boldsymbol{\mu}}_i \cdot \left[q_j f_4^{ij}(r_{ij}) \mathbf{T}_{ij}^{(0)} \right] - \frac{1}{2} \sum_i \sum_{i \neq j} \vec{\boldsymbol{\mu}}_i \cdot \left[f_6^{ij}(r_{ij}) \mathbf{T}_{ij}^{(1)} \right] \cdot \vec{\boldsymbol{\mu}}_j + \sum_i \frac{|\vec{\boldsymbol{\mu}}_i|^2}{2\alpha_i}.$$

(Eq. II- 21)

Here, the first term represents the charge–dipole interaction energy, the second term represents dipole–dipole interactions, and the third term is the self-energy, which penalises large induced dipoles and represents the energy cost of deforming the electron cloud. The total potential energy in the PIM is thus given by:

$$V_{total} = V_{RIM} + V_{pol}$$

(Eq. II- 22)

From the equations above, it is clear that the effective electric field experienced by each ion depends on the induced dipole of its neighbours, i.e., $\vec{\mathbf{E}}_i(\vec{\boldsymbol{\mu}}_1, \vec{\boldsymbol{\mu}}_2, \ldots, \vec{\boldsymbol{\mu}}_N)$. Consequently, the dipole moments, $\vec{\boldsymbol{\mu}}_i$, must be determined self-consistently. This condition is enforced by minimising the total polarisation energy with respect to each dipole:

$$\frac{\partial V_{pol}}{\partial \vec{\boldsymbol{\mu}}_i} = 0.$$

(Eq. II- 23)

In practice, this leads to an iterative procedure:

$$\vec{\boldsymbol{\mu}}_i^{(n+1)} = \alpha_i \vec{\mathbf{E}}_i\left(\{\vec{\boldsymbol{\mu}}^{(n)}\}\right),$$

(Eq. II- 24)

where the dipoles are updated repeatedly until the convergence criterion:

$$\left|\vec{\boldsymbol{\mu}}_i^{(n+1)} - \vec{\boldsymbol{\mu}}_i^{(n)}\right| < \epsilon$$

(Eq. II- 25)

is reached. This ensures that the induced dipoles and resulting electric field are mutually consistent.

II-2.2. Interaction Potential Parameters

In this work, the NaCl–$MgCl_2$–$LaCl_3$–LaOCl system involves five ionic species: Na^+, Mg^{2+}, La^{3+}, Cl^-, and O^{2-}. A total of nine interaction potential parameters—associated with each ion and each ion pair—were fitted on the DFT level. These parameters include:

- α_i, the static atomic polarisability of ion i;
- B^{ij} and α^{ij}, the Born–Mayer short-range repulsion parameters for the i–j ion pair;
- C_6^{ij} and C_8^{ij}, the dispersion coefficients corresponding to the dipole–dipole and dipole–quadrupole interactions, respectively;
- b_6^{ij} and b_8^{ij}, the Tang–Toennies damping parameters associated with the dispersion terms C_6^{ij} and C_8^{ij};
- b_4^{ij} and c_4^{ij}, the Tang–Toennies damping parameter and prefactor applied to the charge–dipole interaction term in the polarisation model.

The fitted parameters for all ions and ion pairs used in this work are listed in **Table II-1 to II-3**.

Table II-1. Atomic polarisabilities for molten salt ions (in atomic units)

Ions	α_i $(a.u.)$	Ref.
Na^+	0.900	[98]
Mg^{2+}	0.000	[99]
La^{3+}	8.445	[100]
Cl^-	20.000	[98]
O^{2-}	10.740	This Work

Table II-2. Born–Mayer (RIM) potential parameters. All parameters are reported in atomic units.

Ion Pairs	B^{ij}	α^{ij}	C_6^{ij}	C_8^{ij}	b_6^{ij}	b_8^{ij}	Ref.
Na^+–Na^+	0.000	5.000	11.700	51.800	1.70	1.70	[98]
Mg^{2+}– Mg^{2+}	0.000	5.000	0.000	0.000	1.70	1.00	This Work
La^{3+}– La^{3+}	0.000	3.000	47.700	100.000	1.50	1.00	[99]
Cl^- – Cl^-	275.100	1.797	140.000	280.000	1.70	1.70	[98]
O^{2-} – O^{2-}	290.400	2.406	25.400	491.600	1.000	1.000	This Work
Na^+– Mg^{2+}	0.000	5.000	0.000	0.000	1.70	1.00	This Work
Na^+– La^{3+}	0.000	3.529	23.624	71.972	1.50	1.00	This Work
Na^+– Cl^-	67.500	1.726	47.400	187.300	1.70	1.70	[98]
Na^+– O^{2-}	201.080	2.219	2.1793	25.305	2.206	2.206	[101]

Mg^{2+}– La^{3+}	0.000	3.529	0.000	0.000	1.50	1.00	This Work
Mg^{2+} – $Cl^{–}$	51.426	1.652	0.000	0.000	1.70	1.00	This Work
Mg^{2+} – $O^{2–}$	53.403	1.772	2.1793	25.305	2.206	2.206	This Work
La^{3+} – $Cl^{–}$	392.395	1.800	81.719	167.332	1.50	1.00	[100]
La^{3+} – $O^{2–}$	101.980	1.614	57.000	731.000	2.206	2.206	This Work
$Cl^{–}$ – $O^{2–}$	266.000	2.027	59.632	371.000	1.180	1.180	This Work

Table II-3. Tang–Toennies damping parameters for charge–dipole interactions in ion pairs. The first ion has charge, the second ion has a dipole.

Ion Pairs	b_4^{ij}	c_4^{ij}	Ref.
Na^{+} – $Cl^{–}$	1.760	3.000	[98]
$Cl^{–}$ – Na^{+}	1.760	0.697	[98]
Mg^{2+} – $Cl^{–}$	1.768	2.302	This Work
La^{3+} – $Cl^{–}$	1.250	1.000	[100]
$Cl^{–}$ – La^{3+}	1.250	−1.000	[100]
Na^{+}– $O^{2–}$	2.137	3.334	[101]
$O^{2–}$ – Na^{+}	2.137	2.857	[101]
Mg^{2+} – $O^{2–}$	2.529	4.770	This Work
La^{3+} – $O^{2–}$	2.130	4.957	This Work
$O^{2–}$– La^{3+}	2.130	–1.000	This Work
$O^{2–}$– $O^{2–}$	2.513	2.227	This Work

II-2.3. MD Simulation Protocol

Classical MD simulations with the PIM were carried out using the MetalWalls software [102,103]. Initial atomic configurations were generated using PACKMOL [104], in which ions were randomly packed into cubic periodic simulation boxes. The initial box lengths were estimated from reported molten-state densities of the pure chloride components.

Electrostatic interactions within the PIM framework were treated using the Ewald summation method, which separates each interaction into short-range (real-space) and long-range (reciprocal-space) components. In the PIM formalism, all interaction terms possess a short-range part, but only the Coulombic charge–charge, charge–dipole, and dipole–dipole interactions contribute to the long-range component. A real-space Ewald cutoff, r_c, defines the domain in which real-space contributions to electrostatic interactions are computed explicitly, while contributions beyond r_c are evaluated in the reciprocal space.

Additionally, a separate van der Waals (vdW) cutoff radius, r_{vdW}, was applied to the short-range Born–Mayer repulsion and dispersion terms of the RIM potential (Eq. II-15). To avoid unphysical interactions between atoms and their own periodic images, r_{vdW} was chosen not to exceed half the box length. A standard tail-correction scheme was used to compensate for the missing van der Waals contribution beyond this cutoff. For computational convenience, r_c and r_{vdw} are set to equal numerical values for all simulations performed in this work.

The induced dipoles in the PIM were obtained by minimising the total polarisation energy through the self-consistent iterative procedure, described in (Eq. II-25). Convergence thresholds of $\epsilon < 10^{-7}$ were applied to both the charge and dipole residuals.

All MD simulations were performed in either the canonical NPT or NVT ensemble, using Nosé-Hoover thermostats to regulate temperature. In NPT simulations, a standard pressure of 1 bar was set using a barostat scheme.

For each MD simulation, the number of atoms depended on the salt composition and the specific property under investigation. "Large" simulation boxes (2000–4000 atoms, **Table II-4**) were used for structural analysis and derivation of thermophysical properties for molten chlorides, whereas "small" simulation boxes (230–500 atoms, **Table II-5**) were employed to generate trajectories for subsequent first-principles NMR calculations. r_c and r_{vdW} were set to 10.6 Å for "large" simulation boxes and to 6.0 Å for "small" simulation boxes.

Table II-4. Molten salt compositions and their respective number of ions used for "large" box simulations (x=1–5)

Molten Salt Composition (mol%)				N_{Na}	N_{Mg}	N_{La}	N_{Cl}	N_O	N_{total}
NaCl	$MgCl_2$	$LaCl_3$	LaOCl						
0	0	100	0	–	–	1000	3000	–	4000
5	0	95	0	50	–	950	2900	–	3900
20	0	80	0	200	–	800	2600	–	3600
35	0	65	0	350	–	650	2300	–	3300
50	0	50	0	500	–	500	2000	–	3000
65	0	35	0	650	–	350	1700	–	2700
80	0	20	0	800	–	200	1400	–	2400
95	0	5	0	950	–	50	1100	–	2100
100	0	0	0	1000	–	–	1000	–	2000
16	4	80	0	160	40	800	2640	–	3640
0	5	95	0	–	50	950	2950	–	3950
95	5	0	0	950	50	–	1050	–	2050
28	7	65	0	280	70	650	2370	–	3370
10	10	80	0	100	100	800	2700	–	3700
40	10	50	0	400	100	500	2100	–	3100
52	13	35	0	520	130	350	1830	–	2830
4	16	80	0	40	160	800	2760	–	3760
64	16	20	0	640	160	200	1560	–	2560
18	17	65	0	180	170	650	2470	–	3470
76	19	5	0	760	190	50	1290	–	2290
0	20	80	0	–	200	800	2800	–	3800

80	20	0	0	800	200	–	1200	–	2200
25	25	50	0	250	250	500	2250	–	3250
7	28	65	0	70	280	650	2580	–	3580
32.5	32.5	35	0	325	325	350	2025	–	3025
0	35	65	0	–	350	650	2650	–	3650
10	40	50	0	100	400	500	2400	–	3400
40	40	20	0	400	400	200	1800	–	2800
48	47	5	0	480	470	50	1570	–	2570
5	48	47	0	50	480	470	2420	–	3420
0	50	50	0	–	500	500	2500	–	3500
50	50	0	0	500	500	–	1500	–	2500
13	52	35	0	130	520	350	2220	–	3220
16	64	20	0	160	640	200	2040	–	3040
0	65	35	0	–	650	350	2350	–	3350
19	76	5	0	190	760	50	1860	–	2860
0	80	20	0	–	800	200	2200	–	3200
20	80	0	0	200	800	–	1800	–	2800
0	95	5	0	–	950	50	2050	–	3050
5	95	0	0	50	950	–	1950	–	2950
0	100	0	0	–	1000	–	2000	–	3000
80	0	$20 - x$	x	800	–	200	$1400 - 20x$	$10x$	$2400 - 10x$
64	16	$20 - x$	x	640	160	200	$1560 - 20x$	$10x$	$2560 - 10x$
40	40	$20 - x$	x	400	400	200	$1800 - 20x$	$10x$	$2800 - 10x$
16	64	$20 - x$	x	160	640	200	$2040 - 20x$	$10x$	$3040 - 10x$
0	80	$20 - x$	x	–	800	200	$2200 - 20x$	$10x$	$3200 - 10x$

Table II-5. Molten salt compositions and their respective number of ions used for "small" box simulations (x=1–5)

Molten Salt Composition (mol%)				N_{Na}	N_{Mg}	N_{La}	N_{Cl}	N_O	N_{total}
NaCl	$MgCl_2$	$LaCl_3$	LaOCl						
0	0	100	0	–	–	100	300	–	400
10	0	90	0	10	–	90	280	–	380
20	0	80	0	20	–	80	260	–	360
30	0	70	0	30	–	70	240	–	340
40	0	60	0	40	–	60	220	–	320
50	0	50	0	50	–	50	200	–	300
60	0	40	0	60	–	40	180	–	280
70	0	30	0	70	–	30	160	–	260
80	0	20	0	80	–	20	140	–	240
90	0	10	0	90	–	10	120	–	220
100	0	0	0	100	–	–	100	–	200
0	10	90	0	–	10	90	290	–	390
0	20	80	0	–	20	80	280	–	380

0	30	70	0	–	30	70	270	–	370
0	40	60	0	–	40	60	260	–	360
0	50	50	0	–	50	50	250	–	350
0	60	40	0	–	60	40	240	–	340
0	70	30	0	–	70	30	230	–	330
0	80	20	0	–	80	20	220	–	320
0	90	10	0	–	90	10	210	–	310
0	100	0	0	–	100	–	200	–	300
8	2	90	0	8	2	90	282	–	382
16	4	80	0	16	4	80	264	–	364
24	6	70	0	24	6	70	246	–	346
32	8	60	0	32	8	60	228	–	328
40	10	50	0	40	10	50	210	–	310
48	12	40	0	48	12	40	192	–	292
56	14	30	0	56	14	30	174	–	274
64	16	20	0	64	16	20	156	–	256
72	18	10	0	72	18	10	138	–	238
80	20	0	0	80	20	–	120	–	220
8	72	20	0	8	72	20	212	–	312
16	64	20	0	16	64	20	204	–	304
24	56	20	0	24	56	20	196	–	296
32	48	20	0	32	48	20	188	–	288
40	40	20	0	40	40	20	180	–	280
48	32	20	0	48	32	20	172	–	272
56	24	20	0	56	24	20	164	–	264
72	8	20	0	72	8	20	148	–	248
80	0	$20 - x$	x	80	–	20	$140 - 2x$	x	$240 - x$
64	16	$20 - x$	x	64	16	20	$156 - 2x$	x	$256 - x$
40	40	$20 - x$	x	40	40	20	$180 - 2x$	x	$280 - x$
16	64	$20 - x$	x	16	64	20	$204 - 2x$	x	$304 - x$
0	80	$20 - x$	x	–	80	20	$220 - 2x$	x	$320 - x$

The chosen ensemble conditions also depended on the specific property being investigated:

1. *Structural analysis*. NPT simulations were performed on "large" simulation boxes in the following order: a 0.2 ns non-polarisable equilibration, a 0.5 ns polarisable equilibration, and a 5.0 ns polarisable production, all with a 1.0 fs timestep. Ion trajectories from the production step were analysed using the TRAVIS code [105,106] to compute radial distribution functions and coordination numbers. Additionally, a Fortran routine, previously used in [107] and [108], was used to analyse polymer chain lengths in molten chlorides.

2. *Density*. The same NPT simulation protocol was applied. Density, ρ, was calculated as:

$$\rho = \frac{N_{frames}}{\sum_i^{N_{frames}} V_i} \cdot M_{total},$$

(Eq. II-26)

where N_{frames} is the number of frames in the production trajectory, V_i is the box volume at the ith frame, and M_{total} is the total mass of atoms in the simulation box.

3. *Enthalpy*. The same NPT protocol simulation was applied. The absolute enthalpy, H, was obtained from:

$$H = \frac{1}{N_{frames}} \sum_i^{N_{frames}} (U_i + PV_i),$$

(Eq. II-27)

where U_i is the internal energy at the ith frame. The enthalpy of formation, H_f, was calculated by subtracting a reference enthalpy, H_{ref}, from the absolute enthalpy:

$$H_f = H - H_{ref}.$$

(Eq. II-28)

For the NaCl–$MgCl_2$–$LaCl_3$ system, H_{ref} corresponds to the molar sum of the reference enthalpies of the pure components. In the molten state, reference enthalpies for the pure components were derived from the FactPS database on FactSage [109]: $H_{ref,NaCl} = -367\ kJ/mol$, $H_{ref,MgCl_2} = -1705\ kJ/mol$, $H_{ref,LaCl_3} = -3053\ kJ/mol$. Since there is no melting data on pure LaOCl, $H_{ref,LaOCl}$ cannot be quantified and H_f for LaOCl-containing systems are not evaluated.

4. *Heat Capacity*. The same NPT simulation protocol was applied at five temperatures—two above and two below the target temperature—at 10 °C increments. For example, to determine the heat capacity at 850 °C, NPT simulations were performed at 830, 840, 850, 860, and 870 °C. The constant-pressure heat capacity, C_P, is obtained from the derivative of the enthalpy of formation:

$$C_P = \frac{\partial H_f}{\partial T}.$$

(Eq. II-29)

For molten chlorides, the enthalpy exhibits an approximately linear dependence on temperature, i.e., $H_f = a + bT$. Thus, C_P is extracted from the slope, b, using a linear regression of H_f versus T. Because the reference enthalpies of pure components are largely insensitive to temperature over the narrow thermal

intervals used here, the approximation $\frac{\partial H_f}{\partial T} = \frac{\partial H}{\partial T}$ holds. Consequently, heat capacities of LaOCl-containing systems can also be evaluated, even though $H_{ref,LaOCl}$ is unavailable.

5. *Volumetric expansion*. The same NPT simulation protocol used for the heat capacity calculations was applied. The volumetric expansion coefficient, β, is defined as:

$$\beta = \frac{1}{V}\left(\frac{\partial V}{\partial T}\right),$$

(Eq. II-30)

where V is the average box volume at the target temperature. Since molten chlorides also exhibit an approximately linear dependence of volume on temperature, the same linear regression scheme can be used to obtain β.

6. *Viscosity and self-diffusivity*. MD simulations were performed on "large" simulation boxes in the following order: a non-polarisable NPT equilibration of 0.2 ns, a polarisable NPT equilibration of 0.5 ns, and a polarisable NVT production of 10.0 ns, all at a 1.0 fs timestep. During the production step, stress tensors and ion trajectories were recorded at 10.0 fs and 1.0 ps intervals, respectively.

Viscosities, η, were computed using the Green–Kubo formalism, which relates viscosity to the time integral of the autocorrelation function of the off-diagonal components of the stress tensor:

$$\eta = \frac{V}{k_B T}\int_0^\infty dt' \left\langle \tau_{\alpha\beta}(t') \cdot \tau_{\alpha\beta}(0) \right\rangle,$$

(Eq. II-31)

where V is the volume of the simulation box, k_B is the Boltzmann constant, T is the absolute temperature, and $\tau_{\alpha\beta}$ denotes an off-diagonal element of the stress tensor (*xy*, *xz* or *yz*). To eliminate statistical noise and improve convergence of the integral, a cepstral filter [110] was applied, following the methodology outlined in [76].

Self-diffusion coefficients, D_i, were derived from ion trajectories using Einstein's relation for mean-squared displacement:

$$D_i = \frac{1}{6}\lim_{t\to\infty}\frac{d}{dt}\left\langle \frac{1}{N}\sum_{k=1}^{N}\left|\vec{\boldsymbol{r}}_{i,k}(t) - \vec{\boldsymbol{r}}_{i,k}(0)\right|^2 \right\rangle,$$

(Eq. II- 32)

where N is the number of ions of species i and and $\vec{\boldsymbol{r}}_{i,k}(t)$ is the position of the kth ion of species i at time t. To correct for finite-size effects in periodic simulation cells, the Yeh–Hummer correction [111,112] was applied:

$$D_{i,\infty} = D_i + \frac{2.837298 k_B T}{6\pi\eta L},$$

(Eq. II- 33)

where $D_{i,\infty}$ is the self-diffusion coefficient in infinite systems and L is the edge length of the cubic simulation box.

7. *First-principles NMR calculations*. MD simulations were performed on "small" simulation boxes in the following order: a 0.2 ns non-polarisable NPT equilibration, a 0.5 ns polarisable NPT equilibration, and a 5.0 ns polarisable NPT production, all using a timestep of 1.0 fs. Ion trajectories were recorded every 1.0 ps, and configurations were sampled at regular intervals from the production trajectory for subsequent first-principles NMR calculations. The theoretical background and computational details of these calculations are presented in the following section.

II-3. First-Principles NMR Calculations

In previous sections, NMR experiments and classical MD simulations were presented independently to investigate the local structure of molten chlorides. Although each method provides structural insight, it is pivotal to establish whether the atomistic configurations obtained from MD are consistent with the NMR-derived local environments. To enable this multimodal verification, first-principles NMR calculations were performed on MD-generated ion trajectories using the DFT approach. By comparing DFT-predicted NMR chemical shifts with experimental measurements, the agreement between simulated and experimental structural information can be rigorously assessed. This provides a direct bridge between experiment and theory, strengthening the reliability of structural conclusions drawn in this work.

II-3.1. Theoretical Background of DFT

Because NMR shielding arises from the electronic response to external magnetic fields, first-principles NMR calculations require an accurate quantum-mechanical description of the electronic structure. Compared to other first-principles methods such as Hartree–Fock, DFT offers a favourable balance between computational cost and accuracy, making it well-suited for evaluating NMR parameters in condensed-phase systems. The fundamental concepts underlying DFT-based NMR calculations are summarised below.

The starting point for all quantum mechanical treatments is the Schrödinger equation. For a single particle, its time-independent form is:

$$\left[-\frac{\hbar^2}{2m_i}\nabla^2 + V(\vec{\boldsymbol{r}})\right]\psi_i(\vec{\boldsymbol{r}}) = E_i\psi_i(\vec{\boldsymbol{r}}),$$

(Eq. II- 34)

where $\hbar = 1.05457 \times 10^{-34}\, J/s$ is the reduced Planck's constant, m_i is the mass of particle i, ∇^2 is the Laplacian operator, $V(\vec{\boldsymbol{r}})$ is the potential energy at position $\vec{\boldsymbol{r}}$, ψ_i is the corresponding wavefunction, and E_i is its energy eigenvalue. The expression is often written more compactly as:

$$\hat{H}\psi_i(\vec{\boldsymbol{r}}) = E_i\psi_i(\vec{\boldsymbol{r}}),$$

(Eq. II- 35)

where $\hat{H}$ is the Hamiltonian operator.

For many-body systems containing n electrons and N nuclei, the equation generalises into:

$$\hat{H}\Psi\left(\vec{\boldsymbol{r}}_{\boldsymbol{1}}, \vec{\boldsymbol{r}}_{\boldsymbol{2}}, \dots, \vec{\boldsymbol{r}}_{\boldsymbol{n}}; \vec{\boldsymbol{R}}_{\boldsymbol{1}}, \vec{\boldsymbol{R}}_{\boldsymbol{2}}, \dots, \vec{\boldsymbol{R}}_N\right) = E\Psi\left(\vec{\boldsymbol{r}}_{\boldsymbol{1}}, \vec{\boldsymbol{r}}_{\boldsymbol{2}}, \dots, \vec{\boldsymbol{r}}_{\boldsymbol{n}}; \vec{\boldsymbol{R}}_{\boldsymbol{1}}, \vec{\boldsymbol{R}}_{\boldsymbol{2}}, \dots, \vec{\boldsymbol{R}}_N\right),$$

(Eq. II- 36)

with the Hamiltonian given by:

$$\hat{H} = \hat{T}_e + \hat{T}_n + \hat{V}_{ee} + \hat{V}_{nn} + \hat{V}_{ext},$$

(Eq. II- 37)

where $\hat{T}_e$ and $\hat{T}_n$ are the electronic and nuclear kinetic energy operators, $\hat{V}_{ee}$ and $\hat{V}_{nn}$ are electron–electron and nuclear–nuclear Coulombic repulsions, and $\hat{V}_{ext}$ represents electron–nuclear interactions.

Evidently, obtaining an exact solution to this full many-body problem is computationally infeasible for all but the smallest systems, as the difficulty grows exponentially with the number of particles. Consequently, a series of controlled approximations is required to make practical electronic-structure calculations possible.

One such simplification is the Born–Oppenheimer approximation, which takes advantage of the large mass difference between electrons and nuclei. As electrons are several orders of magnitude lighter, they move much faster, allowing the nuclei to be treated as effectively stationary while solving the electronic problem. Under this approximation, the total wavefunction can be separated into electronic and nuclear components, and the electronic Schrödinger equation becomes:

$$\hat{H_e}\left(\vec{\boldsymbol{R}}\right)\Psi_{\mathrm{e}}\left(\vec{\boldsymbol{r}}_{\boldsymbol{1}}, \vec{\boldsymbol{r}}_{\boldsymbol{2}}, \dots, \vec{\boldsymbol{r}}_{\boldsymbol{n}}; \vec{\boldsymbol{R}}\right) = E_e\left(\vec{\boldsymbol{R}}\right)\Psi_{\mathrm{e}}\left(\vec{\boldsymbol{r}}_{\boldsymbol{1}}, \vec{\boldsymbol{r}}_{\boldsymbol{2}}, \dots, \vec{\boldsymbol{r}}_{\boldsymbol{n}}; \vec{\boldsymbol{R}}\right)$$

(Eq. II- 38)

where $\vec{\boldsymbol{R}}$ denotes the set of fixed nuclear coordinates. In the context of this work, snapshots from MD trajectories supply these nuclear configurations, and the electronic Schrödinger equation is solved for each snapshot to calculate NMR shielding.

Even with the Born–Oppenheimer approximation, solving the many-electron problem remains computationally intractable due to the presence of n electron coordinates—that is, $3n$ continuous variables. The DFT framework provides a workaround to this difficulty by reformulating the problem in terms of the electron density, $\rho(\vec{\boldsymbol{r}})$, reducing the complexity to a function of only three spatial variables.

The Hohenberg–Kohn theorems [113] lay the formal foundations of DFT:

1. First theorem—Uniqueness:
   For interacting electrons in an external potential, the ground-state electron density uniquely determines the external potential up to a constant. All ground-state properties are therefore functionals of the density.

2. Second theorem—Variational principle:
   There exists a universal energy functional, $E[\rho]$, such that the exact ground-state density minimises this functional, and the minimum value equals the true ground-state energy.

Taken together, these theorems establish that the ground-state electron density $\rho(\vec{\boldsymbol{r}})$ is a sufficient variable from which all properties of the interacting many-electron system can be determined. To make DFT computationally practical, the Kohn–Sham formalism decomposes the universal energy functional as:

$$E[\rho] = T_s[\rho] + E_{ext}[\rho] + E_H[\rho] + E_{xc}[\rho],$$

(Eq. II-39)

where T_s is the kinetic energy of a fictitious system of non-interacting electrons, E_{ext} reflects the energy of electron–nuclear interactions, E_H represents the energy of the classical Hartree Coulomb repulsion, and E_{xc} describes the exchange–correlation energy, which accounts for all the remaining many-body effects—including the kinetic energy of interacting electrons, quantum mechanical exchange (Pauli exclusion), dynamic Coulomb correlation, and self-interaction correction.

Substituting this functional into the Schrödinger equation yields the Kohn–Sham equations:

$$\left[-\frac{\hbar^2}{2m_e}\nabla^2 + V_{eff}(\vec{\boldsymbol{r}})\right]\psi_i(\vec{\boldsymbol{r}}) = \epsilon_i\psi_i(\vec{\boldsymbol{r}}),$$

(Eq. II-40)

with the electron density reconstructed as:

$$\rho(\vec{r}) = \sum_{i} |\psi_i(\vec{r})|^2,$$

(Eq. II-41)

and the effective potential energy given by:

$$V_{eff} = V_{ext} + V_H + V_{xc}$$

(Eq. II-42)

The Kohn–Sham approach reduces the original interacting many-electron problem to a set of self-consistent single-particle equations governed by three potential energy components. Strategies to evaluate these contributions are discussed below:

1. *External potential, V_{ext}.*

   In real many-body systems, V_{ext} originates from the Coulomb interaction between electrons and nuclear point charges. In practical plane-wave DFT calculations, the pseudopotential framework smooths the wavefunction in the rapidly oscillating all-electron wavefunction in the core region so that it can be represented efficiently using plane waves, while replicating the effect of V_{ext} on the valence electrons. The plane-wave cutoff energy sets the completeness of the wavefunction basis set.

   For NMR calculations, an accurate description of the electron density close to the nucleus is critical because magnetic shielding is strongly influenced by core–electron contributions and their coupling to the valence states. In this regard, conventional pseudopotentials—such as norm-conserving and ultrasoft types—tend to oversmooth core regions and distort magnetic shielding values.

   The Projector Augmented Wave (PAW) method addresses this limitation by reconstructing the all-electron (AE) wavefunction from the pseudo (PS) wavefunction:

$$|\Psi^{\mathrm{AE}}\rangle = |\Psi^{\mathrm{PS}}\rangle + \sum_{a} (|\phi_a^{\mathrm{AE}}\rangle - |\phi_a^{\mathrm{PS}}\rangle)\langle p_a|\Psi^{\mathrm{PS}}\rangle,$$

(Eq. II-43)

   where p_a are projector functions, while ϕ_a^{AE}, ϕ_a^{PS} are all-electron and pseudo partial waves, respectively. This reconstruction enables the accurate evaluation of properties highly sensitive to near-nuclear electronic structure, while retaining the computational efficiency of a plane-wave basis.

   In periodic systems described using a plane-wave basis, the following Bloch condition applies:

$$\Psi_{n\vec{k}}(\vec{r}) = e^{i\vec{k}\cdot\vec{r}}\psi_n(\vec{r}),$$

(Eq. II-44)

where $\vec{\boldsymbol{k}}$ is a reciprocal space wavevector within the first Brillouin zone. Consequently, the Kohn–Sham Hamiltonian becomes *k*-dependent as each *k*-point corresponds to an independent eigenvalue problem. The total energy is therefore obtained via Brillouin-zone integration:

$$E_{tot} = \frac{1}{\Omega_{BZ}} \int_{BZ} E(\vec{\boldsymbol{k}})\, d\vec{\boldsymbol{k}} \approx \sum_{\vec{\boldsymbol{k}}} \omega_k E(\vec{\boldsymbol{k}}),$$

(Eq. II- 45)

where Ω_{BZ} is the volume of the Brillouin zone and ω_k are the quadrature weights. Because the density of the *k*-point mesh controls how accurately the electronic structure is integrated over the Brillouin zone, appropriate *k*-point sampling is instrumental for reliable NMR shielding tensors. The sampling strategies employed in this work are discussed in Chapter II-3.2.

2. *Hartree potential, V_H*

V_H represents the classical electrostatic repulsion between electrons, and is defined as:

$$V_H(\vec{\boldsymbol{r}}) = e^2 \int \frac{\rho(\vec{\boldsymbol{r}}')}{|\vec{\boldsymbol{r}} - \vec{\boldsymbol{r}}'|} d\vec{\boldsymbol{r}}'.$$

(Eq. II-46)

Although conceptually simple, this description includes an unphysical contribution in which each electron interacts with its own charge density. Hence, this spurious self-interaction must be removed by the exchange–correlation (XC) term.

3. *Exchange–correlation potential, V_{xc}*

As described earlier, V_{xc} embodies the remaining quantum many-body effects, including the kinetic energy of interacting electrons, exchange effects arising from the Pauli principle, dynamical Coulomb correlation, and correction of self-interaction errors. The exact form of V_{xc} is unknown, and practical DFT relies on approximate XC functionals, such as:

- Local Density Approximation (LDA),
- Generalised Gradient Approximation (GGA),
- Meta-GGA and hybrid functionals.

For nuclei containing partially filled *d*- or *f*-orbitals, self-interaction errors in common XC functionals tend to spread out valence states in an unphysical manner. This artificial delocalisation affects the induced electronic currents, often leading to significant systematic errors in determining NMR shielding. The DFT+U method introduces an on-site Hubbard correction that imposes an energy penalty for occupying these valence orbitals,

thereby restoring the appropriate degree of electronic localisation [114]. In this work, the DFT+U method is applied to the La-4*f* orbitals. Details of this method are presented in Chapter II-3.2.

The fundamental NMR observable is the chemical shielding tensor, $\boldsymbol{\sigma}$, which quantifies how the electronic environment surrounding a nucleus modifies the magnetic field it experiences. The linear-response theory is often used to obtain $\boldsymbol{\sigma}$, where the Kohn–Sham equations are perturbed by a weak magnetic field, and the shielding tensor is then evaluated as:

$$\sigma_{\alpha\beta} = \frac{\partial^2 E_{tot}}{\partial B_\alpha \partial \mu_\beta},$$

(Eq. II-47)

where E_{tot} is the total electronic energy, B_α is the external magnetic field vector along the α-direction, and μ_β is the nuclear magnetic dipole moment along the β-direction.

In practice, the isotopic chemical shielding, σ_{iso}, is computed as in (Eq. II-7) and the isotropic chemical shift, δ_{iso}, is calculated as:

$$\delta_{iso} = a + b\sigma_{iso},$$

(Eq. II-48)

where a and b are constants determined from linear regression between DFT-calculated σ_{iso} values and experimentally measured δ_{iso} of reference solid-state compounds.

II-3.2. NMR Calculations with DFT

In this work, first-principles NMR shielding calculations were performed using the VASP code [115]. The Perdew–Burke–Ernzerhof (PBE) functional was used for the Generalized Gradient Approximation (GGA) of the exchange-correlation energy [116]. No dispersion corrections were applied. The PAW formalism was employed throughout, using the recommended GW potential datasets [117], e.g., *Na_sv_GW*, *Mg_sv_GW*, *La_GW*, *Cl_GW*, *O_GW*.

For solid-state compounds, fixed nuclear coordinates were obtained from crystallographic information files (CIF) retrieved from the ICSD database and converted into VASP POSCAR format. A Gaussian smearing scheme (`ISMEAR=0`) with a width of `SIGMA=0.01 eV` was applied. The plane wave cutoff energy was set to `ENCUT=600 eV`, exceeding the ENMAX among all PAW datasets used. The electronic self-consistent loop was converged to `EDIFF=10-8 eV`. Regular Monkhorst–Pack *k*-point meshes (*n*×*n*×*n*) were determined individually for each compound by performing convergence tests on total energy with respect to *k*-point density until changes were below 1 meV/atom. The LEFG and LCHIMAG tags were enabled to calculate electric field gradients and magnetic shielding parameters.

VASP directly outputs σ_{iso}, which were benchmarked against experimental δ_{iso} values of ^{35}Cl [118], ^{17}O [119], and ^{139}La [120,121]. Calibration was obtained using linear regression of δ_{iso} versus σ_{iso} (Eq. II-48), as shown in **Figure II-11**.

Initial VASP calculations revealed that the predicted ^{35}Cl chemical shift of $LaCl_3$ (one Cl site) and ^{17}O chemical shifts of La_2O_3 (two O sites) deviated strongly from the calibration curve. To address this error, a Hubbard correction (U) of +2 to +8 eV to the La-4*f* orbitals was introduced in 2 eV increments. The deviation for the three anomalous points was minimised at U=+6 eV. When this correction was extended to other La-containing compounds, the coefficient of determination (R^2) for the ^{139}La calibration curve improved substantially from 0.754 to 0.834 (**Figure II-11d**). Accordingly, a Hubbard U of +6 eV was adopted for all subsequent calculations involving La-4*f* states.

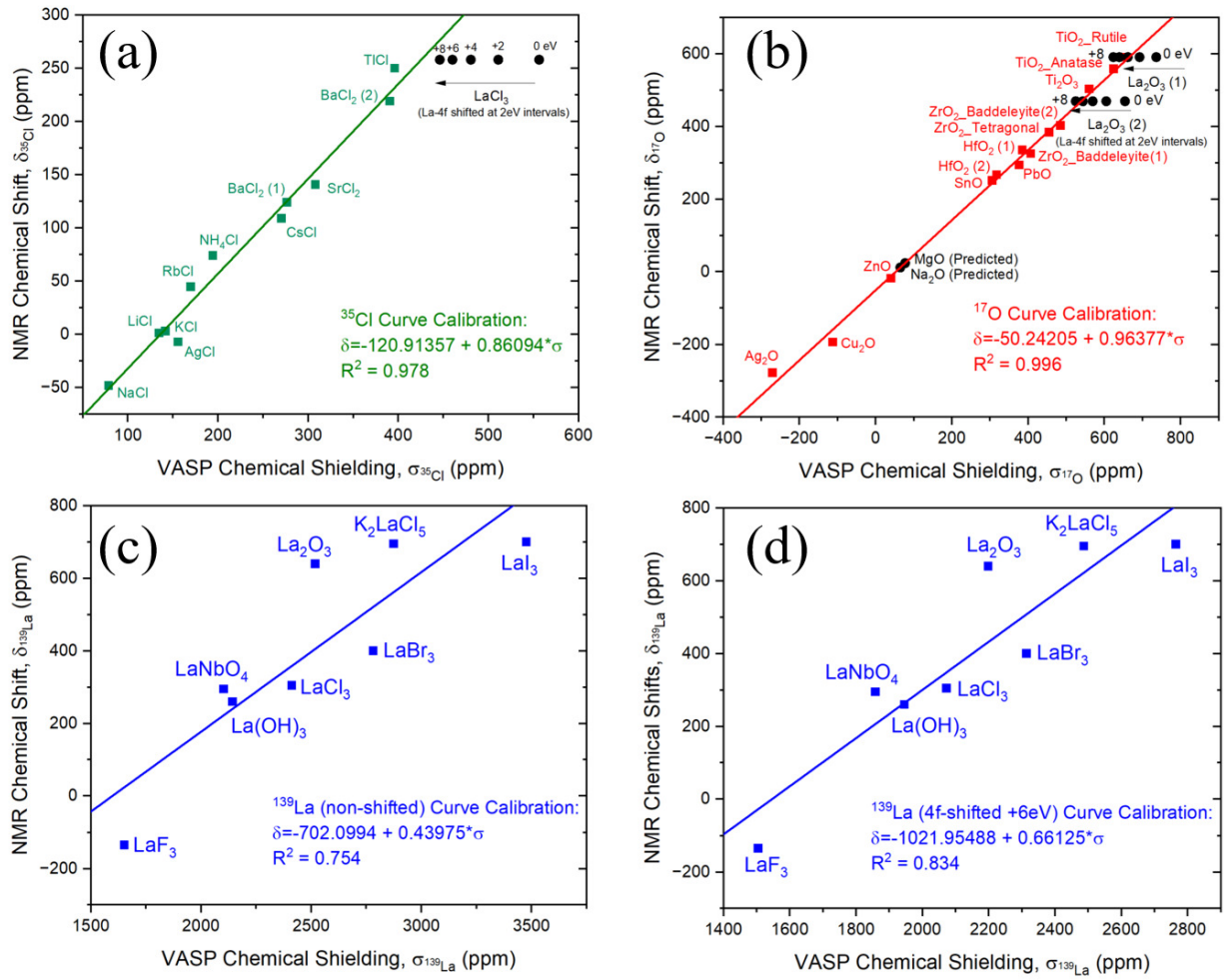

Figure II-11. Calibration curves of NMR chemical shifts (δ_{iso}) against VASP chemical shieldings (σ_{iso}) for (a) ^{35}Cl, (b) ^{17}O, (c) unshifted ^{139}La, and (d) 4f-shifted ^{139}La. Data points in black are not used in the calibration process.

For molten-state calculations, regularly spaced snapshots from the "small box" MD trajectories (**Table II-5**) were converted into VASP POSCAR format. To quantify chemical shifts for a specific nucleus (^{35}Cl, ^{17}O, or ^{139}La), the number of snapshots was chosen such that at least 50 targeted atoms were evaluated per composition, with a minimum

of 10 snapshots per composition. The same smearing settings were retained (`ISMEAR = 0` and `SIGMA = 0.01 eV`), while other parameters were relaxed to improve computation efficiency: `ENCUT=450 eV` (slightly above the ENMAX of all PAW datasets), `EDIFF=10-6`, Γ-point sampling, and a real-space solution of the Hamiltonian. The output σ_{iso} values were converted to δ_{iso} using the linear regression equations in **Figure II-11**, and the ensemble average was taken as the predicted chemical shift for each composition.

II-3.3. Geometry Optimisation with DFT

To improve the accuracy of NMR calculations for solid-state compounds, geometry optimisations were performed using VASP to relax crystallographic structures to their DFT ground states. In addition, geometry optimisation was applied to representative MD snapshots of the 80 NaCl–15 $LaCl_3$–5 LaOCl molten salt composition in order to verify the structural consistency between PIM-based and first-principles calculations.

For these calculations, most computational parameters were retained from the NMR calculations of the molten systems, with the following modifications:

- `ISPIN = 2` was used to enable spin-polarization;
- `LEFG = F` and `LCHIMAG = F` were set to disable EFG and NMR calculations during structural relaxation;
- `ALGO = Fast` was employed to accelerate electronic convergence during ionic relaxation;
- `SIGMA = 0.03 eV` was used to allow slightly increased electronic smearing;
- `NSW = 120` limited the number of ionic relaxation steps to 120;
- `ISIF = 2` (ionic relaxation only) or `ISIF = 3` (ionic and cell relaxation) was applied to examine the influence of cell degrees of freedom;
- `EDIFFG = -0.01 eV` was set as the convergence criterion for the ionic relaxation loop.

Geometry optimisation had a negligible impact on the chemical shielding–shift calibrations shown in **Figure II-11**, indicating that the crystal structures used for the calibration are already sufficiently relaxed at the DFT level. Among the systems examined, only the Cs_3LaCl_6 crystal [122]—which was not used in the calibration set—exhibited a significant structural change upon optimisation. This relaxation resulted in a marked improvement of the calculated NMR and EFG parameters and is discussed further in Chapter III-2.

In contrast, geometry optimisation of the molten salt snapshots did not reach the `EDIFFG` convergence criterion, most likely due to their intrinsically disordered configurations. Nevertheless, the operations terminated normally upon reaching the `NSW` limit and resulted in more symmetric bond geometries. The implications of these results for molten-state structures are discussed further in Chapter V-3.2.

Chapter III

Propriétés Structurelles
/
Structural Dynamics

Résumé (Français)

Dans les sels fondus, les interactions électrostatiques intenses entre les ions induisent un ordre à courte portée bien défini. La structure locale résulte alors des différences de rayons ioniques, de densités de charge et de préférences de coordination des espèces constitutives, qui déterminent les configurations atomiques énergétiquement favorables. Cette structure locale joue ensuite un rôle clé dans les propriétés macroscopiques des sels fondus, telles que la viscosité, la capacité thermique et la conductivité thermique.

Le chapitre III s'attache à établir les interactions ioniques fondamentales dans les sels combustibles des MCFR, en prenant comme référence la composition NaCl–$MgCl_2$–$PuCl_3$–$AmCl_3$ proposée pour le réacteur français ARAMIS-A. Toutefois, en raison de leur radiotoxicité et des risques de prolifération associés, le $PuCl_3$ et l'$AmCl_3$ sont soumis à des contraintes réglementaires strictes et ne peuvent être manipulés expérimentalement au CEMHTI. Dans ce contexte, le $LaCl_3$ est retenu comme substitut structurel non radioactif des trichlorures d'actinides, en raison de sa similitude chimique et structurale, ainsi que de son isotope ^{139}La actif en RMN.

Le chapitre III-1 est consacré aux mesures *in situ* de RMN HT des déplacements chimiques du ^{35}Cl et du ^{139}La, réalisées pour différentes compositions et températures dans le combustible proxy NaCl–$MgCl_2$–$LaCl_3$. Les principaux résultats peuvent être résumés comme suit :

- L'évolution des déplacements chimiques du ^{35}Cl met en évidence des comportements distincts entre les systèmes binaires. Elle varie de manière linéaire dans le système NaCl–$MgCl_2$, tandis qu'elle suit des tendances paraboliques dans les mélanges NaCl–$LaCl_3$ et $MgCl_2$–$LaCl_3$. Cette différence est attribuée à la formation de ponts La–Cl–La, prédominante dans les systèmes contenant du $LaCl_3$. La courbure plus prononcée observée dans NaCl–$LaCl_3$, par rapport à $MgCl_2$–$LaCl_3$, suggère une formation plus marquée de réseaux entre les complexes $[La_xCl_y]^{3x-y}$ dans ce système. Par ailleurs, les valeurs de déplacement chimique du ^{35}Cl montrent une faible sensibilité à la température, en raison de variations limitées du nombre de coordination Cl–La ($CN_{Cl–La}$).

- Les déplacements chimiques du ^{139}La évoluent de manière similaire dans les systèmes NaCl–$LaCl_3$ et $MgCl_2$–$LaCl_3$. Toutefois, la plage des valeurs est nettement plus large dans le système NaCl–$LaCl_3$, indiquant une plus forte sensibilité du nombre de coordination La–Cl ($CN_{La–Cl}$) à la composition. Contrairement au ^{35}Cl, les valeurs de déplacement chimique du ^{139}La présentent une dépendance marquée à la température, traduisant une désorganisation progressive de la sphère de coordination La–Cl due à la migration d'ions Cl^- vers l'extérieur lorsque la température augmente.

- Dans l'ensemble, ces résultats indiquent que le $MgCl_2$ favorise des nombres de coordination La–Cl plus élevés ainsi que la formation d'unités $[LaCl_n]^{3-n}$ relativement isolées. À l'inverse, le NaCl tend à réduire le $CN_{La–Cl}$ et à promouvoir la formation de réseaux étendus de type La–Cl–La.

- Les mesures RMN HT réalisées sur le système ternaire NaCl–$MgCl_2$–$LaCl_3$ confirment ces tendances. L'augmentation du rapport $MgCl_2$/NaCl conduit à une diminution progressive de la courbure parabolique des déplacements chimiques du ^{35}Cl, signe d'une réduction des ponts chlorure, tandis que les déplacements chimiques du ^{139}La diminuent significativement, traduisant une coordination La–Cl accrue.

Le chapitre III-2 est dédié aux expériences de RMN ES réalisées sur des composés cristallins contenant du $LaCl_3$, à savoir $LaCl_3$ ($CN_{La–Cl} = 9$, $CN_{Cl–La} = 3$), K_2LaCl_5 ($CN_{La–Cl} = 7$, $CN_{Cl–La} = 1$ ou 2) et Cs_3LaCl_6 ($CN_{La–Cl} = 5$ ou 6, $CN_{Cl–La} = 1$). Ces expériences visent à établir des corrélations quantitatives entre les nombres de coordination et les déplacements chimiques observés en RMN. Les principaux résultats peuvent être résumés comme suit :

- La valeur du déplacement chimique du ^{139}La diminue lorsque le $CN_{La–Cl}$ augmente.
- La valeur du déplacement chimique du ^{35}Cl augmente avec le $CN_{Cl–La}$, traduisant une augmentation du degré de pontage chlorure.

Le chapitre III-3 présente des simulations classiques de DM fondées sur le PIM, utilisées pour générer des trajectoires ioniques à partir desquelles les fonctions de distribution radiale (RDF), les nombres de coordination et la connectivité du réseau La–Cl–La sont analysés de manière quantitative. Les principaux résultats sont résumés comme suit :

- L'analyse des RDF met en évidence des différences marquées dans le comportement de mélange des systèmes binaires NaCl–$LaCl_3$ et $MgCl_2$–$LaCl_3$. Le NaCl forme une « couche séparatrice » favorisant un mélange hétérogène avec le $LaCl_3$; en conséquence, les ions La^{3+} ont tendance à se regrouper et à former des réseaux La–Cl–La étendus et interconnectés. À l'inverse, le $MgCl_2$ se mélange de manière plus homogène avec le $LaCl_3$, ce qui perturbe la formation de chaînes continues du réseau La–Cl–La.
- La visualisation des polyèdres de coordination La–Cl montre que, dans le système NaCl–$LaCl_3$, ces polyèdres présentent majoritairement des coordinations à six ou sept voisins et partagent fréquemment des arêtes ou des faces, traduisant un fort degré de connectivité. En revanche, dans le système $MgCl_2$–$LaCl_3$, les polyèdres La–Cl présentent plus souvent des coordinations à sept ou huit voisins et tendent à être davantage isolés.
- L'analyse combinée des RDF et de la structure locale par visualisation (Visual Molecular Dynamics) du système ternaire NaCl–$MgCl_2$–$LaCl_3$ est cohérente avec les rôles respectifs du NaCl et du $MgCl_2$. Toutefois, l'analyse des chaînes polymérisées et du partage polyédrique dans le système ternaire, avec une fraction de $LaCl_3$ fixée à 20 mol %, ne met pas en évidence de différences significatives de structure locale lorsque le rapport NaCl/$MgCl_2$ varie. Ce résultat inattendu est attribué à l'apport d'ions Cl^- supplémentaires par le $MgCl_2$ (par rapport au NaCl), qui offrent davantage de possibilités de pontage chlorure et entrent en compétition avec l'effet perturbateur du $MgCl_2$ sur le réseau La–Cl–La.

Le chapitre III-4 décrit les calculs RMN basés sur les premiers principes, utilisés afin d'évaluer la cohérence entre les structures locales déduites des expériences RMN et celles obtenues par simulations DM. Les principaux résultats peuvent être résumés comme suit :

- Les calculs RMN réalisés à l'aide du code VASP reproduisent de manière satisfaisante l'évolution des valeurs du déplacement chimique en fonction de la composition, indiquant une bonne concordance entre les expériences RMN et les simulations DM.

- Une analyse détaillée des déplacements chimiques calculés pour chaque atome montre que les tendances observées expérimentalement en RMN ES sont généralement bien reproduites par les calculs. La principale exception concerne la RMN du ^{35}Cl dans les compositions riches en $LaCl_3$, pour lesquelles le $CN_{Cl–La}$ plus faible conduit à des déplacements chimiques plus élevés. Ce comportement est attribué à la présence de lacunes locales, qui induisent un effet de désblindage marqué et entraînent une augmentation des valeurs du déplacement chimique.

Prises ensemble, ces approches expérimentales et numériques complémentaires établissent un cadre de vérification multimodale robuste pour l'élucidation des interactions à l'échelle atomistique dans les sels fondus. Cette approche est essentielle pour approfondir la compréhension de l'influence de la structure à courte portée sur les propriétés macroscopiques des combustibles des réacteurs rapides à chlorure fondu.

Introduction

Liquids are conventionally regarded as disordered and essentially structureless. However, in molten salts, strong electrostatic interactions between ions give rise to a measurable degree of short-range ordering within the liquid matrix. Such ordering originates from differences in ionic radii, charge densities, and coordination preferences of the constituent species, which dictate the energetically favourable atomic configurations. As a result, the local structure may exert a significant influence on their macroscopic properties, including viscosity, heat capacity, and thermal conductivity.

This chapter establishes the fundamental ionic interactions in MCFR fuel salts, with particular reference to the NaCl–$MgCl_2$–$PuCl_3$–$AmCl_3$ mixture proposed for the French ARAMIS-A reactor. Nevertheless, owing to their radiotoxicity and proliferation risks, $PuCl_3$ and $AmCl_3$ are subjected to strict handling regulations and not permitted for experimental use at CEMHTI. A common approach to circumvent these stringent restrictions on actinide trichlorides ($AnCl_3$) is to employ non-radioactive, proliferation-resistant lanthanide trichlorides ($LnCl_3$) as structural surrogates. This is because $LnCl_3$ typically share closely analogous chemical behaviour with $AnCl_3$, including identical crystal structures, comparable ionic radii, and similar metal–chloride bond lengths. In this work, the NMR-active and non-paramagnetic $LaCl_3$ was selected as a surrogate for $PuCl_3$ and $AmCl_3$.

Using the NaCl–$MgCl_2$–$LaCl_3$ system as a proxy fuel composition, *in situ* HT NMR measurements were performed to obtain ^{139}La and ^{35}Cl chemical shifts across different compositions and temperatures. To interpret these shifts, SS NMR experiments were conducted on $LaCl_3$-containing crystalline compounds, enabling the correlation of specific coordination environments with their characteristic chemical shifts. In parallel, classical MD simulations employing the PIM were used to generate ion trajectories, from which the radial distribution functions, coordination numbers, and La–Cl–La network connectivity were extracted. Finally, DFT calculations were carried out on regularly spaced MD snapshots to obtain ensemble-averaged chemical shifts in disordered molten salt systems, providing a direct means to validate the consistency between NMR experiments and MD simulations.

Taken together, these complementary techniques establish a self-consistent framework to elucidate the molecular-level interactions in molten salts, laying the groundwork for understanding how short-range structure influences the macroscopic behaviour of MCFR fuel systems.

III-1. High-Temperature NMR

HT NMR serves as the principal experimental method in this chapter, with a particular focus on the effects of composition and temperature on the ^{139}La and ^{35}Cl chemical shifts. Measurements were performed on the three binary subsystems of the NaCl–$MgCl_2$–$LaCl_3$ system, namely NaCl–$MgCl_2$, NaCl–$LaCl_3$, and $MgCl_2$–$LaCl_3$, at 10 mol% composition intervals. In the ternary phase space, measurements were primarily conducted along compositional lines with varying NaCl–$MgCl_2$ ratios while maintaining a fixed $LaCl_3$ content of 20 mol% (chosen to more closely reflect the $AnCl_3$ concentration in the ARAMIS-A fuel composition). NMR measurements were acquired over a temperature

range extending from T_m+10 °C to 900 °C, where the liquidus temperatures, T_m, were estimated from the ternary phase diagram generated using FactSage [109], shown in **Figure III-1**. Thermochemical data for the end-members (NaCl, $MgCl_2$, $LaCl_3$) and intermediate compounds ($NaMgCl_3$, Na_2MgCl_4, $Na_3La_5Cl_{18}$) were sourced from the FactPS database; thermodynamic optimisation of the ternary system was performed in this work, yielding the parameters in **Table III-1 and III-2**.

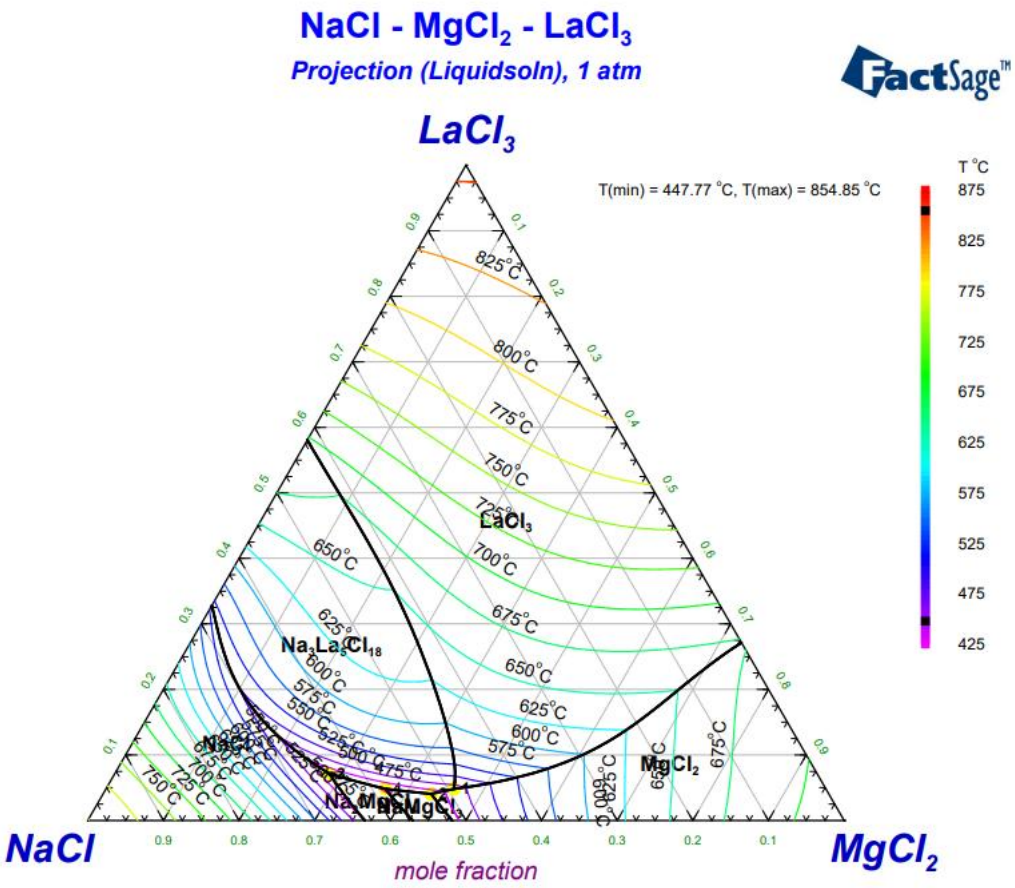

Figure III-1. Ternary liquidus projection of the NaCl–$MgCl_2$–$LaCl_3$ mixture. Ternary projection is done using the Toop–Kohler interpolation scheme, with $LaCl_3$ as the asymmetric component.

Table III-1. Excess binary Gibbs free energy parameters, $\Delta g_{AB/X}$ in constituent binary mixtures. No excess ternary interaction parameters were introduced in this work.

AX	BX	$\Delta g_{AB/X}\ (J/mol)$
NaCl	$LaCl_3$	$-10866 + (3687.17 + 1.76387\ T)\ X_{AA} - 3303.57\ X_{BB} - 7341.74\ X_{AA}^2$
$MgCl_2$	$LaCl_3$	$(1905.65 - 2.5349\ T) + (2096.66 + 1.26675\ T)\ X_{AA} + (2047.08 + 3.28697\ T)\ X_{BB}$
NaCl	$MgCl_2$	$-10395.8 + 660.5\ X_{AA} - 4641.5\ X_{BB}$

Table III-2. Cation–Cation coordination numbers used for the modified quasichemical model (MQM)

A	B	Z_{AB}^{A}	Z_{BA}^{B}
Na^+	La^{3+}	3	6
Mg^{2+}	La^{3+}	4	6
Na^+	Mg^{2+}	3	6

III-1.1. Binary Systems

Figure III-2 shows the ^{35}Cl chemical shift evolution of the three binary subsystems of NaCl–$MgCl_2$–$LaCl_3$ as a function of composition, measured at T_m+10 °C of each composition. In NaCl–$MgCl_2$, the ^{35}Cl chemical shift evolves approximately linearly with composition. In contrast, distinct non-linear behaviour is observed in both the NaCl–$LaCl_3$ and $MgCl_2$–$LaCl_3$ binaries.

This nonlinearity can be attributed to the tendency for Cl^- ions to form bridging environments between two or more neighbouring La^{3+} ions in the melt [123]. In NaCl–$MgCl_2$, Cl^- ions behave predominantly as "free" anions. By contrast, in NaCl–$LaCl_3$ and $MgCl_2$–$LaCl_3$, Cl^- ions tend to be more strongly bound, being shared between adjacent La^{3+} centres to help satisfy the high coordination number required for local charge neutrality [124]. Corradini *et al.* quantified this phenomenon using cage-correlation function analysis, demonstrating that Cl^- ions exhibit longer lifetimes in the La^{3+} solvation shell in molten salts with increasing $LaCl_3$ content [125]. As will be discussed in Chapter III-4, bridging Cl^- ions are generally more deshielded than non-bridging Cl^- ions, resulting in more positive chemical shifts and a progressive deviation from linearity. Furthermore, the stronger deviation from linearity in NaCl–$LaCl_3$ compared to $MgCl_2$–$LaCl_3$ suggests that chloride bridging is more pronounced in the former system.

The temperature dependence of the ^{35}Cl chemical shifts was also examined for the NaCl–$LaCl_3$ system (**Figure III-3**). With increasing temperature, a noticeable narrowing of the NMR linewidths and a concomitant increase in signal intensity are observed. These changes are consistent with faster ion dynamics and enhanced motional averaging at elevated temperatures, which reduce residual anisotropic interactions contributing to line broadening, thereby boosting the observed peak amplitudes. Despite these temperature-dependent changes in linewidth and intensity, the corresponding variations in peak positions remain small relative to the overall compositional shift range. This limited temperature sensitivity on the ^{35}Cl chemical shifts is consistent with the findings of Hudry *et al.* [126] and Zhang and Farnan [127], who reported similarly weak temperature effects in $(LiCl–KCl)_{eut}$–$LaCl_3$ and $(LiCl–KCl)_{eut}$–$CeCl_3$ systems, respectively. The weak temperature dependence can be attributed to the minimal change in average Cl^- coordination environment over the temperature range studied. The slight chemical shift increase is attributed to the increased La–Cl separation with temperature, increasing deshielding of ^{35}Cl nuclei. Consequently, temperature effects on ^{35}Cl chemical shifts were not pursued further in this work, and subsequent analysis of ^{35}Cl chemical shifts focuses primarily on the compositional effects.

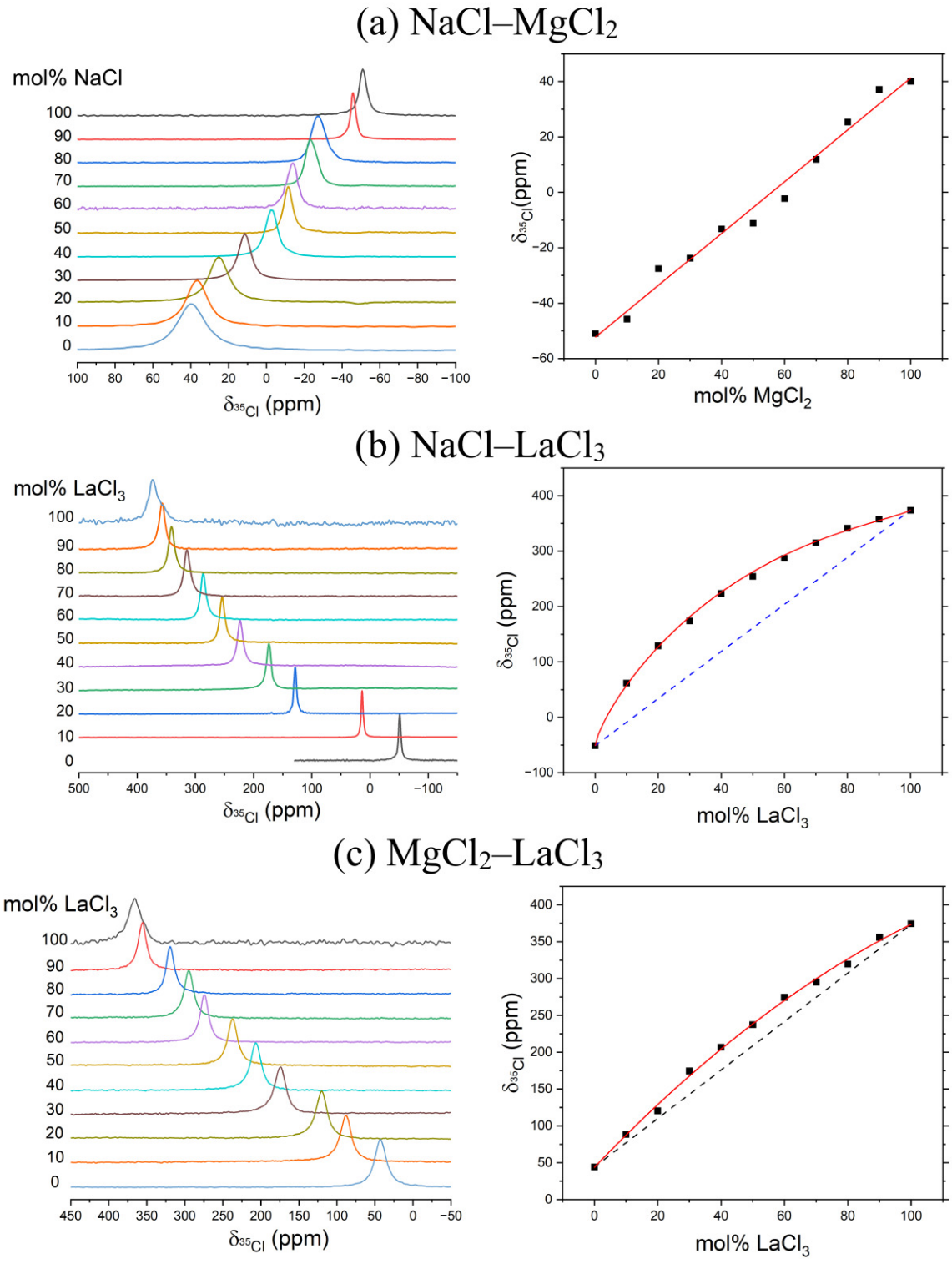

Figure III-2. ^{35}Cl chemical shift evolutions for (a) $NaCl–MgCl_2$, (b) $NaCl–LaCl_3$ and (c) $MgCl_2–LaCl_3$, measured by in-situ HT NMR as a function of composition at T_m + 10 ˚C of the respective salts.

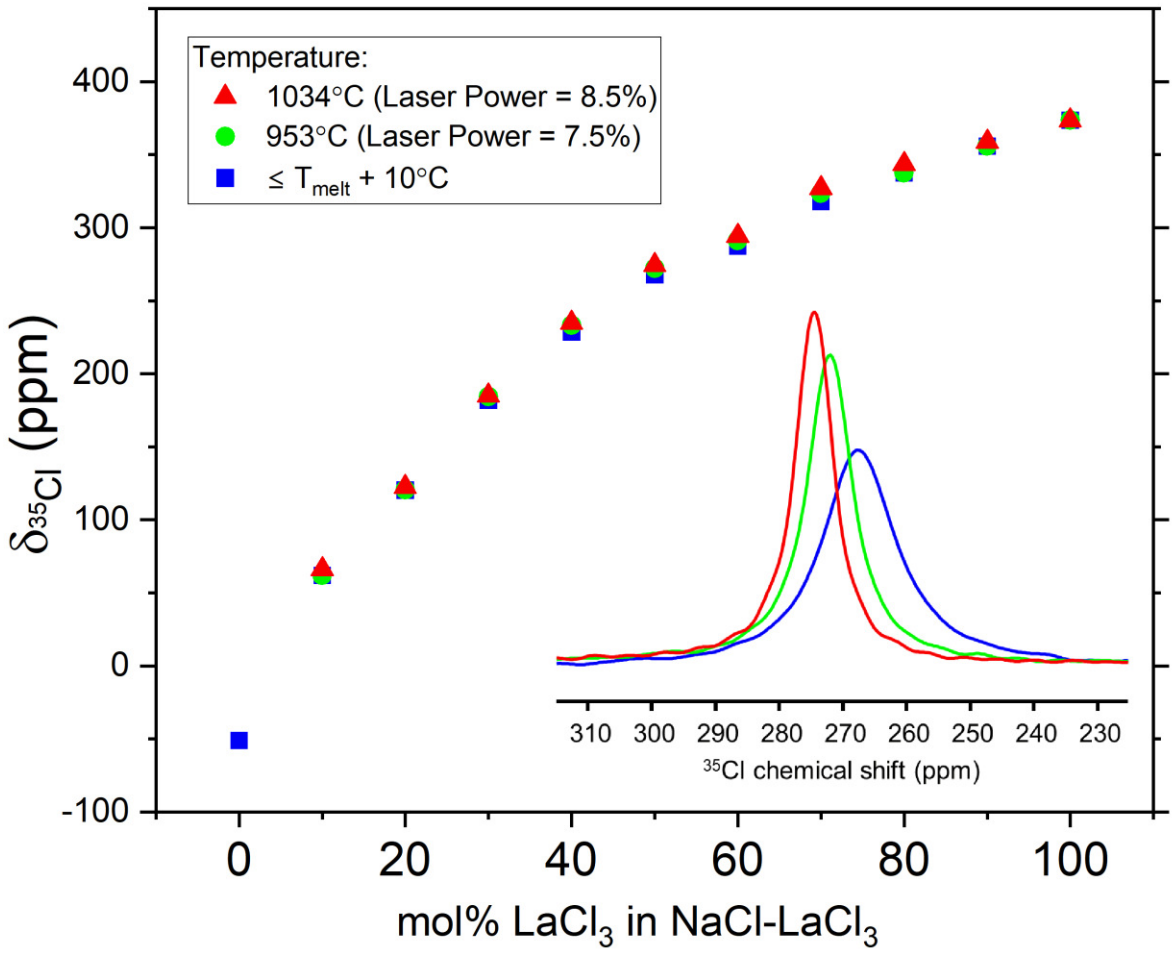

Figure III-3. ^{35}Cl chemical shift evolution for NaCl–$LaCl_3$, measured by in-situ HT NMR as a function of composition and temperature. Measured peaks of the 50 mol% NaCl–50 mol% $LaCl_3$ at varying temperatures are given as an example in the bottom right of the figure. Note that while the changes in chemical shifts appear significant on the absolute scale, they remain small relative to the scale of the range of chemical shift evolutions. The error in the temperature estimation is ±10 °C.

The ^{139}La chemical shifts in the NaCl–$LaCl_3$ and $MgCl_2$–$LaCl_3$ systems were examined as functions of both composition and temperature (**Figure III-4**). Compositional effects were analysed using chemical shift values acquired at T_m+10 °C. Here, two linear fits were applied to the chemical shift evolution at lower and higher compositional fractions of the spectra. Notably, the intersections of these lines closely coincide with the eutectic compositions of the binary mixtures. This close correspondence suggests a change in the local La^{3+} environment associated with the onset of melting. Specifically, at the onset of melting, the ^{139}La chemical shift appears to be dominated by the prevailing La^{3+}-containing phase at each composition. Furthermore, the ^{139}La chemical shift range in the NaCl–$LaCl_3$ system is larger than that in $MgCl_2$–$LaCl_3$, indicating greater variation of the average La–Cl coordination number in the former.

In stark contrast to ^{35}Cl chemical shifts, temperature induces a pronounced positive evolution in the ^{139}La chemical shifts for both NaCl–$LaCl_3$ and $MgCl_2$–$LaCl_3$. This trend indicates the increasing deshielding of ^{139}La nuclei with rising temperature, which can be attributed to widened La–Cl distances and consequently a reduction in coordination

number. This strong temperature sensitivity is consistent with the findings of Emerson *et al.* [128], who, through classical MD simulations, demonstrated a progressive decrease in La–Cl coordination with increasing temperature in the $NaCl–LaCl_3$ melt.

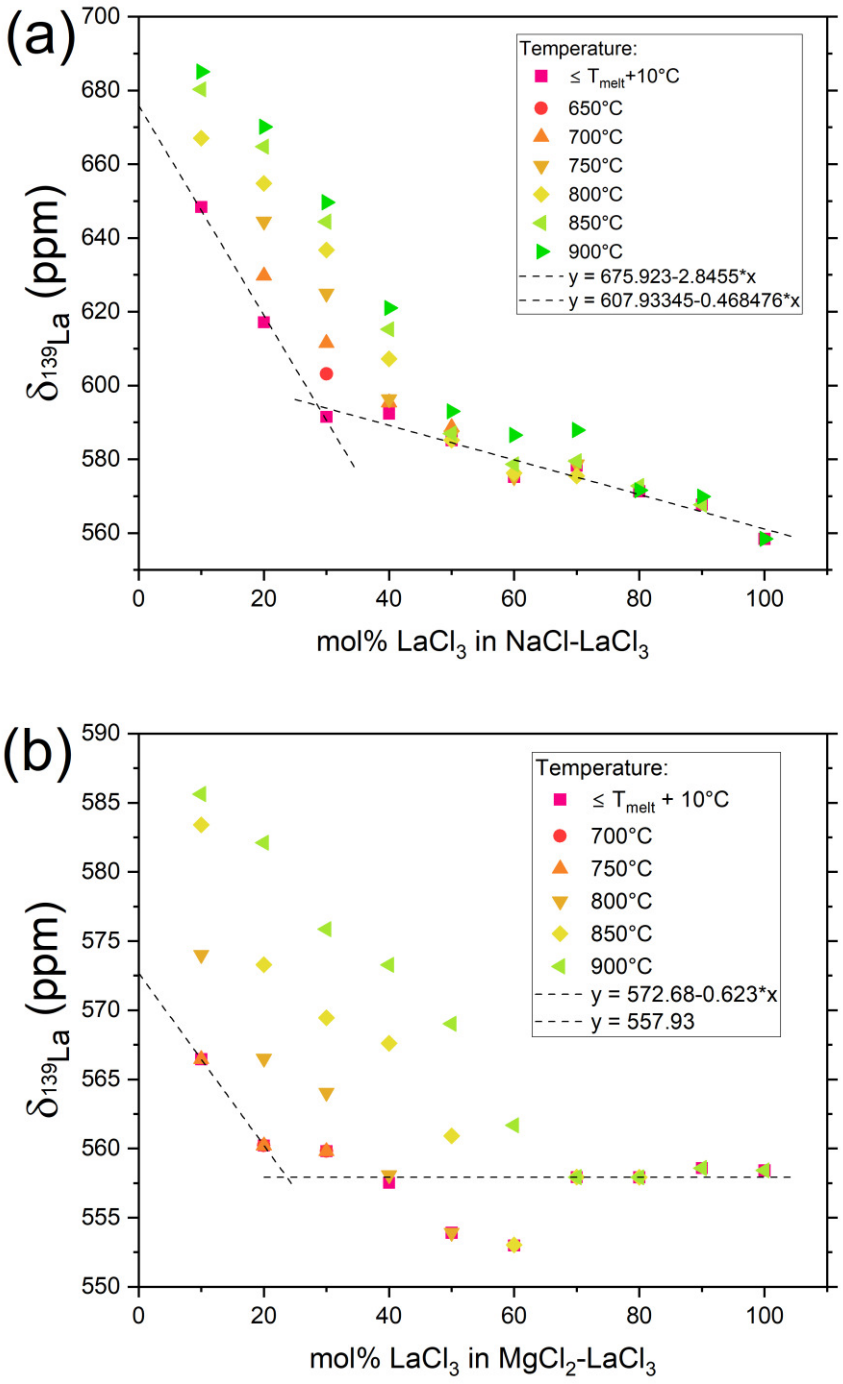

Figure III-4. ^{139}La chemical shift evolutions for (a) $NaCl–LaCl_3$ and (b) $MgCl_2–LaCl_3$, measured by in-situ HT NMR as functions of composition and temperature. The error in the temperature estimation is ±10 °C.

III-1.2. Ternary Systems

Building on the analysis of binary systems, the HT NMR investigation was extended to the ternary $NaCl–MgCl_2–LaCl_3$ system. To better reflect the proposed ARAMIS-A fuel composition of 62 NaCl–15 $MgCl_2$–23 $(Pu,Am)Cl_3$ (in mol%) [37], chemical shift evolutions of ^{139}La and ^{35}Cl were measured along the compositional paths (100 – x) $(NaCl)_{0.80}(MgCl_2)_{0.20}$– x $LaCl_3$ and 80 $(NaCl)_{1-x}(MgCl_2)_x$ –20 $LaCl_3$ (where all values are in mol%).

Figure III-5a compares the ^{35}Cl chemical shift evolution for the generalised composition (100 – x) $(NaCl)_{1-y}(MgCl_2)_y$– x $LaCl_3$ (x=0–100 mol% at 10 mol% intervals; y=0–1 at 0.2 intervals). Here, the area between the parabolically fitted curve and the theoretical linear line connecting the end points is used as a metric for the deviation from ideal linear behaviour. The results show that deviation from linearity increases systematically with increasing $NaCl/MgCl_2$ ratio, supporting earlier conclusions that NaCl promotes greater chloride bridging between La^{3+} ions than $MgCl_2$. A simple stoichiometric analysis supports this argument: since NaCl is monovalent and $MgCl_2$ is divalent, replacing $MgCl_2$ with NaCl reduces the overall availability of $Cl^–$ ions in the melt. To preserve local charge neutrality, chloride ions must therefore be shared between adjacent La^{3+} centres, resulting in enhanced chloride bridging. In contrast, the higher $Cl^–$ availability provided by $MgCl_2$ favours the formation of more independent $[LaCl_n]^{3-n}$ complexes, thereby reducing the extent of chloride bridging.

Figure III-5b presents a contour plot of the ^{139}La chemical shift evolution as a function of temperature and the $MgCl_2$ content along the compositional line 80 $(NaCl)_{1-x}(MgCl_2)_x$ –20 $LaCl_3$. Consistent with the observations on binary systems, increasing the fraction of $MgCl_2$ results in more positive ^{139}La chemical shifts, while increasing the fraction of NaCl shifts the signal in the opposite direction. In addition, increasing the temperature leads to a systematic positive shift of the ^{139}La resonance. These trends confirm that $MgCl_2$ promotes higher average La–Cl coordination environments, whereas NaCl favours lower La–Cl coordination environments, and that thermal expansion promotes ^{139}La deshielding through the loss of La–Cl coordination.

In summary, *in situ* HT NMR provides critical insight into the structural dynamics of the $NaCl–MgCl_2–LaCl_3$ molten salt system. The deviation from linearity in ^{35}Cl chemical shift evolution serves as a quantitative indicator for chloride bridging, while the ^{139}La chemical shift directly reflects the average La–Cl coordination number in the melt. Together, these results demonstrate a strong, systematic link between NMR response and variations of the local coordination environment with composition and temperature.

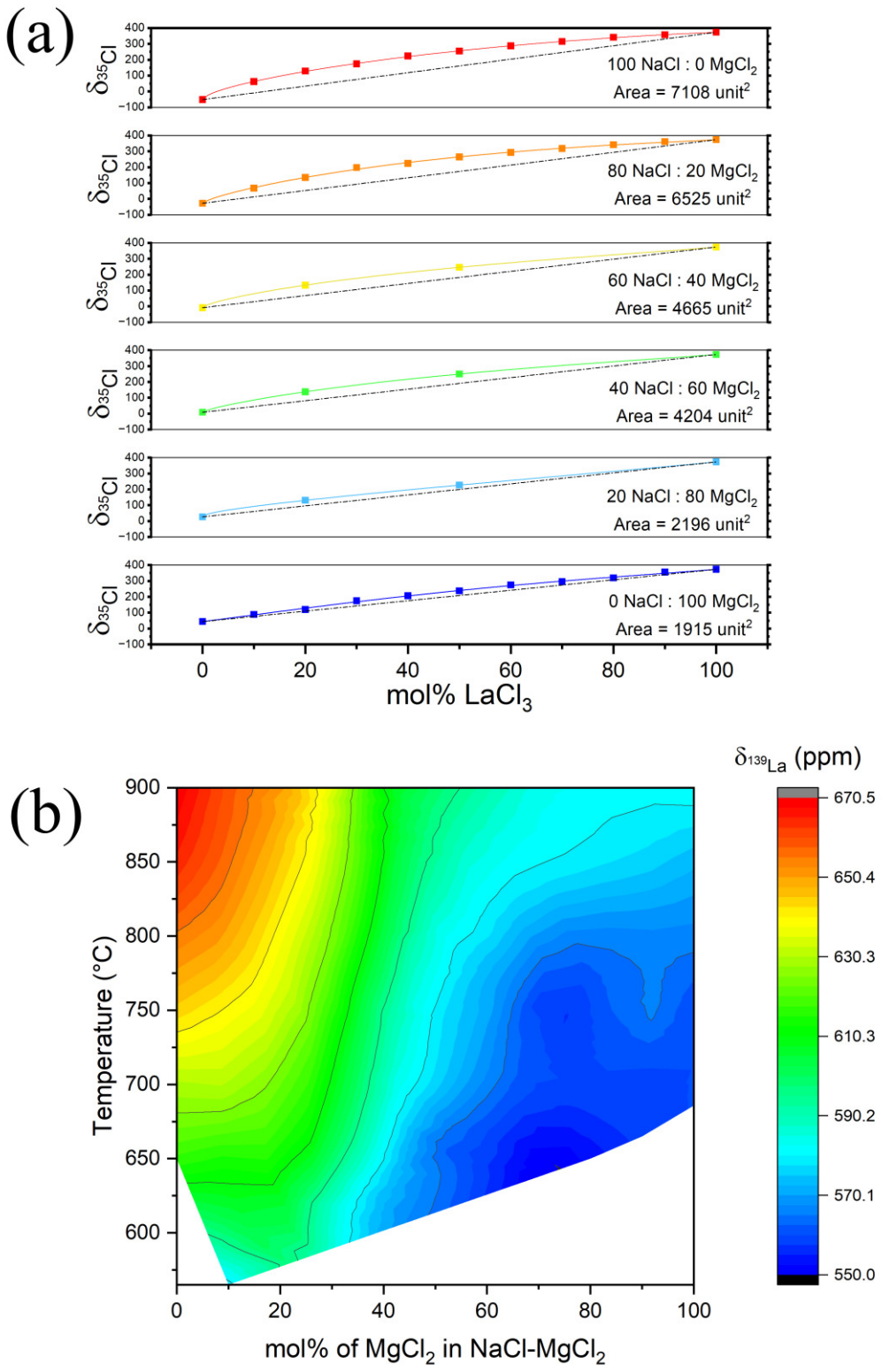

Figure III-5. (a) ^{35}Cl chemical shift evolutions of ternary salts at varying NaCl/$MgCl_2$ ratios measured at T_m + 10 °C of the respective salts (individual curves are offset for better visualisation); (b) ^{139}La chemical shift evolution of ternary salts with $LaCl_3$ fixed at 20 mol% as functions of temperature and NaCl:$MgCl_2$ ratio. The ^{35}Cl chemical shift evolutions were fitted using a beta-spline function with fixed end points, $\delta = \delta_0(1-t) + \delta_{100}t + At^{\alpha}(1-t)^{\beta}$, where $t = x/100$ and A, α, and β are fitting parameters. The error in the temperature estimation is ±10 °C.

III-2. Solid-State NMR

SS NMR measurements were performed to delineate the relationship between coordination number and chemical shift. Unlike molten salts, solid salts typically exhibit a consistent three-dimensional structure, characterised by the periodic and ordered geometry of ions, which defines the crystalline arrangement of a Bravais lattice. As a result, such materials show minimal variation in bond lengths and well-defined coordination numbers.

In this chapter, SS NMR was applied to three lanthanum chloride compounds, namely $LaCl_3$, K_2LaCl_5, and Cs_3LaCl_6. To the best of current knowledge, these are the only La–Cl compounds with well-defined crystal structures reported to date. Structural information of these salts is summarised in **Table III-3**. $LaCl_3$ (AnhydroBeads, ≥99.99%) was used as received. K_2LaCl_5 and Cs_3LaCl_6 were synthesised via a conventional solid-state reaction: fine powders of KCl (Merck, ≥99.5%) and $LaCl_3$, and CsCl (Alfa Aesar, 99%) and $LaCl_3$, were thoroughly homogenised according to their respective stoichiometric ratios. The mixtures, contained in high-purity BN crucibles, were held above their congruent melting temperatures (650 °C for K_2LaCl_5 and 800 °C for Cs_3LaCl_6 [109]) under a saturated argon atmosphere in a tube furnace for one hour and slowly cooled to ambient temperature at a rate of 0.25 °C/min.

Table III-3. Structural Data of Crystalline Salts used in SS NMR Experiments

Compound	La–Cl Bond Lengths (Å)	$CN_{La–Cl}$	$CN_{Cl–La}$	La sites	Cl sites	Ref.
$LaCl_3$	2.95	9	3	1	1	[129]
K_2LaCl_5	2.81–2.89	7	1, 2*	1	4	[130]
Cs_3LaCl_6	La_1: 2.59–2.84 La_2: 2.67–2.92	5, 6†	1	2	6	[122], This Work

*Three Cl sites are non-bridging, the multiplicity of these sites is 1; one Cl site is bridging, the multiplicity of this site is 2.

†The literature [122] reports only 6-fold La–Cl coordination; DFT geometry optimisation reveals a combination of 5- and 6-fold coordinations.

Figure III-6 presents the powdered X-ray diffraction (XRD) patterns of the synthesised compounds. Both K_2LaCl_5 and Cs_3LaCl_6 exhibit excellent agreement with the reported X-ray diffraction spectra [122,130], confirming successful synthesis. Minor traces of BN were detected in both samples, originating from the crucibles used during synthesis. A small amount of KCl was also detected in the K_2LaCl_5 sample. Nonetheless, these secondary phases are considered insignificant for the SS NMR spectra measurements: the Larmor frequencies of ^{11}B and ^{15}N do not overlap with those of ^{139}La and ^{35}Cl, whereas KCl produces a sharp, easily distinguishable ^{35}Cl resonance near 0 ppm due to its simple cubic crystal structure.

Given that NMR is highly sensitive to subtle changes in bond lengths and coordination environments, the isotropic chemical shifts obtained from SS NMR are expected to vary greatly between different compounds, making them efficient indicators of trends in coordination chemistry. **Figure III-7** shows the ^{139}La NMR spectra from static and MAS measurements on the crystalline salts, recorded under two magnetic fields: 17.6 and 20 T. The spectra were fitted

using a consistent set of parameters and compared with literature data [120] as well as with the NMR parameters obtained from the DFT calculations performed in this work (**Table III-4**).

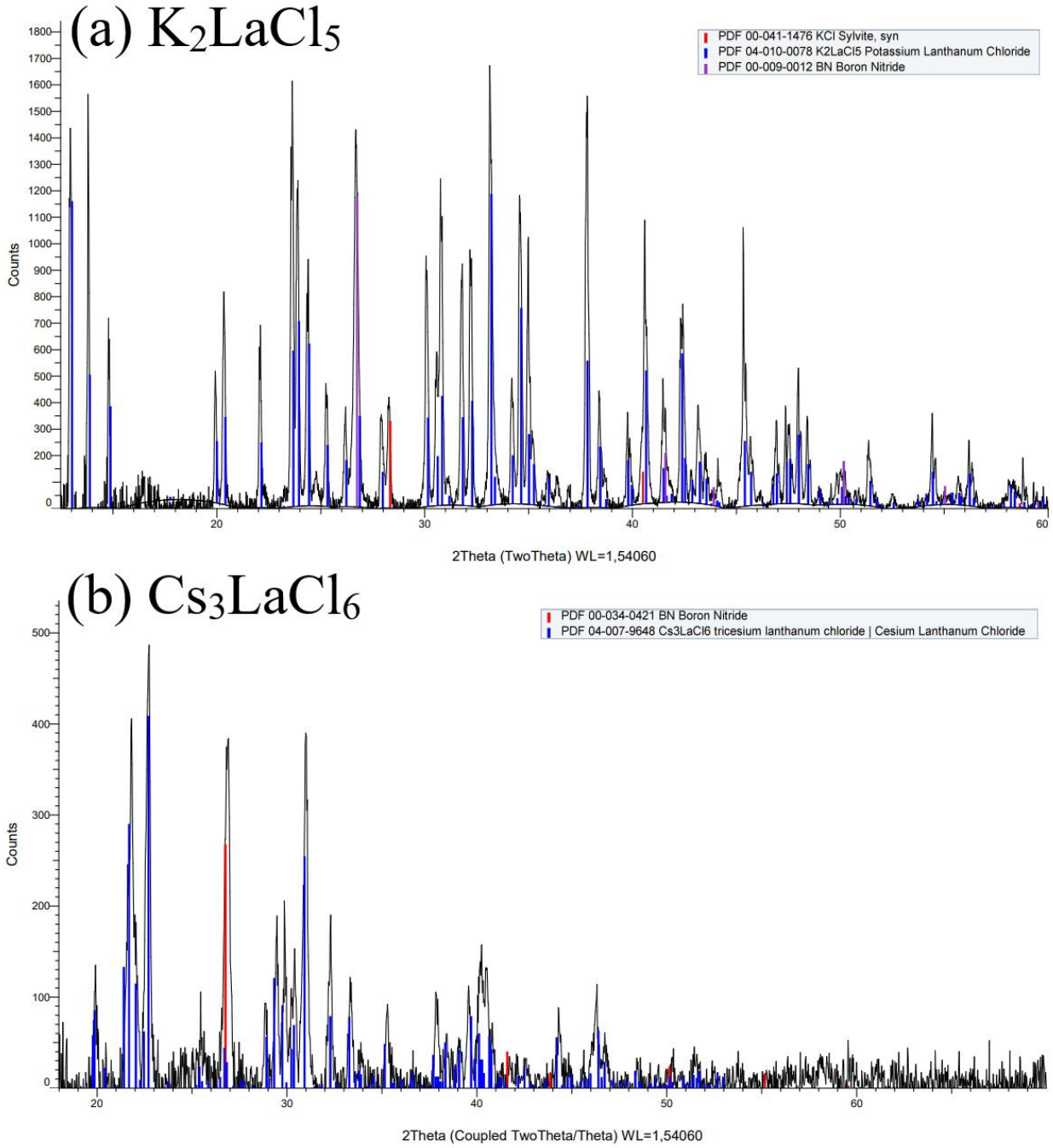

Figure III-6. Powdered XRD analysis of the synthesised intermediate compounds: (a) K_2LaCl_5 and (b) Cs_3LaCl_6 (bottom). XRD measurements were conducted with the samples sealed in a dome-sealed, gas-tight sample holder under an argon atmosphere.

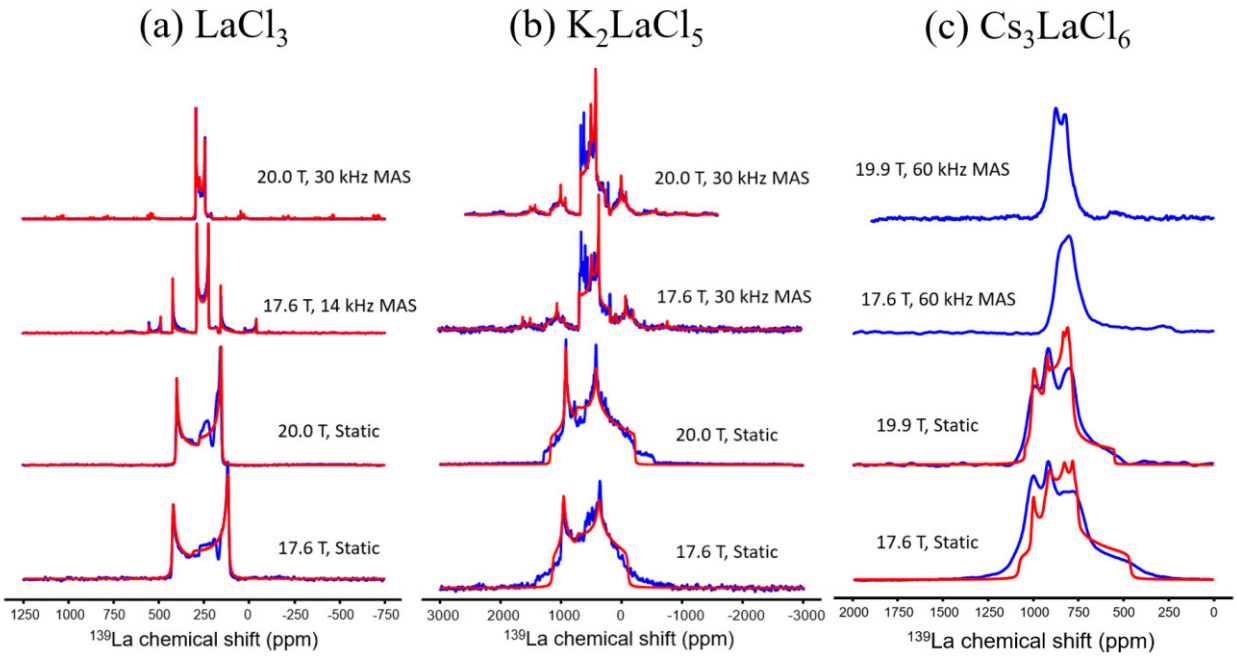

Figure III-7. ^{139}La SS NMR spectra of (a) $LaCl_3$, (b) K_2LaCl_5, and (c) Cs_3LaCl_6. Measured spectra are given in blue and fitted spectra are given in red. Fitting for Cs_3LaCl_6 spectra is omitted for reasons discussed in the text.

Table III-4. ^{139}La SS NMR Parameters Obtained from Line Fitting and DFT Calculations

Compound	Method	δ_{iso} (ppm)	C_Q (MHz)	η
$LaCl_3$	SS NMR (This Work)	311 ± 3	15.9 ± 0.5	0.00
	SS NMR [120]	305 ± 5	15.5	0.00
	DFT	348	15.1	0.00
K_2LaCl_5	SS NMR (This Work)	703 ± 20	30.1 ± 2.4	0.54 ± 0.1
	DFT	622	29.3	0.72
Cs_3LaCl_6	SS NMR (This Work, Static spectra only)	La_1: 878 ± 3 La_2: 924 ± 3	La_1: 17.7 ± 0.3 La_2: 14.6 ± 0.4	La_1: 0.10 La_2: 0.78 ± 0.03
	DFT (without geometric relaxation [122])	La_1: 833 La_2: 844	La_1: 44.7 La_2: 79.0	La_1: 0.08 La_2: 0.51
	DFT (with geometric relaxation)	La_1: 773 La_2: 833	La_1: 20.2 La_2: 15.2	La_1: 0.81 La_2: 0.77

For $LaCl_3$ and K_2LaCl_5, the fitted parameters generally agree well with the DFT-predicted values: C_Q is accurately reproduced, whereas a modest discrepancy between fitted and calculated δ_{iso} can be attributed to the relatively large uncertainty in the ^{139}La calibration curve (as shown in **Figure II-11d**). While η also shows reasonable agreement, it is

not emphasised here due to its sensitivity to small deviations in the principal EFG components. Despite the good agreement, the fitted spectra do not fully capture all peaks observed in the measured spectra, a discrepancy particularly evident in the MAS spectra of K_2LaCl_5. These unaccounted peaks are attributed to the difference in orientation between the principal axis systems of the chemical shift tensor and quadrupolar moment (i.e., Euler angles). While fitting Euler angles is challenging, they do not significantly affect the main parameters discussed and are omitted from consideration herein.

In contrast, the NMR parameters calculated for Cs_3LaCl_6 show significant discrepancies with experiment. These differences arise from two main factors: (1) structural inaccuracies in the reported crystal model and (2) dynamic effects not captured in static DFT calculations.

First, the initial Cs_3LaCl_6 crystallographic structure [122] used as input appears to deviate from the minimum-energy structure at the DFT level. Geometry optimisation using VASP reduces the La–Cl coordination number from six to five for half of the La sites (**Figure III-8**). This structural modification substantially improves agreement between calculated and experimental quadrupolar coupling constants (C_Q) and the relative chemical shift differences between the two La sites. However, the absolute chemical shifts remain significantly offset, which is attributed to the large uncertainty in the ^{139}La chemical shift calibration curve. In contrast, similar geometric relaxation for $LaCl_3$ and K_2LaCl_5 produces negligible changes in predicted NMR parameters, indicating that the issue is specific to Cs_3LaCl_6.

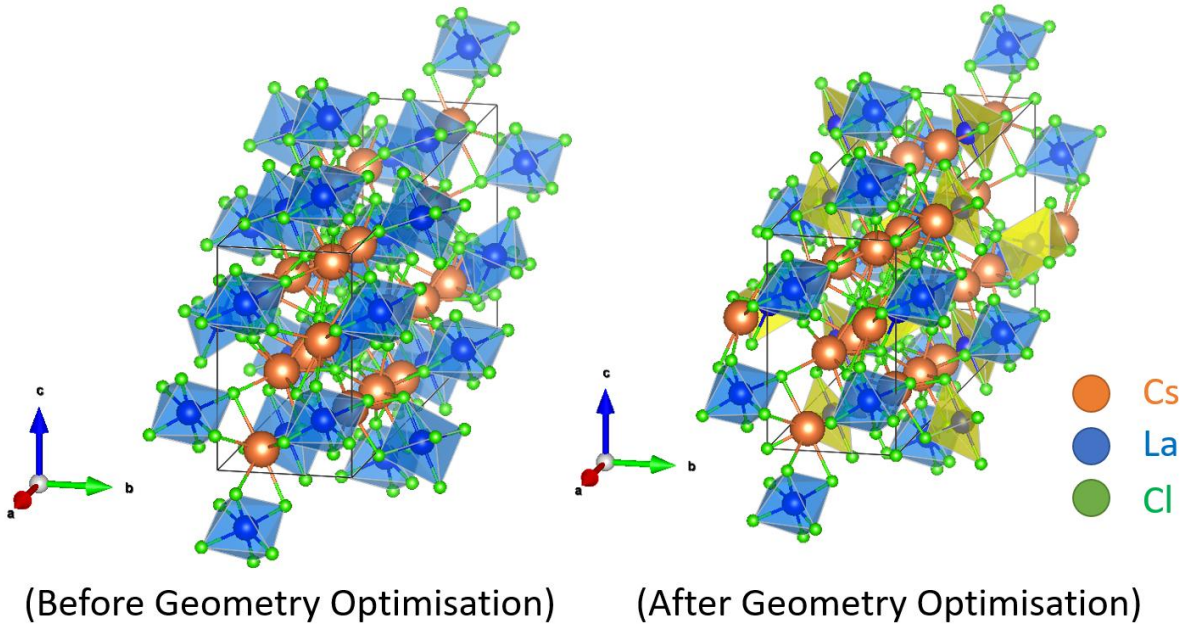

Figure III-8. Crystallographic structure of Cs_3LaCl_6 before and after geometry optimisation operations using VASP. Only ion positions were optimised, while cell dimensions were kept fixed (ISIF=2). Cs^+, La^{3+}, and Cl^- ions are represented by orange, blue, and green spheres, respectively. La–Cl coordination polyhedra are illustrated to highlight the changes in the La–Cl coordination environment after geometry optimisation: 6-fold coordination polyhedra are coloured in blue, whereas 5-fold coordination polyhedra are coloured in yellow.

Second, a marked discrepancy exists between the static and MAS ^{139}La NMR spectra of Cs_3LaCl_6, which cannot be explained by structural considerations alone. This behaviour is instead attributed to dynamic processes originating from the elpasolite-derived structure [131] of Cs_3LaCl_6. Recent studies on related compounds, such as K_3AlF_6, Rb_3AlF_6 [132], and Rb_3ScF_6 [133], revealed that $[AlF_6]^{3-}$ or $[ScF_6]^{3-}$ octahedra may undergo dynamic rotations in certain phases. By analogy, the $[LaCl_6]^{3-}$ octahedra in Cs_3LaCl_6 are likely to undergo rotational motion in the room-temperature phase. Such motion modulates the local electric field gradient at the La nucleus. In static experiments, this leads to partial averaging of the quadrupolar interaction and a reduction in linewidth. However, because chloride ligands are heavier relative to fluorides, the rotational dynamics are slower and likely occur on a timescale comparable to the NMR interaction, resulting in incomplete averaging and a non-zero observed C_Q. Under MAS conditions, sample spinning partially averages quadrupolar interactions, narrowing the linewidth. At the same time, the internal rotational motion of the $[LaCl_6]^{3-}$ octahedra further reduces the residual anisotropy responsible for spinning sidebands. The combined effects of MAS and internal dynamics produce spectra that differ substantially from both the static experimental spectra and the static DFT predictions. Finally, the presence of two crystallographically distinct La sites leads to broad, overlapping resonances, further complicating spectral deconvolution under both static and MAS conditions.

Overall, accurate modelling of Cs_3LaCl_6 requires not only an improved structural description but also explicit treatment of dynamic effects, which are not captured in standard static DFT calculations. Further work is therefore needed to resolve the room-temperature structure and its associated dynamics.

The SS NMR spectra of ^{35}Cl are particularly challenging to resolve. This is mainly due to the strong overlap of several ^{35}Cl NMR signals from chlorine atoms in nonequivalent crystallographic positions, each exhibiting large quadrupolar broadening. **Figure III-9** shows the static ^{35}Cl NMR spectra of the three solid compounds. While the ^{35}Cl NMR spectra of $LaCl_3$ can be easily extracted, those of K_2LaCl_5 and Cs_3LaCl_6 show superpositions of multiple lines from different Cl sites with broad quadrupolar coupling, making it prohibitively difficult to resolve them individually.

To address this limitation, the δ_{iso} values of the distinct Cl sites in these two compounds were obtained from DFT calculations (**Table III-5**). The results indicate that bridging Cl^- ions generally exhibit larger chemical shifts than non-bridging Cl^- ions. For example, in K_2LaCl_5, the chemical shift at the bridging Cl_4 site is calculated to be 266 ppm, while those of the non-bridging Cl sites range from 197 to 228 ppm. Similarly, all Cl sites in the geometrically optimised Cs_3LaCl_6 crystal structure are non-bridging and exhibit chemical shifts smaller (218–250 ppm) than those of bridging Cl sites in other structures. These results support the earlier interpretation that chloride bridging contributes to a positive deviation from linear behaviour in the ^{35}Cl NMR curve. Moreover, a higher degree of chloride bridging is generally associated with higher chemical shifts. For instance, the triple-bridging Cl^- in $LaCl_3$ is predicted to have a chemical shift of 289 ppm, which is greater than the double-bridging Cl^- in K_2LaCl_5 at 266 ppm. Nevertheless, caution should be exercised when directly comparing ^{35}Cl chemical shifts across different compounds, as the chemical identity of neighbouring cations can significantly influence the local electronic environment of Cl^-.

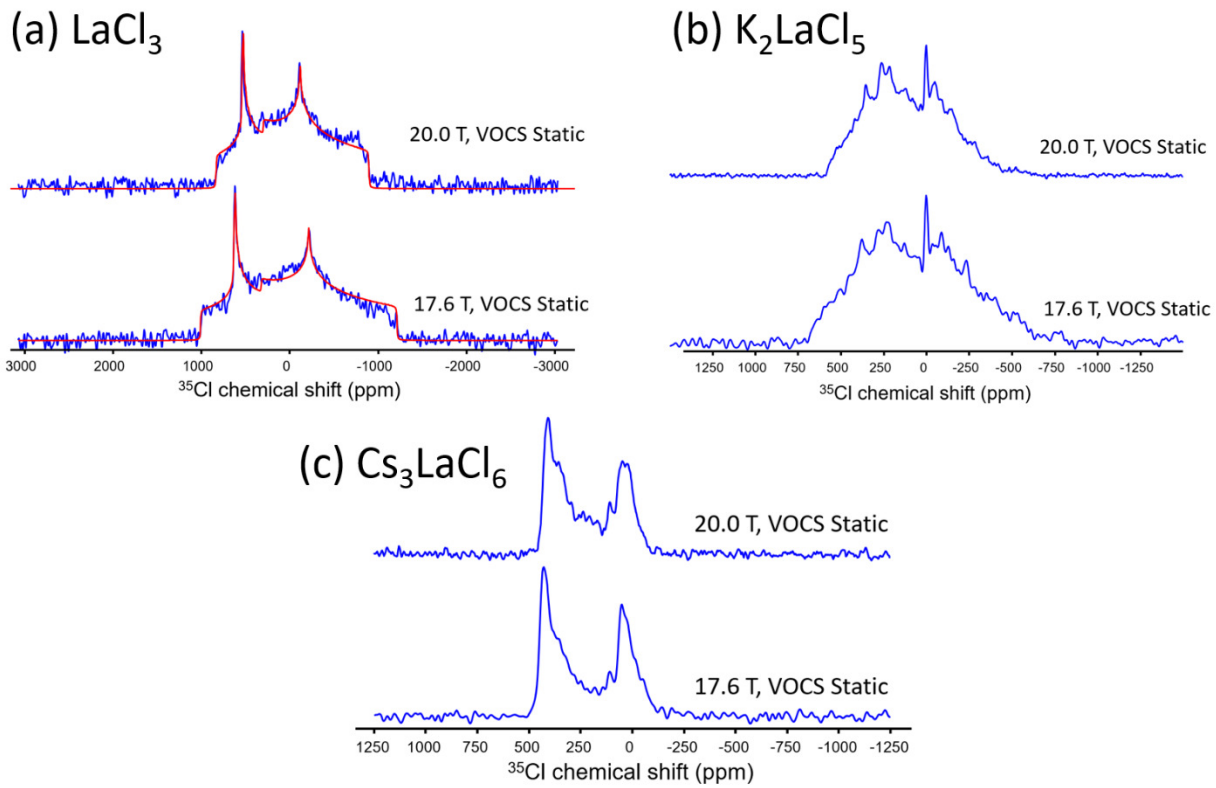

Figure III-9. ^{35}Cl SS-NMR spectra of (a) $LaCl_3$, (b) K_2LaCl_5, and (c) Cs_3LaCl_6. Measured spectra are given in blue and fitted spectra are given in red.

Table III-5. ^{35}Cl SS NMR Parameters Obtained from Line Fitting and DFT Calculations

Compound	Method	Site	δ_{iso} (ppm)	C_Q (MHz)	η
$LaCl_3$	SS NMR	Cl_1	258 ± 2	7.945 ± 0.01	0.51± 0.02
	DFT	Cl_1	289	8.584	0.55
K_2LaCl_5	DFT	Cl_1	228	5.991	0.22
		Cl_2	202	5.921	0.92
		Cl_3	197	4.367	0.23
		Cl_4 [§]	266	6.025	0.86
Cs_3LaCl_6	DFT	Cl_1	236	2.657	0.38
(with Geometry		Cl_2	237	4.167	0.70
Optimisation)		Cl_3	218	1.818	0.45
		Cl_4	219	2.015	0.83
		Cl_5	250	3.498	0.87
		Cl_6	232	5.627	0.62

[§]Only this site is bridging. All other sites in K_2LaCl_5 are non-bridging.

III-3. Molecular Dynamics

Classical MD simulations using the PIM were employed as a complementary technique to quantitatively analyse the local structure of molten salt systems. In this context, MD simulations generated ion trajectories, from which the RDFs, CNs, and La–Cl–La network connectivity were derived. These analyses were performed for the NaCl–$LaCl_3$ and $MgCl_2$–$LaCl_3$ binary systems, as well as for ternary compositions along the lines of 80 $(NaCl)_{1-x}(MgCl_2)_x$ –20 $LaCl_3$ and (100-x) $(NaCl)_{0.80}(MgCl_2)_{0.20}$ –x $LaCl_3$.

III-3.1. Binary Systems

Figure III-10 shows the calculated RDF and the running CNs of La^{3+}–Cl^-, Cl^-–La^{3+}, La^{3+}–La^{3+} and Cl^-–Cl^- pairs in NaCl–$LaCl_3$ and $MgCl_2$–$LaCl_3$ binary systems at 850 °C. These ion pairs were chosen because they most clearly highlight the structural differences between the two binary systems. The isotherm of 850 °C was selected because it ensures that all mixtures exist in the molten state while still within the temperature range of the HT NMR measurements.

For the La^{3+}–Cl^- ion pair, CN_{La-Cl} increases with $LaCl_3$ content in NaCl–$LaCl_3$, but remains roughly constant in the case of $MgCl_2$–$LaCl_3$. This observation signifies that CN_{La-Cl} in NaCl–$LaCl_3$ is more sensitive to $LaCl_3$ content than CN_{La-Cl} in $MgCl_2$–$LaCl_3$. This finding also complements the results of HT NMR measurements, whereby the range of ^{139}La chemical shift evolution for NaCl–$LaCl_3$ is noticeably larger than for $MgCl_2$–$LaCl_3$ (**Figure III-4**). Moreover, for the Cl^-–La^{3+} ion pair, CN_{Cl-La} in their respective first solvation shells were calculated to be 0.96 for 80 NaCl–20 $LaCl_3$ and 0.65 for 80 $MgCl_2$–20 $LaCl_3$, supporting the claim that chloride ions exhibit a higher degree of bridging in NaCl–$LaCl_3$.

The RDF of La^{3+}–La^{3+} ion pairs shows that the primary-to-secondary peak ratio diminishes with decreasing $LaCl_3$ content in NaCl–$LaCl_3$, while this ratio remains constant for $MgCl_2$–$LaCl_3$, regardless of $LaCl_3$ content. Considering that Coulomb ordering induces an alternation of anionic and cationic shells around a given ion, this observation suggests that in the presence of Na^+ ions, La^{3+} ions are more likely to appear in the fourth coordination sphere than in the second coordination sphere of other La^{3+} ions. A plausible explanation may be that $[La_xCl_y]^{3x-y}$ complexes in NaCl–$LaCl_3$ are generally spaced by Na^+, creating local La^{3+}-depleted regions that align with the "spacer salt" concept proposed by Emerson *et al.* [128]. $MgCl_2$ does not exhibit this spacer salt property and the mixing behaviour with $LaCl_3$ is more homogeneous [99]. From a thermodynamic perspective, the homogeneous mixing explanation complements the observation that NaCl–MCl_3 (where M is a trivalent lanthanide or actinide cation) mixtures often exhibit enthalpy of mixing (ΔH_{mix}) values nearly an order of magnitude higher than $MgCl_2$–MCl_3 [39,40,134,135], indicating more ideal mixing behaviour in the latter.

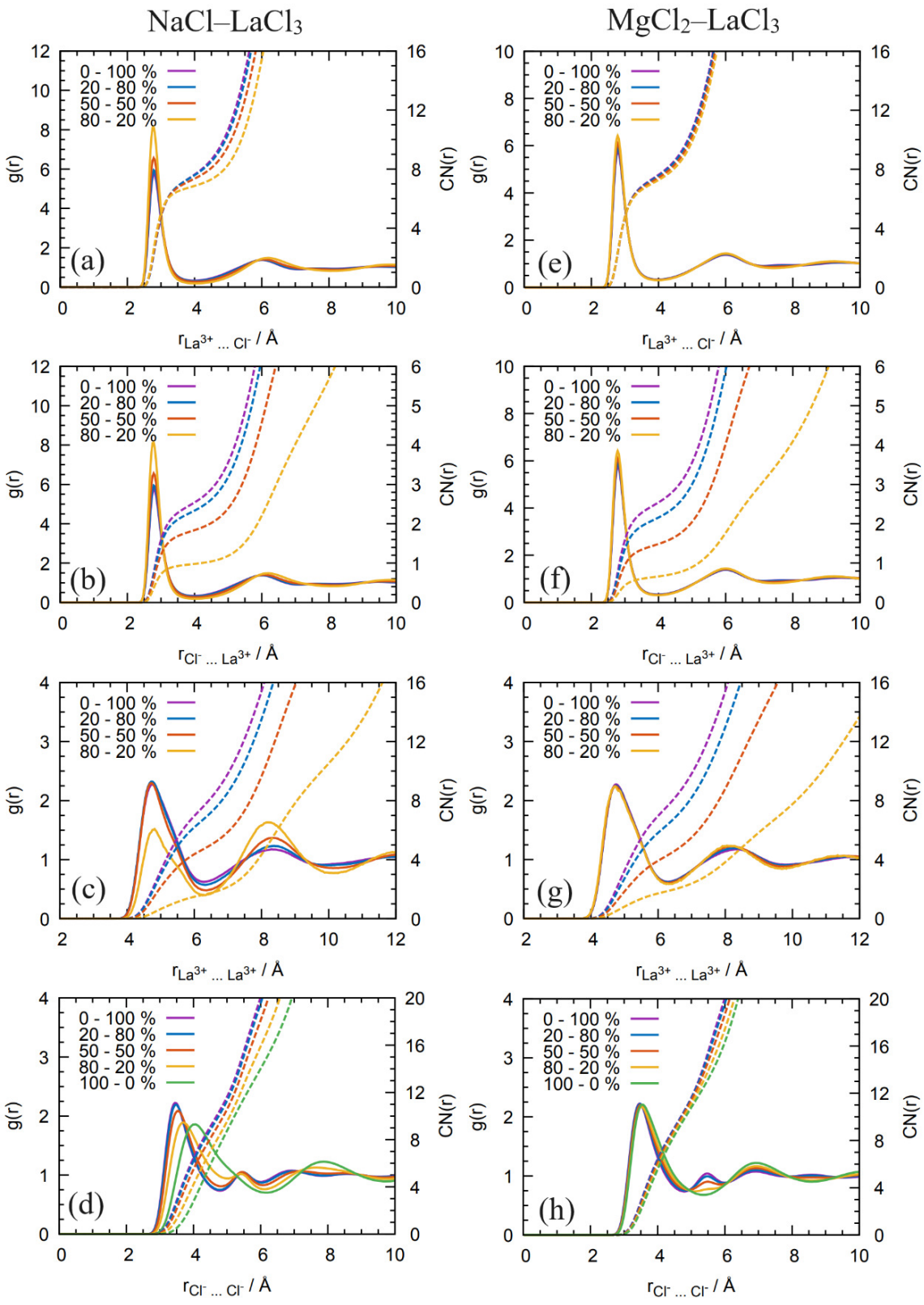

Figure III-10. Comparison of radial distribution functions, g(r), in solid lines, and coordination numbers, CN(r), in dotted lines, for key ion pairs in (a–d) NaCl–$LaCl_3$ and (e–h) $MgCl_2$–$LaCl_3$ binary molten salt systems.

The RDF of the Cl^-–Cl^- ion pair further substantiates the idea of homogeneous mixing. The position of the first RDF peak shifts towards lower values with increasing $LaCl_3$ content for NaCl–$LaCl_3$, but remains almost unchanged for $MgCl_2$–$LaCl_3$. This result may appear counterintuitive as the mean La–Cl distance in molten $LaCl_3$ (2.82 Å) is closer to that of Na–Cl in molten NaCl (2.66 Å) than that of Mg–Cl in molten $MgCl_2$ (2.41 Å), giving the initial impression that NaCl would mix more uniformly with $LaCl_3$. A convenient method to address this discrepancy is to perform a simplified analysis based on the general coordination environment of the pure solid salts: $LaCl_3$ can be approximated as a network of isotropic 9-fold coordination polyhedra, while NaCl and $MgCl_2$ are treated as networks of isotropic 6-fold octahedra (**Figure III-11**). Despite different cation–anion bond lengths, the edge lengths (i.e., neighbouring Cl–Cl distances) of the $LaCl_3$ and $MgCl_2$ polyhedra are quite similar, around 3.4 to 3.6 Å [129,136]. This allows Mg^{2+} ions to be more seamlessly incorporated into the $LaCl_3$ network without significantly perturbing Cl^- ion positions, resulting in more ideal mixing. This explanation is further supported by the absence of peaks for the Cl^-–Cl^- RDF of pure $MgCl_2$ in the even-numbered peak positions of pure $LaCl_3$. These positions correspond to the Cl–Cl distances (e.g., 5.56 Å) that exist in $LaCl_3$ but do not exist in $MgCl_2$, indicating that similar anion spacings facilitate the ideal mixing of binary mixtures.

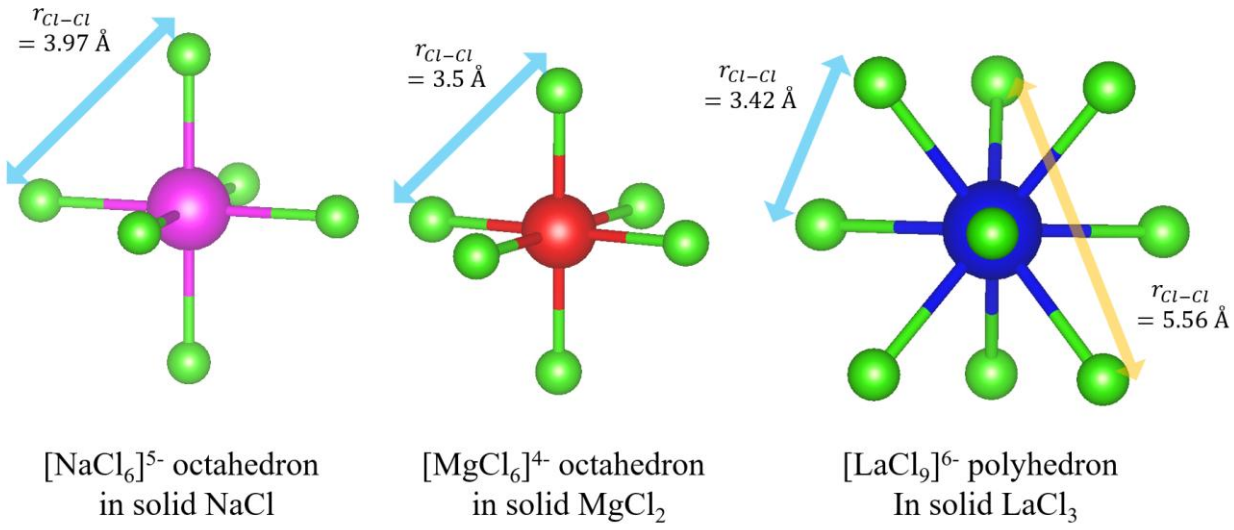

Figure III-11. Schematic illustration of isotropic coordination polyhedra in solid NaCl, $MgCl_2$, and $LaCl_3$. Blue arrows indicate the nearest-neighbour Cl–Cl distances in each polyhedron. The yellow arrow highlights the Cl–Cl spacing corresponding to the second Cl–Cl RDF peak in $LaCl_3$-containing molten salt systems—a distance that is noticeably absent in both solid $MgCl_2$ and the Cl–Cl RDF of $MgCl_2$.

To provide a more intuitive understanding of differences in the local structure of NaCl–$LaCl_3$ and $MgCl_2$–$LaCl_3$, **Figure III-12** presents single-frame snapshots of the 80 NaCl–20 $LaCl_3$ and 80 $MgCl_2$–20 $LaCl_3$ systems, obtained from "small" box simulations for better visualisation. Comprehensive analyses of the distribution of La–Cl and Cl–La coordination numbers in the binary systems are also provided in **Table III-6 and III-7** respectively. A combined inspection reveals that 6-fold and 7-fold La–Cl coordinations are preferred in NaCl–$LaCl_3$, while 7-fold and 8-fold

La–Cl coordinations are favoured in $MgCl_2$–$LaCl_3$. Additionally, chloride bridging is more prevalent in NaCl–$LaCl_3$ than in $MgCl_2$–$LaCl_3$, evidenced by the prevalence of edge- and corner-sharing interactions in the former. Furthermore, **Figure III-12** also exemplifies the tendency of Na^+ ions to form spacer layers between $[La_xCl_y]^{3x-y}$ complexes in NaCl–$LaCl_3$, a structural property not observed with Mg^{2+} ions in $MgCl_2$–$LaCl_3$. Instead, Mg^{2+} ions can even appear to act as an intermediary between two distinct, isolated $[LaCl_n]^{3-n}$ complexes. These observations align with the mixing homogeneity explanation discussed in the RDF analysis above.

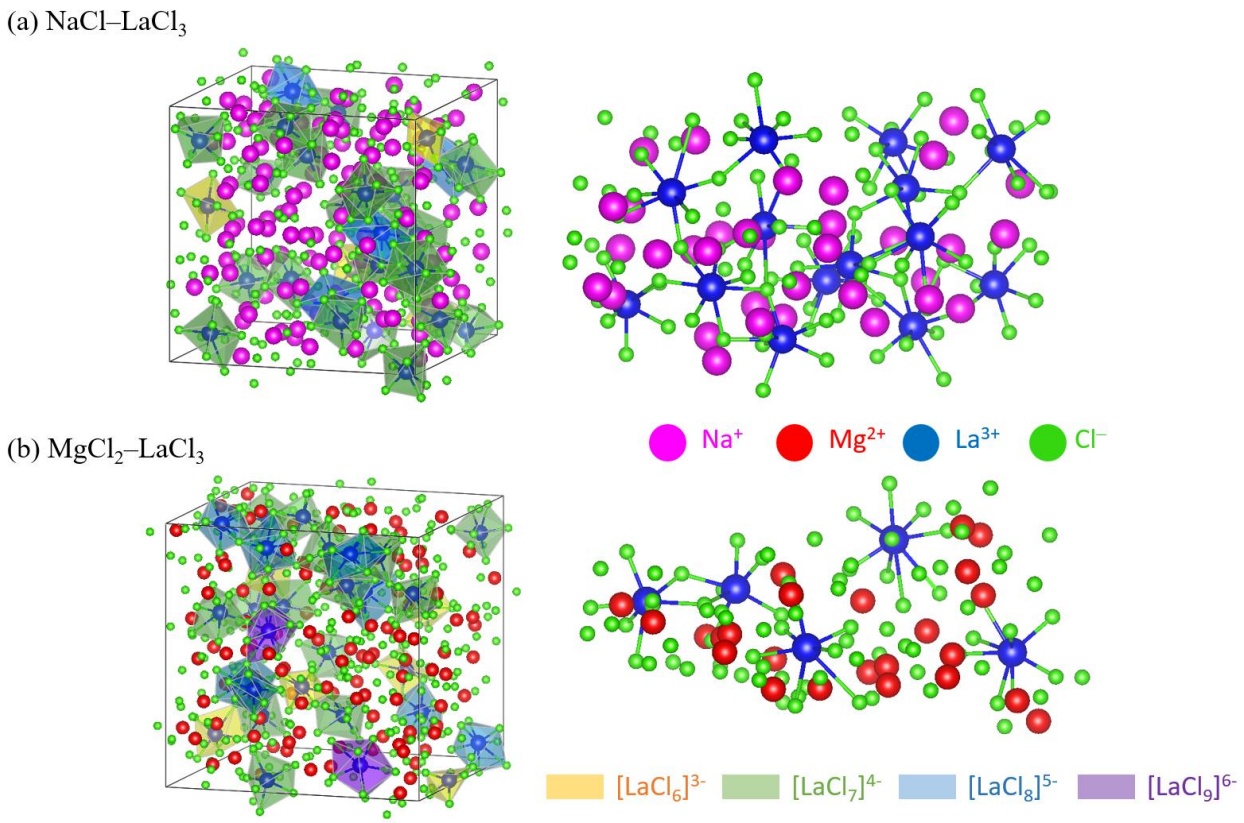

Figure III-12. Snapshots of (a) 80 mol% NaCl–20 mol% $LaCl_3$ and (b) 80 mol% $MgCl_2$–20 mol% $LaCl_3$ at 850 °C. Ions are represented based on colour: Na^+(violet), Mg^{2+}(red), La^{3+} (dark blue) and Cl^- (green). The La–Cl bond length cutoff is set at 4.00 Å, based on the first minimum observed in the RDFs. La–Cl coordination polyhedra are drawn around La^{3+} ions in the "full" screenshot to highlight the difference in coordination environments: 6-fold coordination is represented in yellow, 7-fold coordination is represented in green, 8-fold coordination is represented in blue, and 9-fold coordination is represented in violet.

Table III-6. Distribution of La–Cl coordination numbers across select binary molten salt compositions, as derived from the analysis of the "large" simulation box. The La–Cl bond length is set at 4.00 Å to reflect the radius of the first coordination sphere. All values are presented as percentages (%).

Composition (in mol%)	Percentage of La atoms with La–Cl Coordination Number ($CN_{La–Cl}$)					
	5	6	7	8	9	10
100 $LaCl_3$	0.26	8.55	36.54	41.30	12.43	0.90
20 NaCl – 80 $LaCl_3$	0.25	8.78	37.94	41.24	11.12	0.66
50 NaCl – 50 $LaCl_3$	0.33	13.59	44.87	35.00	6.01	0.19
80 NaCl – 20 $LaCl_3$	0.50	31.96	50.50	16.17	0.85	0.01
20 $MgCl_2$ – 80 $LaCl_3$	0.33	9.94	38.60	39.58	10.82	0.71
50 $MgCl_2$ – 50 $LaCl_3$	0.47	12.64	41.90	36.26	8.28	0.44
80 $MgCl_2$ – 20 $LaCl_3$	0.72	16.84	45.30	31.27	5.63	0.23

Table III-7. Distribution of Cl–La coordination numbers across select binary molten salt compositions, as derived from the analysis of the "large" simulation box. The Cl–La bond length cutoff is set at 4.00 Å to reflect the radius of the first coordination sphere. All values are presented as percentages (%).

Composition (in mol%)	Percentage of Cl atoms with Cl–La Coordination Number ($CN_{Cl–La}$)				
	0	1	2	3	4
100 $LaCl_3$	0.00	0.72	50.57	43.49	5.16
20 NaCl – 80 $LaCl_3$	0.01	6.73	57.22	32.69	3.31
50 NaCl – 50 $LaCl_3$	0.73	30.81	53.68	13.94	0.83
80 NaCl – 20 $LaCl_3$	19.96	63.05	16.20	0.79	0.01
20 $MgCl_2$ – 80 $LaCl_3$	1.21	15.60	52.71	27.90	2.56
50 $MgCl_2$ – 50 $LaCl_3$	11.85	39.13	38.62	9.84	0.55
80 $MgCl_2$ – 20 $LaCl_3$	47.15	40.80	11.07	0.96	0.02

III-3.2. Ternary Systems

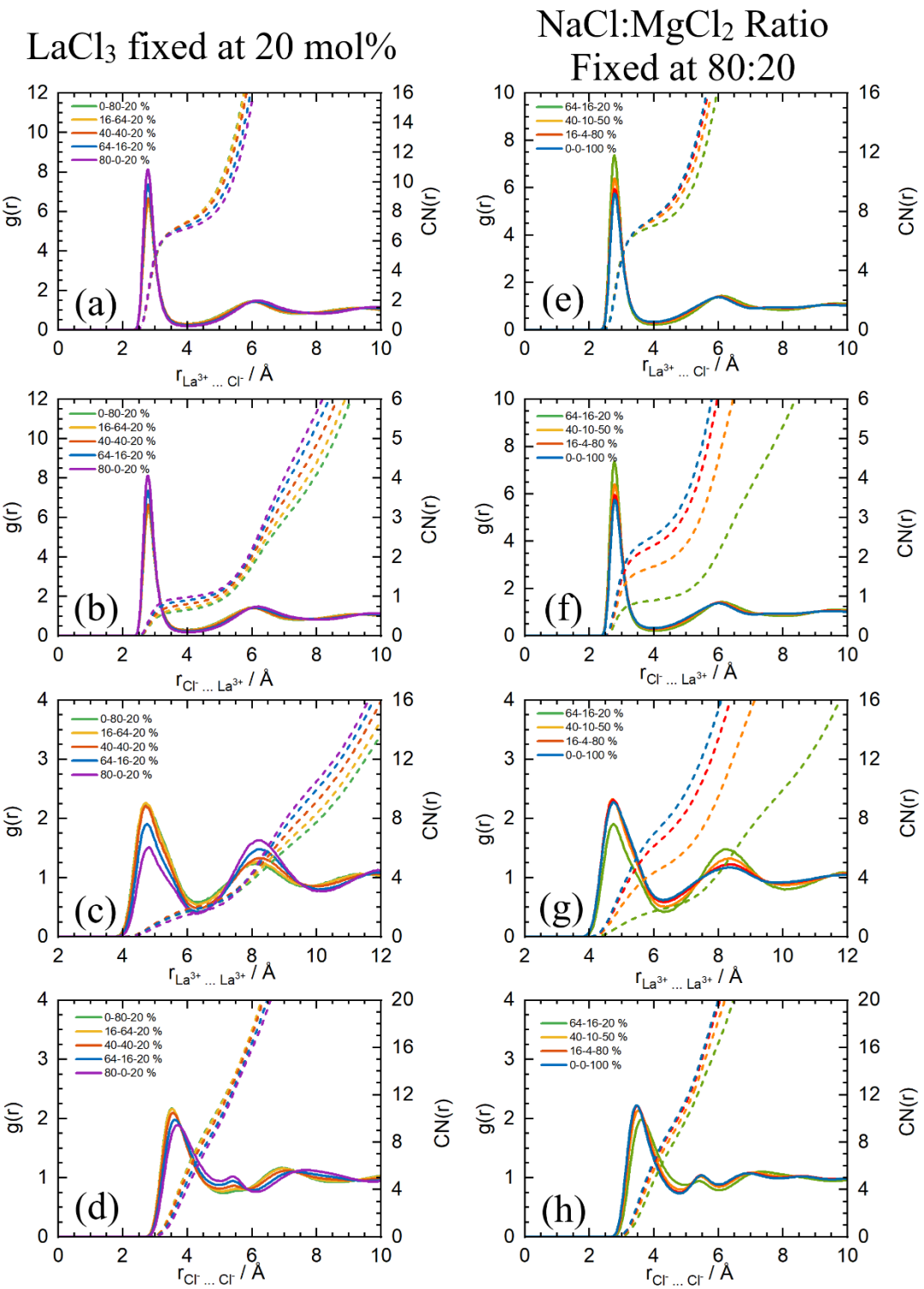

Figure III-13. Comparison of radial distribution functions, g(r), in solid lines, and coordination numbers, CN(r), in dotted lines, for key ion pairs in NaCl–$MgCl_2$–$LaCl_3$ along the compositional lines of (a–d) 80 $(NaCl)_{1-x}(MgCl_2)_x$ –20 $LaCl_3$ and (e–h) (100-x) $(NaCl)_{0.80}(MgCl_2)_{0.20}$ –x $LaCl_3$.

The same analytical protocol was applied to ternary systems to further examine the inferences from binary systems. **Figure III-13** compares the RDF and running CNs of key ion pairs between different salt compositions in the NaCl–$MgCl_2$–$LaCl_3$ ternary system. With $LaCl_3$ fixed at 20 mol%, the La^{3+}–Cl^- RDF shows a marked increase in $CN_{La–Cl}$ from 6.94 to 7.25 (**Figure III-13a**), while the Cl^-–La^{3+} RDF reveals a decrease in $CN_{Cl–La}$ from 0.99 to 0.66 as the $MgCl_2$ content rises (**Figure III-13b**). These results are consistent with HT NMR measurements of ternary systems (**Figure III-5**), upholding the role of $MgCl_2$ in enhancing La–Cl coordination and reducing chloride bridging. Furthermore, the shifting primary-to-secondary peak ratio in the La^{3+}–La^{3+} RDF reinforces the spacer salt effect present in NaCl but absent in $MgCl_2$ (**Figure III-13c**). Additionally, the Cl^-–Cl^- ion pair RDF contrasts the mixing homogeneity induced by NaCl and $MgCl_2$; the secondary peak, indicative of the unique Cl–Cl distances in $LaCl_3$, diminishes with increasing $MgCl_2$ content, suggesting that Mg^{2+} ions can be more seamlessly incorporated into the La–Cl network than Na^+ ions. (**Figure III-13d**) Meanwhile, when the NaCl/$MgCl_2$ ratio is fixed at 80:20, the RDFs exhibit similar behaviour as those in **Figure III-10**, albeit with characteristics reflecting both NaCl and $MgCl_2$. These results suggest that the structural behaviour in the NaCl–$MgCl_2$–$LaCl_3$ ternary system is essentially a superposition of the individual binary subsystems.

To further illustrate this point, **Figure III-14** presents single-frame snapshots of the ternary mixtures: (a) 64 NaCl–16 $MgCl_2$–20 $LaCl_3$, (b) 40 NaCl–40 $MgCl_2$–20 $LaCl_3$, and (c) 16 NaCl–64 $MgCl_2$–20 $LaCl_3$ at 850 °C. The corresponding $CN_{La–Cl}$ and $CN_{Cl–La}$ distributions are also provided in **Table III-8 and III-9**. As the NaCl/$MgCl_2$ ratio decreases, La^{3+} ions appear more evenly dispersed, and higher-fold coordination environments become more prevalent.

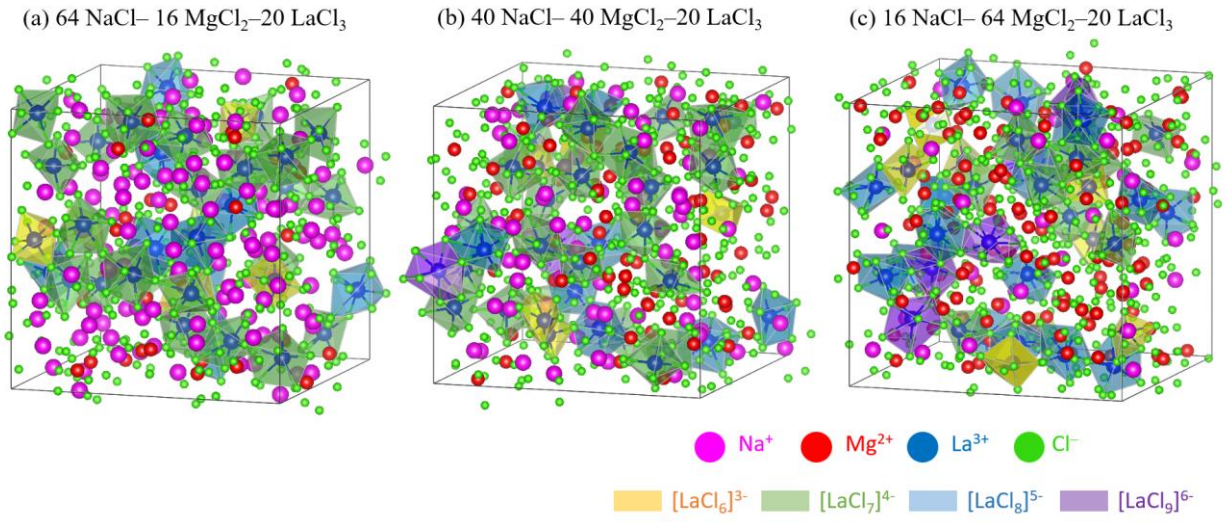

Figure III-14. MD Snapshots of (a) 64 NaCl–16 $MgCl_2$–20 $LaCl_3$, (b) 40 NaCl–40 $MgCl_2$–20 $LaCl_3$, and (c) 16 NaCl–64 $MgCl_2$–20 $LaCl_3$ at 850 °C. Ions are represented based on colour: Na^+(violet), Mg^{2+}(red), La^{3+} (dark blue) and Cl^- (green). La–Cl coordination polyhedra are drawn around La^{3+} ions to highlight the difference in network formation behaviour. The La–Cl bond length cutoff is set at 4.00 Å, based on the first minimum observed in the RDFs.

Table III-8. Distribution of La–Cl coordination numbers across select ternary molten salt compositions, as derived from the analysis of the "large" simulation box. The La–Cl bond length is set at 4.00 Å to reflect the radius of the first coordination sphere. All values are presented as percentages (%).

Composition (in mol%)	Percentage of La atoms with La–Cl Coordination Number ($CN_{La–Cl}$)					
	5	6	7	8	9	10
64 NaCl–16 $MgCl_2$–20 $LaCl_3$	0.56	23.90	50.06	23.34	2.12	0.03
40 NaCl–40 $MgCl_2$–20 $LaCl_3$	0.50	16.40	46.93	31.41	4.63	0.12
16 NaCl–64 $MgCl_2$–20 $LaCl_3$	0.56	15.22	45.22	32.95	5.84	0.22
40 NaCl–10 $MgCl_2$– 50 $LaCl_3$	0.32	12.08	43.20	36.90	7.22	0.27
16 NaCl–4 $MgCl_2$–80 $LaCl_3$	0.26	8.90	37.97	40.99	11.19	0.69

Table III-9. Distribution of Cl–La coordination numbers across select ternary molten salt compositions, as derived from the analysis of the "large" simulation box. The Cl–La bond length cutoff is set at 4.00 Å to reflect the radius of the first coordination sphere. All values are presented as percentages (%).

Composition (in mol%)	Percentage of Cl atom with Cl–La Coordination Number ($CN_{Cl–La}$)				
	0	1	2	3	4
64 NaCl–16 $MgCl_2$–20 $LaCl_3$	28.78	53.52	16.56	1.12	0.02
40 NaCl–40 $MgCl_2$–20 $LaCl_3$	37.19	46.55	14.96	1.27	0.03
16 NaCl–64 $MgCl_2$–20 $LaCl_3$	43.48	42.75	12.63	1.12	0.03
40 NaCl–10 $MgCl_2$– 50 $LaCl_3$	3.36	32.31	50.09	13.42	0.82
16 NaCl–4 $MgCl_2$–80 $LaCl_3$	0.17	8.70	56.21	31.71	3.17

On this basis, a reduction in the average length of $[La_xCl_y]^{3x-y}$ chains may be expected as the $MgCl_2$ content increases. To test this hypothesis, polyhedral connectivity and polymer chain analyses were performed on the (80-*x*) NaCl–*x* $MgCl_2$–20 $LaCl_3$ systems (*x*=0, 16, 40, 64, 80) using the Fortran code previously applied to the molten salt systems in [107] and [108]. The average degree of polymerisation (D.P.) was calculated as:

$$D.P. = \frac{\sum_{x=1}^{\infty} x \cdot N_x}{\sum_{x=1}^{\infty} N_x},$$

(Eq. III- 1)

where *x* is the number of La atoms in a $[La_xCl_y]^{3x-y}$ chain, and N_x is the number of polymer chains containing *x* La atoms.

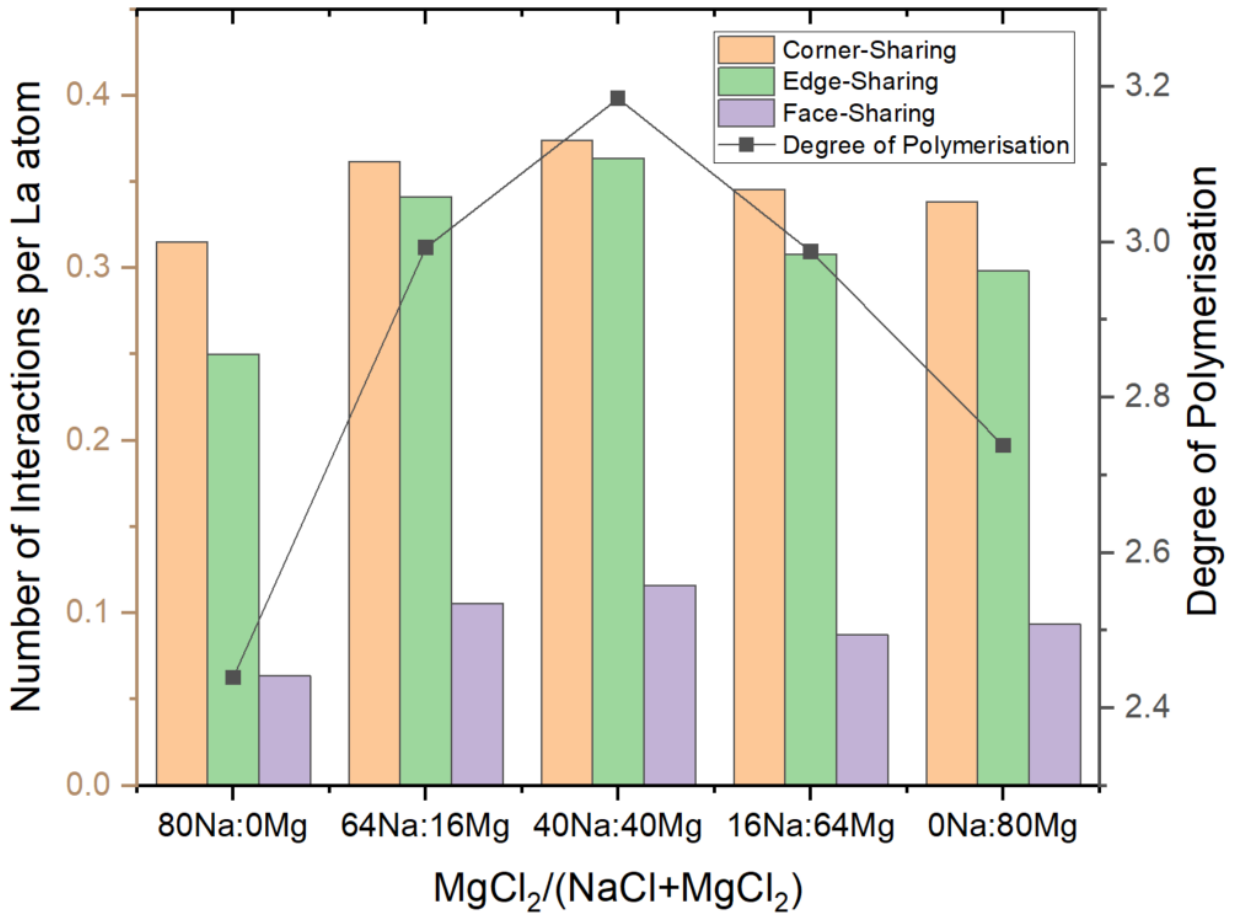

Figure III-15. Number of polyhedral sharing interactions per La atom (left axis) and average degree of polymerisation (right axis) for NaCl–$MgCl_2$–$LaCl_3$ with $LaCl_3$ content fixed at 20 mol%. All calculations are derived from the "large" simulation box.

The analysis, shown in **Figure III-15**, reveals a more complex behaviour: the number of shared polyhedral interactions initially increases with $MgCl_2$ content, reaching a maximum at an approximately 1:1 NaCl/$MgCl_2$ ratio, before decreasing at higher $MgCl_2$ fractions. The D.P. follows the same non-monotonic behaviour. A closer examination of the polymer chain length distributions (**Figure III-16**) shows that binary systems contain a higher proportion of smaller polymer chains ($x < 8$), whereas ternary systems exhibit an increased probability of longer chains ($x \geq 8$).

This behaviour likely reflects the competing roles of NaCl and $MgCl_2$ in the melt: Na^+ ions act as a heterogeneous spacer layer, promoting the formation of extended $[La_xCl_y]^{3x-y}$ units; whereas, Mg^{2+} ions mix more homogeneously with $LaCl_3$, disrupting the continuity of La–Cl polymer networks. At the same time, $MgCl_2$ contributes additional Cl^-

ions, creating more avenues for chloride bridging and polyhedral sharing. The balance between these opposing effects likely gives rise to the observed non-monotonic trends.

While the detailed polymer analysis provides insight into the atomic-scale connectivity of the melt, these polymers are inherently transient—with lifetimes on the order of picoseconds, far shorter than the effective timescales of NMR measurements—rendering such connectivity undetectable in practice.

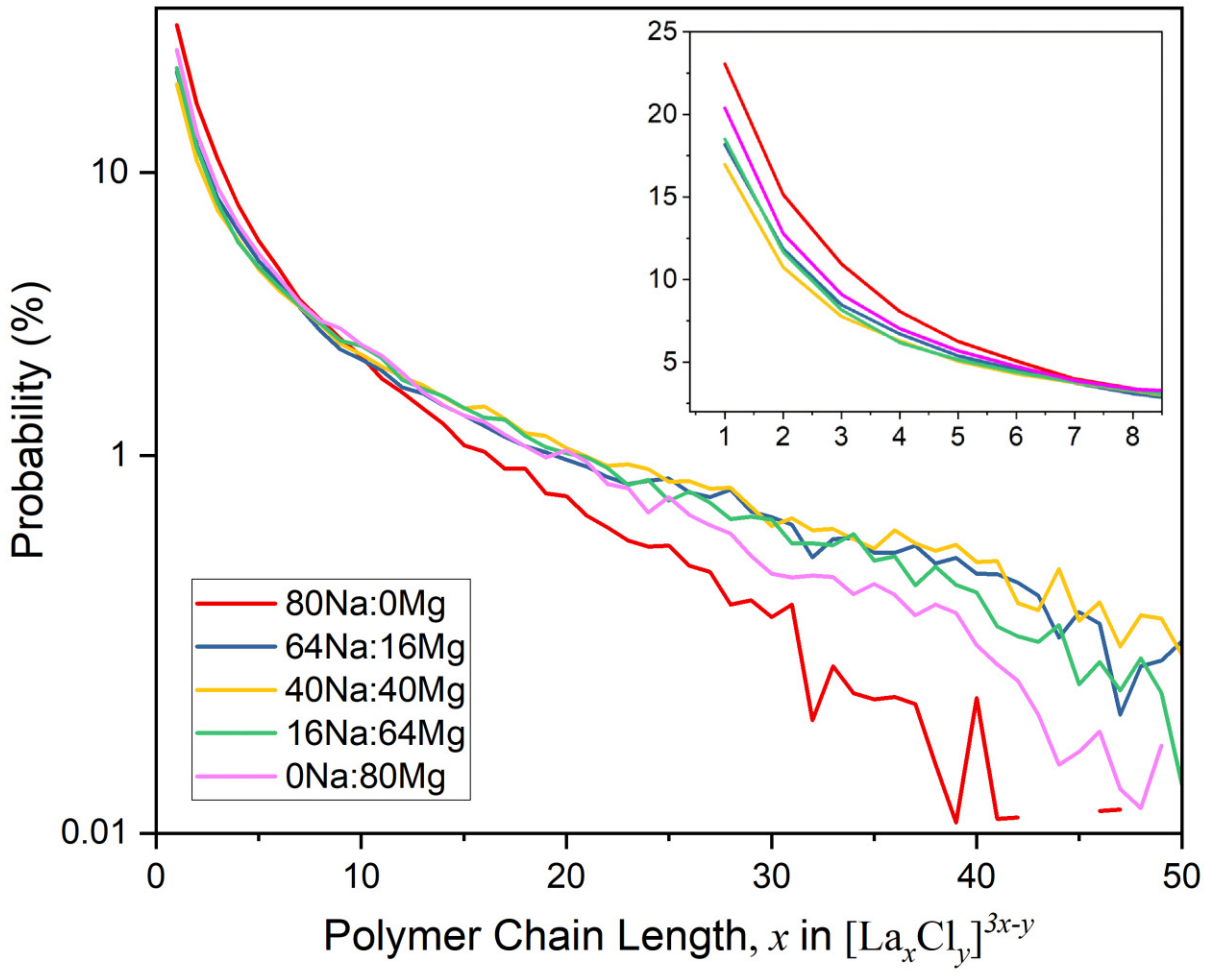

Figure III-16. Polymer chain length distribution in NaCl–$MgCl_2$–$LaCl_3$. All calculations are derived from the "large" simulation box.

III-4. DFT Calculations of NMR Parameters

From the preceding sections, the local structure of NaCl–$MgCl_2$–$LaCl_3$ was characterised by independent HT NMR and MD investigations. To assess the consistency between the two approaches, DFT calculations (using the VASP code) were performed on selected MD snapshots to compute the corresponding NMR parameters. Specifically, the

δ_{iso} values of all ^{139}La and ^{35}Cl nuclei were calculated for ten regularly spaced MD configurations, and the ensemble average was taken as the predicted chemical shift for each molten salt composition.

Figure III-17 compares the predicted and experimental ^{35}Cl and ^{139}La chemical shifts across different compositions. The DFT-predicted values consistently reproduce the experimental trends, with deviations below 30 ppm for ^{139}La shifts and below 35 ppm for ^{35}Cl shifts. These discrepancies likely arise from uncertainties in the chemical shielding–shift calibration (**Figure II-11**), finite-temperature effects that are not fully captured by the MD interatomic potential (discussed further in Chapter V-3.2), and the limited size of the simulation cell (**Table II-5**). Despite this modest systematic deviation, the close correspondence between measured and calculated trends indicates strong agreement between the local structures inferred from HT NMR and those obtained from MD simulations.

To elucidate the role of coordination environments on chemical shifts, nuclei were grouped based on their CN, as shown in **Figure III-18 to III-21**. The diagram reveals that for a given CN, chemical shifts in molten salts are not single-valued, but are normally distributed, reflecting variations in interatomic distances and spatial configurations. Moreover, the CN–chemical shift relationship differs for ^{139}La and ^{35}Cl. For ^{139}La, chemical shifts decrease monotonically with CN for all compositions, consistent with SS NMR results. In contrast, ^{35}Cl chemical shifts show composition-dependent behaviour: at low $LaCl_3$ concentrations, the chemical shift increases with CN, complying with SS NMR trends; yet, in $LaCl_3$-rich compositions, the trend is reversed.

This discrepancy can be rationalised by considering nearest-neighbour deshielding. For La^{3+}, which is always coordinated by Cl^-, an increase in the number of Cl^- neighbours enhances La-shielding, thereby lowering their chemical shift. However, for Cl^-, the identity of the neighbouring cations is critical. In general, La^{3+} ions exert a stronger deshielding effect than Na^+ or Mg^{2+}, hence Cl^- ions involved in La–Cl–La interactions (i.e., bridging Cl^-) tend to exhibit larger chemical shifts than their non-bridging counterparts.

Vacancies further influence the ^{35}Cl chemical shifts. Unlike in crystalline solids, where Cl^- ions are saturated with cation neighbours, Cl^- ions in molten salts may instead be adjacent to vacancy-like sites. These sites induce an even greater deshielding effect than La^{3+} ions. In $LaCl_3$-rich compositions, Cl^- ions with lower $CN_{Cl–La}$ are more likely to be adjacent to vacancies than to Na^+ or Mg^{2+}, resulting in larger chemical shifts. This accounts for the counterintuitive trend observed in $LaCl_3$-rich compositions.

Overall, the DFT-derived NMR parameters provide multimodal verification of the structural models derived from HT NMR and MD. The excellent correspondence between the predicted and measured chemical shifts supports the consistency of the two independent approaches.

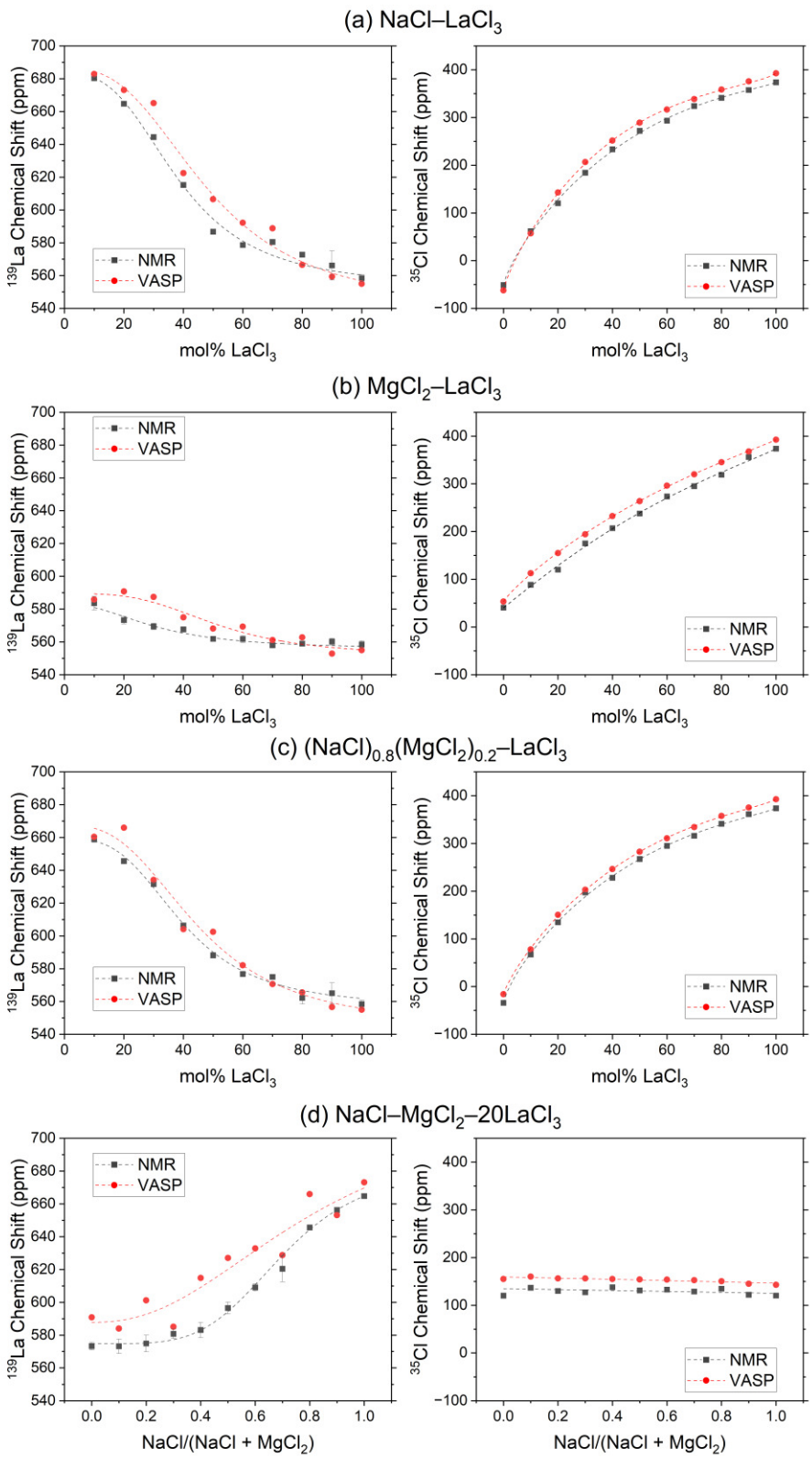

Figure III-17. Comparison of DFT-predicted (red circles) and HT-NMR-measured (black squares) chemical shifts for ^{139}La (left panel) and ^{35}Cl (right panel) nuclei across various molten salt compositions at 850 °C. Error bars for HT NMR data represent the numerical fitting uncertainty; they are visible for ^{139}La but smaller than the marker size for ^{35}Cl.

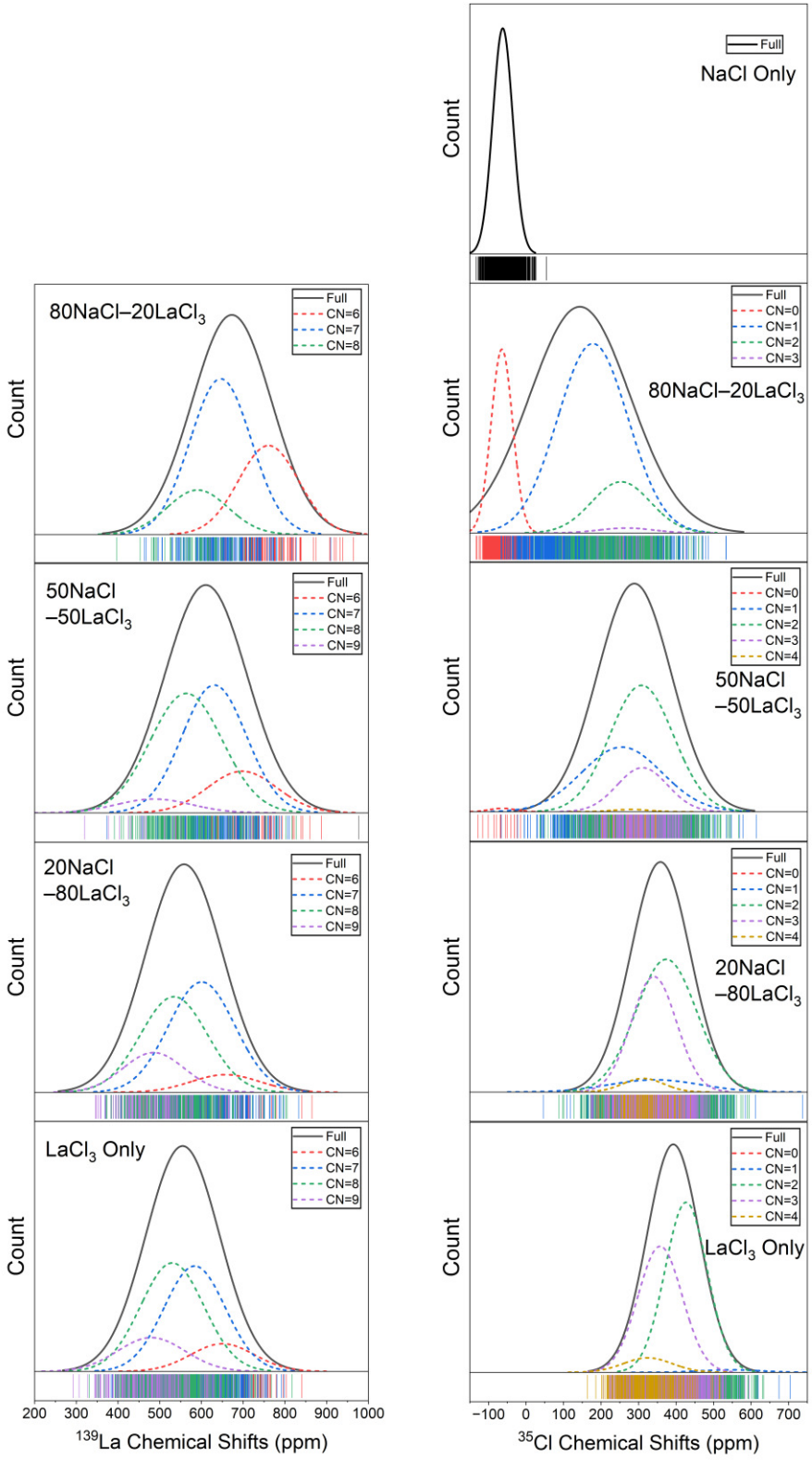

Figure III-18. Normalised distributions of calculated δ_{iso} values for ^{139}La (left panel) and ^{35}Cl (right panel) in NaCl–$LaCl_3$. Solid lines depict the distribution for all species, while dashed lines illustrate the distribution of species categorised by CN. CN categories representing less than 1% of the total species population have been omitted for clarity.

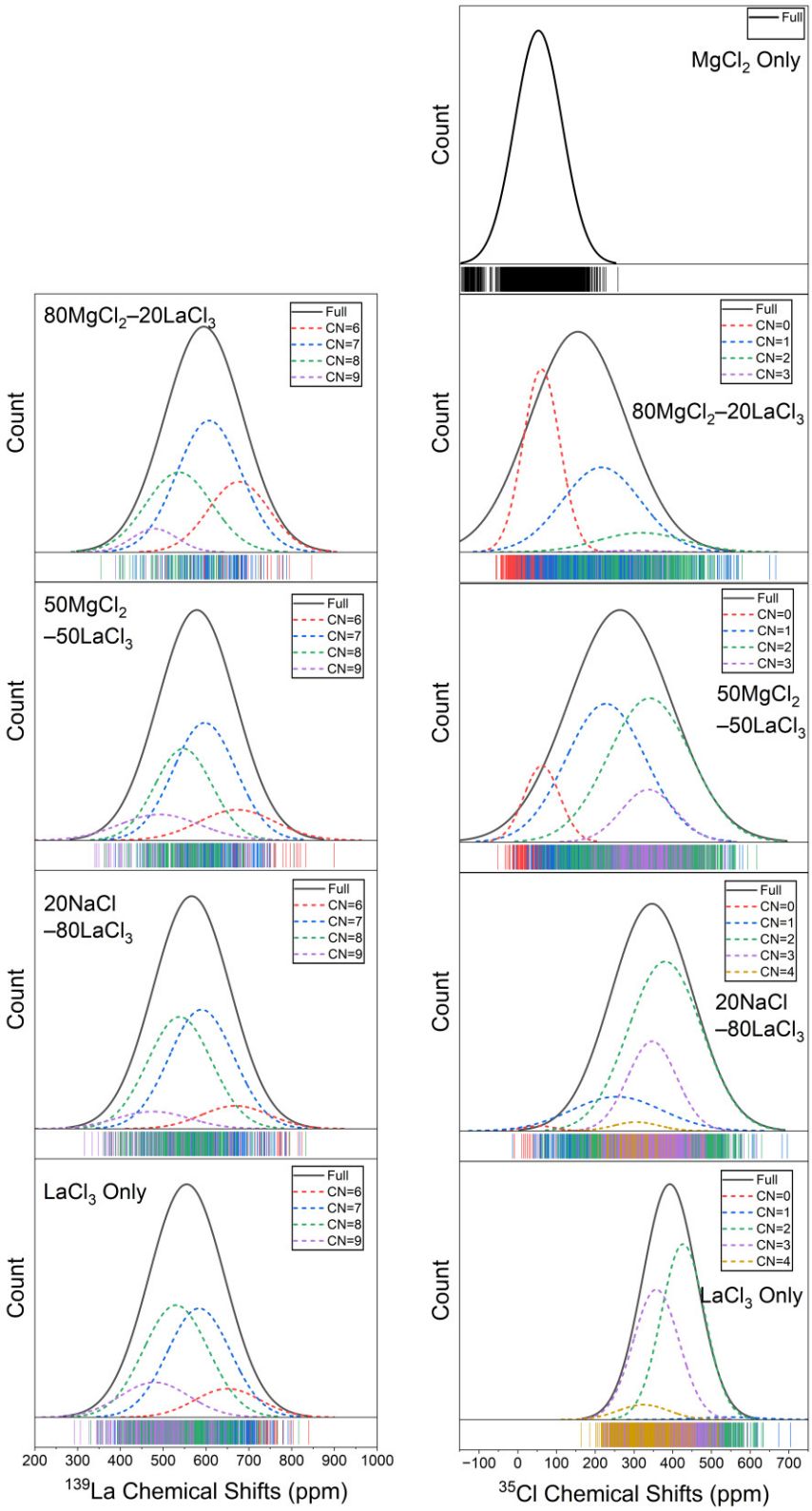

Figure III-19. Normalised distributions of calculated δ_{iso} values for ^{139}La (left panel) and ^{35}Cl (right panel) in $MgCl_2$–$LaCl_3$. Solid lines depict the distribution for all species, while dashed lines illustrate the distribution of species categorised by CN. CN categories representing less than 1% of the total species population have been omitted for clarity.

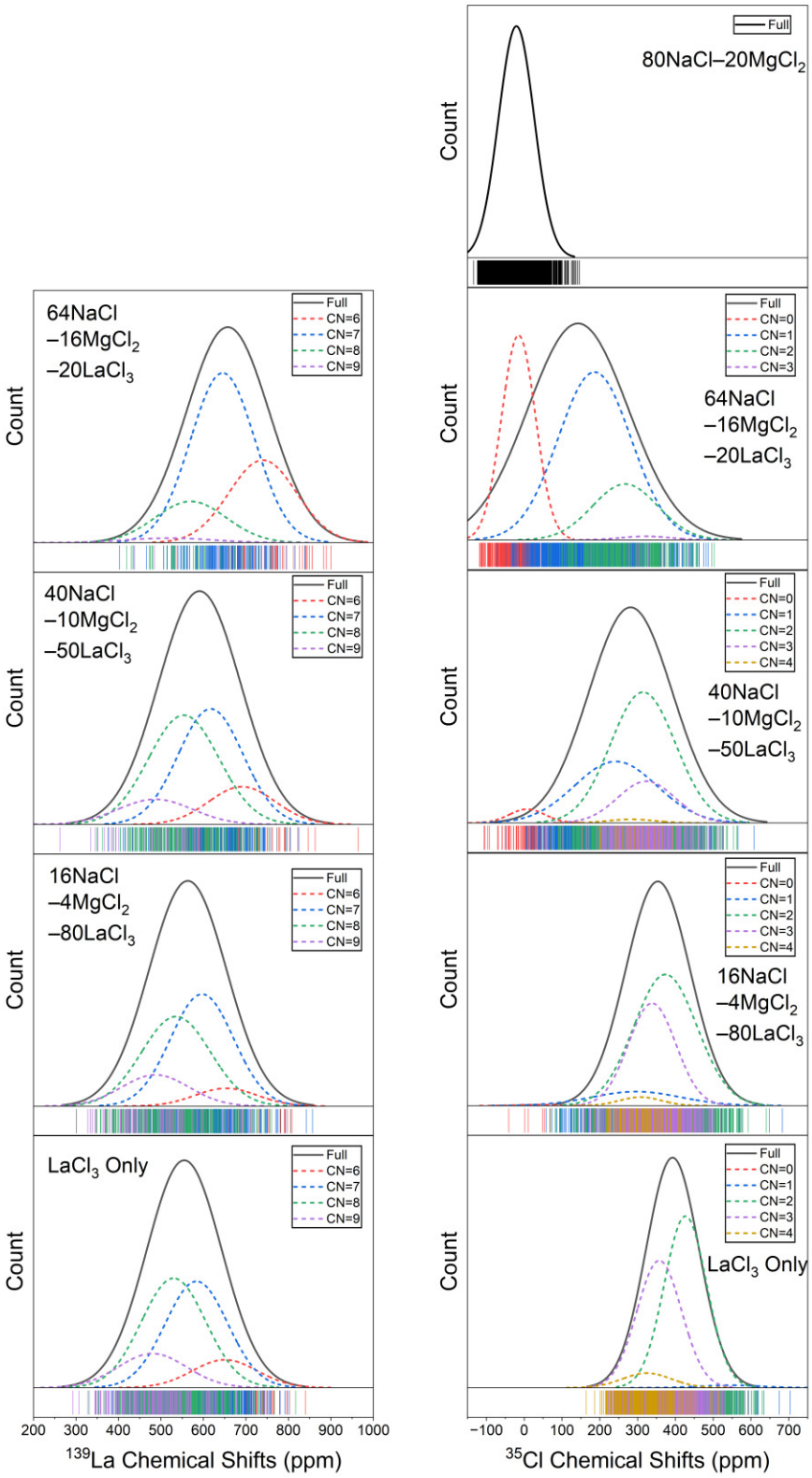

Figure III-20. Normalised distributions of calculated δ_{iso} values for ^{139}La (left panel) and ^{35}Cl (right panel) in $(NaCl)_{0.80}(MgCl_2)_{0.20}$–$LaCl_3$. Solid lines depict the distribution for all species, while dashed lines illustrate the distribution of species categorised by CN. CN categories representing less than 1% of the total species population have been omitted for clarity.

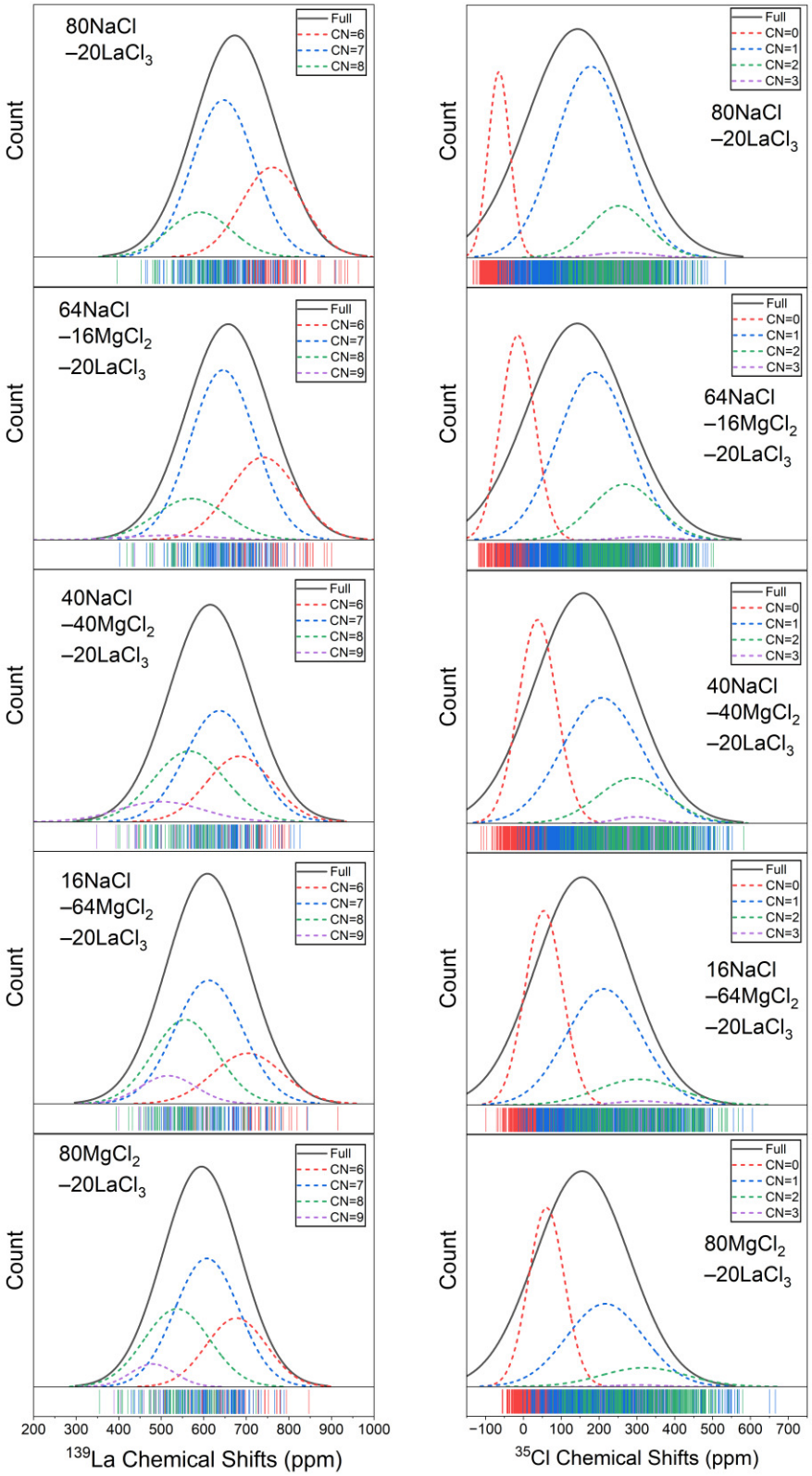

Figure III-21. Normalised distributions of calculated δ_{iso} values for ^{139}La (left panel) and ^{35}Cl (right panel) in 80 mol% $(NaCl)_{1-x}(MgCl_2)_x$–20 mol% $LaCl_3$. Solid lines depict the distribution for all species, while dashed lines illustrate the distribution of species categorised by CN. CN categories representing less than 1% of the total species population have been omitted for clarity.

Conclusions

In this chapter, an in-depth investigation of the local structure in molten NaCl–$MgCl_2$–$LaCl_3$ systems was conducted: *in situ* HT NMR was employed to probe the chemical shift evolutions with composition and temperature; SS NMR established the relationship between chemical shifts and coordination environments; classical MD simulations using the PIM provided quantitative analysis of the RDFs, CNs, and La–Cl–La network structures; DFT calculations of NMR parameters enabled assessments of the consistency between local structures derived from HT NMR and MD.

These self-consistent analyses reveal that the average La–Cl coordination number is lower in NaCl–$LaCl_3$ than in $MgCl_2$–$LaCl_3$ at comparable $LaCl_3$ concentrations. Moreover, chloride bridging is more prevalent in NaCl–$LaCl_3$ systems, resulting in more complex La–Cl–La networks; whereas, more isolated $[LaCl_n]^{3-n}$ units are found in $MgCl_2$–$LaCl_3$ systems. These trends extend into the NaCl–$MgCl_2$–$LaCl_3$ ternary system; however, the polymerisation and polyhedral sharing interactions notably deviate from the expected behaviour, likely due to competing effects arising from the coexistence of NaCl and $MgCl_2$.

These results suggest that in NaCl–$MgCl_2$–$LaCl_3$, NaCl acts as a heterogeneous spacer layer that encourages the formation of larger continuous La–Cl–La networks, while $MgCl_2$ mixes homogeneously with $LaCl_3$, disrupting continuous La–Cl–La network formation. Extending this to MCFR fuel salts, the inclusion of $MgCl_2$ could potentially lower fuel viscosity. Another possible advantage may be the suppression of oxide precipitation, as the more isolated $[LaCl_n]^{3-n}$ units may reduce the energy required to incorporate an oxygen atom between two adjacent La^{3+} ions—such as described in [137] and [138]—effectively making it more soluble.

By examining molecular-level structure and dynamics, this chapter elucidates the role of salt constituents and their impact on molten salt properties, which will be indispensable for the design and performance of MCFR fuel salts. In the next chapters, the potential benefits of $MgCl_2$ in lowering fuel viscosities and sequestering oxygen impurities are studied.

Chapter IV

Propriétés de Transport
/
Transport Properties

Résumé (Français)

L'efficacité thermique des RSF est étroitement liée aux propriétés thermophysiques de leur combustible, telles que la densité, la viscosité, la dilatation thermique, la capacité thermique et la conductivité thermique, qui déterminent les transferts de chaleur. Parmi ces grandeurs, la viscosité occupe une place centrale pour l'exploitation du réacteur, car elle gouverne les régimes d'écoulement du combustible et conditionne le dimensionnement ainsi que le nombre de pompes de circulation nécessaires. Toutefois, la mesure expérimentale de la viscosité des sels fondus demeure particulièrement délicate, en raison des températures de fonctionnement élevées, de la corrosivité des milieux, de la faible résistance à l'écoulement, de l'hygroscopicité des sels et, dans le cas des combustibles nucléaires, de leur radiotoxicité. En conséquence, les données expérimentales relatives à la viscosité des combustibles des MCFR restent très limitées, et les évaluations disponibles reposent majoritairement sur des estimations issues de modélisations numériques.

Le chapitre IV a pour objectif de combler partiellement cette lacune en confrontant les propriétés de transport obtenues par simulations DM à des mesures expérimentales, et en analysant l'influence du $MgCl_2$ sur le couplage entre structure locale et propriétés de transport dans un combustible MCFR de substitution ($NaCl–MgCl_2–LaCl_3$). Dans ce chapitre, les propriétés de transport considérées concernent spécifiquement les viscosités et les coefficients d'autodiffusion des ions. Bien que la conductivité thermique constitue également une propriété de transport essentielle, elle n'est pas abordée ici, en raison du nombre restreint de données expérimentales disponibles et des difficultés de convergence associées à son calcul dans le cadre des simulations DM classiques.

Le chapitre IV-1 met en évidence la capacité des simulations DM fondées sur le PIM à décrire de manière fiable les propriétés de transport des sels fondus. Cette validation est réalisée par une comparaison directe entre les viscosités calculées et les mesures de viscosimétrie capillaire rapportées dans la littérature, ainsi qu'entre les coefficients d'autodiffusion des ions Na^+ issus des simulations et ceux mesurés par RMN–PFG au CEMHTI. Les simulations DM reproduisent de manière satisfaisante les valeurs expérimentales des viscosités et des diffusivités ioniques dans le système binaire $NaCl–LaCl_3$ et parviennent également à restituer correctement les effets de la température. Néanmoins, ces comparaisons restent limitées au système $NaCl–LaCl_3$, en raison de l'absence de données de viscosité disponibles dans la littérature pour les autres systèmes binaires. Par ailleurs, les mesures RMN–PFG sur des compositions contenant du $MgCl_2$ se sont révélées particulièrement délicates, en raison des fortes interactions de surface entre le $MgCl_2$ fondu et les creusets en nitrure de bore.

Le chapitre IV-2 est consacré à l'évaluation des propriétés de transport du système ternaire $NaCl–MgCl_2–LaCl_3$ et à la caractérisation de l'influence du $MgCl_2$ sur ces propriétés. Globalement, la teneur en $LaCl_3$ apparaît comme le facteur dominant des comportements de transport: la viscosité augmente fortement avec l'augmentation de la concentration en $LaCl_3$, en raison de la formation de réseaux étendus La–Cl–La, qui constituent des complexes hydrodynamiques fortement interconnectés et favorisent la dissipation visqueuse. L'effet du $MgCl_2$ sur les propriétés de transport est plus nuancé, car il dépend fortement de la concentration en $LaCl_3$. Dans les compositions riches en $LaCl_3$, les ions Mg^{2+}

perturbent les réseaux continus La–Cl–La, conduisant à la formation de complexes $[La_xCl_y]^{3x-y}$ plus isolés, qui entravent moins efficacement l'écoulement du fluide. À l'inverse, dans les compositions pauvres en $LaCl_3$, l'ajout de $MgCl_2$ conduit à une augmentation de la viscosité, associée à la formation de complexes $[Mg_xCl_y]^{2x-y}$.

En résumé, le chapitre IV démontre la faisabilité et le faible coût des simulations DM basées sur le PIM pour la modélisation fiable des propriétés de transport des sels fondus. Il met également en évidence un double rôle du $MgCl_2$ dans les propriétés de transport, jusque-là non identifié, et l'examine pour la première fois dans le cadre du couplage entre structure locale et transport.

Introduction

MSRs convert thermal energy from nuclear fission into electrical energy through heat transfer across several intermediate circulation loops. As with any thermal power system, efficient heat transfer is central to their design and engineering. In this context, the heat transfer efficiency of MSRs is often assessed using Bonilla's Figure of Merit (FOM) [139], defined as:

$$FOM = \left(\frac{\eta^s}{\beta^t \rho^u C_P^v \lambda^w}\right)^r,$$

(Eq. IV- 1)

where η is the viscosity, β is the thermal expansivity, ρ is the density, C_P is the constant-pressure molar heat capacity, λ is the thermal conductivity, while *r, s, t, u, v, and w* are flow-regime-dependent exponents (**Table IV-1**).

Table IV-1. Flow-regime-dependent exponent values for Bonilla's FOMs

FOM	Convection	Regime	*r*	*s*	*t*	*u*	*v*	*w*
1	Forced	Turbulent	1.00	0.2	0.0	2.0	2.8	0.0
2	Natural	Turbulent	0.36	0.2	1.0	2.0	1.8	0.0
3	Natural	Laminar	0.50	1.0	1.0	2.0	1.0	0.0
4	–	–	1.00	0.2	1.0	0.3	0.6	0.6

Among these thermophysical properties, viscosity is particularly difficult to measure reliably. Several factors contribute to this challenge: 1) high operating temperatures and the corrosive nature of molten salts necessitate the use of specialised and robust equipment; 2) low flow resistance makes viscosity measurements susceptible to minor temperature fluctuations and mechanical vibrations, therefore requiring instruments with high sensitivity and precision; 3) susceptibility to moisture and oxygen impurities often reduces the reproducibility of measurements; 4) radiotoxicity of actinide salts poses additional safety and handling concerns. As a result, experimental data on the viscosities of actinide-bearing chloride melts remain scarce, and most assessments of MCFR fuel viscosities rely heavily on computational predictions.

This chapter aims to bridge this gap by benchmarking MD-calculated transport properties of the surrogate MCFR fuel against experimental measurements. Specifically, viscosities and ion self-diffusion coefficients of the NaCl–$LaCl_3$ binary system were obtained from capillary viscometry (literature) and PFG–NMR (this work), respectively, and were compared directly with MD simulations.

Furthermore, this chapter examines the role of Mg^{2+} ions in modifying the transport properties of MCFR-relevant compositions. Chapter III showed that $MgCl_2$ effectively disrupts La–Cl–La network connectivity, and previous studies have established that molten salt transport properties are heavily governed by the local structure [56,107]. Building on these insights, this chapter elucidates how the addition of $MgCl_2$ influences viscosity and diffusion,

interpreting the resulting trends through the lens of structural dynamics and coordination environments. Thermal conductivity, although also a transport property, was not considered because of the limited availability of experimental data and its poor convergence in conventional MD simulations.

IV-1. Binary Mixtures: Transport Properties of the NaCl–$LaCl_3$ System

Among the three binary subsystems of NaCl–$MgCl_2$–$LaCl_3$, only the transport properties (viscosity, self-diffusion coefficient) of NaCl–$LaCl_3$ were experimentally assessed in this work. Experimental evaluations of NaCl–$MgCl_2$ and $MgCl_2$–$LaCl_3$ transport properties were not pursued due to reasons discussed in Chapters IV-1.1 and 1.3.

IV-1.1. Viscosity

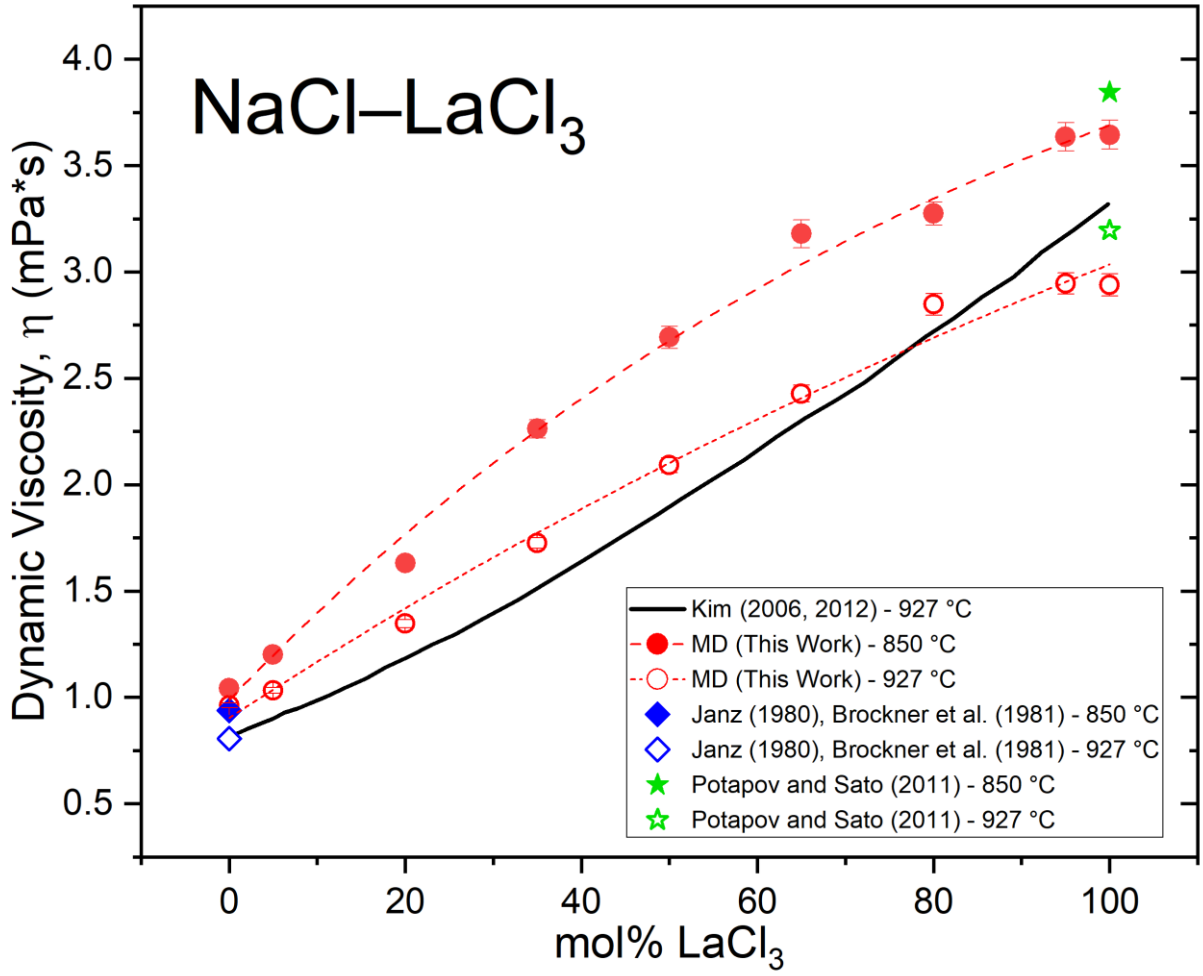

Figure IV-1. Comparison between the dynamic viscosities of NaCl–$LaCl_3$ binary melts.

By definition, viscosity is a fluid's internal resistance to flow. When adjacent layers of fluid move at different velocities, friction-like interactions develop between them, causing the faster layer to slow down. To maintain a steady flow, an opposing shear stress must be applied to overcome this resistance. The dynamic viscosity, μ, is defined as the proportionality constant between the applied shear stress and the velocity gradient between the fluid layers.

Figure IV-1 compares the dynamic viscosities of NaCl–$LaCl_3$ binary melts obtained from MD simulations (following the protocol in Chapter II-2.3) with the available experimental data. Based on available information, the only reported measurements of this binary system are from Kim [140,141], who used capillary viscometry at 927 °C. To supplement the comparison, reference viscosities of pure NaCl and $LaCl_3$ melts have been included: for NaCl, torsional oscillation viscometry measurements by Janz [142] and Brockner *et al.* [143] between 807–1027 °C are used; for $LaCl_3$, capillary viscometry data by Potapov and Sato [144] in the temperature range of 867–923 °C are used.

Molten salt viscosities follow Arrhenius behaviour, where relatively small temperature changes can lead to sharp drops in viscosity. For example, NaCl melts experience a 16.3 % reduction in viscosity from 850 to 927 °C, while $LaCl_3$ melts exhibit a 20.3 % drop from 867 to 923 °C. Consequently, the initial MD results at 850 °C showed a sizable discrepancy from Kim's measurements at 927 °C. To enable a direct comparison, additional viscosity calculations at 927 °C were performed. The MD-calculated viscosity data points at 850 and 927 °C are provided in Annexe-A. The new calculations show excellent agreement with the experimental data, with a minor overprediction of <0.2 mPa·s for compositions with <80 mol% $LaCl_3$ and a slight underprediction of <0.4 mPa·s at higher $LaCl_3$ content. This composition-dependent transition from slight overprediction to underprediction may arise from the finite size of the simulation box relative to the increasingly interdigitated La–Cl–La networks at high $LaCl_3$ content.

Another notable trend is the steep increase in viscosities with increasing $LaCl_3$ content. Structural dynamics analyses of NaCl–$LaCl_3$ melts in Chapter III-3.1 have shown that $LaCl_3$ tends to form extended La–Cl–La chains and large $[La_xCl_y]^{3x-y}$ complexes, with this behaviour becoming increasingly prevalent at higher $LaCl_3$ concentrations. On a microscopic scale, these large, interconnected units impede flow by increasing internal resistance to deformation and raising the shear stress required to sustain motion, thereby elevating viscosity.

To date, no experimental viscosity data have been reported for the NaCl–$MgCl_2$ and $MgCl_2$–$LaCl_3$ binary systems. Hence, their viscosities are only computationally evaluated and discussed together with the ternary systems in Chapter IV-2.1.

IV-1.2. Self-diffusivity

In molten salts, self-diffusion refers to the random motion of ions in the absence of concentration or thermal gradients. In this work, ion self-diffusivities in molten salts were measured using PFG–NMR. However, as discussed in Chapter II-1.6, reliable PFG–NMR measurements require T_1 and T_2 relaxation times of at least ~5 ms for the nuclei of interest. Accordingly, the T_1 and T_2 values of ^{23}Na, ^{139}La, and ^{35}Cl were measured following the procedures in Chapter II-1.3. As shown in **Table IV-2**, only ^{23}Na exhibited sufficiently long relaxation times; therefore, self-diffusion measurements were limited to Na^+ ions.

Table IV-2. Measured T_1 and T_2 relaxation times of molten NaCl–$LaCl_3$ binary compositions at 850 °C in the NMR spectrometer operating at 9.4 T.

Molten Salt Compositions (mol%)	T_1 Relaxation Times (ms) ± 10% Uncertainty			T_2 Relaxation Times (ms) ± 10% Uncertainty		
	^{23}Na	^{139}La	^{35}Cl	^{23}Na	^{139}La	^{35}Cl
Pure NaCl	1120	–	137	5.93	–	2.48
80 NaCl – 20 $LaCl_3$	78.0	0.426	2.57	32.7	0.693	2.31
50 NaCl – 50 $LaCl_3$	70.2	0.355	0.402	29.7	0.211	0.937
20 NaCl – 80 $LaCl_3$	45.5	0.074	0.662	13.1	0.109	0.702

Figure IV-2a compares the sodium ion diffusivities across NaCl–$LaCl_3$ binary compositions obtained from PFG–NMR measurements and MD simulations at 850 °C. Values of the measured and calculated diffusion coefficients are provided in Annexe-A. Diffusivity data for pure NaCl by Janz and Bansal [145] are included to provide an additional reference for benchmarking. The close agreement between our MD calculations and experimental results corroborates our computational approach. As $LaCl_3$ content increases, sodium ion diffusivities decrease markedly. A similar trend is observed for the calculated diffusivities of La^{3+} and Cl^- ions, which also decrease rapidly with increasing $LaCl_3$ concentration (**Figure IV-2b**).

A useful metric to evaluate this flow behaviour is the hydrodynamic radius, r_H, defined via the Stokes–Einstein relation:

$$r_{H,i} = \frac{k_B T}{c' \pi \eta D_{i,\infty}},$$

(Eq. IV-2)

where c' is a constant that depends on boundary conditions ($c' = 4$ for "slip" and $c' = 6$ for "stick"). **Table IV-3** presents the calculated slip and stick hydrodynamic radii of ions for NaCl–$LaCl_3$ binary compositions. Under slip boundary conditions, the hydrodynamic radii for Na^+ and Cl^- ions closely resemble their Shannon crystal radii [146] (**Table IV-4**). This suggests that, in molten salts, Na^+ and Cl^- ions behave as nearly spherical diffusing particles that slip past surrounding fluids with little tangential drag. In contrast, both slip and stick hydrodynamic radii for La^{3+} ions are substantially larger than the corresponding bare crystal radii, indicating that La^{3+} transport couples strongly to the surrounding fluid. This behaviour is consistent with La^{3+} ions diffusing as part of interdigitated $[La_xCl_y]^{3x-y}$ complexes. These anisotropic clusters act like sticky hydrodynamic objects that transfer tangential momentum to the surrounding melt [147], thereby increasing viscous dissipation. Taken together, this hydrodynamic analysis reinforces prior findings that lanthanide and actinide trichlorides markedly increase the viscosity of molten salt systems.

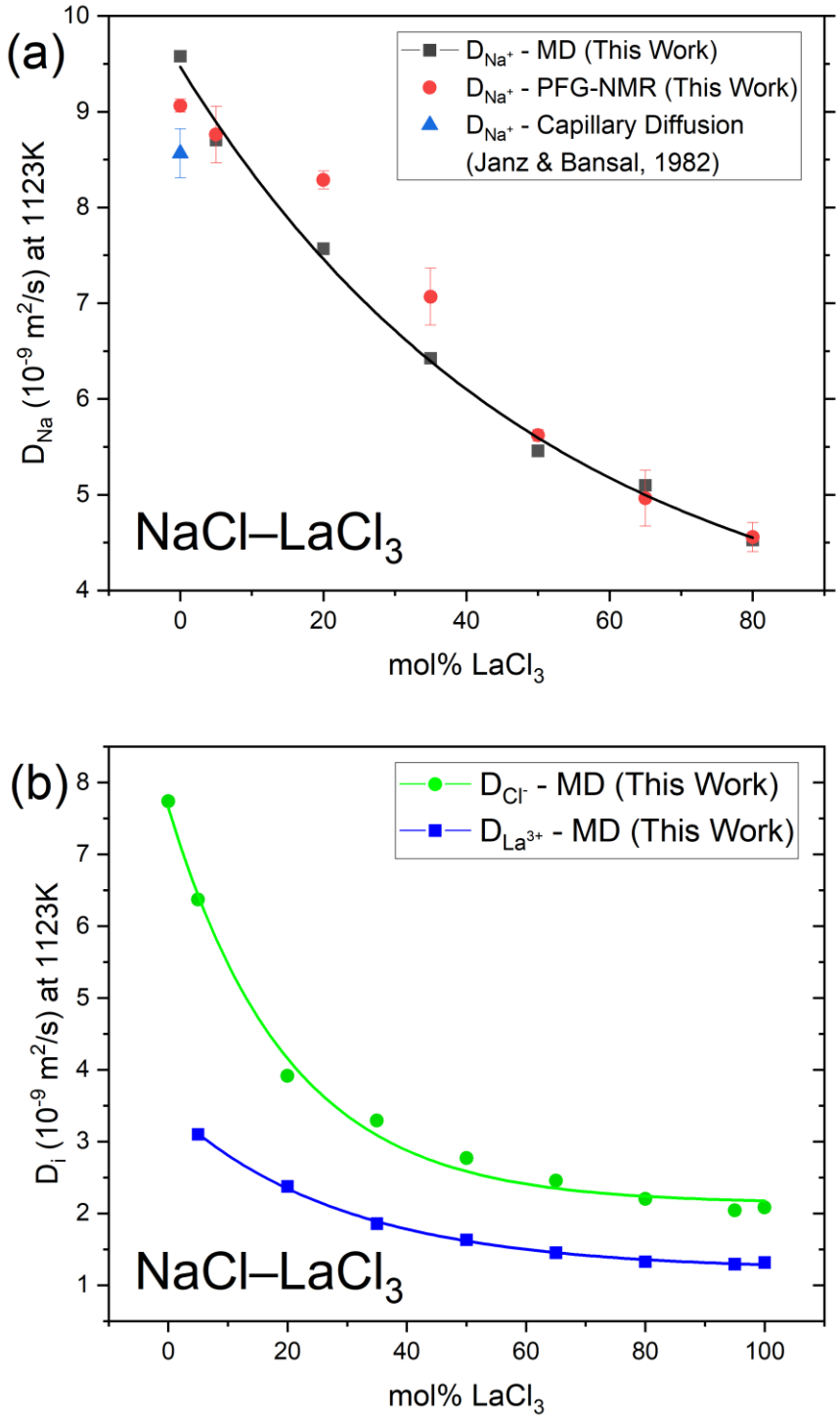

Figure IV-2. (a) Calculated and measured Na^+ self-diffusion coefficients in NaCl–$LaCl_3$ binary melts at 850 °C; (b) Calculated La^{3+} and Cl^- self-diffusion coefficients in NaCl–$LaCl_3$ binary melts at 850 °C.

Table IV-3. Calculated hydrodynamic radii of ions in NaCl–$LaCl_3$ binary compositions at 850 °C.

Molten Salt Composition (mol%)	Hydrodynamic Radius (Å)					
	Slip Conditions ($c' = 4$)			Stick Conditions ($c' = 6$)		
	r_{H,Na^+}	$r_{H,La^{3+}}$	r_{H,Cl^-}	r_{H,Na^+}	$r_{H,La^{3+}}$	r_{H,Cl^-}
100 $LaCl_3$	–	2.608	1.648	–	1.739	1.099
5 NaCl – 95 $LaCl_3$	0.805	2.625	1.663	0.537	1.750	1.108
20 NaCl – 80 $LaCl_3$	0.833	2.838	1.713	0.555	1.892	1.142
35 NaCl – 65 $LaCl_3$	0.761	2.672	1.581	0.507	1.782	1.054
50 NaCl – 50 $LaCl_3$	0.840	2.810	1.654	0.560	1.873	1.103
65 NaCl – 35 $LaCl_3$	0.849	2.936	1.657	0.566	1.957	1.105
80 NaCl – 20 $LaCl_3$	1.001	3.189	1.936	0.668	2.126	1.290
95 NaCl – 5 $LaCl_3$	1.179	3.310	1.611	0.786	2.207	1.074
100 NaCl	1.235	–	1.529	0.823	–	1.019

Table IV-4. Reference Shannon radii for ions [146]

Ion	Coordination	Crystal Radius (Å)
Na^+	VI	1.16
Mg^{2+}	VI	0.86
La^{3+}	VI	1.17
	VII	1.24
	VIII	1.30
	IX	1.356
Cl^-	VI	1.67

IV-1.3. Limitations of PFG–NMR on $MgCl_2$-Containing Systems

PFG–NMR measurements could not be performed on molten salts containing $MgCl_2$ due to material incompatibilities with BN. In these systems, $MgCl_2$ was found to interact strongly with the BN inserts used to suppress convection during measurements, leading to anomalous peak splitting in the NMR spectra (**Figure IV-3**) and preventing reliable measurements.

To determine whether the BN inserts were responsible, they were removed, and the Five-Pulse Stimulated Echo (FPSTE) pulse sequence was employed to suppress convection effects while simultaneously carrying out the phase-encoding role of the STGE pulse sequence. Despite these efforts, the peak splitting persisted, indicating that the problem also originates from strong wetting interactions between molten $MgCl_2$ and the BN crucible walls. This behaviour is likely exacerbated by the reduced diameter (6 mm) of the BN crucibles used for PFG–NMR, which increases the surface-to-volume ratio and amplifies surface interactions.

Supporting this interpretation, $MgCl_2$-containing melts were consistently observed to creep along BN surfaces, often resulting in severe leakage during heating. This creeping and leakage occurred not only in the narrow PFG–NMR crucibles but also, to a lesser extent, in the larger BN crucibles (9mm diameter) used in standard HT NMR measurements.

These limitations highlight the need for alternative crucibles and insert materials to enable reliable diffusion measurements in molten salts containing $MgCl_2$.

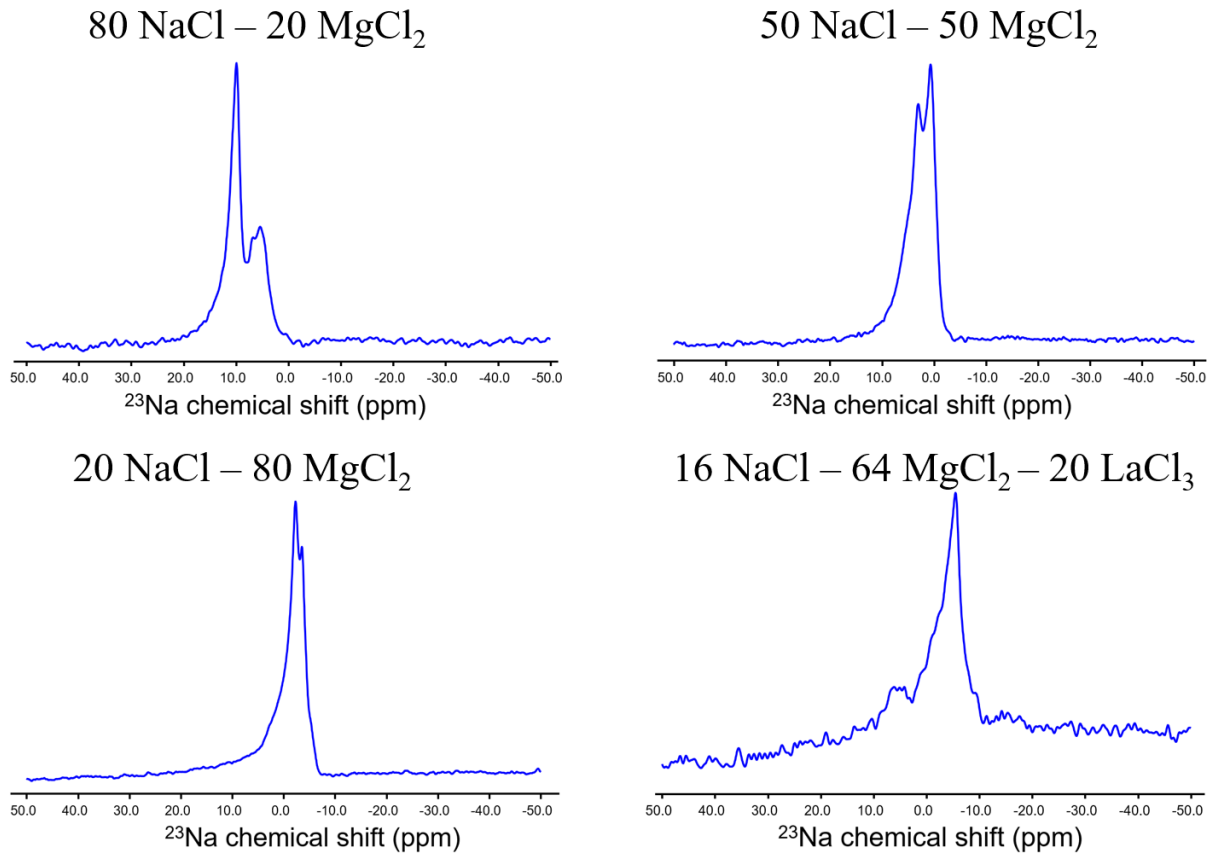

Figure IV-3. Anomalous peak splitting observed during PFG–NMR measurements of $MgCl_2$-containing molten salt mixtures at 850 °C. In these systems, three BN fragments were inserted into the molten salt mixture to suppress convection currents. Measurements were acquired using the STGE pulse sequence.

IV-2. Ternary Mixtures: Influence of Mg^{2+} ions on Transport Properties in NaCl–$MgCl_2$–$LaCl_3$

Given the experimental challenges associated with $MgCl_2$-containing systems, the influence of $MgCl_2$ on the viscosities and diffusion coefficients of NaCl–$LaCl_3$ melts was evaluated solely through classical MD simulations.

IV-2.1. Viscosity

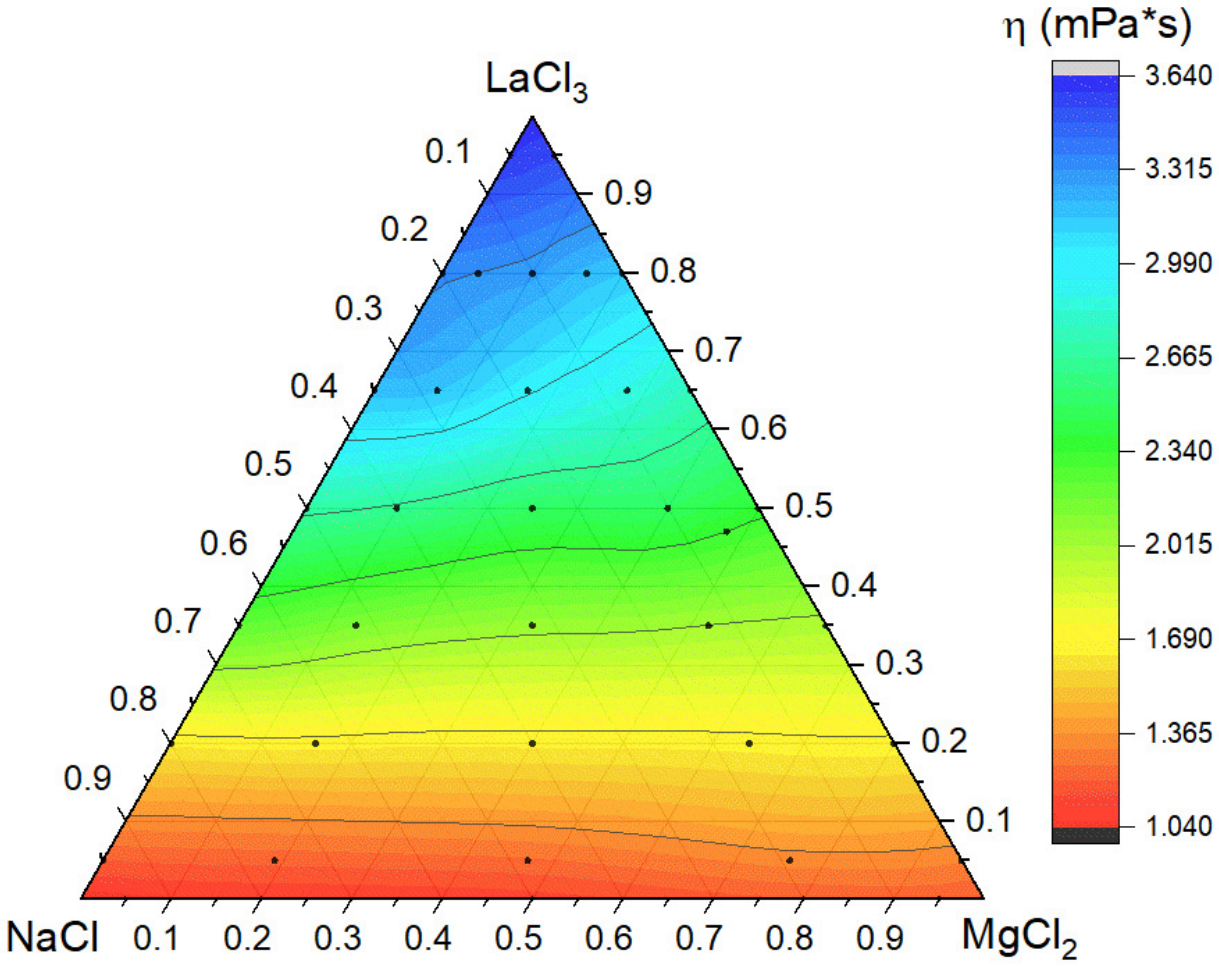

Figure IV-4. Calculated dynamic viscosities of the NaCl–$MgCl_2$–$LaCl_3$ ternary system at 850 °C. Black dots indicate the 41 reference compositions used in the interpolation.

Figure IV-4 presents the calculated dynamic viscosities of the NaCl–$MgCl_2$–$LaCl_3$ ternary system at 850 °C. Viscosities were assessed at 41 distinct compositions and interpolated with a complementary smoothing algorithm to produce a continuous contour map. The raw viscosity data points are tabulated in Annexe-A.

At first glance, it is evident that $LaCl_3$ concentration exerts the largest effect on melt viscosities: as $LaCl_3$ content increases, the melt becomes significantly more viscous. As discussed earlier, this corresponds directly to the formation of large $[La_xCl_y]^{3x-y}$ clusters that hinder ion mobility and impede flow.

In contrast, the effects of $MgCl_2$ addition are more nuanced. At higher $LaCl_3$ concentrations (>20 mol%), increasing $MgCl_2$ content results in a noticeable reduction of melt viscosities. This is attributable to the role of $MgCl_2$ in disrupting the formation of extensive La–Cl–La networks, leading to smaller and more isolated $[La_xCl_y]^{3x-y}$ units [99]. Under this less rigid framework, ions experience fewer barriers to mobility and less internal resistance to flow, thus leading to lower viscosities. However, below the threshold of 20 mol% $LaCl_3$, the impact of $MgCl_2$ appears less pronounced—and conversely, the melt viscosities tend to increase slightly with $MgCl_2$. In these more dilute regimes, the formation of $[La_xCl_y]^{3x-y}$ clusters is less prominent. Consequently, melt viscosities become more dependent on the intrinsic mobilities of constituent ions in NaCl and $MgCl_2$.

IV-2.2. Self-diffusivity

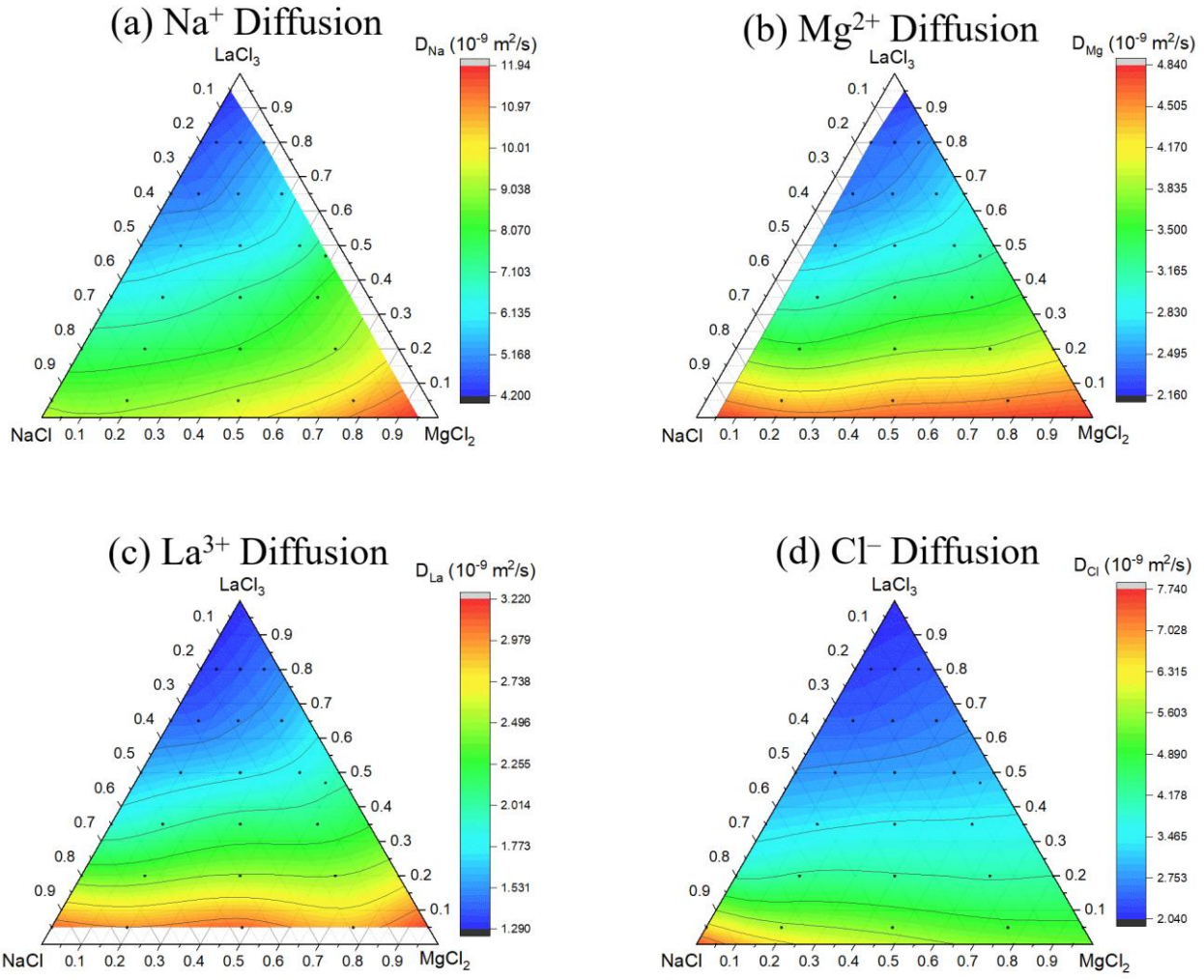

Figure IV-5. Calculated self-diffusion coefficients of (a) Na^+, (b) Mg^{2+}, (c) La^{3+}, and (d) Cl^- ions in NaCl–$MgCl_2$–$LaCl_3$ ternary system at 850 °C. Black dots indicate the 41 reference compositions used in the interpolation.

Characterising the ion self-diffusivity helps elucidate the observed trends in viscosity. **Figure IV-5** depicts the self-diffusion coefficients of Na^+, Mg^{2+}, La^{3+}, and Cl^- ions across the same compositional spectrum. Here, the colour scheme is chosen to mirror that of the viscosity contour plot, accentuating ion mobility instead of absolute diffusivity values. It is worth noting that the magnitude of ion diffusivities consistently decreases in the order of $Na^+ > Cl^- > Mg^{2+} > La^{3+}$ across all compositions, mirroring the trend of increasing hydrodynamic radii (**Figure IV-6**). This correspondence highlights the utility of the hydrodynamic radius as a metric for evaluating relative ion mobilities.

As expected, all ion diffusivities decline sharply with increasing $LaCl_3$ concentration, reflecting the dominant effect of $[La_xCl_y]^{3x-y}$ clusters in retarding ion mobility. Within this overall trend, cations and anions behave differently. Cation diffusivities are enhanced by increasing the $MgCl_2$-to-NaCl ratio at all $LaCl_3$ concentrations, consistent with the role of $MgCl_2$ in disrupting La–Cl–La network formation. Anions, by contrast, show diffusivity trends more akin to that of viscosity: at high $LaCl_3$ concentrations, Cl^- diffusion increases with $MgCl_2$ content because smaller, more isolated $[La_xCl_y]^{3x-y}$ complexes reduce Cl^- ion confinement to bridging interactions within clusters; at lower $LaCl_3$ concentrations, Cl^- ion diffusivity decreases slightly with $MgCl_2$, reflecting a more complex role of $MgCl_2$ under dilute $LaCl_3$ conditions.

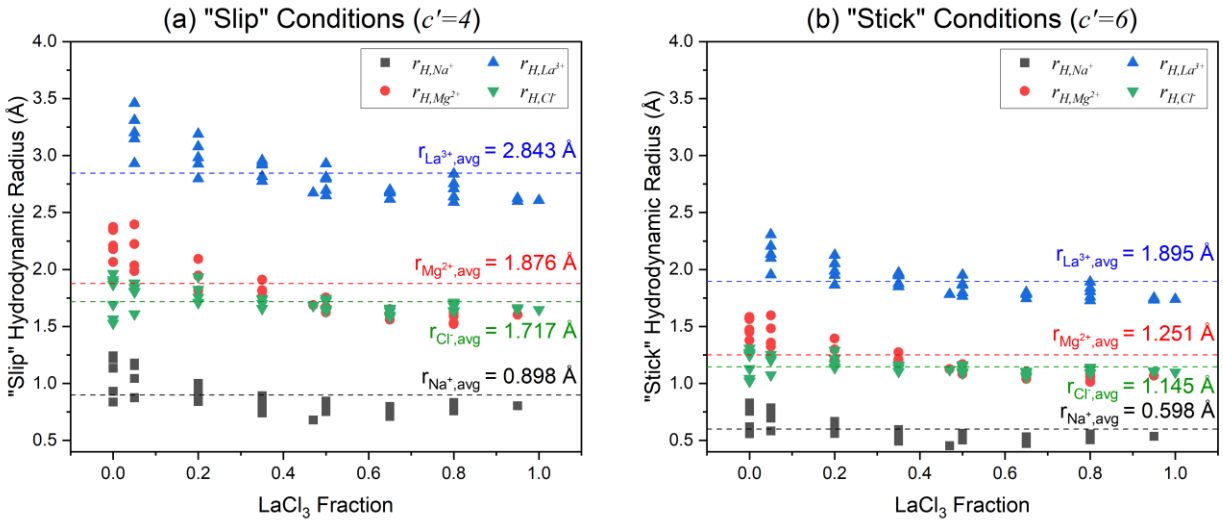

Figure IV-6. Calculated hydrodynamic radii of Na^+, Mg^{2+}, La^{3+} and Cl^- ions in NaCl–$MgCl_2$–$LaCl_3$ ternary system at 850 °C under (a) slip and (b) stick conditions.

IV-2.3. Effects of $MgCl_2$ on the Ion Transport Mechanism

To rationalise the observed trends in diffusivities, the free energy profile between ion pairs is examined using the potential of mean force (PMF), ω_{ij}, defined as:

$$\omega_{ij}(r) = -k_B T \ln g_{ij}(r),$$

(Eq. IV- 3)

where $g_{ij}(r)$ is the RDF for the i–j ion pair. In this work, ω_{ij} was specifically evaluated at the first RDF maximum, R_{max}. RDFs of Mg^{2+}–Cl^- and Mg^{2+}–Mg^{2+} ion pairs for several representative molten salt compositions are shown in **Figure IV-7**. In these cases, the PMF between ion pairs was evaluated at 2.38 Å for Mg^{2+}–Cl^- and between 3.90 and 3.95 Å for Mg^{2+}–Mg^{2+}.

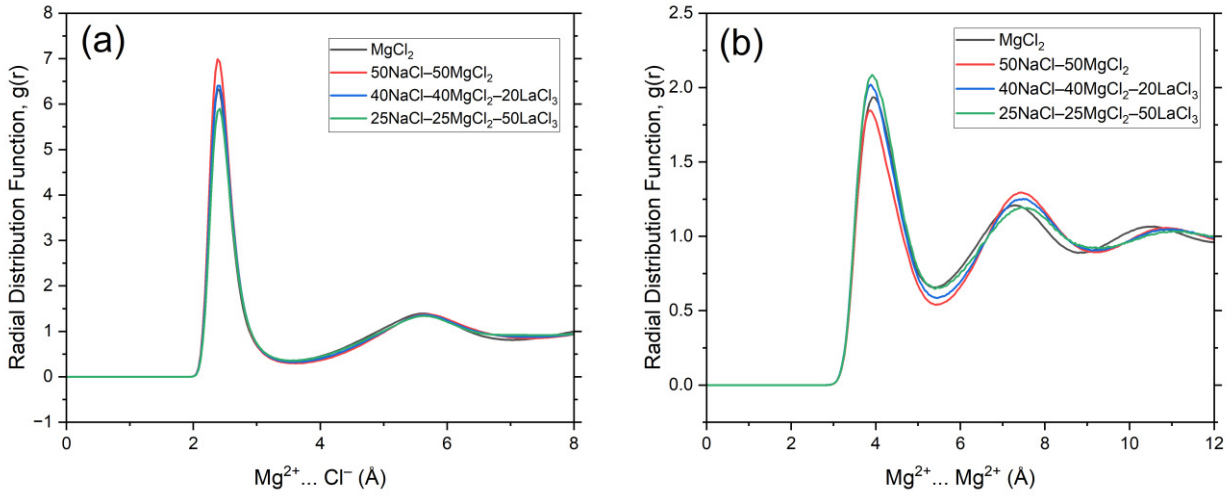

Figure IV-7. RDFs of (a) Mg^{2+}–Cl^- and (b) Mg^{2+}–Mg^{2+} ion pairs of several molten NaCl–$MgCl_2$–$LaCl_3$ compositions (in mol%) at 850 °C.

Figure IV-8 presents the corresponding PMFs across all compositions. The Mg^{2+}–Cl^- PMF indicates the strongest correlations in NaCl-rich compositions, which weaken as $MgCl_2$ content rises and are the weakest in the $LaCl_3$-rich region. This trend reflects competition between cations of differing charge density for Cl^- coordination. At low $LaCl_3$ concentrations, stronger Mg^{2+}–Cl^- electrostatic interactions slow down Cl^- motion (relative to Na^+–Cl^-), therefore reducing its diffusivity.

Another plausible explanation for reduced Cl^- mobility in $MgCl_2$-rich compositions involves the formation of $[Mg_xCl_y]^{2x-y}$ complexes. In this compositional region, the Mg^{2+}–Mg^{2+} PMF reveals enhanced correlations, consistent with the formation of interconnected Mg–Cl–Mg networks. In low-$LaCl_3$ melts, these $[Mg_xCl_y]^{2x-y}$ complexes act as the primary sticky hydrodynamic units that impede flow, leading to greater viscous dissipation. This explanation parallels the intermediate-ranged ordering of $MgCl_2$ previously observed in molten KCl–$MgCl_2$ [148]. The large discrepancy between Mg^{2+} hydrodynamic (**Figure IV-6**) and Shannon radii (**Table IV-4**) further supports this picture. Because Cl^- anions are the nearest neighbours of Mg^{2+}, their diffusivity in low-$LaCl_3$ concentration regimes is strongly influenced by $[Mg_xCl_y]^{2x-y}$ clustering; whereas, this clustering effect on the mobility of secondary-neighbour cations is less pronounced.

In short, the dual role of $MgCl_2$ reconciles the contrasting diffusivity trends: In $LaCl_3$-rich compositions, $MgCl_2$ acts as a La–Cl–La network disruptor that improves ion diffusivity; whereas, at low $LaCl_3$ concentrations, $MgCl_2$ forms

sticky hydrodynamic complexes that hinder ion mobility. Given that Cl^- ions constitute a majority species in NaCl–$MgCl_2$–$LaCl_3$, these competing effects also explain why the viscosity landscape most closely mirrors Cl^- diffusivity.

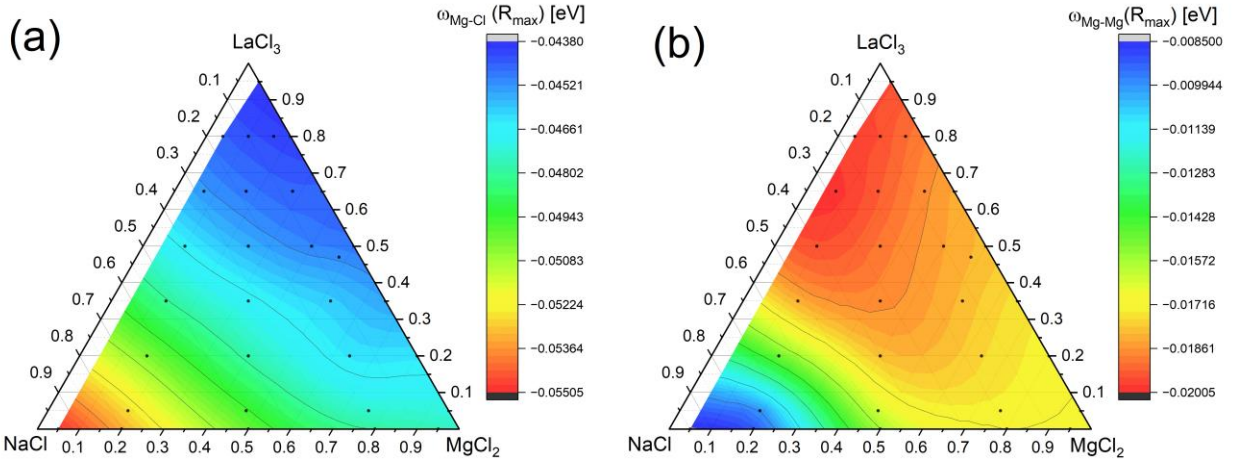

Figure IV-8. PMF values for (a) Mg^{2+}–Cl^- and (b) Mg^{2+}–Mg^{2+} ion pairs across all compositions at 850 °C. All PMFs here are evaluated at the first RDF maximum of each composition, R_{max}. Black dots indicate the 41 reference compositions used in the interpolation.

Conclusions

In this chapter, classical MD simulations with the PIM were employed to evaluate viscosities and self-diffusion coefficients of 41 compositions across the NaCl–$MgCl_2$–$LaCl_3$ ternary space. The accuracy of the simulations for NaCl–$LaCl_3$ binary compositions was validated against capillary viscometry data from Kim [140,141] and PFG–NMR measurements conducted at CEMHTI. As far as is known, viscosity measurements on the NaCl–$MgCl_2$ and $MgCl_2$–$LaCl_3$ binary systems are unavailable in the literature, and PFG–NMR measurements could not be performed due to compatibility issues between molten $MgCl_2$ and BN crucibles.

Overall, this chapter showed that $MgCl_2$ reduces molten salt viscosity when $LaCl_3$ concentrations exceed 20 mol%, primarily due to its ability to disrupt the formation of large $[La_xCl_y]^{3x-y}$ clusters and thereby enhance ion mobility. Below this threshold, however, NaCl contributes to slightly lower viscosities than $MgCl_2$. This is attributed to the tendency of $MgCl_2$ to form $[Mg_xCl_y]^{2x-y}$ complexes in $LaCl_3$-deficient regimes, thereby impeding ion mobility. The excellent agreement between simulation results and experimental data confirms the reliability of the interatomic potentials in accurately capturing the atomic-scale structure and transport of molten salts. Additionally, the smooth continuity of the calculated values throughout the ternary composition space demonstrates the consistency of the simulation protocol and shows that converged transport properties can be obtained using moderate box sizes (<5000 atoms) and relatively short simulation timescales (~10 ns).

In short, the work in this chapter demonstrates the feasibility of computationally efficient and precise modelling of molten salt transport properties. These results offer valuable insights and benchmarks for the advancement of molten salt R&D, not only limited to MSR technology, but also for other energy and industrial applications, such as pyroprocessing, concentrated solar power, and electrorefining.

Chapter V

Solubilité de l'Oxygène
/
Oxygen Solubility

Résumé (Français)

Les RSF de nouvelle génération visent une durée de vie opérationnelle d'au moins 60 ans. Malgré des avancées significatives dans l'amélioration de leur maturité technologique et de leur viabilité économique, la corrosivité intrinsèque des sels fondus demeure l'un des principaux verrous au déploiement industriel de la technologie RSF. Dans les RSF à base de chlorures, le $MgCl_2$ a été proposé comme composant du combustible afin de séquestrer des impuretés oxygénées qui pourraient contribuer à la corrosion. Toutefois, le mécanisme moléculaire sous-jacent à la solubilité de l'oxygène assistée par le $MgCl_2$ reste encore insuffisamment compris.

Le chapitre V apporte des preuves directes à l'échelle moléculaire permettant d'élucider le mécanisme de solubilité de l'oxygène médiée par le $MgCl_2$ dans les sels fondus chlorurés. À cette fin, la RMN HT a été mise en œuvre pour mesurer les déplacements chimiques du ^{17}O dans des mélanges fondus NaCl–$MgCl_2$–$LaCl_3$ contenant des quantités contrôlées de LaOCl enrichi en ^{17}O. Plus précisément, le système (80-α) NaCl–α $MgCl_2$–(20-x) $LaCl_3$–x LaOCl a été étudié, simulant un scénario idéal de contamination oxygénée du combustible RSF par substitution de deux ions Cl^- par un ion O^{2-}. Les variations marquées et systématiques des déplacements chimiques du ^{17}O en fonction du rapport $MgCl_2$/NaCl traduisent directement la diversification des environnements de coordination de l'oxygène dans les mélanges fondus. Des simulations complémentaires de DM fondées sur le PIM, ainsi que des calculs RMN basés sur les premiers principes, ont été réalisées afin de fournir un cadre théorique cohérent pour l'interprétation des observations expérimentales.

Le chapitre V-1 est consacré à la synthèse et à la caractérisation du LaOCl, composé clé permettant la réalisation des mesures RMN du ^{17}O à haute température. Le LaOCl enrichi en ^{17}O a été synthétisé par hydratation de 1,0 g de poudre fine de $LaCl_3$ à l'aide d'un excès d'eau enrichie à 90 wt % en ^{17}O, dans une boîte à gants sous atmosphère d'argon. La suspension obtenue a ensuite été homogénéisée, puis séchée pendant une nuit à 650 °C. L'analyse par diffraction des rayons X (DRX) des poudres synthétisées met en évidence la formation d'un LaOCl stable et monophasé, résultat confirmé par des mesures de RMN à l'état solide.

Le chapitre V-2 explore la dynamique de l'oxygène dans les chlorures fondus à travers des simulations DM. Des comparaisons visuelles entre les systèmes 80 NaCl–15 $LaCl_3$–5 LaOCl et 80 $MgCl_2$–15 $LaCl_3$–5 LaOCl montrent que l'oxygène tend à se regrouper autour des ions La^{3+} dans le premier système, tandis qu'il est distribué de manière plus homogène dans le second. Ces observations suggèrent que les ions Mg^{2+} perturbent les agrégats O–La en favorisant la coexistence d'environnements de coordination O–Mg et O–La dans la phase fondue, alors que la coordination O–Na apparaît énergétiquement défavorable. L'analyse des RDFs des paires ioniques O^{2-}–X^{n+}, La^{3+}–La^{3+} et Mg^{2+}–Mg^{2+} vient corroborer ces tendances.

Le chapitre V-3 est consacré à l'analyse de la spéciation de l'oxygène dans les chlorures fondus à partir de mesures de RMN HT et de calculs RMN basés sur les premiers principes. En s'appuyant sur les résultats des simulations DM concernant les préférences de coordination O–Na et O–Mg, il est possible de prédire les tendances attendues des déplacements chimiques du ^{17}O dans les systèmes de sels fondus étudiés. Étant donné que les valeurs de déplacement

chimique du ^{17}O dans le La_2O_3 solide (469 et 590 ppm) sont nettement plus élevées que celles observées dans le Na_2O (11,8 ppm) et le MgO (24,2 ppm), les déplacements chimiques correspondants dans les compositions riches en NaCl sont attendus à des valeurs plus élevées, en raison d'une coordination préférentielle de l'oxygène avec le lanthane. À l'inverse, dans les systèmes riches en $MgCl_2$, les déplacements chimiques plus faibles sont attendus, reflétant une coordination mixte de l'oxygène avec les ions Mg^{2+} et La^{3+}.

Les mesures de RMN HT présentées au chapitre V-3.1 confirment ces tendances, en montrant que les valeurs de déplacement chimique du ^{17}O diminuent progressivement avec l'augmentation de la concentration en $MgCl_2$, jusqu'à atteindre un rapport NaCl/$MgCl_2$ de 1:1. Au-delà de cette composition, aucune évolution systématique supplémentaire des déplacements chimiques n'est observée, ce qui indique une saturation de la sphère de coordination de l'ion O^{2-} par les ions Mg^{2+}, ainsi qu'un équilibre entre les nombreux environnements de coordination accessibles. Malgré la bonne concordance globale entre les déplacements chimiques mesurés et ceux prédits, un élargissement anormal des raies du ^{17}O a été observé dans certaines compositions. Ce phénomène a initialement conduit à envisager une solubilité incomplète du LaOCl. Toutefois, une analyse croisée combinant calorimétrie différentielle à balayage (DSC), analyse thermogravimétrique différentielle (TG–DTA) et DRX *ex situ* a démontré que le LaOCl est entièrement dissous dans l'ensemble des compositions étudiées à 770 °C. L'élargissement des raies RMN a finalement été attribué à la volatilisation des sels chlorurés aux températures de mesure élevées (850 et 1000 °C), entraînant une évolution temporelle de la composition de la phase fondue. Néanmoins, ces artefacts ont pu être maîtrisés en limitant les temps d'acquisition RMN (donc les temps de chauffage laser), ce qui a permis de préserver la fiabilité des tendances observées sur les déplacements chimiques.

Au chapitre V-3.2, les calculs RMN basés sur les premiers principes ont été réalisés afin d'évaluer la cohérence entre les structures locales générées par les simulations DM et les observations expérimentales issues de la RMN HT. Trois isotopes ont été considérés : ^{17}O, ^{139}La et ^{35}Cl. Dans l'ensemble, les déplacements chimiques calculés reproduisent correctement les tendances expérimentales, bien que des écarts de précision variables soient observés selon l'isotope. Les principaux résultats peuvent être résumés comme suit :

- **^{17}O** : les déplacements chimiques calculés reproduisent les tendances expérimentales, mais présentent une surestimation systématique d'environ 150 ppm par rapport aux valeurs mesurées. Cette différence est attribuée, d'une part, à la prise en compte limitée des effets de température finie dans les calculs RMN effectués sur des configurations instantanées issues des simulations DM, et, d'autre part, aux limites intrinsèques de la DFT statique pour la description précise de la structure électronique des liaisons La–O fortement hybridées.
- **^{139}La** : les déplacements chimiques calculés suivent globalement les tendances expérimentales, mais leur précision dépend fortement du rapport $MgCl_2$/NaCl. La principale source d'erreur est attribuée à une description insuffisante des déplacements chimiques associés aux environnements de coordination La–O, plus fréquents dans les compositions riches en NaCl que dans celles riches en $MgCl_2$. Cette limitation est liée aux effets HAHA (*heavy-atom-on-heavy-atom*), pour lesquels des ions La^{3+} voisins dans des motifs La–O–La sont fortement couplés par l'intermédiaire de liaisons La–O à caractère covalent polaire.

- **^{35}Cl** : les déplacements chimiques calculés reproduisent exactement les tendances mesurées. Malgré la nature anionique du chlore, les prédictions sont globalement précises en raison du caractère essentiellement ionique des liaisons La–Cl. En conséquence, les orbitales moléculaires associées aux liaisons La–Cl sont moins sensibles aux effets dépendants de la température que celles impliquées dans les liaisons La–O. De plus, les ions La^{3+} voisins dans des motifs La–Cl–La sont plus faiblement couplés, ce qui les rend quasi indépendants du point de vue RMN.

Malgré ces limitations, les calculs RMN basés sur les premiers principes confirment sans ambiguïté les interprétations proposées précédemment. Dans les compositions riches en NaCl, l'ion O^{2-} se coordonne préférentiellement et de manière exclusive aux ions La^{3+}, conduisant à des environnements de type $[La_3O]^{7+}$ associés à des déplacements chimiques élevés (550–700 ppm). À l'inverse, dans les compositions riches en $MgCl_2$, des environnements de coordination mixtes tels que $[La_2MgO]^{6+}$ (400–550 ppm) et $[LaMg_2O]^{5+}$ (200–400 ppm) deviennent prédominants, entraînant une diminution progressive des déplacements chimiques globaux.

Enfin, le chapitre V-4 examine l'influence de la concentration en oxygène soluble sur les propriétés thermophysiques des sels fondus. Les calculs DM indiquent que la densité, le coefficient de dilatation thermique et la capacité thermique sont largement insensibles au rapport de composition $MgCl_2$/NaCl sur l'ensemble des concentrations en oxygène étudiées. En revanche, la viscosité présente une dépendance couplée à la fois à la concentration en oxygène dissous et à la composition du mélange fondu : les compositions riches en $MgCl_2$ atténuent les augmentations brusques de viscosité induites par l'accroissement de la teneur en oxygène soluble, en cohérence avec le rôle du $MgCl_2$ dans la perturbation du regroupement des espèces oxygénées.

Dans l'ensemble, le chapitre V établit une base mécanistique solide et cohérente permettant d'ajuster la composition des sels fondus chlorurés par l'ajout de $MgCl_2$ afin d'accroître la solubilité de l'oxygène et de limiter la précipitation d'oxydes. Ces résultats contribuent à la conception de combustibles de RSF à base de chlorures et présentent une pertinence qui dépasse le seul cadre des applications nucléaires.

Introduction

Modern MSR designs target operational lifetimes of at least 60 years [149]. Despite considerable progress in advancing their technological maturity and economic viability, the corrosive nature of molten salts remains a critical barrier to the widespread deployment of MSR technology. Efforts to extend reactor lifetimes have focused on several complementary strategies, including the development of corrosion-resistant structural alloys [150–153], investigations of the redox chemistry of fuel salts [154–156], the development of *in situ* monitoring techniques [157], and the refinement of salt purification methods [158–160]. Nevertheless, a broad scientific consensus has emerged that trace salt impurities—most notably H_2O and oxygen—are the main driving factor in accelerating the oxidation of alloying elements, thereby exacerbating corrosion and ultimately limiting reactor lifetimes [161,162].

Historically, ZrF_4 was used as an oxygen absorber during the pilot Molten Salt Reactor Experiment to control oxide contamination [18]. By analogy, $MgCl_2$ has been proposed as a component in chloride-based reactor fuels to sequester oxygen and limit the formation of insoluble oxide phases [15]. This approach is motivated by prior observations from magnesium electrowinning of magnesium metal, where the solubility of MgO in $NdCl_3$ melts is significantly enhanced in the presence of $MgCl_2$ [163]. This salient role of $MgCl_2$ in oxygen control comes in parallel to the numerous ancillary benefits, including lowering fuel melting temperatures [39,164], reducing viscosity (see Chapter IV), and contributing to redox potential control [156].

Despite these advantages, the precise mechanism of $MgCl_2$-mediated oxygen solubility remains insufficiently understood. Structural studies using X-ray diffraction and Raman spectroscopy suggested that the formation of $Mg_xNd_yOCl_{2x+3y-2}$ networks promotes oxygen solubility in liquid mixtures of $NdCl_3$–$MgCl_2$–MgO [165]. Bulk solubility measurements by EDTA volumetric analysis indicated that increasing $MgCl_2$ and $NdCl_3$ concentrations similarly improve MgO solubility, likely via the formation of soluble NdOCl [166]. Preliminary unpublished electrochemical data indicate slower oxide precipitation in lanthanide trichloride melts containing $MgCl_2$, consistent with the formation of soluble lanthanide oxychloride species [167]. Extending beyond chloride systems, studies on other molten fluorides containing transition metals or lanthanides likewise support the formation of complex oxyhalide species [138], such as $NbOF_5^{2-}$/$NbO_2F_4^{3-}$/$NbO_4F_2^{5-}$ [168], $TaOF_5^{2-}$/$TaOF_6^{3-}$/$TaO_2F_2^{-}$/$TaO_2F_3^{2-}$ [169], $NdOF_4^{3-}$/$NdOF_5^{4-}$/$Nd_2OF_8^{4-}$/$Nd_2OF_{10}^{6-}$ [170], $ZrOF_5^{3-}$/$HfOF_5^{3-}$ [171], $Lu_2OF_8^{4-}$/ $Lu_2O_2F_4^{2-}$/ $Lu_2O_2F_6^{4-}$ [172], and $LaO_xF_y^{3-x-y}$ [173].

In this chapter, direct molecular-level evidence is presented to elucidate the mechanism of $MgCl_2$-assisted oxygen solubility in chloride melts. To this end, HT NMR was employed to measure ^{17}O chemical shifts in molten NaCl–$MgCl_2$–$LaCl_3$ containing varying amounts of dissolved ^{17}O-enriched LaOCl. The pronounced and systematic variations in ^{17}O chemical shifts as a function of the $MgCl_2$-to-NaCl composition ratio directly reflect the diversification of oxygen coordination environments within the melts. Complementary MD simulations with the PIM and first-principles NMR calculations were performed to provide a robust theoretical framework for interpreting experimental observations. Collectively, these results establish a comprehensive mechanistic picture of $MgCl_2$-mediated oxygen solubility in molten, which informs the control of oxygen solubility through compositional design.

V-1. Synthesis and Characterisation of LaOCl

Oxygen solubility in chloride melts was investigated using the (80-α) NaCl–α $MgCl_2$–(20-x) $LaCl_3$–x LaOCl mixture (compositions given in mol%; α=*0–80*; x=*0–5*). This compositional framework models the substitution of two Cl^- ions by one O^{2-} ion in an idealised MSR fuel contamination scenario. To enable ^{17}O NMR measurements, LaOCl was enriched with 90 at% ^{17}O, ensuring that the oxygen signals originated from the intentionally added oxide species rather than from trace salt impurities. Here, LaOCl was selected over more conventional options such as La_2O_3 and MgO because it is more straightforward for isotope labeling, preserves the lanthanum stoichiometry, and has higher solubility in chloride melts [174,175].

LaOCl as a simulated contaminant most closely mimics inadequately purified actinide trichlorides ($AnCl_3$) in fresh MSR fuels, which typically present as partially hydrated ($AnCl_3 \cdot xH_2O$) or oxychloride (AnOCl) species. It also approximates unintended O_2 or H_2O ingress during MSR operation, where oxygen preferentially coordinates with actinide species in the melt. It is noted, however, that H_2O ingress scenarios involve HCl evolution from chloride hydrolysis—a well-established corrosion pathway[160]—which is not captured in the present contamination framework.

^{17}O-labelled LaOCl was synthesised by hydrating 1.0 g of fine $LaCl_3$ powder with an excess of 90 at% ^{17}O-enriched water in an argon-filled glove box. Hydration was performed gradually due to the extremely exothermic nature of the reaction. The resulting slurry was continuously mixed using a mortar and pestle to ensure homogeneity and complete conversion. Subsequently, the reaction product was transferred to an open-sided alumina crucible and dried in an argon-filled tube furnace at 650 °C overnight [176].

Powdered XRD was performed on the dried product under ambient conditions (**Figure V-1**). All measured peaks matched those of the reference PDF card (04-008-5087), with no detectable $LaCl_3$ or $LaCl_3 \cdot 6H_2O$ impurities, confirming that the synthesised LaOCl is phase-pure and stable.

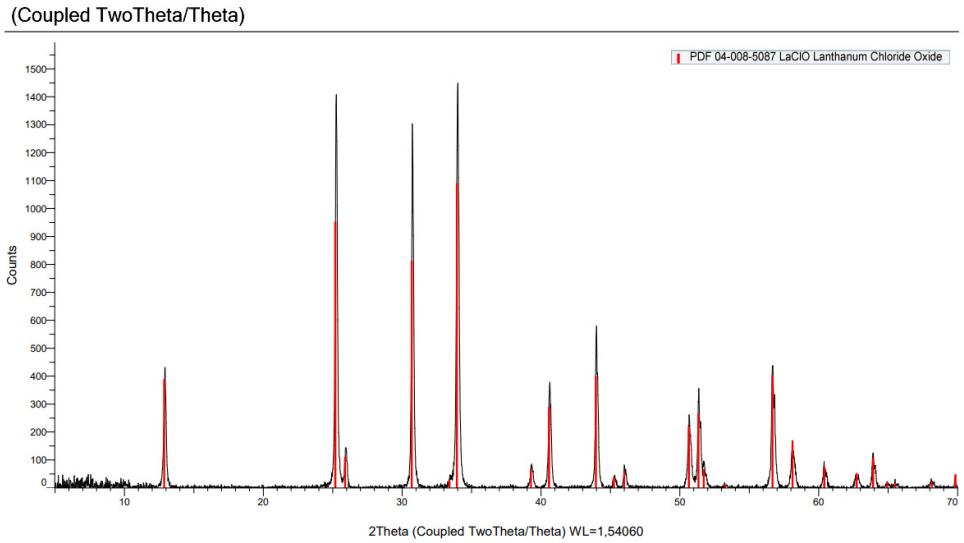

Figure V-1. Powdered XRD analysis of the synthesised LaOCl under ambient conditions.

The phase purity of the synthesised LaOCl was further evaluated using SS NMR spectroscopy (**Figure V-2**). The SS NMR spectra of the ^{139}La, ^{17}O, and ^{35}Cl nuclei were acquired under nucleus-specific experimental conditions. For ^{17}O and ^{35}Cl, the NMR spectra were collected at a spinning frequency of 14 kHz. Single-pulse excitation was used for ^{17}O due to its short transverse relaxation time (T_2), whereas a spin echo pulse sequence was employed for ^{35}Cl. In contrast, ^{139}La exhibits a large quadrupolar coupling, resulting in linewidths exceeding the maximum achievable MAS spinning frequency; consequently, all ^{139}La spectra were acquired under static conditions. To accommodate the extensive quadrupolar broadening, the VOCS technique [97] was used to combine multiple subspectra recorded at different transmitter offsets into a single continuous spectrum spanning a wide frequency range. A spin echo pulse sequence was applied for ^{139}La, enabled by its sufficiently long T_2 relaxation time.

All spectra exhibit well-defined resonances consistent with single crystallographic sites, indicating the absence of residual precursor phases. In addition, the experimentally determined electric field gradient parameters (C_Q and η) are in good agreement with those calculated using the VASP code (**Table V-1**), indicating that the crystallographic geometry corresponds well with that in the reference LaOCl structure [177]. By contrast, a noticeable discrepancy is observed between the measured and calculated isotropic chemical shifts (δ_{iso}), an issue that is addressed in Chapter V-3.2.

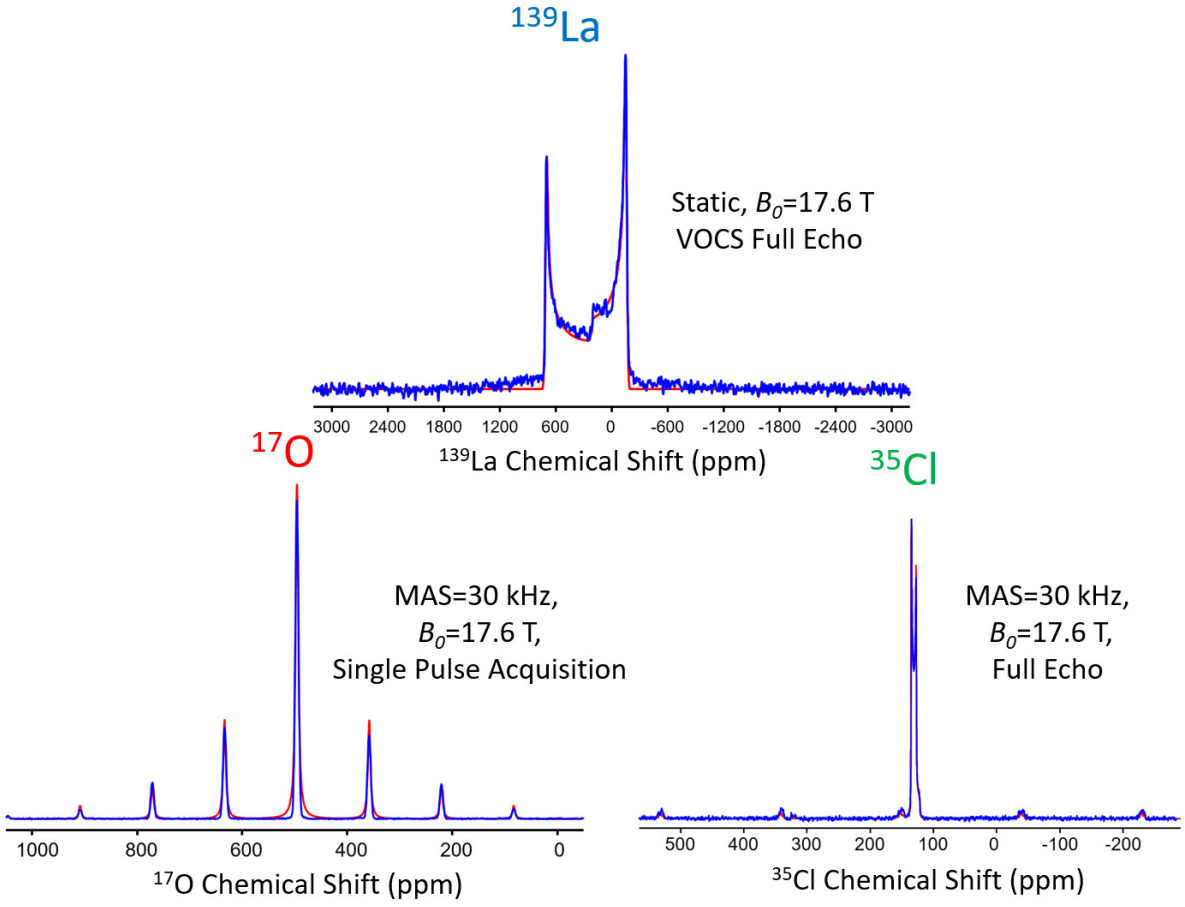

Figure V-2. Solid-state NMR spectra of synthesised LaOCl for the ^{139}La, ^{17}O, and ^{35}Cl nuclei. Measured spectra are given in blue and fitted spectra are given in red.

Table V-1. Comparison of SS NMR parameters of LaOCl from line fitting (± spectral fitting uncertainty) and DFT calculations

Nucleus	Method	Isotropic chemical shift, δ_{iso} (ppm)	Quadrupolar coupling, C_Q (MHz)	Assymetry parameter, η
^{139}La	DFT (VASP)	295	27.4	0.00
	SS NMR	395 ± 1	27.3 ± 0.1	0.00
^{17}O	DFT (VASP)	475	0.011	0.00
	SS NMR	497 ± 1	0.165 ± 0.002	0.02
^{35}Cl	DFT (VASP)	138	0.796	0.00
	SS NMR	137 ± 1	1.176 ± 0.001	0.04

V-2. Oxygen Dynamics in Molten Chlorides: A Molecular Dynamics Perspective

The behaviour of oxygen in chloride melts was first examined through the lens of its local coordination environments in the NaCl–$MgCl_2$–$LaCl_3$–LaOCl system. **Figure V-3** compares the MD snapshots of the 80 NaCl–15 $LaCl_3$–5 LaOCl and the 80 $MgCl_2$–15 $LaCl_3$–5 LaOCl systems at 850 °C. In the NaCl-based system, oxygen atoms are observed to cluster around lanthanum. By contrast, in the $MgCl_2$-based system, they appear more evenly distributed in the matrix. Analysis of the O–La polymer chain lengths (**Table V-2**) confirms this trend: NaCl-rich melts favour longer O–La chains; whereas, $MgCl_2$-rich melts prefer shorter O–La chains. These results suggest that Mg^{2+} disrupts O–La clustering by promoting a mixture of O–Mg and O–La coordination environments in the melt. Thermodynamically, these insights are also consistent with the unfavourable O–Na and favourable O–Mg/O–La interactions shown in **Figure V-4**, which promote a multiplicity of coordination motifs in the latter system.

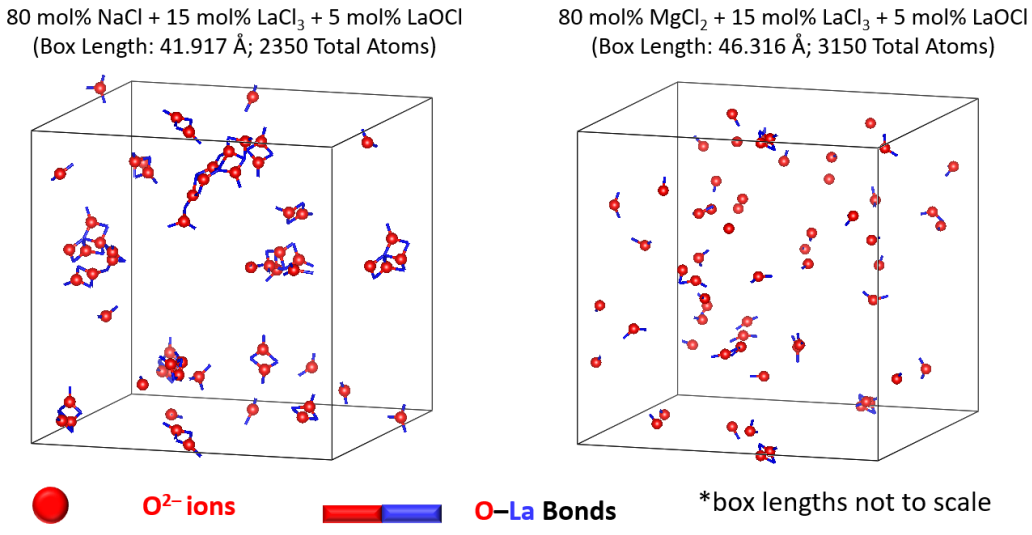

Figure V-3. Visualisation of O–La bond distribution inside a simulation cell of 80 NaCl–15 $LaCl_3$–5 LaOCl and 80 $MgCl_2$–15 $LaCl_3$–5 LaOCl (both in mol%) at 850 °C. The La–O bond length cutoff is set at 3.38 Å to reflect the first coordination sphere of oxygen. For better visibility of the O–La clustering behaviour, only O^{2-} ions and O–La bonds are shown; all other ions and bonds are omitted.

Table V-2. Percentage of O^{2-} ions in O–La polymers of chain length n for different molten salt compositions at 850 °C.

Molten Salt Mixture (in mol%)	Percentage of O^{2-} ions in $-(O-La)_n-$ polymer (%)			
	n=1	*n=2*	*n=3*	*n>4*
80 NaCl–15 $LaCl_3$–5 LaOCl	17.4	46.0	10.6	26.0
64 NaCl–16 $MgCl_2$–15 $LaCl_3$–5 LaOCl	46.4	39.5	9.21	4.91
40 NaCl–40 $MgCl_2$–15 $LaCl_3$–5 LaOCl	59.3	35.6	2.52	2.60
16 NaCl–64 $MgCl_2$–15 $LaCl_3$–5 LaOCl	71.2	25.0	2.78	0.99
80 $MgCl_2$–15 $LaCl_3$–5 LaOCl	78.8	20.4	0.85	0.00

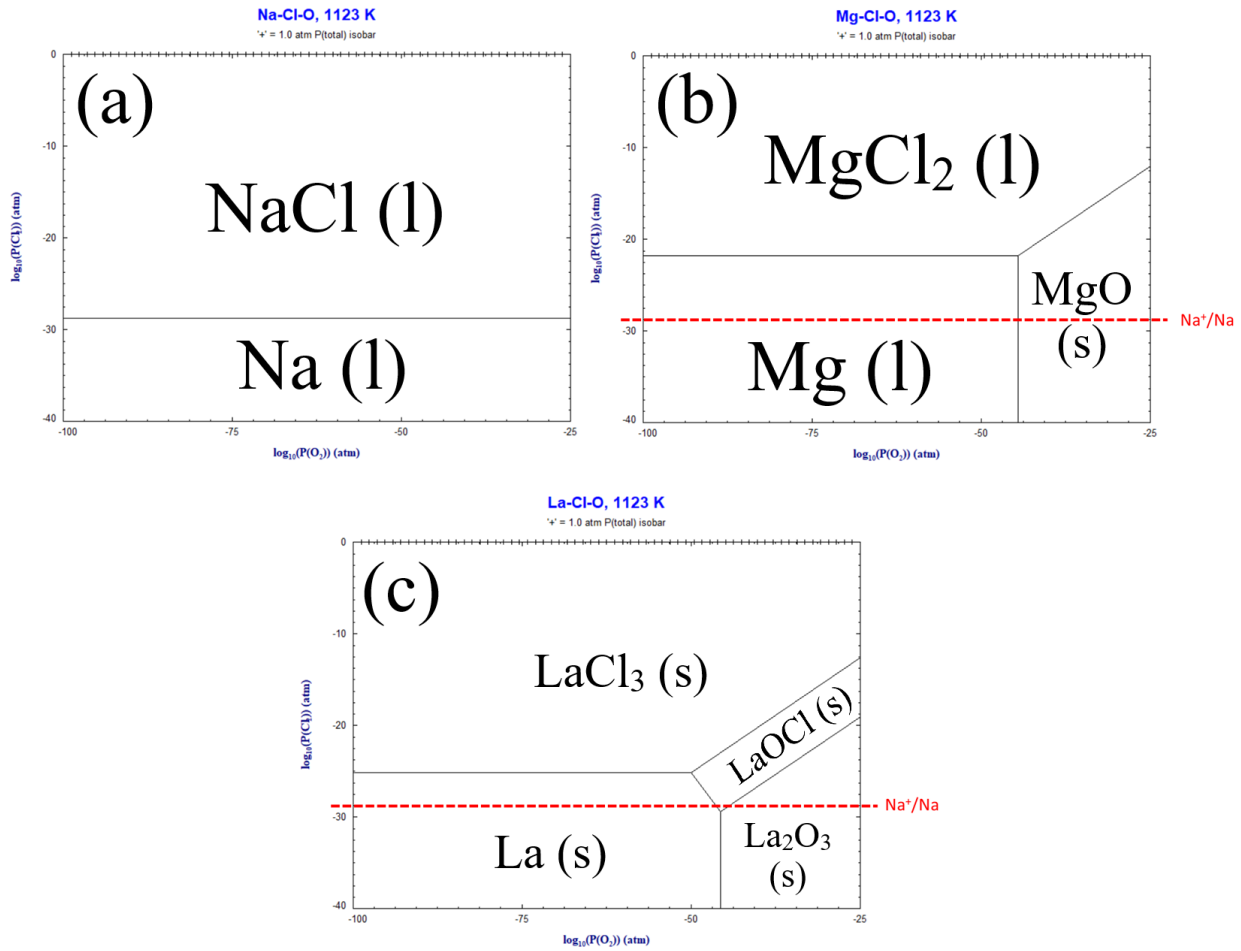

Figure V-4. Thermodynamic stability diagrams at 850 °C for (a) Na–Cl–O, (b) Mg–Cl–O, and (c) La–Cl–O as functions of $p(Cl_2)$ and $p(O_2)$, generated using the FactPS database on FactSage [109]. Axis ranges were chosen to match those used in thermodynamic stability diagrams reported in the reference [156].

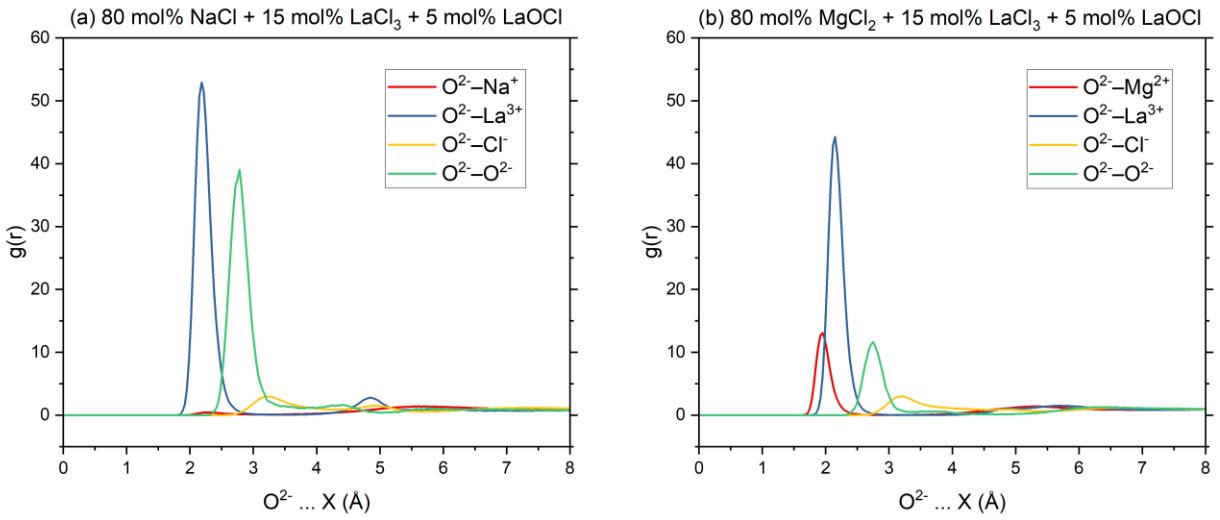

Figure V-5. RDFs of O^{2-} with its neighbouring ions for (a) 80 NaCl–15 $LaCl_3$–5 LaOCl and (b) 80 $MgCl_2$–15 $LaCl_3$–5 LaOCl at 850°C.

To better quantify these coordination trends, RDF analysis of O^{2-} and its neighbouring ions was performed. **Figure V-5** compares the RDF for the same two systems as in **Figure V-3**. The O–Na peak is nearly absent compared to the O–Mg peak, confirming the thermodynamically unfavourable nature of the O–Na interaction. Additionally, the stronger O–O correlation in the NaCl-based system corroborates the oxygen clustering around La^{3+} observed in **Figure V-3**.

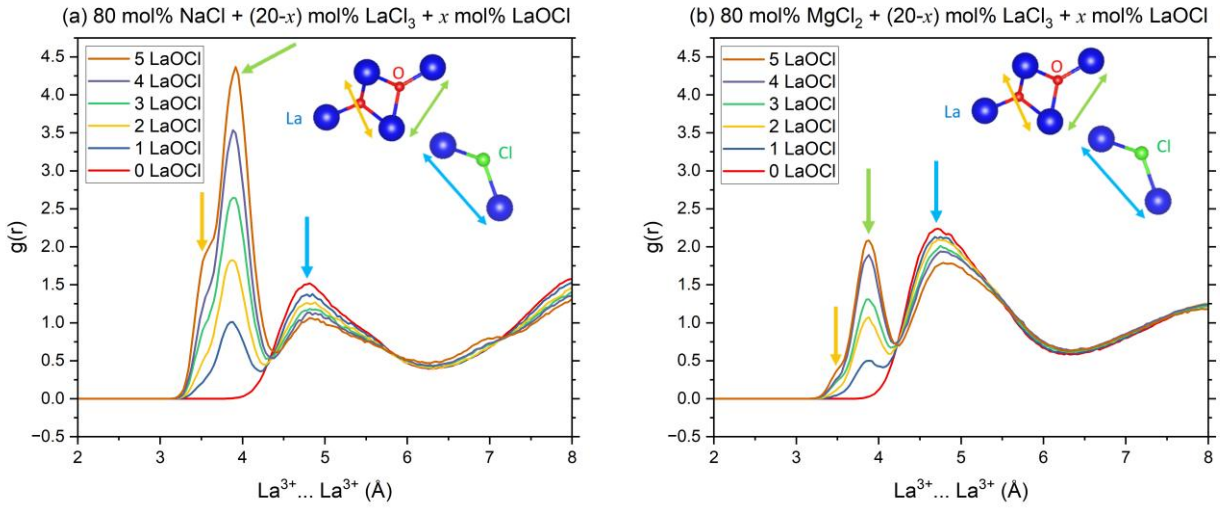

Figure V-6. La^{3+}–La^{3+} RDFs for (a) 80 NaCl–(20-x) $LaCl_3$–x LaOCl and (b) 80 $MgCl_2$–(20-x) $LaCl_3$–x LaOCl (x=0–5) at 850°C. Arrows mark characteristic La spacings corresponding to La–Cl–La (blue), La–O–La (green), and double oxygen-bridged La (orange) linkages.

To further assess clustering, the La^{3+}–La^{3+} RDFs for NaCl–(20-*x*) $LaCl_3$–*x* LaOCl and $MgCl_2$–(20-*x*) $LaCl_3$–*x* LaOCl systems (*x=0–5*) were compared (**Figure V-6**). Here, three characteristic peaks emerge: (i) the broad peak at 4.8 Å from La–Cl–La linkages, which has been well characterised in the case of pure molten chlorides [128], (ii) a sharp peak at 3.9 Å corresponding to La^{3+} ions bridged by a single O^{2-} ion, and (iii) a shoulder peak at 3.5 Å associated with multiple O^{2-} bridges. A quasi-isosbestic point at approximately 4.4 Å separates peak (i) from peaks (ii) and (iii). With increasing LaOCl concentration, peaks (ii) and (iii) intensify at the expense of peak (i) in both systems. Nonetheless, the magnitudes of peaks (ii) and (iii) are significantly diminished in the $MgCl_2$-based system, evidencing a marked reduction in La–O clustering.

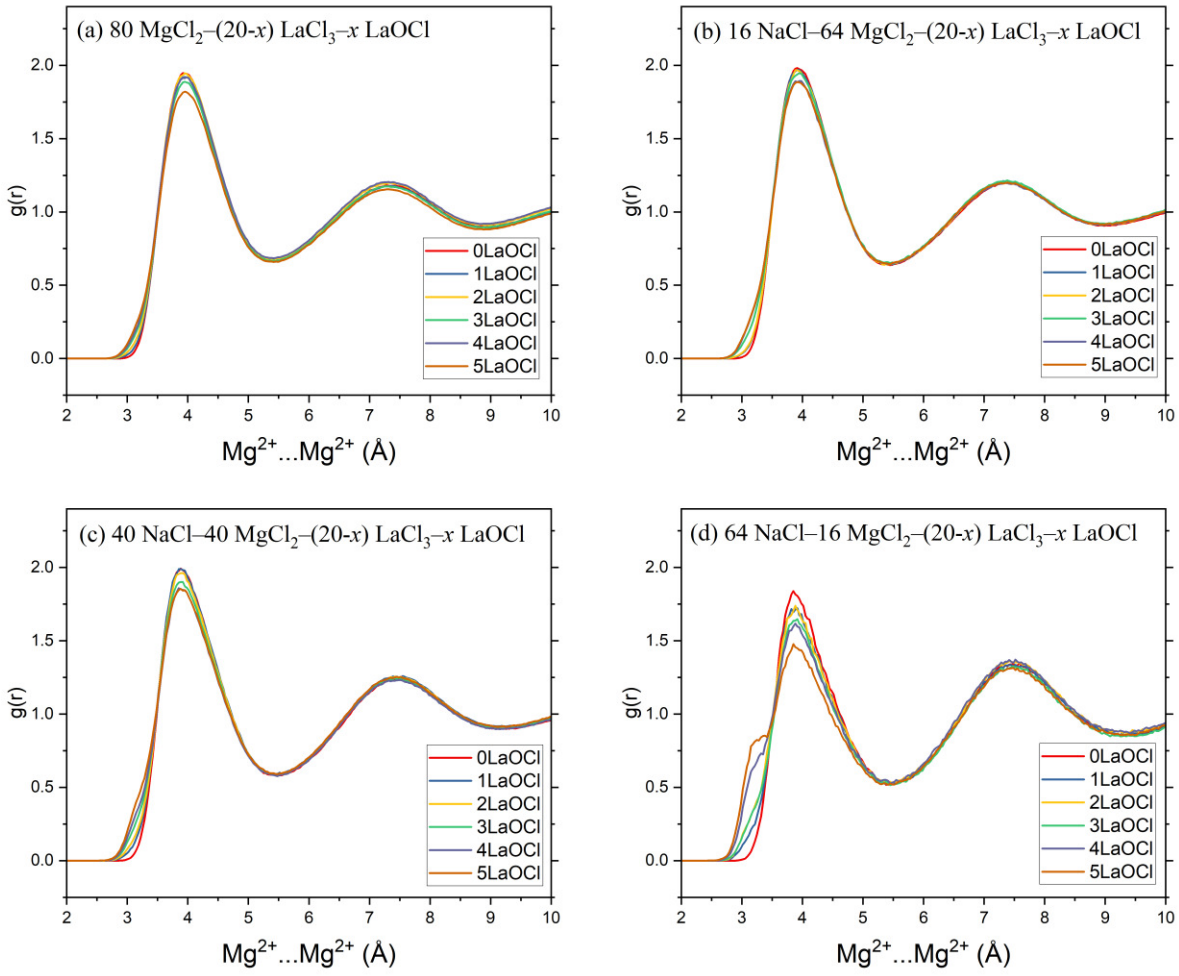

Figure V-7. Mg^{2+}–Mg^{2+} RDFs for (80-α) NaCl– α $MgCl_2$ –(20-x) $LaCl_3$–x LaOCl (in mol%; α=16–80; x= 0–5) at 850 °C.

The role of $MgCl_2$ in mitigating La–O clustering is further supported by Mg^{2+}–Mg^{2+} RDFs of (80-α) NaCl–α $MgCl_2$–(20-x) $LaCl_3$–x LaOCl (α=*16–80*; x=*0–5*). The RDFs, shown in **Figure V-7**, exhibit two major humps at 4.0 and 7.3 Å, characteristic of the Mg–Mg spacings in Mg–Cl–Mg–Cl–Mg [178]. Additional shoulders appearing at ~3.3 Å correspond to Mg–O–Mg linkages. The intensity of these shoulders increases with: (1) higher LaOCl concentration and (2) lower $MgCl_2$ content, highlighting the role of Mg^{2+} in binding and evenly dispersing O^{2-} ions within the molten salt matrix. In practical MSR settings, this suggests that $MgCl_2$ may enhance the solubility of oxide species in chloride fuels by mitigating the clustering and subsequent precipitation of actinide-rich oxide phases. Effectively, this $MgCl_2$-assisted mechanism curbs a prominent pathway for oxide deposition, thereby lowering the risk of deposit-induced corrosion of MSR structural surfaces.

V-3. Oxygen Speciation in Molten Chlorides: An NMR Perspective

Based on the MD analysis of O–Na and O–Mg coordination preferences, it is possible to predict the expected ^{17}O NMR chemical shifts in our molten salt systems. Solid-state ^{17}O NMR of the corresponding oxides provides useful benchmarks: La_2O_3 (*P3m1* symmetry) has two oxygen sites, with reported chemical shifts of 469 and 590 ppm [119]; Na_2O [179] and MgO [180] only have a single oxygen site each, with first-principles VASP calculations predicting chemical shifts of 11.8 and 24.2 ppm, respectively (**Figure II-11b**). The much larger chemical shifts in La_2O_3 indicate that oxygen bound exclusively to La^{3+} will produce high ^{17}O chemical shifts. Therefore, in NaCl–$LaCl_3$ melts, since oxygen coordinates only with La^{3+}, large chemical shifts are expected. By gradually replacing NaCl with $MgCl_2$, oxygen increasingly interacts with Mg^{2+} as well as La^{3+}, and the corresponding ^{17}O chemical shifts are projected to decrease accordingly. In this sub-chapter, HT NMR experiments and first-principles NMR calculations are carried out to verify these predictions.

V-3.1. HT NMR Experiments

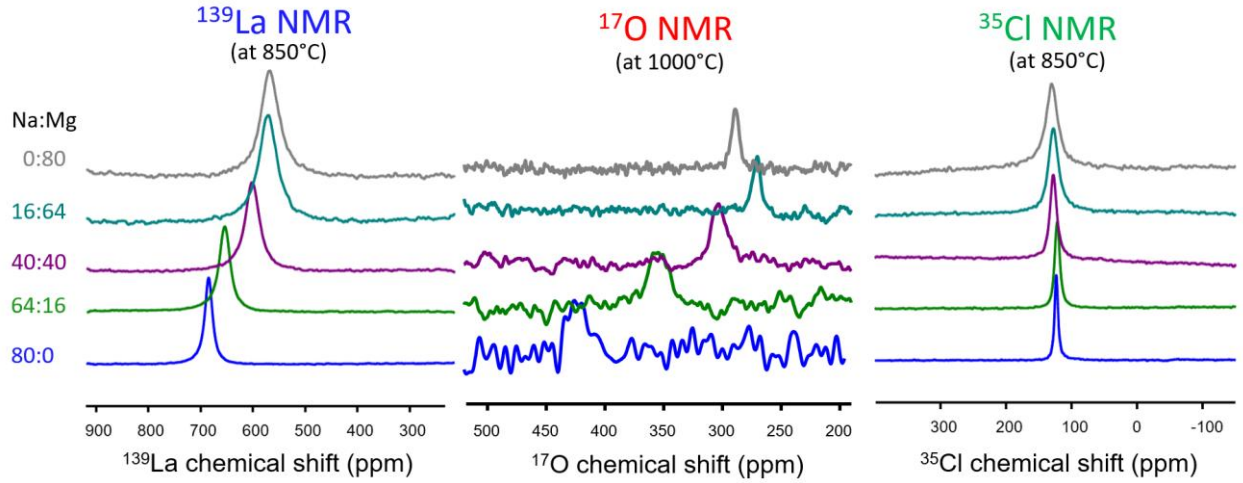

Figure V-8. Measured ^{139}La, ^{17}O, and ^{35}Cl NMR spectra of the (80-α) NaCl–α $MgCl_2$–15 $LaCl_3$–5 LaOCl (α=0–80) system. ^{139}La and ^{35}Cl spectra were acquired at 850 °C ; ^{17}O spectra were collected at 1000 °C to enhance signal quality.

Figure V-8 shows ^{139}La, ^{17}O, and ^{35}Cl NMR spectra measured on the molten (80-α) NaCl–α $MgCl_2$–15 $LaCl_3$–5 LaOCl (α=*0–80)* system. In these measurements, ^{17}O NMR provides direct insight into the oxygen coordination environment, whereas the ^{139}La and ^{35}Cl spectra serve as internal benchmarks for comparisons with VASP calculations discussed later. While ^{139}La and ^{35}Cl NMR measurements at 850 °C yielded strong, low-noise resonances with sharp peaks, ^{17}O NMR measurements needed to be performed at 1000 °C to increase ion mobility and obtain measurable signals. Attempts to measure ^{17}O NMR at 850 °C for the 80 NaCl–15 $LaCl_3$–5 LaOCl and 64 NaCl–16 $MgCl_2$–15 $LaCl_3$–5 LaOCl systems produced no detectable signal. Despite elevated temperatures and extended acquisition times, the ^{17}O NMR signals remained comparatively weak, broadened, and exhibited noisy baselines.

The origins of these artefacts were investigated using a combination of complementary techniques:

- *Differential scanning calorimetry (DSC)*. DSC was performed on the theoretically least soluble 80 NaCl–15 $LaCl_3$–5 LaOCl composition using a SETARAM Ligne 96 DSC device. The sample was loaded into a tightly screwed BN crucible, heated at 5 °C/min up to 1500 °C, and subsequently cooled at the same rate to room temperature under an inert argon atmosphere. The results are shown in **Figure V-9**, where signals between 1000 and 1500 °C were omitted due to excessive thermal noise. The first endothermic onset at 531 °C corresponds to the solidus temperature of the 80 NaCl–15 $LaCl_3$–5 LaOCl system, slightly lower than the solidus temperature of 80 NaCl–20 $LaCl_3$ (544 °C), predicted using the FTSalt database on FactSage [109]. This depression likely arises from the additional configurational entropy introduced by the oxygen in the mixture. The second endothermic onset at 626 °C marks the beginning of the melting of the remaining solid phases (most likely NaCl and LaOCl). The endset at 756 °C is taken as the liquidus temperature, beyond which all solids are dissolved in the melt. This assignment is supported by the onset of the exothermic peaks in the cooling curve at 729 °C, which reflects a slightly supercooled crystallisation. Notably, the liquidus temperature of 80 NaCl–15 $LaCl_3$–5 LaOCl is substantially higher than the calculated liquidus temperature of 80 NaCl–20 $LaCl_3$ at 654 °C, consistent with the strong La–O bonds raising the melting enthalpy threshold.

- *Thermogravimetric–differential thermal analysis (TG–DTA)*. TG–DTA was performed on the 80 NaCl–15 $LaCl_3$–5 LaOCl composition using a NETZSCH STA 449 F3 Jupiter. The sample was loaded into an open Pt–Ir crucible and heated under flowing argon at 5 °C/min up to 770 °C, held isothermally for 10 minutes, and subsequently cooled at the same rate to room temperature. The TG–DTA heating curve (**Figure V-10**) is in close agreement with the DSC heating result. The initial strong and sharp peak at 544 °C is attributed to the eutectic melting of NaCl–$LaCl_3$ subsystem, while the broader peak terminating at 755 °C corresponds to the liquidus transition of the 80 NaCl–15 $LaCl_3$–5 LaOCl. In contrast, the cooling behaviour observed in TG–DTA differs significantly from that recorded in DSC. Upon cooling, two weak thermal events are observed: a broad peak at 734 °C and a sharp peak at 672 °C. Subsequently, the strong, sharp peak reappears at a slightly supercooled temperature of 525 °C in TG–DTA, corresponding to eutectic freezing. Notably, this eutectic freezing is absent in the DSC cooling curves. This discrepancy is attributed to substantial and irreversible salt volatilisation during the DSC measurements, which involved heating up to 1500 °C, resulting in a modified melt composition upon cooling.

The complementary TG signal substantiates this interpretation. Upon initial heating up to 200 °C, a mass loss of about 2 wt% is observed, attributed to the release of adsorbed and residual moisture. The salt mass remains relatively stable up to the liquidus transition temperature. Above this point, a continuous mass loss is detected, amounting to an additional 4.5 wt%. This mass loss is attributed to the volatilisation and vapour-phase transport of chloride species, as evidenced by the severe contamination of the Pt–Ir crucible outer surfaces with white condensate following the measurements. Moreover, the rate of mass loss increases with active cooling, suggesting that enhanced temperature gradients promote convective and condensative transport of volatilised salt species. Notably, the mass loss stops shortly after the eutectic freezing temperature at 525 °C, consistent with the suppression of vapour transport once the melt fully solidifies. In our DSC measurements, heating to and cooling from 1500 °C most likely caused significant irreversible volatilisation of chloride components from the sealed BN crucibles, thereby eliminating the eutectic freezing signal upon cooling. These observations and inferences are consistent with those in previous TG analysis of LaOCl-containing xerogels [181].

- *Ex-situ XRD*. Ex-situ powdered XRD was performed on a modified composition in which LaOCl was intentionally replaced by La_2O_3 (i.e., 80 NaCl–15 $LaCl_3$–5 La_2O_3). This experiment was designed to directly test whether La_2O_3 persists or converts to LaOCl under conditions comparable to those used for LaOCl-containing samples. The La_2O_3-containing mixture was treated under identical conditions as the LaOCl-containing mixture: homogenised in an argon-filled glove box, tightly sealed in high-purity BN crucibles, irradiated for 30 minutes at 1000 °C in the HT NMR platform, and rapidly cooled to ambient temperature by switching off the lasers. The powdered XRD analysis of the mixture before and after irradiation (**Figure V-11**) clearly shows that all La_2O_3 has been converted to LaOCl after irradiation, evidencing the thermodynamic stability of LaOCl in the chloride melt.

Taken together, the combined DSC, TG–DTA, and XRD analyses explain the peak broadening phenomena observed in the ^{17}O NMR spectra of LaOCl-containing molten salt mixtures. 5 mol% of LaOCl dissolves completely by 770 °C, even in the theoretically least soluble composition of 80 NaCl–15 $LaCl_3$–5 LaOCl. Moreover, LaOCl does not dissociate into insoluble La_2O_3 in the chloride melt at any given point. However, higher temperatures (1000 °C) and extended acquisition times (~30 mins) are required to compensate for the low concentration and sensitivity of ^{17}O, promoting volatilisation of chloride species during data acquisition. The resulting time-dependent change in melt composition leads to gradual shifts in the position of the ^{17}O signal, manifesting as peak broadening in the accumulated spectra. This artefact is not observed in ^{35}Cl or ^{139}La spectra, as adequate signal-to-noise ratios can be achieved within shorter acquisition times (<5 mins) at 850 °C. To mitigate peak broadening while maintaining sufficient signal quality, ^{17}O HT NMR measurements were therefore limited to acquisition times below 30 minutes.

Despite these challenges, clear trends can still be observed from **Figure V-8**: the ^{17}O chemical shifts progressively decrease with increasing $MgCl_2$ concentration up to a 1:1 NaCl-to-$MgCl_2$ ratio, after which no more systematic decrease is observed. Moreover, ^{17}O resonances are visibly sharper at higher $MgCl_2$ content. This behaviour arises because a good signal quality can be achieved within comparatively short acquisition times (~10 min) in these $MgCl_2$-

rich compositions, limiting chloride volatilisation. These observations also provide qualitative evidence for enhanced oxygen solubility in the presence of $MgCl_2$.

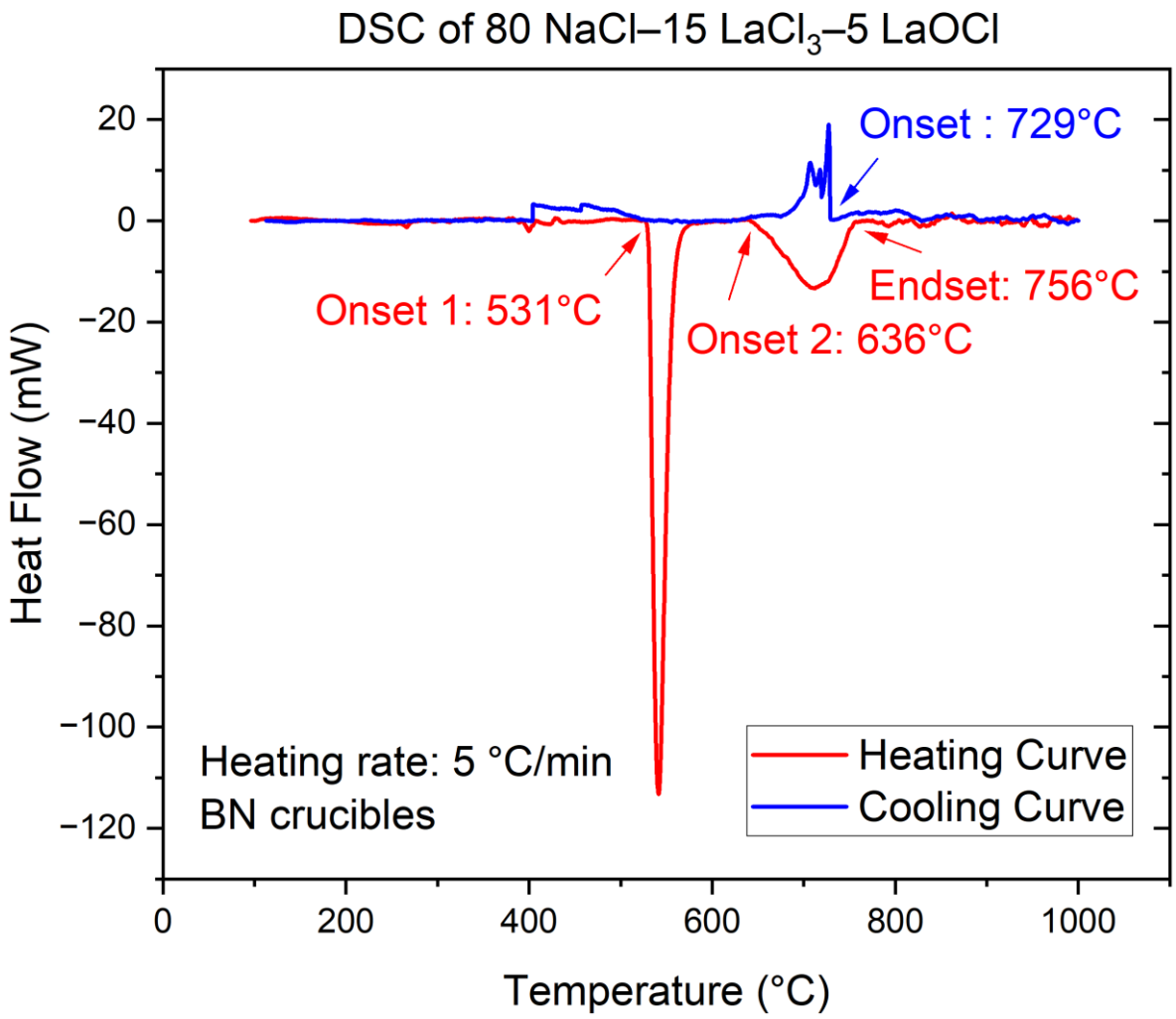

Figure V-9. DSC heating and cooling curves of 80 mol% NaCl–15 mol% $LaCl_3$–5 mol% LaOCl.

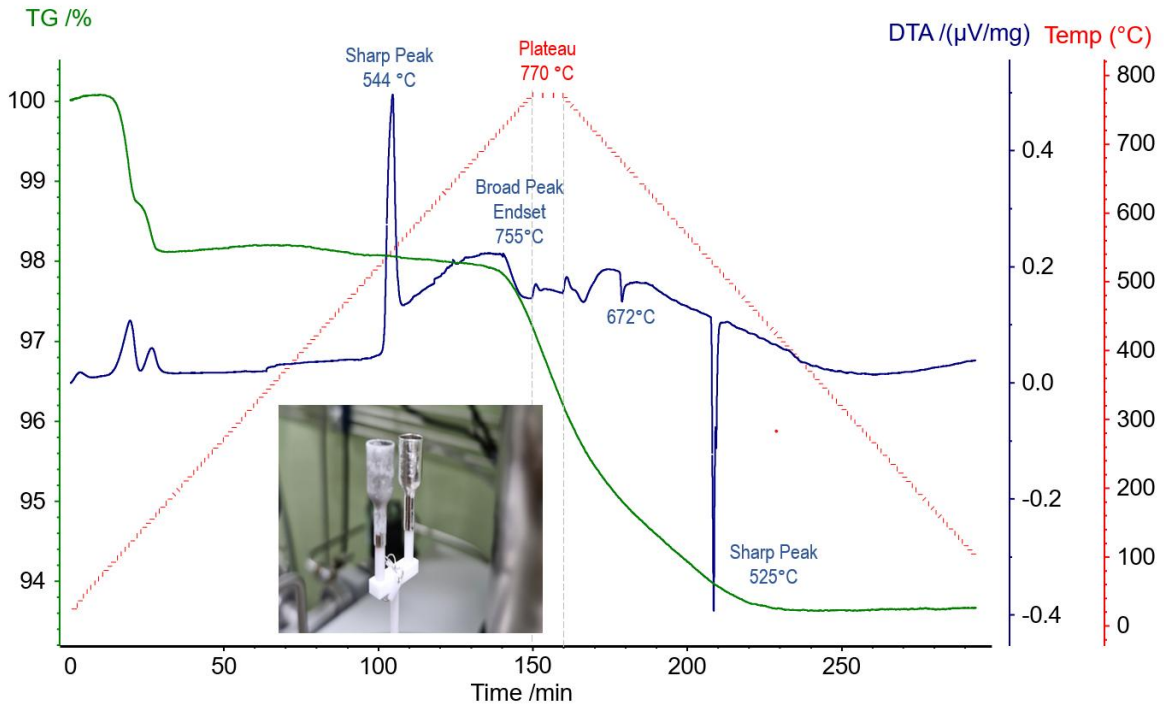

Figure V-10. TG–DTA of the 80 mol% NaCl–15 mol% $LaCl_3$–5 mol% LaOCl molten salt composition. The green solid line corresponds to the TG curve, the blue solid line corresponds to the DTA curve, and the red line indicates the sample temperature. An image of the Pt–Ir crucible surfaces contaminated by white condensate after measurements is included.

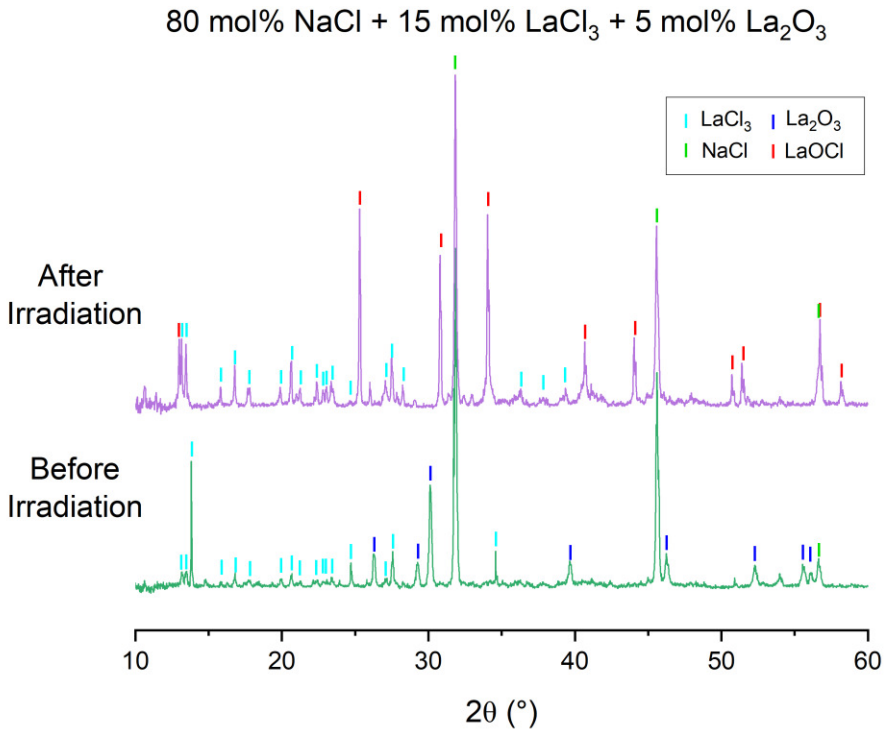

Figure V-11. XRD spectra of the 80 NaCl–15 $LaCl_3$–5 La_2O_3 mixture before and after 30-minute laser irradiation at 1000 °C.

V-3.2. First-Principles NMR Calculations

First-principles NMR calculations were performed using the VASP DFT code to corroborate the agreement between MD-generated structures and HT NMR experiments. Similar to the calculations conducted in Chapter III-4, the isotropic chemical shifts of individual atoms in regular-interval MD snapshots were calculated, and ensemble averages were used to predict ^{139}La, ^{17}O, and ^{35}Cl chemical shifts in each of the studied compositions.

Figure V-12 compares the simulated values with experimental NMR measurements. ^{17}O NMR signals for 80 NaCl–18 $LaCl_3$–2 LaOCl and 80 NaCl–19 $LaCl_3$–1 LaOCl systems could not be resolved experimentally and are therefore omitted. Both the experiment and simulation show the same overall trend: ^{17}O chemical shifts decrease with increasing $MgCl_2$ content, consistent with the MD analysis, which shows that Mg^{2+} mitigates exclusive O–La coordination by diversifying the local oxygen coordination environment. Beyond a 1:1 $MgCl_2$-to-NaCl ratio, the measured and simulated chemical shifts level off and fluctuate. One possible reason is that, under these conditions, the O^{2-} coordination sphere becomes saturated with Mg^{2+}, consequently, and the large number of accessible coordination permutations averages out without producing further systematic changes in ^{17}O chemical shifts.

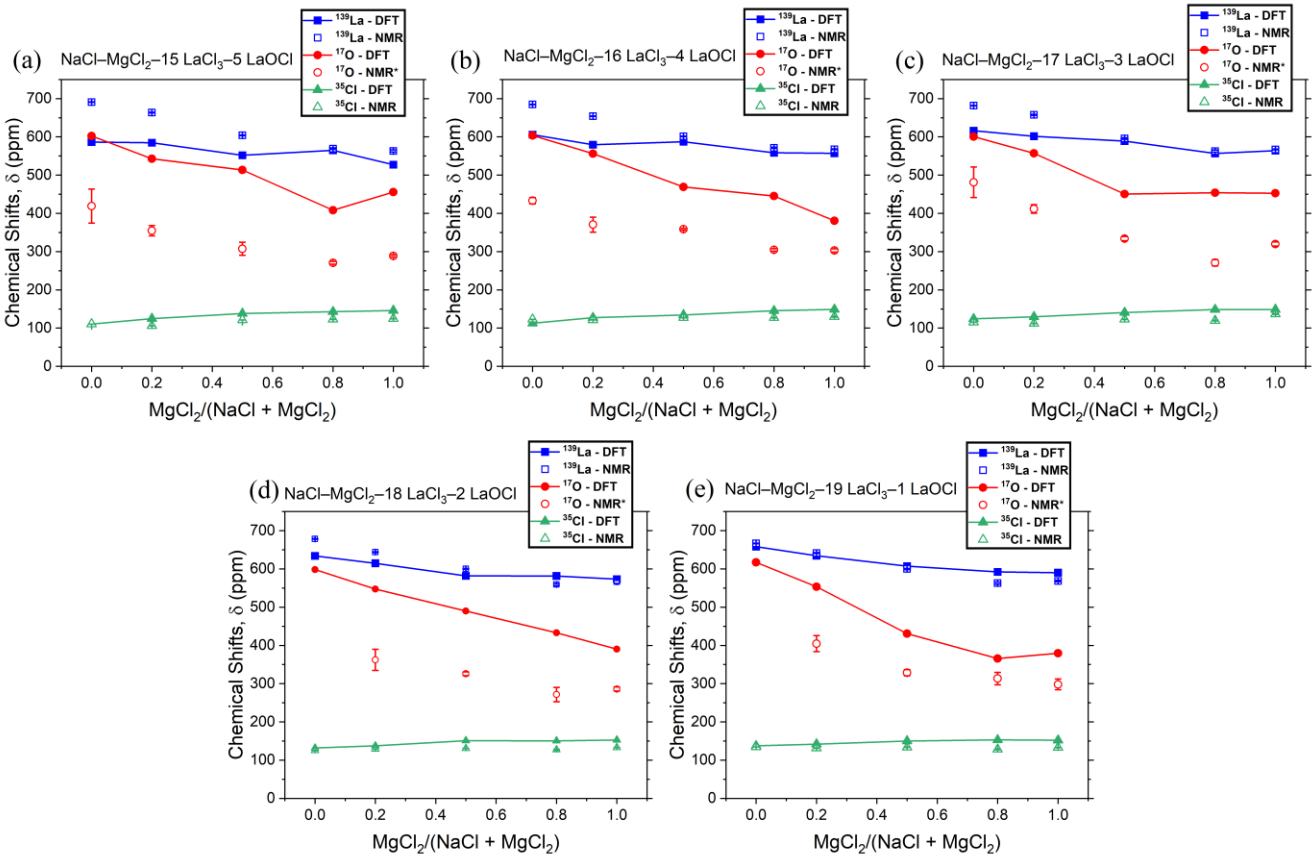

Figure V-12. Comparisons between NMR-measured and DFT-calculated chemical shifts for all studied compositions. DFT calculations were performed on MD snapshots at 850 °C; ^{139}La and ^{35}Cl NMR were measured at 850 °C, while ^{17}O NMR was measured at 1000 °C. No measurable ^{17}O NMR signal was obtained for the compositions of 80 NaCl–18 $LaCl_3$–2 LaOCl and 80 NaCl–19 $LaCl_3$–1 LaOCl. Error bars in NMR measurements correspond to the one-sigma uncertainties from spectral fitting. All measured and calculated values are provided in Annexe-B.

Nonetheless, VASP–NMR calculations systematically overpredict experimental ^{17}O chemical shifts by ~150 ppm. This offset is attributed to two factors. First, the limited treatment of finite-temperature effects in the simulations. Although DFT shieldings were averaged over an ensemble of MD snapshots, these static electronic-structure calculations of frozen snapshots only partially account for thermal motion and structural disorder via configurational diversity. They cannot fully reproduce other finite-temperature effects, such as anharmonic vibrations [182] and dielectric screening [183].

While there is also a nominal temperature mismatch between the ^{17}O NMR measurements at 1000 °C and the calculations performed at 850 °C, repeating the simulations at 1000 °C showed very limited difference in the predicted shifts and local structure. For example, **Table V-3** shows no clear trend in the predicted shifts with temperature. Instead, the main effect of temperature was a broader distribution of the predicted shifts, associated with the increased configurational variability at elevated temperatures. Correspondingly, the predicted ^{17}O chemical shifts also exhibited larger statistical fluctuations. Further analysis on the polymer chain length distributions (**Figure V-13**) and oxygen-neighbour RDFs (**Figure V-14**) revealed no marked structural changes, except for a modest shortening of the $–(O–La)_n–$ chains in 80 NaCl–15 $LaCl_3$–5 LaOCl.

Second, the electronic structure model itself is limited. Even though a Hubbard shift of +6 eV was added to La-4*f* states to fit the ^{17}O and ^{35}Cl chemical shifts of La_2O_3 and $LaCl_3$ to calibration data (**Figure II-11**), the calibration was derived from crystalline phases and does not capture the enhanced bond delocalisation and anharmonic vibrations of La–O at elevated temperatures [184] and in the molten state. Taken together, these omissions leave the computed shifts too high, which manifests as a large systematic offset. Notwithstanding, the agreement between the trends in calculated and measured chemical shifts validates the role of Mg^{2+} as an additional oxygen coordination site to La^{3+}.

Table V-3. Predicted ^{17}O chemical shifts of (80-α) NaCl–α $MgCl_2$–15 $LaCl_3$–5 LaOCl (α=0–80) at 850 and 1000 °C, alongside their measured shifts at 1000 °C.

Composition (mol%)	Predicted ^{17}O Chemical Shifts ± Standard Deviation (ppm)		Measured ^{17}O Shifts ± Fitting Uncertainty (ppm)
	850 °C	1000 °C	1000 °C
80 NaCl–15 $LaCl_3$–5 LaOCl	603 ± 27	615 ± 34	419 ± 45
64 NaCl–16 $MgCl_2$–15 $LaCl_3$–5 LaOCl	543 ± 93	506 ± 113	315 ± 14
40 NaCl–40 $MgCl_2$–15 $LaCl_3$–5 LaOCl	513 ± 110	421 ± 153	307 ± 18
16 NaCl–64 $MgCl_2$–15 $LaCl_3$–5 LaOCl	408 ± 155	445 ± 150	291 ± 4
80 $MgCl_2$–15 $LaCl_3$–5 LaOCl	446 ± 144	421 ± 160	289 ± 3

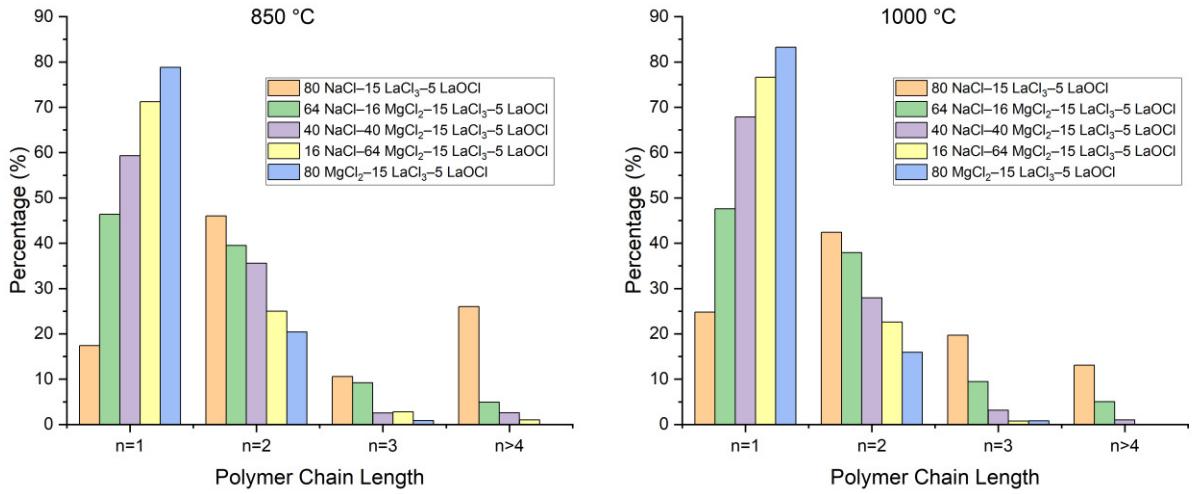

Figure V-13. Distribution of O–La polymer chain lengths of NaCl–$MgCl_2$–15 $LaCl_3$–5 LaOCl at 850 and 1000 °C.

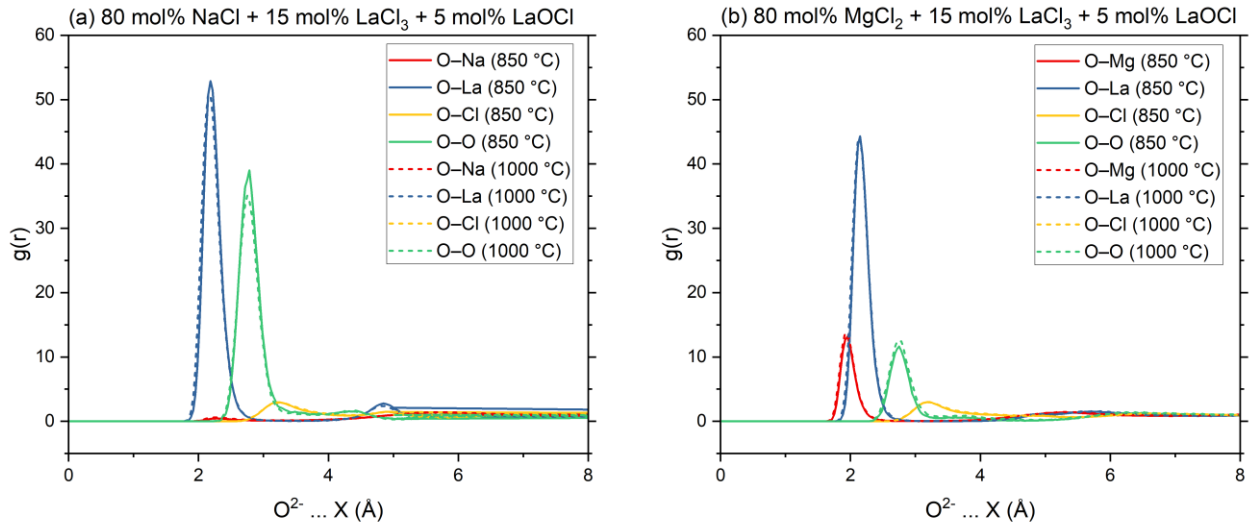

Figure V-14. RDFs of O^{2-} with its neighbouring ions for 80 NaCl–15 $LaCl_3$–5 LaOCl (left) and 80 $MgCl_2$–15 $LaCl_3$–5 LaOCl (right) at 850 °C (solid lines) and 1000 °C (dashed lines).

Since La^{3+} is a primary neighbour of O^{2-}, ^{139}La NMR can also probe oxygen coordination environments. As shown in **Figure V-12**, both calculated and experimental ^{139}La chemical shifts decrease with $MgCl_2$ content. However, because oxide species only constitute a minority of the anionic neighbours of La^{3+}, this decreasing trend primarily reflects changes in La–Cl coordination number when NaCl is substituted with $MgCl_2$ (see Chapter III). Moreover, the calculated ^{139}La chemical shifts are systematically underpredicted for NaCl-rich compositions but show improved agreement with experimental values in $MgCl_2$-rich compositions. This behaviour is attributed to the limited ability of the standard PBE exchange-correlation functional [116] in describing the delocalised electronic structure of La–O bonds. As shown in **Figure II-11**, the calculated La_2O_3 reference point deviates markedly from the calibration curve even with a Hubbard shift of +6 eV on La-4*f* orbitals, indicating a severe underestimation of the ^{139}La shift in La_2O_3. In contrast, the deviation for $LaCl_3$ is substantially smaller. This discrepancy originates from the fundamentally different bonding characters of La–O–La and La–Cl–La linkages, which give rise to contrasting heavy-atom-on-heavy-atom (HAHA) effects on the calculated ^{139}La shielding. In La–Cl–La environments, ^{139}La nuclei behave as electronically isolated, closed-shell heavy atoms with large HOMO–LUMO gaps [185], such that their shielding is dominated by ground-state electrostatic contributions that are well captured by static DFT. By contrast, in polar covalent La–O–La networks, ^{139}La nuclei are strongly electronically coupled through oxygen, rendering the ^{139}La shift a HAHA-dominated property that lies beyond the scope of static DFT. As a result, in $MgCl_2$-rich compositions—where La–O coordination is less prevalent—the predicted shifts show closer agreement with experimental values.

Unlike ^{17}O and ^{139}La, ^{35}Cl NMR does not directly probe oxygen coordination environments, as Cl^- does not coordinate directly with O^{2-} in these molten salt mixtures. Consequently, ^{35}Cl serves primarily as a benchmark for comparing simulations and experiments. The measured ^{35}Cl chemical shifts vary only slightly between 110 and 130 ppm across all compositions, and VASP calculations reproduced these trends accurately. This minimal variation arises because La^{3+} exerts the dominant influence on ^{35}Cl shifts (see Chapter III). Even though the Na^+/Mg^{2+} ratio changes across compositions, the cationic fraction of La^{3+} was fixed at 0.2, keeping the ^{35}Cl shifts largely constant. Importantly, despite the same temperature mismatch affecting ^{17}O, no pronounced systematic offset was observed here. This difference arises from the bonding character: La–Cl is largely ionic, resulting in smaller temperature-dependent distortions of electrons in the La–Cl molecular orbitals; whereas, La–O leans towards polar covalency, making finite-temperature considerations of bond polarisation critical for accurately predicting ^{17}O shifts.

To further substantiate the explanations proposed above for the discrepancies between predicted and measured chemical shifts, the NMR results for crystalline LaOCl (**Table V-1**) were revisited. Varying degrees of discrepancy are observed for the predicted isotropic chemical shifts (δ_{iso}): VASP vastly underpredicts the ^{139}La shifts by 100 ppm, modestly underpredicts the ^{17}O shifts by 20 ppm, and reproduces the ^{35}Cl shifts with an error of only 1 ppm. While the discrepancies in ^{139}La and ^{35}Cl shifts have been addressed above, the 20 ppm underprediction of ^{17}O shifts in the solid state stands in clear contrast to the ~150 ppm overprediction in the molten state. This difference is most likely attributed to the following two factors: 1) finite-temperature effects that are not fully captured in the ensemble-averaged DFT calculations of MD snapshots (as discussed above), and 2) limitations of the MD model in accurately reproducing the average La–O distances in the molten state.

Concerning the second point, it was recently shown using *ab initio* MD that transient covalent U–Cl interactions in molten UCl_3 are not adequately captured by the PIM [186]. This limitation was attributed to the participation of partially occupied U-5*f* orbitals, and is therefore unlikely to apply to La^{3+}, whose 4*f* shell is empty. Nevertheless, to assess whether deficiencies in the classical MD model could affect the predicted La–O coordination in the molten state, additional DFT calculations were performed to verify if the classical MD-generated structures correspond to the structural motifs at the DFT level.

Accordingly, geometry optimisation operations were carried out using VASP on representative MD snapshots of the 80 NaCl–15 $LaCl_3$–5 LaOCl molten salt composition. Upon relaxation, the average La–O bond lengths increased from approximately 2.18 to 2.30 Å, while the distribution became narrower (**Figure V-15b**). This change is accompanied by an enhanced preference for La–O–La bond angles near 109° and 120°, consistent with $[La_4O]^{10+}$ and $[La_3O]^{7+}$ coordination motifs (**Figure V-15c**). Subsequent NMR calculations of the relaxed structures yielded ^{17}O shifts that were only slightly lower (<10 ppm) than those obtained from the unrelaxed MD snapshots (**Figure V-15d**).

These results indicate that the MD-generated configurations are structurally consistent with first-principles relaxed geometries, while additionally capturing thermal disorder inherent to the molten state. As such, inaccuracies in the MD-generated ionic configurations are unlikely to be the primary source of the large discrepancy between calculated and experimental ^{17}O chemical shifts. Instead, the error is attributed to the intrinsic limitations of static, ground-state DFT in describing temperature-dependent bond aharmonicity and dielectric screening in polar covalent La–O bonds under molten conditions. In principle, more advanced exchange-correlation functionals (such as PBE0, PW31, B3LYP), which have been shown to improve the description of heavy-atom effects in solid-state systems [187–189], may offer a more accurate treatment of these effects, albeit at substantially higher computational cost. At present, VASP does not support NMR shielding calculations using the hybrid functionals above.

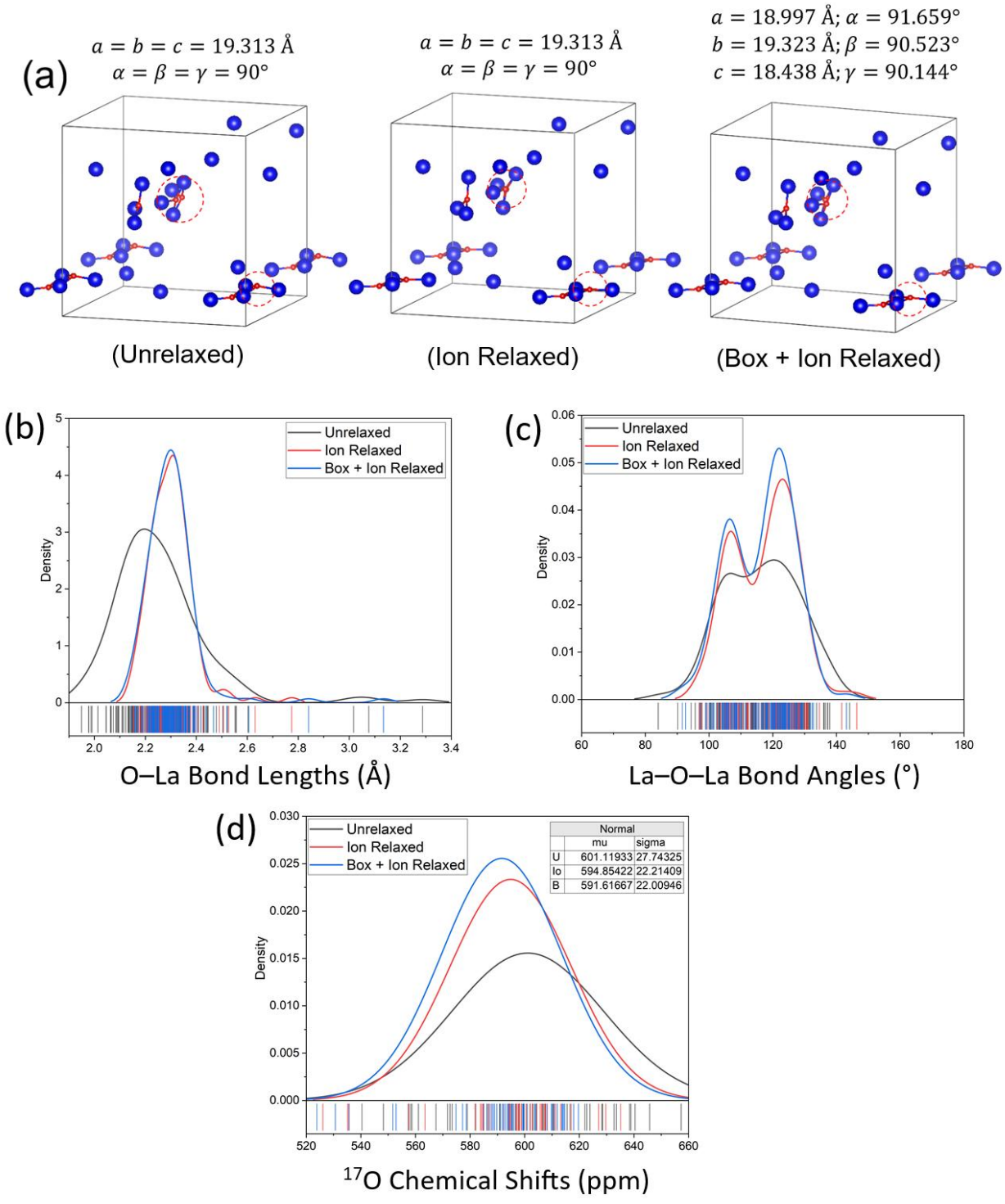

Figure V-15. Changes in 80 NaCl–15 $LaCl_3$–5 LaOCl molten salt local structure before and after VASP geometric relaxation calculations: (a) schematic illustration of the changes in O–La bonding for a representative snapshot (blue: La^{3+}, red: O^{2-}); (b) distribution of O–La bond distances in the first coordination shell of oxygen; (c) distribution of La–O–La bond angles in the first coordination shell of oxygen; (d) normalised distribution of calculated ^{17}O chemical shifts.

Despite these limitations in absolute shift prediction, the strong correlation between oxygen coordination environments and calculated ^{17}O chemical shifts remains robust. Accordingly, the trends in ^{17}O chemical shifts across the (80-α) NaCl–α $MgCl_2$–15 $LaCl_3$–5 LaOCl (α=*0–80)* series can be rationalised by decomposing the predicted shifts into contributions from individual O^{2-} environments. As shown in **Figure V-17**, each vertical line at the bottom represents the chemical shift of a single O^{2-} ion calculated from the MD snapshots, with the resulting distributions plotted as normal curves. The spread of each curve reflects the diversity of local oxygen coordination environments in a given composition. To aid interpretation, chemical shift ranges associated with distinct oxide species are indicated below the distribution plots. For simplicity, these ranges were derived by considering only the first coordination shell, where each O^{2-} ion is coordinated by a total of three cations (a combination of Mg^{2+} and La^{3+}). The ranges represent a span in which ~90% of the predicted shifts for each oxide species fall. Corresponding plots for systems with lower LaOCl concentrations are provided in **Figure V-17**.

Across all compositions, purely NaCl-based systems exhibit the narrowest distribution. This arises because O^{2-} ions coordinate almost exclusively with La^{3+}, resulting in the predicted shifts being large but narrowly confined (550–700 ppm). With the introduction of $MgCl_2$, the predicted shifts gravitate towards smaller values and the distributions broaden, reflecting the increasing prevalence of mixed-species environments such as $[MgLa_2O]^{6+}$ and $[Mg_2LaO]^{5+}$. Beyond a 1:1 $MgCl_2$-to-NaCl ratio, however, the distributions no longer broaden, and the predicted shifts fluctuate without a systematic trend. As discussed earlier, this behaviour reflects the saturation of Mg^{2+} coordination: with Mg^{2+} dominating the local environment, additions of $MgCl_2$ no longer appreciably alter the oxide speciation landscape.

Overall, our speciation analysis systematically addresses the experimental observations: NaCl-rich systems yield large ^{17}O shifts because O^{2-} coordinates exclusively with La^{3+}, whereas increasing $MgCl_2$ content reduces the average shift by promoting diverse mixed-coordination environments. In the context of oxide solubility, these mixed coordination environments mitigate La–O clustering, thereby enhancing oxygen solubility and preventing oxide precipitation.

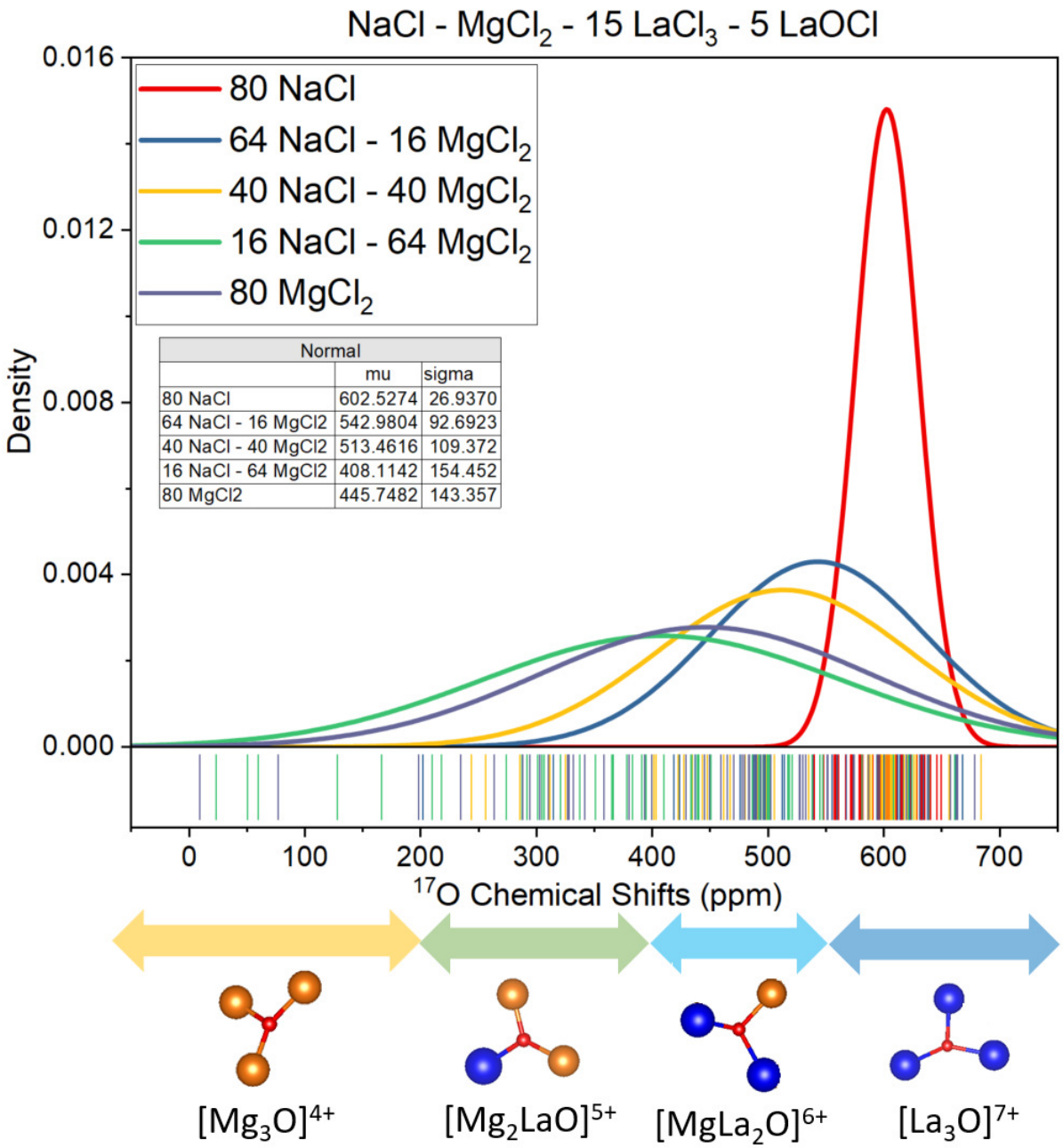

Figure V-16. Distribution of predicted ^{17}O chemical shifts from individual O^{2-} environments in (80-α) NaCl–α $MgCl_2$–15 $LaCl_3$–5 LaOCl (α=0–80). Chemical shift ranges for representative oxide species (considering only the three nearest neighbours) are shown below the x-axis. O^{2-}, Mg^{2+}, and La^{3+}ions are represented by red, orange, and blue spheres, respectively.

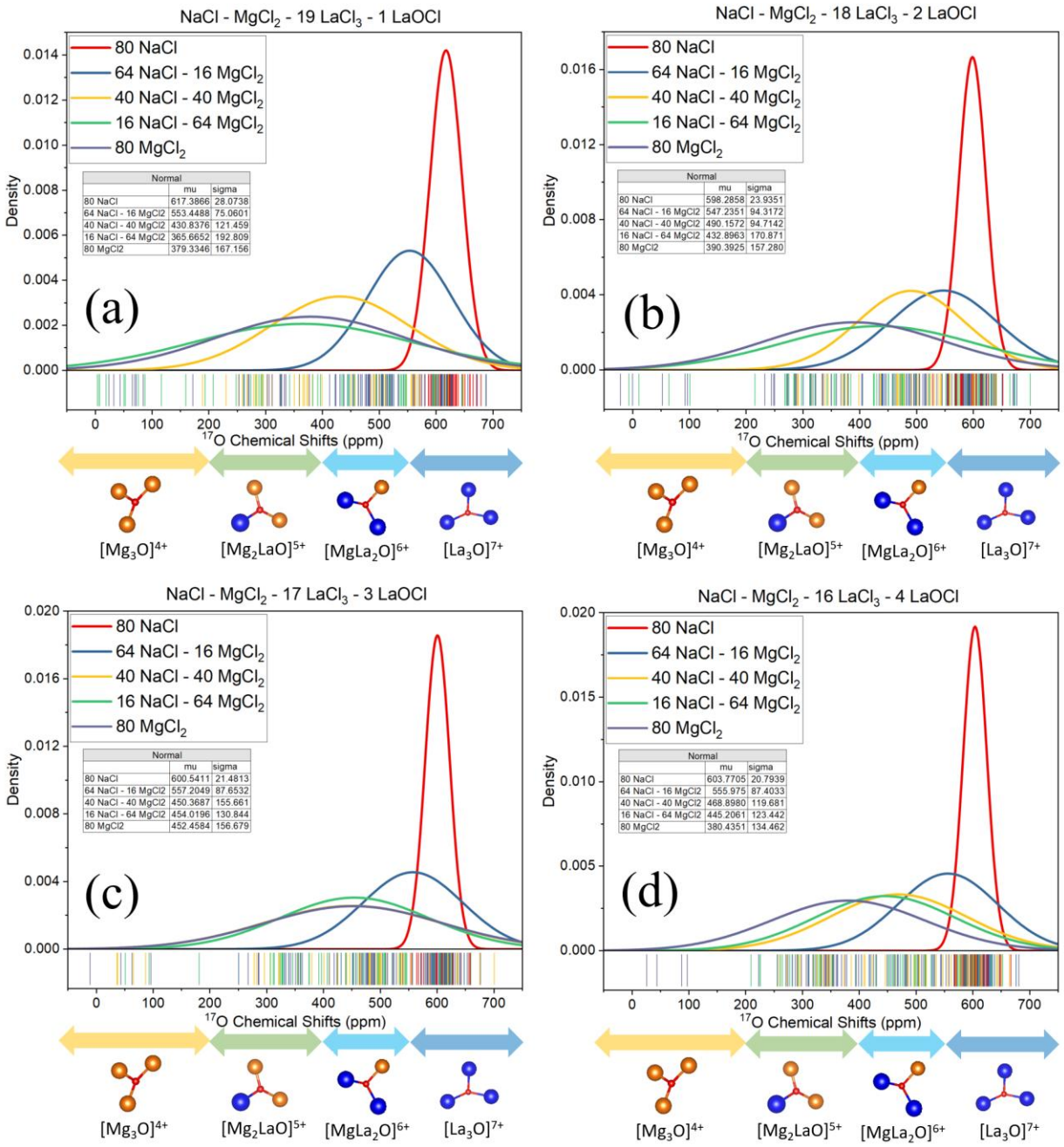

Figure V-17. Distribution of predicted ^{17}O chemical shifts from individual O^{2-} environments in (80-α) NaCl–α $MgCl_2$–(20-x) $LaCl_3$–x LaOCl (in mol%, α=0–80, x=1–4). Chemical shift ranges for representative oxide species (considering only the three nearest neighbours) are shown below the x-axis.

V-4. Effects of Soluble Oxygen Concentration on Thermophysical Properties

Up to this point, oxygen has been shown to be soluble in all (80-α) NaCl–α $MgCl_2$–(20-x) $LaCl_3$–x LaOCl (α=0–80, x=0–5) compositions at 850 °C. In the absence of $MgCl_2$, O^{2-} ions predominantly coordinate with La^{3+}, forming extended –(O–La)$_n$– clusters. Upon the addition of $MgCl_2$, oxygen instead participates in mixed coordination environments involving both Mg^{2+} and La^{3+} ions, leading to a more homogeneous dispersion of O^{2-} within the molten salt matrix. Under the framework of structure–property coupling, these distinct local coordination motifs are expected to give rise to different thermophysical responses as a function of NaCl-to-$MgCl_2$ composition.

In this sub-chapter, the influence of soluble oxygen concentration on molten salt thermophysical properties is investigated using classical MD simulations. The properties considered include density, viscosity, thermal expansivity, and heat capacity. Although thermal conductivity is also an important parameter for assessing heat transfer efficiency (Eq. IV-1), it is not examined here due to its poor convergence in conventional MD simulations.

Figure V-18 illustrates the evolution of the thermophysical properties of the (80-α) NaCl–α $MgCl_2$–(20-x) $LaCl_3$–x LaOCl (α=0–80) molten salt mixtures as a function of oxygen concentration (x=0–5) at 850 °C. Thermal expansivity and heat capacity remain essentially invariant with increasing soluble oxygen content across all compositions. In contrast, the melt density increases linearly with oxygen concentration; however, the magnitude of the density increment is largely independent of the $MgCl_2$-to-NaCl ratio.

Among the properties examined, viscosity is the only one that exhibits a coupled dependence with both the oxygen concentration and the $MgCl_2$-to-NaCl ratio. This dependency is manifested in the composition-dependent onset of abrupt viscosity increases. Initially (at x=0), all compositions display comparable viscosities, and increasing oxygen content leads to systematic viscosity increases. In $MgCl_2$-free melts, a sharp rise in viscosity occurs at relatively low oxygen concentrations (around x=2). As the $MgCl_2$ fraction increases, the viscosity jump is progressively shifted to higher oxygen contents. In $MgCl_2$-rich compositions, the viscosity transition becomes less abrupt, with viscosity increasing more smoothly as a function of oxygen concentration.

Taken together, these trends reinforce the close coupling between local structure and transport properties in molten salts. Oxygen clustering in $MgCl_2$-poor compositions leads to pronounced increases in viscosity with soluble oxygen content, whereas the more homogeneous oxygen distribution in $MgCl_2$-rich compositions mitigates the abrupt viscosity changes. Nevertheless, these results should be regarded as preliminary, as only discrete oxygen concentrations were sampled and the associated uncertainties for each data point remain significant relative to the observed viscosity range. A more comprehensive dataset with finer compositional resolution will be required to adequately characterise the viscosity transitions identified here—an endeavour that is reserved for future work.

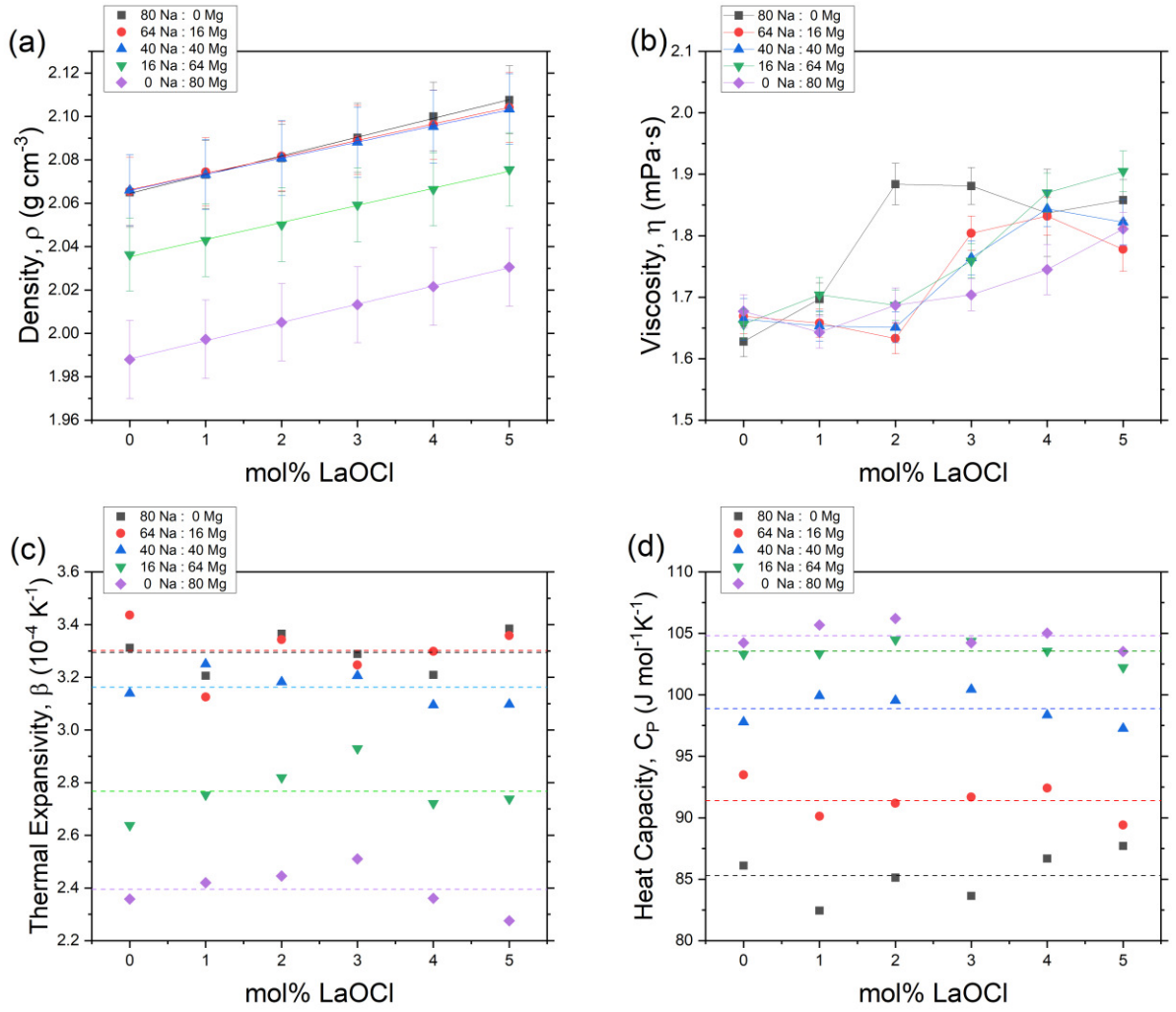

Figure V-18. Evolution of the thermophysical properties of the (80-α) NaCl–α $MgCl_2$–(20-x) $LaCl_3$–x LaOCl (α=0–80) molten salt mixtures as a function of oxygen concentration (x=0–5) at 850 °C : (a) density, (b) viscosity, (c) thermal expansivity, and (d) heat capacity.

Conclusions

In this chapter, a $MgCl_2$-mediated oxygen solubility mechanism in molten chlorides was examined by performing ^{17}O NMR on NaCl–$MgCl_2$–$LaCl_3$–LaOCl and validating the results using MD and DFT calculations. To this end, minor quantities of 90 at% ^{17}O-enriched LaOCl were added to simulate oxygen contamination in NaCl–$MgCl_2$–$LaCl_3$, a proxy for the ARAMIS-A fuel composition of NaCl–$MgCl_2$–$PuCl_3$–$AmCl_3$.

The results show that $MgCl_2$ addition lowers ^{17}O chemical shifts, indicating Mg^{2+} disrupts La–O clustering by promoting mixed coordination environments such as $[MgLa_2O]^{6+}$ and $[Mg_2LaO]^{5+}$. This mechanistic insight demonstrates how the incorporation of divalent Mg^{2+} cations enhances oxygen solubility and modifies oxide speciation in molten salt mixtures containing heavy lanthanide or actinide ions. In MSR-relevant compositions, such behavior provides the added benefit of sequestering oxygen contaminants, mitigating the deposition of actinide-rich oxide

precipitates on MSR structural surfaces and suppressing a prominent pathway for deposit-induced corrosion. It should be noted, however, that these insights from the La-based surrogate system may not extend directly to actinide-bearing systems, where more complex bonding and redox chemistry could alter the relevant speciation behavior.

At the same time, the strong affinity for oxygen implies that $MgCl_2$ can also act as an impurity carrier if it is not sufficiently purified. This caveat underscores the importance of rigorous salt purification to harness the oxygen-sequestering capability of $MgCl_2$ without introducing additional impurities.

With respect to the impact of soluble oxygen on thermophysical properties, MD calculations indicate that density, thermal expansivity, and heat capacity are largely insensitive to the $MgCl_2$-to-NaCl compositional ratio across the oxygen concentrations examined. Only viscosity exhibits a coupled dependence on both the oxygen concentration and the melt composition: $MgCl_2$-rich compositions mitigate abrupt viscosity increases with increasing soluble oxygen content, consistent with the role of $MgCl_2$ in disrupting oxygen clustering. While these trends are robust, the present results remain preliminary, and more extensive datasets will be required to more precisely quantify this behaviour.

Altogether, this chapter lays out a mechanistic basis for sensibly tuning molten salt compositions with $MgCl_2$ to enhance oxygen solubility and suppress oxide precipitation—an effect that may otherwise contribute to corrosion. These results provide critical insights that inform the compositional design of high-temperature molten salt systems.

Chapter VI

Conclusions et Perspectives
/
Conclusions and Perspectives

Conclusions et Perspectives (Français)

Le chapitre VI est consacré à la synthèse des principaux résultats de cette thèse, à l'identification de ses limites et à la présentation des perspectives susceptibles de prolonger ces travaux.

Cette thèse élucide les relations structure–propriétés dans les RSF à base de chlorures, en mettant un accent particulier sur le rôle du $MgCl_2$ dans la régulation de la structure locale et sur son impact sur les propriétés physiques à l'échelle macroscopique. Dans le combustible proxy de RSF de composition NaCl–$MgCl_2$–$LaCl_3$, le $MgCl_2$ perturbe la formation de réseaux polymériques continus d'espèces trivalentes, analogues aux réseaux d'actinides observés dans les systèmes réels. Par extrapolation aux compositions RSF contenant des trichlorures d'actinides ($AnCl_3$), cette modification structurale contribue à limiter l'augmentation de la viscosité aux fortes concentrations en $AnCl_3$, ce qui est susceptible d'améliorer les performances de transfert thermique et de favoriser la circulation naturelle du combustible. Par ailleurs, la forte affinité des ions Mg^{2+} pour les ions O^{2-} favorise la solubilité de l'oxygène dans les combustibles RSF à base de chlorures, facilitant ainsi la séquestration des impuretés oxygénées résiduelles et limitant la précipitation d'oxydes susceptibles de se déposer sur les surfaces structurelles.

Malgré ces avantages, le $MgCl_2$ est notoirement hygroscopique et peut introduire des quantités significatives d'humidité et d'impuretés oxygénées s'il n'est pas rigoureusement purifié. Ces impuretés constituent un facteur majeur d'accélération de la corrosion des matériaux structurels des MSR et doivent, par conséquent, être strictement maîtrisées. En outre, à faibles concentrations d'$AnCl_3$ (< 20 mol %), le $MgCl_2$ peut légèrement augmenter la viscosité du mélange combustible en raison de la formation de complexes de type $[Mg_xCl_y]^{2x-y}$. À la composition de référence ARAMIS-A (23 mol % de $(Pu,Am)Cl_3$), le $MgCl_2$ ne réduit pas significativement la viscosité du combustible, ce qui indique que ses effets bénéfiques demeurent fortement dépendants de la composition.

Le savoir-faire méthodologique acquis au cours de ces travaux constitue un apport significatif pour l'étude de systèmes hautement désordonnés et pour le développement de la RMN appliquée aux noyaux lourds. Dans le domaine des sels fondus, un intérêt existe actuellement au CEMHTI pour appliquer les approches développées ici à la caractérisation RMN du système NaCl–$ZrCl_4$ ainsi qu'à l'analyse EXAFS du système NaCl–$MgCl_2$–$LaCl_3$. Au-delà des sels fondus, des perspectives s'ouvrent également vers l'application des méthodes de calcul de viscosité à la prédiction des viscosités dépendantes de la composition dans le système verrier ternaire Al_2O_3–MgO–ZrO_2, ainsi que vers l'exploitation de l'expertise acquise en RMN des noyaux lourds pour le calcul des paramètres RMN de sels solides à base de LuF_3.

L'auteur espère que les connaissances et les méthodologies développées dans cette thèse contribueront de manière significative aux efforts en cours visant à la maturation technologique des systèmes RSF, tout en participant à l'avancement des méthodes de caractérisation en chimie inorganique.

VI-1. Conclusions

This thesis elucidates the structure–property relationships in MCFR fuel salts, with particular emphasis on the role of $MgCl_2$ in governing local structural dynamics and its impact on macroscopic properties such as viscosity and oxygen solubility.

Chapter I provides an overview of MSRs, covering their historical development, renewed global interest in the 21st century, the evolution of modern concepts, fuel characteristics, and the current state of fuel chemistry research. Chapter II introduces the theoretical background and experimental/computational methodologies in this study, including NMR, classical MD, and DFT calculations of NMR parameters. Chapter III examines the structural dynamics of the NaCl–$MgCl_2$–$LaCl_3$ surrogate fuel, revealing how local network structures and coordination environments evolve with composition and temperature. Chapter IV demonstrates the strong coupling between local structure and transport properties, showing how viscosity and ion diffusivities vary with network connectivity. Chapter V provides mechanistic insight into the role of $MgCl_2$ in enhancing oxygen solubility in molten chloride systems.

Although La^{3+} may not be an electronically perfect surrogate for Pu^{3+} and Am^{3+}—given their differences in *f*-orbital occupancy and accessible oxidation states—the structural validity of the $LaCl_3$ surrogate is supported by comparison with studies on real actinide-bearing systems. For example, the La^{3+}–Cl^- and La^{3+}–La^{3+} distances in the NaCl–$MgCl_2$–$LaCl_3$ system were confirmed by the multimodal NMR–MD–DFT framework to be approximately 2.78 Å and 4.72 Å, respectively. These values fall well within the range of M^{3+}–Cl^- (2.7 to 2.8 Å) and M^{3+}–M^{3+} (4.7 to 4.8 Å) distances reported for NaCl–$PuCl_3$ [76,79], NaCl–UCl_3 [190,191], and NaCl–$MgCl_2$–UCl_3 [59] molten salt systems. Furthermore, the disruption of continuous La–Cl–La network chains upon addition of $MgCl_2$, identified in this thesis, finds a direct parallel in the shortening of U–Cl oligomeric chains observed when $MgCl_2$ is introduced into NaCl–UCl_3 [59]. Taken together, these structural correspondences lend confidence that the critical insights obtained from using $LaCl_3$ as a structural surrogate are transferable to actinide-bearing MCFR fuel salts.

The key findings of this thesis highlight the added benefits of incorporating $MgCl_2$ into MCFR fuels. Beyond its previously recognised advantages—such as lowering fuel melting temperatures, improving heat capacity, and enhanced thermal conductivity—$MgCl_2$ disrupts continuous actinide polymer networks, thereby reducing fuel viscosity at higher actinide trichloride ($AnCl_3$) concentrations. This reduction in viscosity improves the heat transfer performance and contributes to the passive safety of MSRs by enhancing natural circulation and reducing reliance on active pumping systems. Furthermore, the strong affinity of Mg^{2+} ions for O^{2-} ions promotes the formation of mixed-coordination environments, such as $[MgAn_2O]^{6+}$ and $[Mg_2AnO]^{5+}$, a behaviour that is thermodynamically unfavourable for Na^+ ions. This feature enhances oxygen solubility in MCFR fuels, aiding the sequestration of residual oxygen impurities and mitigating the precipitation of actinide oxides that can deposit on structural surfaces and contribute to corrosion.

Despite these benefits, the use of $MgCl_2$ in MCFR fuels is associated with several drawbacks. Most prominently, $MgCl_2$ is notoriously hygroscopic and can introduce substantial oxygen and moisture impurities if not rigorously

purified. These impurities are the primary driver of accelerated corrosion in MSR structural materials and must therefore be carefully controlled. In addition, at lower $AnCl_3$ concentrations (<20 mol%), $MgCl_2$ may slightly increase the viscosity of the fuel mixture due to the formation of $[Mg_xCl_y]^{2x-y}$ complexes. At the ARAMIS-A reference composition of 23 mol% $(Pu,Am)Cl_3$, $MgCl_2$ does not significantly reduce fuel viscosity, indicating that its beneficial effects are composition-dependent.

VI-2. Future Work

The robust set of experimental and computational tools established in this work for elucidating molten salt structure–property relationships can be readily extended to a wider range of disordered materials, including other molten salts, ceramics, and oxide glasses.

At CEMHTI, there is growing interest in applying these methodologies to several material systems of relevance to nuclear and high-temperature materials science. One such system is molten $NaCl–ZrCl_4$, which is closely related to MSR fuel chemistry, as zirconium constitutes a significant fraction of fission products and exhibits high volatility. In addition, the DFT and HALA-related know-how developed for $LaCl_3$-containing systems may be leveraged for NMR parameter calculations in solid LuF_3-based salts. Beyond nuclear materials, interest has also been expressed in predicting the composition-dependent viscosity of the $Al_2O_3–MgO–ZrO_2$ ternary glass system at temperatures that are experimentally inaccessible.

Complementary to the framework presented in this thesis, extended X-ray absorption fine structure (EXAFS) spectroscopy was employed to independently probe the local coordination environments in molten $NaCl–MgCl_2–LaCl_3$ systems. La K-edge EXAFS measurements were performed at the SPring-8 synchrotron facility (Hyogo Prefecture, Japan) in July 2025, following the experimental setup and procedures described in [85]. Comparison of the absorption spectra for solid $LaCl_3$ and molten 80 NaCl–20 $LaCl_3$ (**Figure VI-1a**) reveals a pronounced damping of EXAFS oscillations in the molten phase, consistent with increased structural disorder and enhanced dynamic fluctuations at elevated temperatures. Furthermore, the *k*-space oscillations for the two systems exhibit distinctly different behaviour (**Figure VI-1b**), indicating measurable modifications of the La–Cl coordination environment upon melting.

Future EXAFS investigations will adopt a more quantitative analysis framework, including phase-shift corrected Fourier transforms and multiple-scattering calculations using the FEFF code [192], to extract reliable coordination numbers and interatomic distances [193]. Beyond $LaCl_3$, EXAFS provides a powerful route to systematically investigate other molten $LnCl_3$ systems (*Ln=Ce, Pr, Nd, Sm, Eu*), which are not readily accessible by NMR due to paramagnetism or the absence of suitable NMR-active isotopes. Such studies will further enable rigorous experimental validation of MD interatomic potentials for $NaCl–LnCl_3$ systems [100].

MSR technology holds considerable promise for future energy systems, yet remains in its infancy in terms of technological maturity. Continued fundamental research into molten salt chemistry, structure, and transport properties

will be essential for its successful development. The author hopes that the insights and methodologies developed in this thesis will contribute meaningfully to ongoing efforts toward the realisation of safe and efficient MSR technologies.

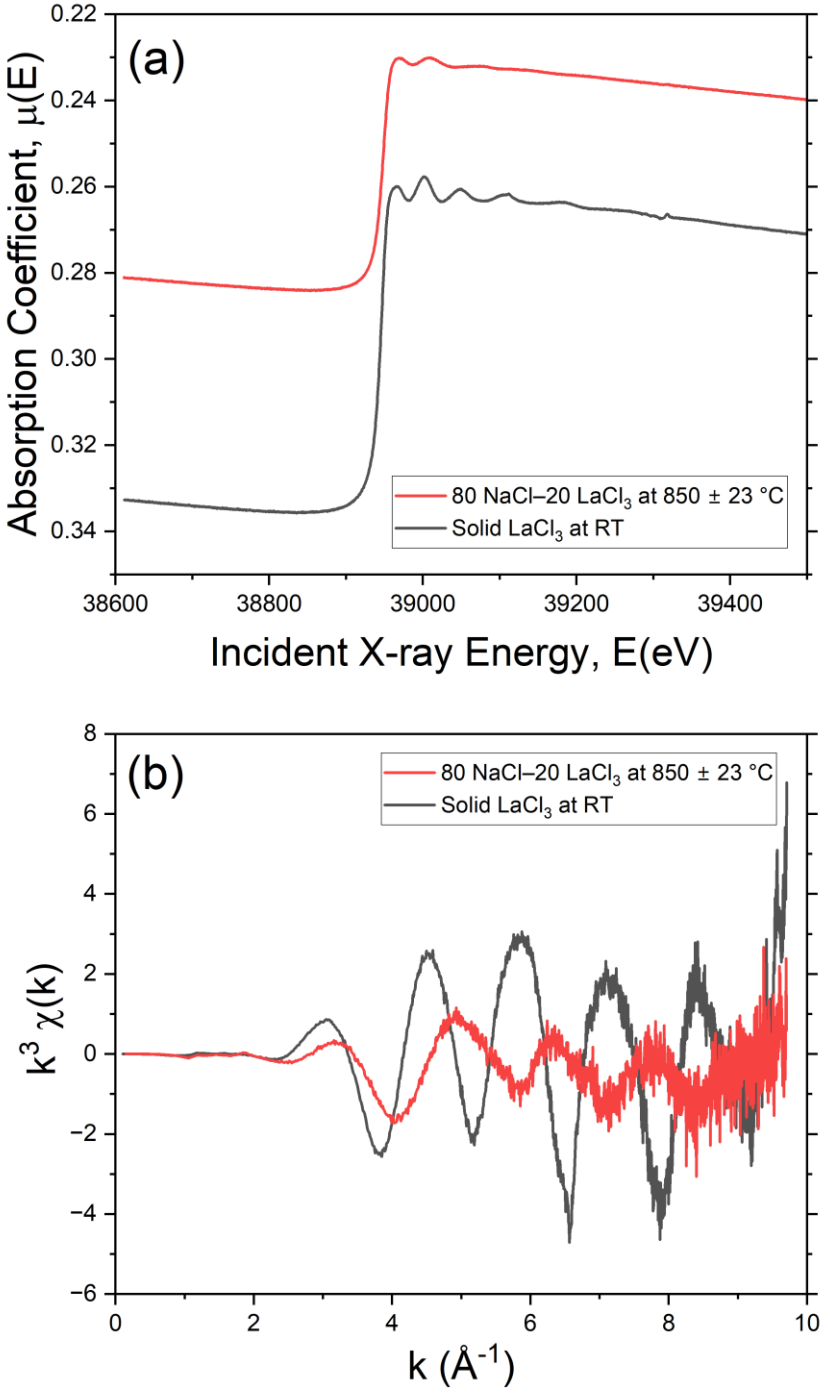

Figure VI-1. (a) EXAFS absorption spectra and (b) k-space oscillation curves, recorded at the La-K edge (38925 eV) for solid $LaCl_3$ at room temperature and the molten 80 mol% NaCl–20 mol% $LaCl_3$ mixture at 850 °C.

Bibliography

[1] International Energy Agency, Global Energy Review 2025, 2025. https://www.iea.org/reports/global-energy-review-2025 (accessed April 17, 2026).

[2] REN21, Renewables 2025 Global Status Report Collection, Global Overview, Paris, 2025. https://www.ren21.net/renewables-2025-global-status-report-global-overview/ (accessed April 17, 2026).

[3] Dominick Reuter, Amazon invests in nuclear energy, hot on the heels of Google and Microsoft, Business Insider (2024). https://www.businessinsider.com/amazon-invests-in-nuclear-for-aws-following-google-and-microsoft-2024-10 (accessed April 17, 2026).

[4] Google partners with Elementl Power on nuclear energy sites as power demand for AI grows, The Associated Press (2025). https://apnews.com/article/google-elementl-nuclear-power-artificial-intelligence-2bd4282af728e16446bdcefe97d37873 (accessed October 24, 2025).

[5] T. Gardner, Google to buy power for AI needs from small modular nuclear reactor company Kairos, Reuters (2024). https://www.reuters.com/technology/artificial-intelligence/google-buy-power-small-modular-nuclear-reactor-company-kairos-ai-needs-2024-10-14/ (accessed October 24, 2025).

[6] C. Mandler, Three Mile Island nuclear plant will reopen to power Microsoft data centers, National Public Radio (NPR) (2024). https://www.npr.org/2024/09/20/nx-s1-5120581/three-mile-island-nuclear-power-plant-microsoft-ai (accessed April 17, 2026).

[7] Meta signs deal with nuclear plant to power AI and datacenters for 20 years, The Guardian (2025). https://www.theguardian.com/technology/2025/jun/03/meta-nuclear-power-ai (accessed October 24, 2025).

[8] Energy, Electricity and Nuclear Power Estimates for the Period up to 2050, 2025. https://doi.org/10.61092/iaea.gwov-o544.

[9] E. Çam, Z. Hungerford, N. Schoch, F.P. Miranda, C.D.Y. de León, Electricity 2024 - Analysis and forecast to 2026, 2024. https://www.iea.org/reports/electricity-2024 (accessed April 17, 2026).

[10] Technology Roadmap Update for Generation IV Nuclear Energy Systems, 2014. https://www.gen-4.org/resources/reports/technology-roadmap-update-generation-iv-nuclear-energy-systems-gif-2014 (accessed April 17, 2026).

[11] S.M. Goldberg, R. Rosner, Nuclear Reactors: Generation to Generation, 2011. https://www.amacad.org/publication/nuclear-reactors-generation-generation (accessed April 17, 2026).

[12] Generation IV Nuclear Reactors, World Nuclear Association (2024). https://world-nuclear.org/information-library/nuclear-fuel-cycle/nuclear-power-reactors/generation-iv-nuclear-reactors (accessed October 24, 2025).

[13] Generation IV Goals, Technologies and GIF R&D Roadmap, Generation IV International Forum (n.d.). https://www.gen-4.org/generation-iv-criteria-and-technologies (accessed October 24, 2025).

[14] Stages of the Nuclear Fuel Cycle, United States Nuclear Regulatory Commission (2020). https://www.nrc.gov/materials/fuel-cycle-fac/stages-fuel-cycle.

[15] M.S. Chenaud, V. Pascal, C. Chabert-Koralewski, J. Serp, P. Laghoutaris, J.C. Garnier, Sudreau F., B. Morel, I. Morales, O. Drouvot, S. David, E. Merle, J.M. Hamy, F. Botte, S. Takenouti, A. Sanna, The French R&D Collaborative Project ISAC on Fast MSR Dedicated to Actinides Transmutation, in: International Conference on the Management of Spent Fuel from Nuclear Power Plants, International Atomic Energy Agency (IAEA), Vienna, 2024.

[16] W.B. Cottrell, H.E. Hungerford, J.K. Leslie, J.L. Meein, Operation of the Aircraft Reactor Experiment, 1955. https://doi.org/10.2172/4237975.

[17] E.S. Bettis, W.B. Cottrell, E.R. Mann, J.L. Meem, G.D. Whitman, The Aircraft Reactor Experiment—Operation, Nuclear Science and Engineering 2 (1957) 841–853. https://doi.org/10.13182/NSE57-A35497.

[18] P.N. Haubenreich, J.R. Engel, Experience with the Molten-Salt Reactor Experiment, Nuclear Applications and Technology 8 (1970) 118–136. https://doi.org/10.13182/NT8-2-118.

[19] H.G. Macpherson, The Molten Salt Reactor Adventure, Nuclear Science and Engineering 90 (1985) 374–380. https://doi.org/10.13182/NSE90-374.

[20] D. Martin, The UK's Forgotten Molten Salt Reactor Programme, Weinberg Next Nuclear (2014). https://web.archive.org/web/20160305130749/http://www.the-weinberg-foundation.org/2014/11/13/the-uks-forgotten-molten-salt-reactor-programme/ (accessed October 29, 2025).

[21] V.M. Novikov, The results of the investigations of Russian Research Center—'"Kurchatov Institute"' on molten salt applications to problems of nuclear energy systems, in: The International Conference on Accelerator-driven Transmutation Technologies and Applications, AIP Publishing, Las Vegas, Nevada, 1995: pp. 138–147. https://doi.org/10.1063/1.49148.

[22] T. Abram, S. Ion, Generation-IV nuclear power: A review of the state of the science, Energy Policy 36 (2008) 4323–4330. https://doi.org/10.1016/j.enpol.2008.09.059.

[23] Integral Molten Salt Reactor: Carbon-free, Low-cost, High-impact. Flexible and Resilient., Terrestrial Energy (2025). https://www.terrestrialenergy.com/technology (accessed April 17, 2026).

[24] T. Taylor, O. Gregoire, P. Haigh, S. Boddington, R. O'Sullivan, Waste Burning Performance of the Moltex SSR-W, in: 5th Generation IV and Small Reactors (G4SR) Conference, Ottawa, ON, Canada, 2024.

[25] T. Honney, Copenhagen Atomics: the story so far, Nuclear Engineering International (2024). https://www.neimagazine.com/analysis/copenhagen-atomics-the-story-so-far/?cf-view (accessed October 29, 2025).

[26] M. Pater, Advanced freeze valves for energy production and conversion systems using molten salts, Technical University of Denmark, 2023. www.fysik.dtu.dk/english/Research/RADPHYS.

[27] Nucléaire: Naarea se défend après son dépôt de bilan par son repreneur Eneris, (2026). https://www.connaissancedesenergies.org/afp/nucleaire-naarea-se-defend-apres-son-depot-de-bilan-par-son-repreneur-eneris-260121 (accessed April 7, 2026).

[28] A. Vieceli, Modified point kinetic code for molten salt liquid fuel applied to the Thorizon One reactor, Politecnico di Torino, 2025.

[29] Flibe Energy: Our Technology, Revolutionizing Nuclear Energy for the World, Flibe Energy (n.d.). https://flibe.com/technology/ (accessed October 29, 2025).

[30] J. Krepel, K.J. Kramer, TerraPower fast chloride reactor, in: Molten Salt Reactors and Thorium Energy, Elsevier, 2024: pp. 953–972. https://doi.org/10.1016/b978-0-323-99355-5.00020-3.

[31] E. Blandford, K. Brumback, L. Fick, C. Gerardi, B. Haugh, E. Hillstrom, K. Johnson, F. Peterson, F. Rubio, F. Sarikurt, S. Sen, H. Zhao, N. Zweibaum, Kairos Power Thermal Hydraulics Research and Development, Nuclear Engineering and Design 364 (2020). https://doi.org/10.1016/j.nucengdes.2020.110636.

[32] China refuels thorium reactor without shutdown, Nuclear Engineering International (2025). https://www.neimagazine.com/news/china-refuels-thorium-reactor-without-shutdown/?cf-view (accessed October 29, 2025).

[33] J.A. Ocádiz Flores, R.J.M. Konings, A.L. Smith, Using the Quasi-chemical formalism beyond the phase Diagram: Density and viscosity models for molten salt fuel systems, Journal of Nuclear Materials 561 (2022) 153536. https://doi.org/10.1016/j.jnucmat.2022.153536.

[34] E. Martin-Lopez, P. Devito, F. Cussol, Séminaire Technique ISAC 2026 - Atelier Lot 2: Quelle serait la machine idéale du point de vue de la maintenance?, (2026).

[35] V. Pascal, P. Gauthé, E.M. Lopez, L. Matteo, Molten Salt Reactor Technology: Opportunities of Molten Salt Fuel for Actinides Management, in: Proceedings of a Technical Meeting, IAEA TECDOC Series, 2022.

[36] M. Mascaron, T. Le Meute, J. Martinet, V. Pascal, F. Bertrand, E. Merle, Study of the ARAMIS molten salt reactor behavior during unprotected transients, in: ICAPP 2023 - 2023 International Congress on Advances in Nuclear Power Plants, in Conjunction with 38th Korea Atomic Power Annual Conference (ICAPP 2023 / KAP Conference), Gyeongju, South Korea, 2023: p. 2023200. https://cea.hal.science/cea-04399511.

[37] M. Mascaron, J. Martinet, V. Pascal, E. Merle, F. Bertrand, An approach to Molten Salt Reactor operation and control and its application to the ARAMIS actinide burner, Ann. Nucl. Energy 210 (2025). https://doi.org/10.1016/j.anucene.2024.110888.

[38] S. Hong, S. Jang, T. Oh, Y. Kim, Preliminary study on the candidate fuel salt of molten chloride salt fast reactor, in: Transactions of the Korean Nuclear Society Virtual Spring Meeting, 2021.

[39] W.J. Ng, H.J. Ryu, Effects of base salt additives on NaCl–UCl_3–$PuCl_3$ fuel systems: Insights from CALPHAD simulations, J. Mol. Liq. 379 (2023). https://doi.org/10.1016/j.molliq.2023.121649.

[40] O. Beneš, R.J.M. Konings, Thermodynamic evaluation of the NaCl–$MgCl_2$–UCl_3–$PuCl_3$ system, Journal of Nuclear Materials 375 (2008) 202–208. https://doi.org/10.1016/j.jnucmat.2008.01.007.

[41] Y. Li, X. Xu, X. Wang, P. Li, Q. Hao, B. Xiao, Survey and evaluation of equations for thermophysical properties of binary/ternary eutectic salts from NaCl, KCl, $MgCl_2$, $CaCl_2$, $ZnCl_2$ for heat transfer and thermal storage fluids in CSP, Solar Energy 152 (2017) 57–79. https://doi.org/10.1016/j.solener.2017.03.019.

[42] H.E. McCoy, An Evaluation of the Molten-Salt Reactor Experiment Hastelloy N Surveillance Specimens - Fourth Group, Oak Ridge, Tennessee, 1971. https://doi.org/10.2172/4093896.

[43] O. Beneš, R.J.M. Konings, Thermodynamic evaluation of the (LiF + NaF + BeF_2 + PuF_3) system: An actinide burner fuel, Journal of Chemical Thermodynamics 41 (2009) 1086–1095. https://doi.org/10.1016/j.jct.2009.04.016.

[44] E. Capelli, O. Beneš, R.J.M. Konings, Thermodynamic assessment of the LiF–NaF–BeF_2–ThF_4–UF_4 system, Journal of Nuclear Materials 449 (2014) 111–121. https://doi.org/10.1016/j.jnucmat.2014.03.009.

[45] E. Capelli, O. Beneš, R.J.M. Konings, Thermodynamic assessment of the LiF–ThF_4–PuF_3–UF_4 system, Journal of Nuclear Materials 462 (2015) 43–53. https://doi.org/10.1016/j.jnucmat.2015.03.042.

[46] N. Vozárová, A.L. Smith, J.Y. Colle, P.E. Raison, D. Bouëxière, R.J.M. Konings, O. Beneš, Thermodynamic determination and assessment of the CsF–ThF_4 system, Journal of Chemical Thermodynamics 114 (2017) 71–82. https://doi.org/10.1016/j.jct.2017.05.008.

[47] E. Capelli, O. Beneš, R.J.M. Konings, Thermodynamics of soluble fission products cesium and iodine in the Molten Salt Reactor, Journal of Nuclear Materials 501 (2018) 238–252. https://doi.org/10.1016/j.jnucmat.2018.01.024.

[48] B. Schacherl, R. Eloirdi, R.J.M. Konings, Thermodynamic Assessment of the NaF–KF–UF_4 System, Thermo 1 (2021) 232–250. https://doi.org/10.3390/thermo1020016.

[49] S. Ghosh, B. Prabhakara Reddy, K. Nagarajan, K.C. Hari Kumar, Experimental investigations and thermodynamic modelling of KCl–LiCl–UCl_3 system, CALPHAD 45 (2014) 11–26. https://doi.org/10.1016/j.calphad.2013.11.001.

[50] W. Zhou, J. Zhang, Thermodynamic evaluation of LiCl–KCl–$PuCl_3$ system, J. Alloys Compd. 695 (2017) 2306–2313. https://doi.org/10.1016/j.jallcom.2016.11.092.

[51] H. Yin, X. Wu, C. Ling, X. Lai, B. Hu, Z. Tang, Thermodynamic optimization of the constitutive binaries of the LiCl/RbCl/$CaCl_2$–NaCl–UCl_3–$PuCl_3$ systems, CALPHAD 77 (2022). https://doi.org/10.1016/j.calphad.2022.102427.

[52] H. Yin, J. Lin, B. Hu, W. Liu, X. Guo, Q. Liu, Z. Tang, Thermodynamic description of the constitutive binaries of the NaCl–KCl–UCl_3–$PuCl_3$ system, CALPHAD 70 (2020) 1–10. https://doi.org/10.1016/j.calphad.2020.101783.

[53] J.A.O. Flores, B.A.S. Rooijakkers, R.J.M. Konings, A.L. Smith, Thermodynamic Description of the ACl–$ThCl_4$ (A = Li , Na , K) Systems, 4 (2021) 122–133.

[54] J.C. Ard, J.A. Yingling, K.E. Johnson, J. Schorne-Pinto, M. Aziziha, C.M. Dixon, M.S. Christian, J.W. McMurray, T.M. Besmann, Development of the Molten Salt Thermal Properties Database − Thermochemical (MSTDB−TC), example applications, and LiCl−RbCl and UF_3−UF_4 system assessments, Journal of Nuclear Materials 563 (2022) 153631. https://doi.org/10.1016/j.jnucmat.2022.153631.

[55] T.M. Besmann, J. Schorne-Pinto, M. Aziziha, A.M. Mofrad, R.E. Booth, J.A. Yingling, J. Paz Soldan Palma, C.M. Dixon, J.A. Wilson, D. Hartanto, Applications of Thermochemical Modeling in Molten Salt Reactors, Materials 17 (2024). https://doi.org/10.3390/ma17020495.

[56] A.L. Smith, Structure-property relationships in actinide containing molten salts – A review : Understanding and modelling the chemistry of nuclear fuel salts, J. Mol. Liq. 360 (2022) 119426. https://doi.org/10.1016/j.molliq.2022.119426.

[57] V.F. Grizzi, S.C. Lee, Y. Zhang, First-Principles Investigation of the Effects of UF_4 and ThF_4 Fuels on the Structural, Dynamic, and Thermodynamic Properties of LiF–NaF, Journal of Physical Chemistry B 128 (2024) 5676–5684. https://doi.org/10.1021/acs.jpcb.4c01243.

[58] Y. Yin, W. Liang, D. Wang, W. Zhou, Local Structure and Ionic Diffusion in LiF–BeF_2–ThF_4 Molten Salts: Insights from Ab Initio Molecular Dynamics, Journal of Physical Chemistry B 129 (2025) 4207–4215. https://doi.org/10.1021/acs.jpcb.5c01173.

[59] B. Li, S. Dai, D. en Jiang, Adding MgCl2 to Molten NaCl−UCl_n (n=3,4): Insights from First-Principles Molecular Dynamics, ChemPhysChem 23 (2022). https://doi.org/10.1002/cphc.202200078.

[60] K. Duemmler, D. Andersson, B. Beeler, First-principles investigation of the thermophysical properties of NaCl, $PuCl_3$, and NaCl–$PuCl_3$ Molten salts, Journal of Nuclear Materials 591 (2024). https://doi.org/10.1016/j.jnucmat.2024.154902.

[61] G. Wang, B. Li, P. Yang, D.A. Andersson, Ab-Initio molecular dynamics simulations of binary NaCl–$ThCl_4$ and ternary NaCl–$ThCl_4$–UCl_3 molten salts, J. Mol. Liq. 385 (2023). https://doi.org/10.1016/j.molliq.2023.122347.

[62] S. Paul, S. Attarian, M. Fratoni, D. Morgan, I. Szlufarska, Influence of transmutation products on the thermophysical properties of eutectic NaCl–UCl_3 fuel salt in a fast-spectrum molten salt reactor, Journal of Nuclear Materials 605 (2025). https://doi.org/10.1016/j.jnucmat.2024.155572.

[63] F. Lantelme, P. Turq, Ionic dynamics in the LiCl–KCl system at liquid state, J. Chem. Phys. 77 (1982) 3177–3187. https://doi.org/10.1063/1.444192.

[64] F. Lantelme, P. Turq, The role of Coulomb forces in the properties of ionic liquids, J. Chem. Phys. 81 (1984) 5046–5052. https://doi.org/10.1063/1.447492.

[65] P.N. Kumta, P.A. Deymier, S.H. Risbud, Improved Rigid Ion Model of Molten Zinc Chloride, Physica B 153 (1988) 85–92. https://doi.org/10.1016/0921-4526(88)90037-3.

[66] M. Wilson, P.A. Madden, "Prepeaks" and "First Sharp DifFraction Peaks" in Computer Simulations of Strong and Fragile Ionic Liquids, 1994. https://doi.org/10.1103/PhysRevLett.72.3033.

[67] V. Bitrián, J. Trullàs, Molecular dynamics study of polarizable ion models for molten AgBr, Journal of Physical Chemistry B 110 (2006) 7490–7499. https://doi.org/10.1021/jp056818u.

[68] M. Salanne, P.A. Madden, Polarization effects in ionic solids and melts, Mol. Phys. 109 (2011) 2299–2315. https://doi.org/10.1080/00268976.2011.617523.

[69] L.C. Dewan, C. Simon, P.A. Madden, L.W. Hobbs, M. Salanne, Molecular dynamics simulation of the thermodynamic and transport properties of the molten salt fast reactor fuel LiF–ThF_4, Journal of Nuclear Materials 434 (2013) 322–327. https://doi.org/10.1016/j.jnucmat.2012.12.006.

[70] A.E. Gheribi, D. Corradini, L. Dewan, P. Chartrand, C. Simon, P.A. Madden, M. Salanne, Prediction of the thermophysical properties of molten salt fast reactor fuel from first-principles, Mol. Phys. 112 (2014) 1305–1312. https://doi.org/10.1080/00268976.2014.897396.

[71] J.X. Dai, W. Zhang, C.L. Ren, X.J. Guo, Prediction of dynamics properties of ThF_4-based fluoride molten salts by molecular dynamic simulation, J. Mol. Liq. 318 (2020). https://doi.org/10.1016/j.molliq.2020.114059.

[72] B. Li, S. Dai, D. Jiang, Molecular dynamics simulations of structural and transport properties of molten NaCl–UCl_3 using the polarizable-ion model, J. Mol. Liq. 299 (2020). https://doi.org/10.1016/j.molliq.2019.112184.

[73] H. Kim, C. Kwon, S. Ham, J. Lee, S.J. Kim, S. Kim, Physical properties of KCl–UCl_3 molten salts as potential fuels for molten salt reactors, Journal of Nuclear Materials 577 (2023). https://doi.org/10.1016/j.jnucmat.2023.154329.

[74] M. Simoes Santos, M. Salanne, T. Kooyman, D. Lambertin, Structural and transport properties of the molten salt NaCl–KCl–UCl_3 using the polarizable ion model, Journal of Nuclear Materials 597 (2024). https://doi.org/10.1016/j.jnucmat.2024.155125.

[75] M.B.J.W. Schreuder, J.A. Ocádiz Flores, A.E. Gheribi, O. Beneš, J.C. Griveau, E. Colineau, R.J.M. Konings, A.L. Smith, Experimental and Computational Exploration of the NaF–ThF_4 Fuel System: Structure and Thermochemistry, Journal of Physical Chemistry B 125 (2021) 8558–8571. https://doi.org/10.1021/acs.jpcb.1c04830.

[76] K. Goloviznina, M. Salanne, What Is a Good Simulant for Plutonium(III) in Molten Chloride Salts?, Journal of Physical Chemistry B 129 (2025) 7826–7830. https://doi.org/10.1021/acs.jpcb.5c03702.

[77] V. Eyert, J. Wormald, W.A. Curtin, E. Wimmer, Machine-learned interatomic potentials: Recent developments and prospective applications, J. Mater. Res. 38 (2023) 5079–5094. https://doi.org/10.1557/s43578-023-01239-8.

[78] M.T. Nguyen, R. Rousseau, P.D. Paviet, V.A. Glezakou, Actinide molten salts: A machine-learning potential molecular dynamics study, ACS Appl. Mater. Interfaces 13 (2021) 53398–53408. https://doi.org/10.1021/acsami.1c11358.

[79] M.T. Nguyen, V.A. Glezakou, R. Rousseau, P.D. Paviet, Exploring NaCl–$PuCl_3$ molten salts with machine learning interatomic potentials and graph theory, Appl. Mater. Today 35 (2023). https://doi.org/10.1016/j.apmt.2023.101951.

[80] A. Rodriguez, S. Lam, M. Hu, Thermodynamic and Transport Properties of LiF and FLiBe Molten Salts with Deep Learning Potentials, ACS Appl. Mater. Interfaces 13 (2021) 55367–55379. https://doi.org/10.1021/acsami.1c17942.

[81] G.Y. Li, Y.H. Lv, L. Zhang, K. Jiang, L. Zhang, Y. Liu, X.L. Tan, T. Bo, Machine Learning-Driven Exploration of Composition- and Temperature-Dependent Transport and Thermodynamic Properties in LiF–NaF–KF Molten Salts for Nuclear Applications, Journal of Physical Chemistry B 129 (2025) 9418–9429. https://doi.org/10.1021/acs.jpcb.5c03444.

[82] H. Tian, T. Liu, X. Lan, Thermal Property and Structure of Toxic Fluoride Molten Salt for Efficient Nuclear Energy Application Using Machine Learning Molecular Dynamics, J. Phys. Chem. B (2025). https://doi.org/10.1021/acs.jpcb.5c06761.

[83] Y. Jiang, Y. Wang, X. Li, Y. Gong, Temperature Extensible Deep Potential Model for Molten NaF–BeF_2–ZrF_4: Predicting Transport Properties and Local Structure, Journal of Physical Chemistry B 129 (2025) 7557–7566. https://doi.org/10.1021/acs.jpcb.5c02080.

[84] S. Attarian, D. Morgan, I. Szlufarska, Studies of Ni–Cr complexation in FLiBe molten salt using machine learning interatomic potentials, J. Mol. Liq. 400 (2024). https://doi.org/10.1016/j.molliq.2024.124521.

[85] C. Bessada, D. Zanghi, O. Pauvert, L. Maksoud, A. Gil-Martin, V. Sarou-Kanian, P. Melin, S. Brassamin, A. Nezu, H. Matsuura, High temperature EXAFS experiments in molten actinide fluorides: The challenge of a triple containment cell for radioactive and aggressive liquids, Journal of Nuclear Materials 494 (2017) 192–199. https://doi.org/10.1016/j.jnucmat.2017.07.023.

[86] C. Bessada, D. Zanghi, M. Salanne, A. Gil-Martin, M. Gibilaro, P. Chamelot, L. Massot, A. Nezu, H. Matsuura, Investigation of ionic local structure in molten salt fast reactor LiF–ThF_4–UF_4 fuel by EXAFS experiments and molecular dynamics simulations, J. Mol. Liq. 307 (2020) 112927. https://doi.org/10.1016/j.molliq.2020.112927.

[87] A.L. Smith, M.N. Verleg, J. Vlieland, D. de Haas, J.A. Ocadiz-Flores, P. Martin, J. Rothe, K. Dardenne, M. Salanne, A.E. Gheribi, E. Capelli, L. van Eijck, R.J.M. Konings, In situ high-temperature EXAFS measurements on radioactive and air-sensitive molten salt materials, J. Synchrotron Radiat. 26 (2019) 124–136. https://doi.org/10.1107/S160057751801648X.

[88] J.A. Ocádiz-Flores, A.E. Gheribi, J. Vlieland, D. De Haas, K. Dardenne, J. Rothe, R.J.M. Konings, A.L. Smith, Examination of the short-range structure of molten salts: ThF_4, UF_4, and related alkali actinide fluoride systems, Physical Chemistry Chemical Physics 23 (2021) 11091–11103. https://doi.org/10.1039/d1cp00566a.

[89] K.O. Bobrova, V.N. Dokutovich, P.N. Mushnikov, Thermophysical Properties of Several Molten Mixtures of the LiF–BeF_2–UF_4 System, Russian Metallurgy (Metally) 2023 (2023) 126–135. https://doi.org/10.1134/S0036029523020039.

[90] M.A. Rose, L.D. Gardner, T.T. Lichtenstein, S.A. Thomas, E. Wu, Property Measurements of NaCl–UCl_3 and NaCl–KCl–UCl_3 Molten Salts, 2023. http://www.osti.gov/.

[91] M.T. Nguyen, M.E. Woods, J. Schorne-Pinto, N.H. Erfurth, S.C. Middlemas, T. Karlsson, Thermophysical Properties of NaCl–UCl_3–$PuCl_3$ Molten Salts: A Combined Computational and Experimental Study, ACS Appl. Energy Mater. 8 (2025) 6482–6491. https://doi.org/10.1021/acsaem.5c00278.

[92] N. Termini, A. Birri, B. Smith, R. Chesser, J. Numbers, K. Garland, E. Wilgocki, C. Gray, V. Glezakou, FY24 Progress Report on Viscosity and Thermal Conductivity Measurements of Nuclear Industry-Relevant Chloride Salts: An Experimental and Computational Study, 2024. https://www.osti.gov/.

[93] G.W. Morley, Still images from animation of a Hahn Echo, (2011). https://en.wikipedia.org/wiki/Spin_echo#/media/File:SpinEcho_GWM_stills.jpg.

[94] K. Machado, Chimie des Bains pour l'Electrolyse de l'Aluminium : Étude RMN Haute Température et Modélisation, Université d'Orléans, 2017. https://theses.hal.science/tel-01952928v1.

[95] D. Massiot, F. Fayon, M. Capron, I. King, S. Le Calvé, B. Alonso, J.O. Durand, B. Bujoli, Z. Gan, G. Hoatson, Modelling one- and two-dimensional solid-state NMR spectra, Magnetic Resonance in Chemistry 40 (2002) 70–76. https://doi.org/10.1002/mrc.984.

[96] A.L. Rollet, V. Sarou-Kanian, C. Bessada, Self-diffusion coefficient measurements at high temperature by PFG NMR, Comptes Rendus Chimie 13 (2010) 399–404. https://doi.org/10.1016/j.crci.2009.11.005.

[97] D. Massiot, I. Farnan, N. Gautier, D. Trumeau, A. Trokiner, J.P. Coutures, ^{71}Ga and ^{69}Ga nuclear magnetic resonance study of β-Ga_2O_3: resolution of four- and six-fold coordinated Ga sites in static conditions, Solid State Nucl. Magn. Reson. 4 (1995) 241–248. https://doi.org/10.1016/0926-2040(95)00002-8.

[98] Y. Ishii, S. Kasai, M. Salanne, N. Ohtori, Transport coefficients and the Stokes-Einstein relation in molten alkali halides with polarisable ion model, Mol. Phys. 113 (2015) 2442–2450. https://doi.org/10.1080/00268976.2015.1046527.

[99] M.S. Emerson, A.S. Ivanov, L.C. Gallington, D.S. Maltsev, P. Halstenberg, S. Dai, S. Roy, V.S. Bryantsev, C.J. Margulis, Heterogeneous Structure, Mechanisms of Counterion Exchange, and the Spacer Salt Effect in Complex Molten Salt Mixtures Including $LaCl_3$, Journal of Physical Chemistry B 128 (2024) 3972–3980. https://doi.org/10.1021/acs.jpcb.4c01429.

[100] K. Goloviznina, M.C. Notarangelo, J. Tranchida, E. Bourasseau, M. Salanne, DFT-Based Polarizable Ion Models for Molten Rare-Earth Chlorides: From Lanthanum to Europium, Journal of Physical Chemistry B (2025). https://doi.org/10.1021/acs.jpcb.4c07931.

[101] F. Pacaud, J.-M. Delaye, T. Charpentier, L. Cormier, M. Salanne, M.S. Struc, Structural study of Na_2O–B_2O_3–SiO_2 glasses from molecular simulations using a polarizable force field, J. Chem. Phys. 147 (2017). https://doi.org/10.1063/1.4992799.

[102] A. Marin-Laflèche, M. Haefele, L. Scalfi, A. Coretti, T. Dufils, G. Jeanmairet, S. Reed, A. Serva, R. Berthin, C. Bacon, S. Bonella, B. Rotenberg, P. Madden, M. Salanne, MetalWalls: A classical molecular dynamics software dedicated to the simulation of electrochemical systems, J. Open Source Softw. 5 (2020) 2373. https://doi.org/10.21105/joss.02373.

[103] A. Coretti, C. Bacon, R. Berthin, A. Serva, L. Scalfi, I. Chubak, K. Goloviznina, M. Haefele, A. Marin-Laflèche, B. Rotenberg, A.M. Lafi, S. Bonella, M. Salanne, MetalWalls: Simulating electrochemical interfaces between polarizable electrolytes and metallic electrodes, J. Chem. Phys. 157 (2022) 184801. https://doi.org/10.1063/5.0101777ï.

[104] L. Martinez, R. Andrade, E.G. Birgin, J.M. Martínez, PACKMOL: A package for building initial configurations for molecular dynamics simulations, J. Comput. Chem. 30 (2009) 2157–2164. https://doi.org/10.1002/jcc.21224.

[105] M. Brehm, B. Kirchner, TRAVIS - A free analyzer and visualizer for monte carlo and molecular dynamics trajectories, J. Chem. Inf. Model. 51 (2011) 2007–2023. https://doi.org/10.1021/ci200217w.

[106] M. Brehm, M. Thomas, S. Gehrke, B. Kirchner, TRAVIS—A free analyzer for trajectories from molecular simulation, Journal of Chemical Physics 152 (2020). https://doi.org/10.1063/5.0005078.

[107] M. Salanne, C. Simon, P. Turq, P.A. Madden, Conductivity-viscosity-structure: Unpicking the relationship in an ionic liquid, Journal of Physical Chemistry B 111 (2007) 4678–4684. https://doi.org/10.1021/jp067073a.

[108] K. Machado, D. Zanghi, M. Salanne, V. Stabrowski, C. Bessada, Anionic Structure in Molten Cryolite-Alumina Systems, Journal of Physical Chemistry C 122 (2018) 21807–21816. https://doi.org/10.1021/acs.jpcc.8b06905.

[109] C.W. Bale, E. Bélisle, P. Chartrand, S.A. Decterov, G. Eriksson, A.E. Gheribi, K. Hack, I.H. Jung, Y.B. Kang, J. Melançon, A.D. Pelton, S. Petersen, C. Robelin, J. Sangster, P. Spencer, M.A. Van Ende, FactSage thermochemical software and databases, 2010-2016, CALPHAD 54 (2016) 35–53. https://doi.org/10.1016/j.calphad.2016.05.002.

[110] L. Ercole, R. Bertossa, S. Bisacchi, S. Baroni, SporTran: A code to estimate transport coefficients from the cepstral analysis of (multivariate) current time series, Comput. Phys. Commun. 280 (2022). https://doi.org/10.1016/j.cpc.2022.108470.

[111] I.C. Yeh, G. Hummer, System-size dependence of diffusion coefficients and viscosities from molecular dynamics simulations with periodic boundary conditions, Journal of Physical Chemistry B 108 (2004) 15873–15879. https://doi.org/10.1021/jp0477147.

[112] E.J. Maginn, R.A. Messerly, D.J. Carlson, D.R. Roe, J.R. Elliot, Best Practices for Computing Transport Properties 1. Self-Diffusivity and Viscosity from Equilibrium Molecular Dynamics [Article v1.0], Living J. Comput. Mol. Sci. 2 (2020). https://doi.org/10.33011/livecoms.1.1.6324.

[113] P. Hohenberg, W. Kohn, Inhomogeneous Electron Gas, Physical Review 136 (1964) 864–871. https://doi.org/10.1103/PhysRev.136.B864.

[114] S.L. Dudarev, G.A. Botton, S.Y. Savrasov, C.J. Humphreys, A.P. Sutton, Electron-energy-loss spectra and the structural stability of nickel oxide: An LSDA+U study, Phys. Rev. B 57 (1998) 1505–1509. https://doi.org/10.1103/PhysRevB.57.1505.

[115] J. Hafner, Ab-initio simulations of materials using VASP: Density-functional theory and beyond, J. Comput. Chem. 29 (2008) 2044–2078. https://doi.org/10.1002/jcc.21057.

[116] J.P. Perdew, K. Burke, M. Ernzerhof, Generalized Gradient Approximation Made Simple, Physics Review Letters 77 (1996) 3865–3868. https://doi.org/10.1103/PhysRevLett.77.3865.

[117] Choosing pseudopotentials, (n.d.). https://www.vasp.at/wiki/Choosing_pseudopotentials (accessed February 9, 2026).

[118] C.M. Widdifield, R.P. Chapman, D.L. Bryce, Chapter 5 Chlorine, Bromine, and Iodine Solid-State NMR Spectroscopy, in: Annu. Rep. NMR Spectrosc., 2009: pp. 195–326. https://doi.org/10.1016/S0066-4103(08)00405-5.

[119] T.J. Bastow, S.N. Stuart, ^{17}O NMR in simple oxides, Chem. Phys. 143 (1990) 459–467. https://doi.org/10.1016/0301-0104(90)87025-7.

[120] K.J. Ooms, K.W. Feindel, M.J. Willans, R.E. Wasylishen, J. V. Hanna, K.J. Pike, M.E. Smith, Multiple-magnetic field ^{139}La NMR and density functional theory investigation of the solid lanthanum(III) halides, Solid State Nucl. Magn. Reson. 28 (2005) 125–134. https://doi.org/10.1016/j.ssnmr.2005.07.002.

[121] L. Spencer, E. Coomes, E. Ye, V. Terskikh, A. Ramzy, V. Thangadurai, G.R. Goward, Structural analysis of lanthanum-containing battery materials using ^{139}La solid-state NMR, Can. J. Chem. 89 (2011) 1105–1117. https://doi.org/10.1139/v11-049.

[122] H.J. Seifert, H. Fink, B. Baumgartner, Structure and Stability of the Low-Temperature Modification of Compounds Cs_3LnCl_6 (Ln = La–Gd), J. Solid State Chem. 107 (1993) 19–26. https://doi.org/10.1006/jssc.1993.1318.

[123] F. Hutchinson, A.J. Rowley, M.K. Walters, M. Wilson, P.A. Madden, J.C. Wasse, P.S. Salmon, Structure of molten MCl_3 systems from a polarizable ion simulation model, Journal of Chemical Physics 111 (1999) 2028–2037. https://doi.org/10.1063/1.479471.

[124] A.L. Rollet, S. Godier, C. Bessada, High temperature NMR study of the local structure of molten LaF_3–AF (A = Li, Na, K and Rb) mixtures, Physical Chemistry Chemical Physics 10 (2008) 3222–3228. https://doi.org/10.1039/b719158h.

[125] D. Corradini, P.A. Madden, M. Salanne, Coordination numbers and physical properties in molten salts and their mixtures, Faraday Discuss. 190 (2016) 471–486. https://doi.org/10.1039/c5fd00223k.

[126] D. Hudry, A. Rakhmatullin, C. Bessada, I. Bardez, F. Bart, S. Jobic, P. Deniard, Reactivity of $NH_4H_2PO_4$ toward $LaCl_3$ in LiCl–KCl melt flux. Step by step formation of monazite-like $LaPO_4$., Inorg. Chem. 48 (2009) 7141–7150. https://doi.org/10.1021/ic9003142.

[127] H. Zhang, I. Farnan, High temperature ^{35}Cl nuclear magnetic resonance study of the LiCl–KCl system and the effect of $CeCl_3$ dissolution, Faraday Discuss. 190 (2016) 367–385. https://doi.org/10.1039/c6fd00003g.

[128] M.S. Emerson, S. Sharma, S. Roy, V.S. Bryantsev, A.S. Ivanov, R. Gakhar, M.E. Woods, L.C. Gallington, S. Dai, D.S. Maltsev, C.J. Margulis, Complete Description of the $LaCl_3$–NaCl Melt Structure and the Concept of a Spacer Salt That Causes Structural Heterogeneity, J. Am. Chem. Soc. 144 (2022) 21751–21762. https://doi.org/10.1021/jacs.2c09987.

[129] B. Morosin, Crystal structures of anhydrous rare-earth chlorides, J. Chem. Phys. 49 (1968) 3007–3012. https://doi.org/10.1063/1.1670543.

[130] C.M. Schurz, T. Schleid, G. Meyer, K_2LaCl_5, Acta Crystallogr. Sect. E Struct. Rep. Online 66 (2010). https://doi.org/10.1107/S1600536810045198.

[131] I.N. Flerov, M. V Gorev, K.S. Aleksandrov, A. Tressaud, J. Grannec, M. Couzi, Phase transitions in elpasolites (ordered perovskites), Materials Science and Engineering : R: Reports 24 (1998) 81–151. https://doi.org/10.1016/S0927-796X(98)00015-1.

[132] A. Rakhmatullin, F. Šimko, E. Véron, M. Allix, C. Martineau-Corcos, A. Fitch, F. Fayon, R.A. Shakhovoy, K. Okhotnikov, V. Sarou-Kanian, M. Korenko, Z. Netriová, I.B. Polovov, C. Bessada, X-ray Diffraction, NMR Studies, and DFT Calculations of the Room and High Temperature Structures of Rubidium Cryolite, Rb_3AlF_6, Inorg. Chem. 59 (2020) 6308–6318. https://doi.org/10.1021/acs.inorgchem.0c00415.

[133] A. Rakhmatullin, M.S. Molokeev, G. King, I.B. Polovov, K. V. Maksimtsev, E. Chesneau, E. Suard, R. Bakirov, F. Šimko, C. Bessada, M. Allix, Polymorphs of Rb_3ScF_6: X-ray and Neutron Diffraction, Solid-State NMR, and Density Functional Theory Calculations Study, Inorg. Chem. 60 (2021) 6016–6026. https://doi.org/10.1021/acs.inorgchem.1c00485.

[134] K. Igarashi, H. Ohtani, J. Mochinaga, Phase Diagram of the System $LaCl_3$–$CaCl_2$–NaCl, Z. Naturforsch 42a (1987) 1421–1424. https://doi.org/10.1515/zna-1987-1212.

[135] Y. Wang, X. Hu, T. Huang, C. Tian, Thermodynamic optimization and calculation of $LaCl_3$–$MgCl_2$ system, Asian Journal of Chemistry 26 (2014) 1655–1657. https://doi.org/10.14233/ajchem.2014.17315.

[136] D.E. Partin, M. O'Keeffe, The Structures and Crystal Chemistry of Magnesium Chloride and Cadmium Chloride, J. Solid State Chem. 95 (1991) 176–183. https://doi.org/10.1016/0022-4596(91)90387-W.

[137] A.L. Rollet, E. Veron, C. Bessada, Fission products behavior in molten fluoride salts: Speciation of La^{3+} and Cs^+ in melts containing oxide ions, Journal of Nuclear Materials 429 (2012) 40–47. https://doi.org/10.1016/j.jnucmat.2012.05.010.

[138] X. Song, S. Li, S. Liu, Y. Fan, J. He, J. Song, Coordination states of metal ions in molten salts and their characterization methods, International Journal of Minerals, Metallurgy and Materials 30 (2023) 1261–1277. https://doi.org/10.1007/s12613-023-2608-7.

[139] C.F. Bonilla, Nuclear Engineering Handbook, in: McGraw-Hill, New York, 1958: pp. 9–90.

[140] K. Kim, Viscosities of $LaCl_3$–NaCl Binary Melts, Journal of the Korean Institute of Surface Engineering (2006) 282–287.

[141] K. Kim, Viscosities of $LaCl_3$–CsCl Binary Melts, Journal of the Korean Institute of Surface Engineering 46 (2013) 87–92. https://doi.org/10.5695/jkise.2013.46.2.087.

[142] G.J. Janz, Molten Salts Data as Reference Standards for Density, Surface Tension, Viscosity, and Electrical Conductance: KNO_3 and NaCl, J. Phys. Chem. Ref. Data 9 (1980) 791–830. https://doi.org/10.1063/1.555634.

[143] W. Brockner, K. Torklep, H.A. Oye, Viscosity of Molten Alkali Chlorides, J. Chem. Eng. Data 26 (1981) 250–253. https://doi.org/10.1021/je00025a007.

[144] A. Potapov, Y. Sato, Viscosity of molten rare earth metal trichlorides II. Cerium subgroup, Zeitschrift Fur Naturforschung - Section A Journal of Physical Sciences 66 (2011) 649–655. https://doi.org/10.5560/ZNA.2011-0016.

[145] G.J. Janz, N.P. Bansal, Molten Salts Data: Diffusion Coefficients in Single and Multi-Component Salt Systems, Journal of Physical Chemistry Reference Data 11 (1982) 1982. https://doi.org/doi.org/10.1063/1.555665.

[146] R.D. Shannon, Revised Effective Ionic Radii and Systematic Studies of Interatomic Distances in Halides and Chalcogenides, Acta Crystallogr. A32 (1976) 751–767. https://doi.org/10.1107/S0567739476001551.

[147] R. Brookes, A. Davies, G. Ketwaroo, P.A. Madden, Diffusion coefficients in ionic liquids: Relationship to the viscosity, Journal of Physical Chemistry B 109 (2005) 6485–6490. https://doi.org/10.1021/jp046355c.

[148] F. Wu, S. Sharma, S. Roy, P. Halstenberg, L.C. Gallington, S.M. Mahurin, S. Dai, V.S. Bryantsev, A.S. Ivanov, C.J. Margulis, Temperature Dependence of Short and Intermediate Range Order in Molten $MgCl_2$ and Its Mixture with KCl, Journal of Physical Chemistry B 124 (2020) 2892–2899. https://doi.org/10.1021/acs.jpcb.0c00745.

[149] T. Allen, J. Busby, M. Meyer, D. Petti, Materials challenges for nuclear systems, Materials Today 13 (2010) 14–23. https://doi.org/10.1016/S1369-7021(10)70220-0.

[150] Y. V. Harinath, T.V.K. Mohan, S. Rangarajan, S.K. Albert, Structural Materials for Molten Salt Reactors, in: A Treatise on Corrosion Science, Engineering, and Technology. Indian Institute of Metals Series, Springer, Singapore., 2022: pp. 169–191. https://doi.org/10.1007/978-981-16-9302-1_10.

[151] R.N. Wright, T.-L. Sham, Status of Metallic Structural Materials for Molten Salt Reactors, 2018. http://www.inl.gov (accessed October 1, 2025).

[152] G. Zheng, K. Sridharan, Corrosion of Structural Alloys in High-Temperature Molten Fluoride Salts for Applications in Molten Salt Reactors, JOM 70 (2018) 1535–1541. https://doi.org/10.1007/s11837-018-2981-2.

[153] A.I. Surenkov, S.S. Abalin, P.N. Ivliev, V. V. Ignatiev, K.S. Klimov, A.S. Subbotin, I.N. Trunkin, V.S. Uglov, Experimental Study of Corrosion Resistance of Nickel-Molybdenum Alloys in the Melt of Lithium and Beryllium Fluoride Salts, Physics of Atomic Nuclei 87 (2024) 1176–1186. https://doi.org/10.1134/S1063778824080131.

[154] J. Zhang, C.W. Forsberg, M.F. Simpson, S. Guo, S.T. Lam, R.O. Scarlat, F. Carotti, K.J. Chan, P.M. Singh, W. Doniger, K. Sridharan, J.R. Keiser, Redox potential control in molten salt systems for corrosion mitigation, Corros. Sci. 144 (2018) 44–53. https://doi.org/10.1016/j.corsci.2018.08.035.

[155] S.A. Walker, M.E. Tano, A. Abou-Jaoude, O. Calvin, Depletion-driven thermochemistry of molten salt reactors: review, method, and analysis, Frontiers in Nuclear Engineering 2 (2023). https://doi.org/10.3389/fnuen.2023.1214727.

[156] S. Delpech, C. Carrière, A. Chmakoff, L. Martinelli, D. Rodrigues, C. Cannes, Corrosion Mitigation in Molten Salt Environments, Materials 17 (2024). https://doi.org/10.3390/ma17030581.

[157] C. Kim, A. Couet, In Situ Monitoring of Molten Chloride Salt Chemistry and Corrosion Using a Microelectrode, J. Am. Chem. Soc. 147 (2025) 19013–19025. https://doi.org/10.1021/jacs.5c03651.

[158] H. Xu, Thorium Energy and Molten Salt R&D in China, in: Thorium Energy for the World, Geneva, Switzerland, 2016: pp. 37–44. https://doi.org/10.1007/978-3-319-26542-1.

[159] R.T. Mayes, J.M. Kurley, P.W. Halstenberg, A. Mcalister, D. Sulejmanovic, S. Raiman, S. Dai, B. Pint, Purification of Chloride Salts for Concentrated Solar Power Applications, 2018. www.osti.gov (accessed October 1, 2025).

[160] A. Burak, S. Raiman, Parametric Study of Metallothermic Purification of Chloride Salts, ACS Omega (2025). https://doi.org/10.1021/acsomega.5c03893.

[161] S.S. Raiman, S. Lee, Aggregation and data analysis of corrosion studies in molten chloride and fluoride salts, Journal of Nuclear Materials 511 (2018) 523–535. https://doi.org/10.1016/j.jnucmat.2018.07.036.

[162] J.M. Kurley, P.W. Halstenberg, A. McAlister, S. Raiman, S. Dai, R.T. Mayes, Enabling chloride salts for thermal energy storage: Implications of salt purity, RSC Adv. 9 (2019) 25602–25608. https://doi.org/10.1039/c9ra03133b.

[163] K.J. Cathro, R.L. Deutscher, R.A. Sharma, Electrowinning magnesium from its oxide in a melt containing neodymium chloride, J. Appl. Electrochem. 27 (1997) 404–413. https://doi.org/10.1023/A:1018457503240.

[164] O. Beneš, R.J.M. Konings, Molten salt reactor fuel and coolant, Elsevier Inc., 2012. https://doi.org/10.1016/B978-0-08-056033-5.00062-8.

[165] H. Mediaas, O. Tkatcheva, V. Dracopoulos, G.N. Papatheodorou, G.J. Kipouros, T. Østvold, Solubilities and Raman Spectra of NdOCl in Some Chloride Melts of Interest for the Electrowinning of Magnesium from Its Oxide, Metallurgical and Materials Transactions B 31B (2000) 631–639. https://doi.org/10.1007/s11663-000-0101-4.

[166] B. Li, J. Li, J. Chen, J. Yu, Solubility of MgO in chloride melts containing $NdCl_3$ or $LaCl_3$, Natural Resources and Environmental Issues 15 (2009) 209–213.

[167] H. Meskine, J. Serp, Rôle de $MgCl_2$, ISAC Internal Presentation - Unpublished Work. (2024).

[168] A.F. Vik, V. Dracopoulos, G.N. Papatheodorou, T. Østvold, Solubility and Raman spectra of Nb(V) in LiF–NaF–KF–Na_2O melts, J. Alloys Compd. 321 (2001) 284–299. https://doi.org/10.1016/S0925-8388(01)00968-9.

[169] X. Liu, B. Wang, H. Fu, C. Wang, Raman spectroscopic and theoretical studies on the structure of Ta (V) fluoro and oxofluoro complexes in molten FLiNaK, J. Mol. Liq. 337 (2021). https://doi.org/10.1016/j.molliq.2021.116409.

[170] E. Stefanidaki, G.M. Photiadis, C.G. Kontoyannis, A.F. Vik, T. Østvold, Oxide solubility and Raman spectra of NdF_3–LiF–KF–MgF_2–Nd_2O_3 melts, Journal of the Chemical Society, Dalton Transactions (2002) 2302–2307. https://doi.org/10.1039/b111563b.

[171] X. Chen, H. Fu, C. Wang, Influence of oxide ions on the speciation in molten KF–ZrF_4 and KF–HfF_4: A Raman spectroscopic and theoretical investigation, J. Mol. Liq. 342 (2021). https://doi.org/10.1016/j.molliq.2021.117476.

[172] X. Liu, Y. Li, B. Wang, C. Wang, Raman and density functional theory studies of lutecium fluoride and oxyfluoride structures in molten FLiNaK, Spectrochim. Acta A Mol. Biomol. Spectrosc. 251 (2021). https://doi.org/10.1016/j.saa.2021.119435.

[173] A.L. Rollet, H. Matsuura, C. Bessada, An in situ spectroscopic study of the local structure of oxyfluoride melts: NMR insights into the speciation in molten LiF–LaF_3–Li_2O systems, Dalton Transactions 44 (2015) 522–529. https://doi.org/10.1039/c4dt00926f.

[174] S. Park, J. Yun, An in-situ Raman spectroscopic study on potential-p_{O2-} phase diagram of lanthanum in LiCl–KCl eutectic melt, Journal of Rare Earths 38 (2020) 793–800. https://doi.org/10.1016/j.jre.2019.06.008.

[175] V. Smolenski, A. Novoselova, Thermodynamic properties and the solubility of the oxide lanthanum compounds in fused 0.36NaCl–0.64CsCl eutectic, Journal of Chemical Thermodynamics 163 (2021). https://doi.org/10.1016/j.jct.2021.106583.

[176] W.W. Wendlandt, The Thermal Decomposition of Yttrium, Scandium, and Some Rare-earth Chloride Hydrates, Journals of Inorganic Nuclear Chemistry 5 (1957) 118–122. https://doi.org/10.1016/0022-1902(57)80052-9.

[177] J. Holsa, M. Lastusaari, J. Valkonen, X-ray powder diffraction study of the stability of solid solutions in $LaO(Cl_{1-x}Br_x)$, J. Alloys Compd. 262~263 (1997) 299–304. https://doi.org/10.1016/S0925-8388(97)00469-6.

[178] K. Duemmler, M. Woods, T. Karlsson, R. Gakhar, B. Beeler, An ab initio molecular dynamics investigation of the thermophysical properties of molten NaCl–$MgCl_2$, Journal of Nuclear Materials 570 (2022). https://doi.org/10.1016/j.jnucmat.2022.153916.

[179] X. Wu, Y. Zhang, J. Zhang, R. Liu, J. Yang, B. Yang, H. Xu, Y. Ma, High pressure X-ray diffraction study of sodium oxide (Na_2O): Observations of amorphization and equation of state measurements to 15.9 GPa, J. Alloys Compd. 823 (2020). https://doi.org/10.1016/j.jallcom.2020.153793.

[180] V.G. Tsirelson, A.S. Avilov, Y.A. Abramov, E.L. Belokoneva, R. Io'raneh, A.D. Feil, X-ray and Electron Diffraction Study of MgO, Acta Cryst 54 (1998) 8–17. https://doi.org/10.1107/S0108768197008963.

[181] C.N. Chervin, B.J. Clapsaddle, H.W. Chiu, A.E. Gash, J.H. Satcher, S.M. Kauzlarich, A non-alkoxide sol-gel method for the preparation of homogeneous nanocrystalline powders of $La_{0.85}Sr_{0.15}MnO_3$, Chemistry of Materials 18 (2006) 1928–1937. https://doi.org/10.1021/cm052301j.

[182] B. Monserrat, R.J. Needs, C.J. Pickard, Temperature effects in first-principles solid state calculations of the chemical shielding tensor made simple, Journal of Chemical Physics 141 (2014). https://doi.org/10.1063/1.4897261.

[183] Z. Han, C. Lee, J. Song, H. Wang, P. Bermel, X. Ruan, Temperature-dependent full spectrum dielectric function of semiconductors from first principles, Phys. Rev. B 107 (2023). https://doi.org/10.1103/PhysRevB.107.L201202.

[184] N.T. Barrett, G.N. Greaves, T.M. Willis, G.M. Antoninill, F.R. Thornley, Anharmonic vibrations in UO_2, as determined by EXAFS, J. Phys. C: Solid State Phys 21 (1988) 791–796. https://doi.org/10.1088/0022-3719/21/22/004.

[185] J. Vĺcha, J. Novotný, S. Komorovsky, M. Straka, M. Kaupp, R. Marek, Relativistic Heavy-Neighbor-Atom Effects on NMR Shifts: Concepts and Trends across the Periodic Table, Chem. Rev. 120 (2020) 7065–7103. https://doi.org/10.1021/acs.chemrev.9b00785.

[186] D.S. Maltsev, D.M. Driscoll, Y. Zhang, J.C. Neuefeind, B. Reinhart, C. Agca, D. Ray, P.W. Halstenberg, M. Aziziha, J. Schorne-Pinto, T.M. Besmann, V.S. Bryantsev, S. Dai, S. Roy, A.S. Ivanov, Transient Covalency in Molten Uranium(III) Chloride, J. Am. Chem. Soc. 146 (2024) 21220–21224. https://doi.org/10.1021/jacs.4c05765.

[187] H. Cho, W.A. De Jong, C.Z. Soderquist, Probing the oxygen environment in UO_2^{2+} by solid-state O^{17} nuclear magnetic resonance spectroscopy and relativistic density functional calculations, Journal of Chemical Physics 132 (2010). https://doi.org/10.1063/1.3308499.

[188] D.E. Smiles, G. Wu, P. Hrobárik, T.W. Hayton, Use of ^{77}Se and ^{125}Te NMR Spectroscopy to Probe Covalency of the Actinide-Chalcogen Bonding in $[Th(E_n)\{N(SiMe_3)_2\}_3]^-$ (E = Se, Te; n = 1, 2) and Their Oxo-Uranium(VI) Congeners, J. Am. Chem. Soc. 138 (2016) 814–825. https://doi.org/10.1021/jacs.5b07767.

[189] D. Reta, F. Ortu, S. Randall, D.P. Mills, N.F. Chilton, R.E.P. Winpenny, L. Natrajan, B. Edwards, N. Kaltsoyannis, The performance of density functional theory for the description of ground and excited state properties of inorganic and organometallic uranium compounds, J. Organomet. Chem. 857 (2018) 58–74. https://doi.org/10.1016/j.jorganchem.2017.09.021.

[190] D.A. Andersson, B.W. Beeler, Ab initio molecular dynamics (AIMD) simulations of NaCl, UCl_3 and NaCl–UCl_3 molten salts, Journal of Nuclear Materials 568 (2022). https://doi.org/10.1016/j.jnucmat.2022.153836.

[191] S. Paul, S. Attarian, D. Andersson, D. Morgan, I. Szlufarska, A molecular dynamics study on local structural features and thermophysical properties of the NaCl–UCl_3 molten salt with machine learning potential, J. Mol. Liq. 456 (2026). https://doi.org/10.1016/j.molliq.2026.129638.

[192] A.L. Ankudinov, B. Ravel, J.J. Rehr, S.D. Conradson, Real-space multiple-scattering calculation and interpretation of x-ray-absorption near-edge structure, 1998. https://doi.org/10.1103/PhysRevB.58.7565.

[193] C. Bessada, D. Zanghi, M. Salanne, A. Gil-Martin, M. Gibilaro, P. Chamelot, L. Massot, A. Nezu, H. Matsuura, Investigation of ionic local structure in molten salt fast reactor LiF–ThF_4–UF_4 fuel by EXAFS experiments and molecular dynamics simulations, J. Mol. Liq. 307 (2020) 112927. https://doi.org/10.1016/j.molliq.2020.112927.

Annexes

Annexe-A: Measured and Calculated Transport Properties

Table A1. Calculated viscosities ($\pm 1\sigma$-uncertainty) of the NaCl–$LaCl_3$ binary system from MD simulations at 850 and 927 °C.

$LaCl_3$ mole fraction, x_{LaCl_3}	Viscosity, η(mPa·s)	
	850 °C	927 °C
0	1.043 ± 0.013	0.963 ± 0.011
0.05	1.202 ± 0.015	1.032 ± 0.014
0.20	1.632 ± 0.026	1.347 ± 0.019
0.35	2.262 ± 0.044	1.725 ± 0.025
0.50	2.692 ± 0.052	2.092 ± 0.035
0.65	3.179 ± 0.066	2.428 ± 0.039
0.80	3.274 ± 0.055	2.848 ± 0.051
0.95	3.634 ± 0.067	2.945 ± 0.050
1	3.645 ± 0.067	2.939 ± 0.052

Table A2. Measured Na^+ diffusion coefficients ($\pm 1\sigma$-uncertainty) of the NaCl–$LaCl_3$ binary system using PFG–NMR at 850 °C.

$LaCl_3$ mole fraction, x_{LaCl_3}	Na^+ Diffusion Coefficient, D_{Na} (10^{-9} m^2/s) ± one-sigma uncertainty
0	9.063 ± 0.067
0.05	8.761 ± 0.296
0.20	8.286 ± 0.094
0.35	7.068 ± 0.296
0.50	5.619 ± 0.062
0.65	4.962 ± 0.293
0.80	4.557 ± 0.152

Table A3. Calculated boxlength, viscosity and diffusion coefficients from MD simulations at 850 °C.

Composition (mole fraction)			L(Å)	η(mPa·s)	Diffusion Coefficients ($\times 10^{-9}\ m^2/s$)			
NaCl	$MgCl_2$	$LaCl_3$			$D_{Na,\infty}$	$D_{Mg,\infty}$	$D_{La,\infty}$	$D_{Cl,\infty}$
0	0	1	50.527	3.645	–	–	1.317	2.084
0.05	0	0.95	50.007	3.634	4.219	–	1.293	2.042
0.2	0	0.8	48.586	3.274	4.525	–	1.328	2.200
0.35	0	0.65	47.375	3.179	5.099	–	1.452	2.455
0.5	0	0.5	45.765	2.692	5.459	–	1.631	2.771

0.65	0	0.35	44.308	2.262	6.424	–	1.858	3.292
0.8	0	0.2	42.659	1.628	7.569	–	2.377	3.915
0.95	0	0.05	40.446	1.202	8.703	–	3.101	6.370
1	0	0	39.977	1.043	9.579	–	–	7.737
0.16	0.04	0.8	48.843	3.29	4.838	2.467	1.361	2.235
0	0.05	0.95	50.324	3.557	–	2.165	1.335	2.102
0.95	0.05	0	39.988	1.091	9.099	4.818	–	7.222
0.28	0.07	0.65	47.402	3.262	4.738	2.423	1.402	2.368
0.1	0.1	0.8	49.083	3.356	4.780	2.264	1.393	2.255
0.4	0.1	0.5	46.295	2.644	5.771	2.665	1.669	2.833
0.52	0.13	0.35	44.903	2.105	6.577	3.067	1.982	3.374
0.04	0.16	0.8	49.436	3.08	5.278	2.521	1.478	2.349
0.64	0.16	0.2	43.521	1.669	7.712	3.534	2.402	4.319
0.18	0.17	0.65	47.967	2.977	5.440	2.509	1.543	2.511
0.76	0.19	0.05	41.738	1.198	8.905	4.301	2.977	5.710
0	0.2	0.8	49.57	3.194	–	2.522	1.491	2.358
0.8	0.2	0	40.964	1.117	9.086	4.655	–	6.526
0.25	0.25	0.5	46.861	2.449	5.964	2.870	1.720	2.885
0.07	0.28	0.65	48.447	2.917	5.954	2.647	1.578	2.588
0.325	0.325	0.35	46.014	2.042	7.395	3.322	2.146	3.551
0	0.35	0.65	49.139	2.713	–	2.844	1.738	2.740
0.1	0.4	0.5	47.494	2.578	6.345	2.948	1.808	2.927
0.4	0.4	0.2	44.635	1.664	8.066	3.757	2.489	4.178
0.48	0.47	0.05	43.461	1.238	9.543	4.483	3.113	5.417
0.05	0.48	0.47	47.943	2.322	7.822	3.148	1.988	3.158
0	0.5	0.5	48.116	2.366	–	3.119	1.935	3.022
0.5	0.5	0	42.949	1.121	9.706	4.662	–	5.891
0.13	0.52	0.35	47.061	1.996	8.344	3.411	2.117	3.547
0.16	0.64	0.2	45.736	1.656	8.852	3.827	2.499	4.083
0	0.65	0.35	47.537	1.985	–	3.527	2.240	3.576
0.19	0.76	0.05	44.844	1.367	10.317	4.544	2.867	4.992
0	0.8	0.2	47.015	1.677	–	4.053	2.630	4.193
0.2	0.8	0	44.921	1.169	11.340	4.778	–	5.525
0	0.95	0.05	46.368	1.31	–	4.628	3.214	5.010
0.05	0.95	0	45.818	1.236	11.923	4.831	–	5.282
0	1	0	46.040	1.179	–	4.804	–	5.326

Annexe-B: Measured and Calculated Chemical Shifts in NaCl–$MgCl_2$–$LaCl_3$–LaOCl

Table B1. Predicted and measured (± spectral fitting uncertainty) chemical shift values for the (80-α) NaCl–α $MgCl_2$–15 $LaCl_3$–5 LaOCl molten salt system (α=0–80).

NaCl:$MgCl_2$ ratio	Chemical Shift Values, δ (ppm)					
	^{139}La		^{35}Cl		^{17}O	
	Predicted (850 °C)	Measured (850 °C)	Predicted (850 °C)	Measured (850 °C)	Predicted (850 °C)	Measured (1000 °C)
0 : 80	586.2	691 ± 1	110.4	111 ± 1	602.5	419 ± 45
16 : 64	584.6	664 ± 1	124.9	106 ± 1	543.0	355 ± 14
40 : 40	551.8	604 ± 1	138.3	121 ± 1	513.5	307 ± 18
64 : 16	564.8	569 ± 2	142.8	123 ± 1	408.1	270 ± 4
80 : 0	527.2	563 ± 3	146.1	124 ± 1	455.6	289 ± 3

Table B2. Predicted and measured (± spectral fitting uncertainty) chemical shift values for the (80-α) NaCl–α $MgCl_2$–16 $LaCl_3$–4 LaOCl molten salt system (α=0–80).

NaCl:$MgCl_2$ ratio	Chemical Shift Values, δ (ppm)					
	^{139}La		^{35}Cl		^{17}O	
	Predicted (850 °C)	Measured (850 °C)	Predicted (850 °C)	Measured (850 °C)	Predicted (850 °C)	Measured (1000 °C)
0 : 80	605.7	685 ± 1	112.6	123 ± 1	603.8	433 ± 9
16 : 64	579.3	654 ± 1	127.2	121 ± 1	556.0	371 ± 20
40 : 40	587.1	601 ± 1	134.4	127 ± 1	468.9	358 ± 3
64 : 16	558.1	571 ± 2	145.5	127 ± 1	445.2	305 ± 4
80 : 0	557.1	568 ± 2	148.9	130 ± 2	380.4	303 ± 5

Table B3. Predicted and measured (± spectral fitting uncertainty) chemical shift values for the (80-α) NaCl–α $MgCl_2$–17 $LaCl_3$–3 LaOCl molten salt system (α=0–80).

NaCl:$MgCl_2$ ratio	Chemical Shift Values, δ (ppm)					
	^{139}La		^{35}Cl		^{17}O	
	Predicted (850 °C)	Measured (850 °C)	Predicted (850 °C)	Measured (850 °C)	Predicted (850 °C)	Measured (1000 °C)
0 : 80	616.1	682 ± 1	124.2	115 ± 1	600.5	481 ± 40
16 : 64	601.6	658 ± 2	129.6	112 ± 1	557.2	412 ± 12
40 : 40	589.2	596 ± 2	140.7	123 ± 1	450.4	334 ± 6
64 : 16	556.5	563 ± 3	148.4	120 ± 1	454.0	271 ± 9
80 : 0	563.9	567 ± 2	148.7	137 ± 2	452.5	320 ± 6

Table B4. Predicted and measured (± spectral fitting uncertainty) chemical shift values for the (80-α) NaCl–α $MgCl_2$–18 $LaCl_3$–2 LaOCl molten salt system (α=0–80).

NaCl:$MgCl_2$ ratio	Chemical Shift Values, δ (ppm)					
	^{139}La		^{35}Cl		^{17}O	
	Predicted (850 °C)	Measured (850 °C)	Predicted (850 °C)	Measured (850 °C)	Predicted (850 °C)	Measured (1000 °C)
0 : 80	633.9	678 ± 1	131.9	125 ± 1	598.3	–
16 : 64	614.7	644 ± 2	137.5	129 ± 1	547.2	362 ± 28
40 : 40	581.8	600 ± 2	151.0	131 ± 1	490.2	326 ± 5
64 : 16	581.6	559 ± 3	150.6	127 ± 2	432.9	271 ± 19
80 : 0	573.0	566 ± 4	152.8	133 ± 1	390.4	286 ± 6

Table B5. Predicted and measured (± spectral fitting uncertainty) chemical shift values for the (80-α) NaCl–α $MgCl_2$–19 $LaCl_3$–1 LaOCl molten salt system (α=0–80).

NaCl:$MgCl_2$ ratio	Chemical Shift Values, δ (ppm)					
	^{139}La		^{35}Cl		^{17}O	
	Predicted (850 °C)	Measured (850 °C)	Predicted (850 °C)	Measured (850 °C)	Predicted (850 °C)	Measured (1000 °C)
0 : 80	658.4	667 ± 1	137.5	134 ± 1	617.4	–
16 : 64	634.7	642 ± 1	141.9	131 ± 1	553.4	405 ± 21
40 : 40	607.2	600 ± 2	150.1	134 ± 1	430.8	329 ± 9
64 : 16	592.2	563 ± 3	152.8	128 ± 2	365.7	313 ± 17
80 : 0	590.2	569 ± 2	152.0	133 ± 1	379.3	298 ± 14

Annexe-C: Scripts for First Principles NMR Calculations of Molten Salt Systems

Script C1 "extract_frames_to_cif.py" - Python script for extracting CIF files from an MD trajectory file.

```
# Outputs CIF file format of the frames in trajectory_file according to the
indices specified in frame_indices

from ase.io import read, write

# === CONFIGURATION ===
trajectory_file = "trajectories.lammpstrj"           # Path to your LAMMPS
trajectory file
frame_indices = [500, 1000, 1500, 2000, 2500, 3000, 3500, 4000, 4500, 5000]  #
Customize this list
output_prefix = "NaMgLa_64_16_20_"                  # Edit based on file.

# === PROCESSING ===
# Load the trajectory
print("Reading trajectory...")
frames = read(trajectory_file, index=':')  # Read all frames

print(f"Total frames available: {len(frames)}")
print(f"Extracting {len(frame_indices)} frames...")

# Write selected frames
for i in frame_indices:
    if i < len(frames):
        out_file = f"{output_prefix}{i}.cif"
        write(out_file, frames[i])
        print(f"Frame {i} saved as {out_file}")
    else:
        print(f"Warning: Frame index {i} is out of bounds.")
```

Script C2 "convert_cif_to_vasp.py"- Python script for converting a batch of CIF files into VASP POSCAR format.

```
import os
from ase.io import read, write

# Loop over all .cif files in the current directory
for filename in os.listdir('.'):
    if filename.endswith('.cif'):
        base = os.path.splitext(filename)[0]
        cif_file = filename
        vasp_file = f"{base}.vasp"

        try:
            atoms = read(cif_file)
            write(vasp_file, atoms, format='vasp', direct=True, vasp5=True)
            print(f"Converted {cif_file} → {vasp_file}")
        except Exception as e:
            print(f"Failed to convert {cif_file}: {e}")
```

Script C3 "extract_shifts.sh"- Bash script for extracting CSA tensors from OUTCAR files in the sub-directories.

```
#!/bin/bash

#Final version modifed by WJ on 19 June 2025.
#Run by bash command in Main Directory. Output File generated by reading CSA
Tensors in OUTCAR files in sub-directory.

#Output file
main_dir=$(basename "$PWD")
output_file="CSA_shifts_${main_dir}.csv"
echo "CSA Tensor Summary" > "$output_file"
echo "==================" >> "$output_file"

total_atoms=0

# Loop through each subdirectory
for subdir in */; do
  echo "Processing directory: $subdir"

  # Make sure POSCAR exists before reading
  if [[ -f "${subdir}/POSCAR" ]]; then
    # Extract ion counts from line 7
    ion_counts=($(sed -n '7p' "$subdir/POSCAR"))

    #total_atoms=0

    #echo "Ion counts in ${subdir}/POSCAR:"
    for count in "${ion_counts[@]}"; do
      clean_count=$(echo "$count" | tr -cd '0-9')
```

```
      #echo "  Raw Count: '$count' | Cleaned Count: '$clean_count'"
      if [[ -n "$clean_count" ]]; then
        total_atoms=$((total_atoms + clean_count))
      fi
     #echo "Total atoms: $total_atoms"
    done

    #echo "Total atoms: $total_atoms"

    nlines=$((total_atoms + 6))
    #echo "Subdir: $subdir"
    #echo "Number of lines: $nlines"

    if [[ -f "${subdir}/OUTCAR" ]]; then
        echo "Directory: $subdir" >> "$output_file"
        echo "--------------------" >> "$output_file"
        #echo "Total atoms: $total_atoms" >> "$output_file"
        #echo "Number of lines: $nlines" >> "$output_file"
        grep -A "$nlines" "CSA tensor" "${subdir}/OUTCAR" >> "$output_file"
        echo -e "\n" >> "$output_file"
    else
      echo "Directory: $subdir - OUTCAR not found." >> "$output_file"
      echo -e "\n" >> "$output_file"
    fi

  else
    echo "Directory: $subdir - POSCAR not found." >> "$output_file"
    echo -e "\n" >> "$output_file"

  fi
  total_atoms=0
done

echo "CSA tensor extraction complete. Output saved to $output_file"
```

Script C4 "convert_shifts.sh"- Bash script for converting chemical shielding values into chemical shift values for individual atoms extracted from the OUTCAR files.

```
#!/bin/bash

#Final version modified by WJ on 19 June 2025.
#Run using bash command after running extract_shift.sh
#Reads output file of extract_shift.sh to convert shielding parameters into
chemical shifts.

# Set input and output filenames based on current directory
main_dir=$(basename "$PWD")
input_file="CSA_shifts_${main_dir}.csv"
output_file="chemical_shifts_${main_dir}.csv"

# Ensure input exists
if [[ ! -f "$input_file" ]]; then
  echo "Input file $input_file not found!"
  exit 1
fi
# Variables
declare -a atom_labels
total_atoms=0
# Extract current subdirectory name from the first match
first_dir=$(awk '/^Directory:/ {print $2; exit}' "$input_file")
first_dir="${first_dir%/}"

# Read POSCAR from that directory
if [[ ! -f "${first_dir}/POSCAR" ]]; then
  echo "POSCAR not found in $first_dir!"
  exit 1
fi
# Extract elements and counts
elements=($(sed -n '6p' "${first_dir}/POSCAR"))
ion_counts=($(sed -n '7p' "${first_dir}/POSCAR"))

# Build atom_labels array
for i in "${!elements[@]}"; do
  count=$(echo "${ion_counts[$i]}" | tr -cd '0-9')
  for ((j=0; j<count; j++)); do
    atom_labels+=("${elements[$i]}")
  done
done
# Start writing output
echo "Directory: $first_dir" > "$output_file"
echo "" >> "$output_file"
echo -e "Atom\tSpecies\tISO_Shift\tChem_Shift" >> "$output_file"

# Parse CSA tensor section
inside_tensor=0
atom_index=0

while IFS= read -r line; do
```

```
  if [[ "$line" == *"CSA tensor"* ]]; then
    inside_tensor=1
    continue
  fi

  # End of block (empty line)
  [[ -z "$line" ]] && inside_tensor=0

  if [[ $inside_tensor -eq 1 && "$line" =~ ^[[:space:]]*[0-9]+ ]]; then
    # Extract atom index and ISO shift (column 1 and 5)
    fields=($line)
    atom_index="${fields[0]}"
    iso_shift="${fields[4]}"

    # Assign species from array
    species_raw="${atom_labels[$((atom_index - 1))]}"
    species=$(echo "$species_raw" | tr -cd '[:alnum:]')

    # Sanitize iso_shift
    iso_shift_clean=$(echo "$iso_shift" | tr -cd '0-9.\-')

    # Convert to chemical shift
    case "$species" in
      Na) chem_shift=$(awk -v iso="$iso_shift_clean" 'BEGIN { printf("%.2f",
iso) }') ;;
      La) chem_shift=$(awk -v iso="$iso_shift_clean" 'BEGIN { printf("%.2f", -
1021.95488 + 0.661251 * iso) }') ;;
      Cl) chem_shift=$(awk -v iso="$iso_shift_clean" 'BEGIN { printf("%.2f", -
113.49917 + 0.85038 * iso) }') ;;
      O)  chem_shift=$(awk -v iso="$iso_shift_clean" 'BEGIN { printf("%.2f", -
50.17209 + 0.959751 * iso) }') ;;
      Mg) chem_shift=$(awk -v iso="$iso_shift_clean" 'BEGIN { printf("%.2f",
iso) }') ;;
      *)  chem_shift="N/A" ;;
    esac

    # Write to output
    printf "%d\t%s\t%s\t%s\n" "$atom_index" "$species" "$iso_shift_clean"
"$chem_shift" >> "$output_file"
  fi
done < "$input_file"

echo ""
echo " Chemical shift conversion complete. Output written to $output_file"
```

Script C5 "get_average.sh"- Bash script for averaging the chemical shift values for individual atoms of the same species and calculating their statistical distribution.

```
#!/bin/bash

#Determine file name
dir=$(basename "$PWD")
input_file="chemical_shifts_${dir}.csv"

# Function to calculate average and standard deviation for a given element
calculate_stats() {
    element=$1
    awk -v el="$element" '
    $2 == el && $4 ~ /^[0-9.-]+$/ {
        values[count++] = $4
        sum += $4
    }
    END {
        if (count > 0) {
            avg = sum / count
            ssd = 0
            for (i = 0; i < count; i++) {
                diff = values[i] - avg
                ssd += diff * diff
            }
            stdev = sqrt(ssd / count)
            printf "Chemical shift for %s: %.4f ± %.4f ppm\n", el, avg, stdev
        } else {
            printf "No valid entries for %s found.\n", el
        }
    }
    ' "$input_file"
}

# Call the function for each element
calculate_stats "La"
calculate_stats "Cl"
calculate_stats "O"
```

Publications

Journal of Nuclear Materials 616 (2025) 156056

Contents lists available at ScienceDirect

Journal of Nuclear Materials

journal homepage: www.elsevier.com/locate/jnucmat

Structural dynamics of molten NaCl–$MgCl_2$–$LaCl_3$: A proxy for molten chloride fast reactor fuels

Woei Jer Ng [a,*], Aydar Rakhmatullin [a], Kateryna Goloviznina [b], Mathieu Salanne [b,c], Catherine Bessada [a]

[a] CEMHTI UPR3079 CNRS, Université d'Orléans F-45071 Orléans, France
[b] Sorbonne Université, CNRS, Physicochimie des Électrolytes et Nanosystémes Interfaciaux F-75005 Paris, France
[c] Institut Universitaire de France (IUF) 75231 Paris, France

HIGHLIGHTS

- HT NMR reveals how La–Cl coordination numbers vary with composition and temperature.
- Solid-state NMR confirms the relationship between chemical shifts and coordination numbers.
- NaCl promotes heterogeneous mixing, lower La–Cl coordination, and increased chloride bridging.
- $MgCl_2$ promotes homogeneous mixing, higher La–Cl coordination, and reduced chloride bridging.
- RDF analysis on MD trajectories supports experimental findings.
- DFT calculations successfully reproduce NMR chemical shift trends from MD trajectories.

GRAPHICAL ABSTRACT

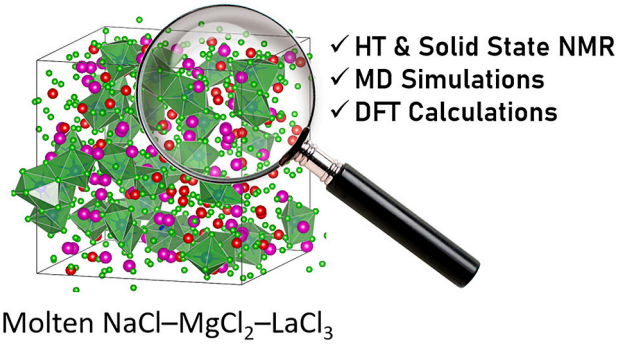

ARTICLE INFO

Keywords:
Molten Salt Reactor
Chloride Salts
High-Temperature NMR
Solid-State NMR
Molecular Dynamics
Density Functional Theory

ABSTRACT

Chloride salts have emerged as the leading candidate fuel for the new generation of molten salt reactors, particularly molten chloride fast reactors (MCFRs). In France, the ARAMIS-A reactor design is exploring the use of NaCl–$MgCl_2$–$PuCl_3$–$AmCl_3$ as fuel for an actinide-burner reactor. However, literature on the structural dynamics of molten chloride fuel salts remains limited, restricting the accurate modelling of fuel performance and behaviour. In this study, we fill this gap by performing in-situ high-temperature nuclear magnetic resonance (HT-NMR) experiments on NaCl–$MgCl_2$–$LaCl_3$, as a surrogate to the (Pu,Am)Cl_3 fuel, to investigate the local structural chemistry of molten chloride salts. By complementing our experimental findings with solid-state nuclear magnetic resonance (SS-NMR) measurements, classical molecular dynamics (MD) simulations and density functional theory (DFT) calculations, we elucidate the complex structural interactions in molten chloride systems, such as lanthanide network formation and chlorine bridging, and illustrate how these interactions vary with temperature and fuel composition. Our results establish a clear relationship between NMR chemical shifts and coordination numbers in molten salts, offering critical insights into the local structural environments that influence the behaviour of actinide-based fuels in molten salt reactors.

* Corresponding author.
E-mail address: woei-jer.ng@cnrs-orleans.fr (W.J. Ng).

https://doi.org/10.1016/j.jnucmat.2025.156056
Received 30 January 2025; Accepted 24 July 2025
Available online 25 July 2025
0022-3115/© 2025 Elsevier B.V. All rights are reserved, including those for text and data mining, AI training, and similar technologies.

1. Introduction

Molten salt reactors (MSRs) are a category of nuclear fission reactor that employs molten salts as the primary coolant and fuel. Initially conceptualised in the 1950s as a compact, high-power-density fuel source for the propulsion of military aircraft [1], MSRs garnered renewed interest from the scientific community as it was unveiled in 2002 as one of the six Generation IV nuclear reactor concepts to promote environmental sustainability efficiency, safety and cost efficiency in the global energy market [2–5]. Compared to other Generation IV reactors, the MSR is appealing due to its inherently safe reactor design, uniform liquid state of the fuel, simple operation under standard atmospheric pressures and ability to transmute long-lived radioactive actinides into short-lived benign isotopes [6].

MSRs employ liquid salt as both fuel and coolant. The primary loop, consisting of a mixture of fissile salts and carrier salts, circulates through a core for fission and heat exchangers for cooling. The secondary loop, consisting of only carrier salts, transfers the heat received to a steam power conversion system. Two types of salts are chosen for the MSR fuel: fluoride salts are preferred for thermal reactors and are effective with the $^{232}Th/^{233}U$ breeding cycle, and chloride salts are preferred for fast reactors with the $^{238}U/^{239}Pu$ breeding cycle [7].

In France, a significant collaboration has been established to explore the conceptual chloride salt actinide-burner reactor, ARAMIS-A, as a long-term strategy to reduce the actinide inventory in spent nuclear fuel repositories [8,9]. Based on the current conceptual design, a reactor fuel composition of 62 mol% NaCl–15 mol% $MgCl_2$–23 mol% $(Pu,Am)Cl_3$ is proposed to achieve optimised fuel salt characteristics [10], neutronics and thermal hydraulics functionality [11,12]. In this fuel design, NaCl acts as a universal "solvent" [13]; $MgCl_2$ serves as the complementary base salt that lowers fuel melting temperatures (T_m) [14,15], augments heat transfer efficiency [16], and improves fuel compatibility with structural materials [17]; finally, $PuCl_3$ functions as the fast fission neutron source to sustain nuclear chain reactions and disintegrate long-lived minor actinides such as $AmCl_3$ [18].

However, experiments to ascertain the properties of MCFR are limited due to the radiotoxicity of actinide salts and the challenges associated with handling them at high temperatures. Rose et al. measured melting temperatures, heat capacities and thermal diffusivities of the binary NaCl–UCl_3 and ternary NaCl–KCl–UCl_3 eutectic salts using differential scanning calorimetry (DSC) and laser flash analysis (LFA) [19]. Karlsson et al. synthesised high-purity NaCl–$PuCl_3$ salts and measured their thermophysical properties such as the density and thermophysical properties, subsequently demonstrating good reproduction of their experimental findings using first-principles MD simulations [20].

Most other studies examining the properties of MCFR fuel salts have been primarily computational. Beneš and Konings performed thermodynamic modelling of the NaCl–$MgCl_2$–UCl_3–$PuCl_3$ molten salt system using the Calculation of Phase Diagrams (CALPHAD) method, finding that the addition of $MgCl_2$ was unable to lower T_m, of fuel compositions with 38 mol% UCl_3 and 7 mol% $PuCl_3$ [14]. Follow-up CALPHAD studies by Ng and Ryu concluded that while $MgCl_2$ was useful for lowering T_m for chloride fuel salts with <30 mol% of actinide trichlorides ($AnCl_3$), KCl is more effective in lowering T_m for fuel salts with a higher proportion of $AnCl_3$ [15]. Different teams of researchers also performed classical molecular dynamics (MD) simulations based on the polarisable ion model (PIM) [21] to evaluate the structural and transport properties of the NaCl–UCl_3 [22], KCl–UCl_3 [23] and NaCl–KCl–UCl_3 systems [24], subsequently assessing the thermophysical properties of the respective fuel systems. Li et al. further employed first-principle MD calculations on NaCl–$MgCl_2$–UCl_n ($n = 3,4$) systems and showed that Mg^{2+}ions disrupt the formation of U–Cl network structures [25]. Using a thermodynamic approach, Delpech et al. evaluated the electrochemical potential of NaCl–UCl_3–$PuCl_3$ against oxide ion (O^{2-}) activity and proposed the use of amphoteric species such as $TiCl_2/TiCl_4$ to control the salt redox potential and reduce corrosivity [26].

Despite these advances, our comprehension of the fundamental ionic interactions of molten chloride mixtures containing lanthanide and actinide cations remains incomplete, limiting our ability to establish precise models for the thermophysical properties of fuel salts. One of the key challenges is the sophisticated electronic interactions in the f-orbitals, which give rise to intricate bonding behaviour and coordination chemistry [27,28]. Jiang et al. exhaustively reviewed experimental and computational techniques for quantifying the coordination chemistry of f-block elements in molten salts, highlighting the challenges and difficulties involved [29].

In this study, we set out to deepen the understanding of the fundamental ionic interactions in chloride salts, specifically those used in MCFR fuel salts. We achieved this by leveraging the in-situ high-temperature nuclear magnetic resonance (HT-NMR) facilities at CNRS Orléans (France), where two uniaxial CO_2 lasers are used to rapidly and uniformly heat salt samples above their melting temperatures [30,31]. This setup enables the measurement of ^{139}La and ^{35}Cl chemical shifts in NaCl–$MgCl_2$–$LaCl_3$ molten salt systems as functions of fuel composition and temperature. Here, $LaCl_3$ acts as a proxy for the highly radiotoxic $PuCl_3$ and $AmCl_3$ due to their similar crystal structures, in addition to their comparable bond lengths and ionic radii. To interpret these chemical shifts, we also conducted solid-state NMR measurements and DFT calculations on $LaCl_3$-containing intermediate compounds. Additionally, classical MD simulations based on the PIM were employed to study the local structure and dynamics in molten salts. DFT calculations were then performed on snapshots extracted from the MD trajectories to simulate NMR chemical shifts, providing a means to validate the consistency between NMR experiments and MD simulations. We discuss the fundamental interactions between constituent ions, such as short- and intermediate-ranged ordering, network formation and chlorine bridging, and suggest some potential implications of our work on MCFR fuel properties.

2. Experimental section

2.1. Materials and synthesis

NaCl (Merck, ≥99.5 %), $MgCl_2$ (Thermo Scientific Chemicals, anhydrous ≥98 %), $LaCl_3$ (Sigma Aldrich, anhydrous ≥99.99 %), KCl (Merck, ≥99.5 %) and CsCl (Alfa Aesar, 99 %) salts were purchased and used without further purification. All chemicals were stored and handled in a glove box under an argon atmosphere, maintained at <0.3 ppm moisture and <0.5 ppm oxygen.

K_2LaCl_5 and Cs_3LaCl_6 were synthesised via the solid-state synthesis method, whereby fine grains of the constituent salts were thoroughly mixed in their given stoichiometric ratios, held above congruent melting temperatures under a saturated argon atmosphere in a tube furnace for one hour and slowly cooled to ambient temperature at a rate of 0.25 K/min. **Figure S1** shows the powdered XRD analysis of the synthesised intermediate compounds. Both K_2LaCl_5 and Cs_3LaCl_6 exhibit remarkable similarity with the reported X-ray diffraction spectra [32,33], signifying that the samples have been well synthesised.

2.2. Sample preparation

All samples were prepared inside a glove box under a dried argon atmosphere. For HT-NMR measurements, NaCl, $MgCl_2$, and $LaCl_3$ were weighed according to the desired composition using an electronic balance. The samples were thoroughly mixed using a mortar and pestle, then transferred into a high-purity boron nitride crucible (0.9 cm diameter × 1.4 cm height) and tightly sealed with a screw cap. For SS-NMR (solid-state NMR) measurements, powdered $LaCl_3$, K_2LaCl_5 and Cs_3LaCl_6 were used to fill Bruker MAS rotors of varying diameters (1.3 mm, 2.5 mm, and 4.0 mm) and securely enclosed with rotor caps.

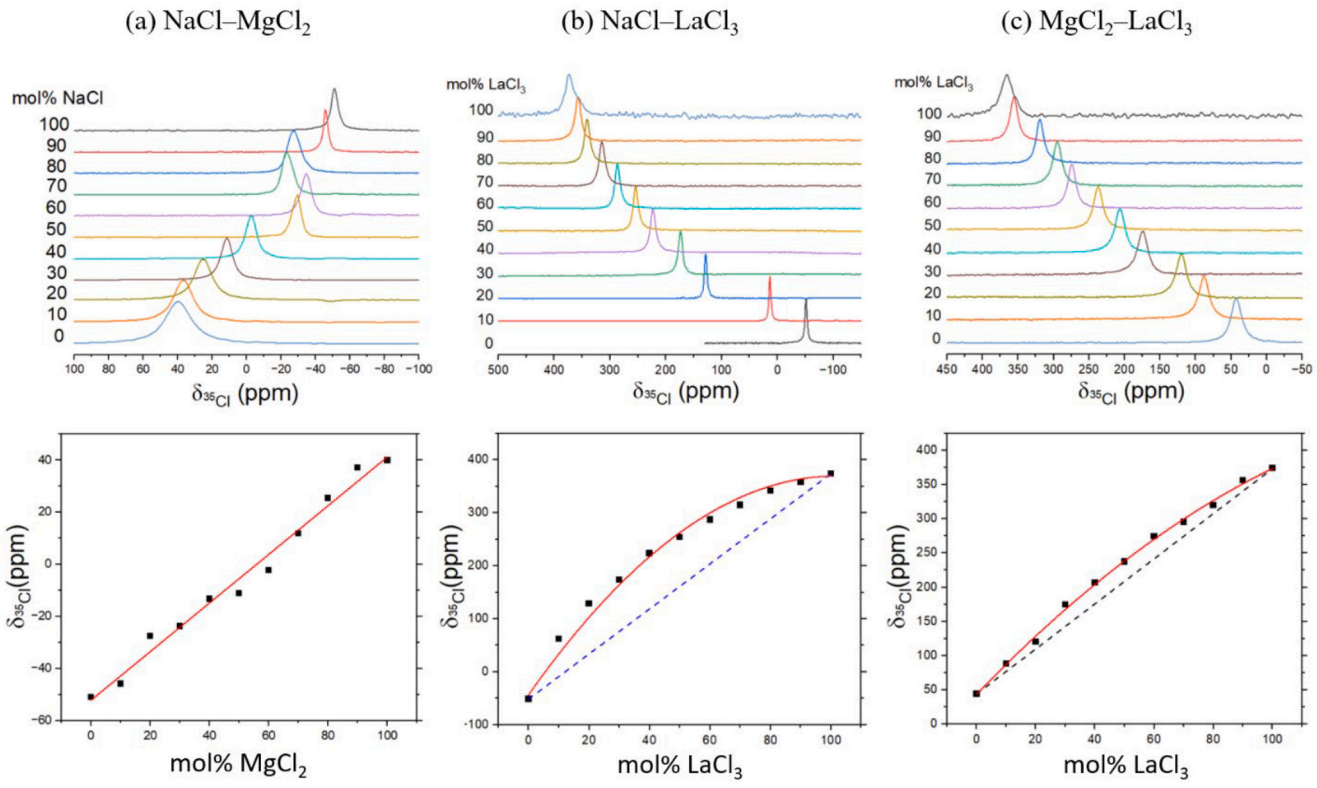

Fig. 1. ^{35}Cl chemical shift evolutions for (a) NaCl–$MgCl_2$, (b) NaCl–$LaCl_3$ and (c) $MgCl_2$–$LaCl_3$, measured by in-situ HT-NMR as a function of composition at $T_m + 10$ °C of the respective salts.

2.3. NMR spectroscopy

In-situ HT-NMR measurements were conducted using a Bruker AVANCE I spectrometer operating at 9.4 T, with two CO_2 lasers positioned above and below the sample to achieve uniform heating to desired temperatures [34–36] . In this setup, the crucibles are inserted into a modified axial NMR probe, designed to focus two laser beams directly and heat the samples up to 1500 °C. To limit oxidation of the crucible, a continuous argon flow of 1.9 cm^3/s was maintained inside the probe before and during laser irradiation.

0.1 M $LaCl_3$ and 1.0 M NaCl solutions were used as the reference chemical shifts for the ^{139}La and ^{35}Cl nuclei, respectively. Measurements on the NaCl–$MgCl_2$–$LaCl_3$ system were conducted at varying compositions (10 mol% intervals of $LaCl_3$) and temperatures ranging from T_m + 10 to 900 °C. T_m of binary systems was obtained from experimental data [37,38]; whereas, T_m of the ternary system was estimated using the Modified Quasichemical Model [39,40] on FactSage [41] without any excess ternary parameters (i.e. $\Delta g_{ABC/X} = 0$). The ternary phase diagram used for estimating T_m is given in **Figure S2**. All ternary samples exhibited Lorentzian NMR signals characteristic of liquid systems at the estimated T_m, validating the reliability of our CALPHAD model.

SS-NMR was performed using Bruker Avance NEO 17.6 T and 20 T spectrometers, to study the effects of La–Cl coordination on the ^{139}La and ^{35}Cl chemical shifts. The reference chemical shifts and 90° pulse lengths of both nuclei were obtained using the same method as described above. The spin echo pulse sequence was used to accumulate the SS-NMR spectra of every compound [42]. For compounds with low signal intensity and sufficiently long T_2 relaxation times, the Carr-Purcell-Meiboom-Gill pulse sequence [43] was used to reduce measurement time and improve the signal-to-noise ratio of the SS-NMR spectra. In the case of compounds that exhibit quadrupolar coupling (C_Q) larger than the irradiation frequency of the NMR pulse, the variable offset cumulative spectra (VOCS) methodology [44] was used to sum up different spectral areas to obtain a continuous spectrum over a wider frequency range. Parameter fitting (δ_{iso}, C_Q, and η) of the NMR spectra was done using Q-Stat ½, Q-MAS ½ and QUASAR modules on the DMFit program [45].

2.4. MD simulations

MetalWalls software [46] was used to simulate the local structure and ion dynamics of molten chlorides using the PIM. The force field parameters for the interactions involving La^{3+}, Na^+, and Cl^- were taken from previous works [47–49]. The interatomic potential for Mg^{2+} ions was re-parameterised using first-principle calculations at the DFT level, following the same procedure described in previous work [30,31]. All potential parameters, in atomic units, are tabulated in **Tables S3–S5**.

Two sets of simulations were performed for each target composition: (1) NPT ensemble simulations of "large" boxes containing 2000 to 4000 atoms (**Table S6**) and (2) NVT ensemble simulations of "small" boxes containing 240 to 500 atoms (**Table S7**). Initial configurations of the cubic periodic simulation boxes were generated with the Packmol utility [50]. Each simulation was performed in the following order: a 0.2 ns non-polarisable equilibration step, a 0.5 ns polarisable equilibration step, and a 5.0 ns polarisable production step, all with a 1.0 fs timestep.

All simulations were run at the fixed temperature of 1123 K using Nosé-Hoover thermostats, and additionally for the NPT simulations, at the standard pressure of 1 bar using Nosé-Hoover barostats. The Ewald summation method was used for all the long-range Coulombic interactions, while the cut-off radii for van der Waals interactions were set to 12.0 Å for "large" boxes and 6.00 Å for "small" boxes. A tail correction was applied to the calculation of energy and pressure. Ion trajectories generated from "large" box simulations were used for structure analysis by applying the TRAVIS code [51,52], while those from "small" box simulations were used for visualisation with the VESTA software [53] and for subsequent DFT calculations of NMR chemical shifts.

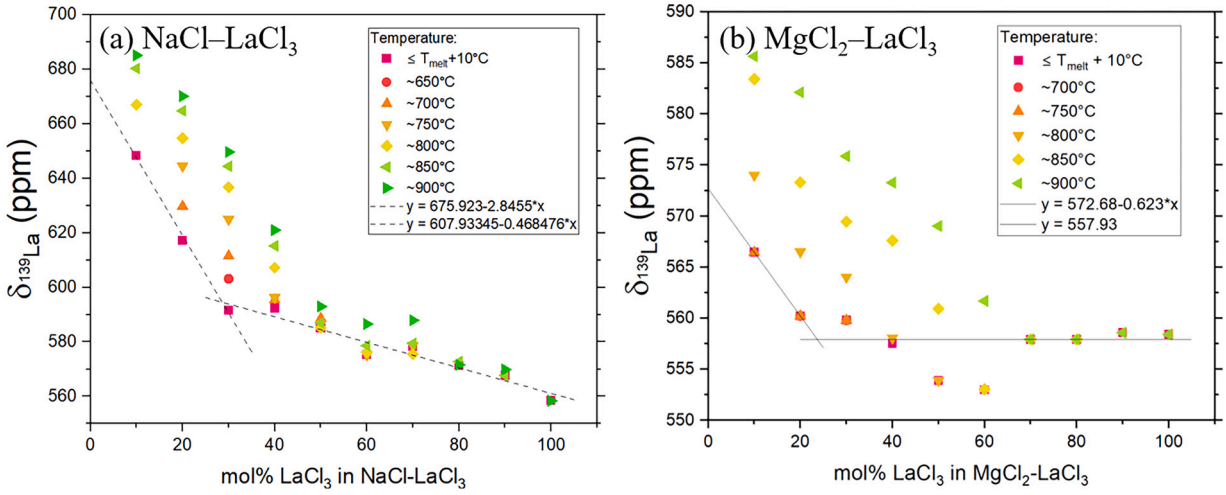

Fig. 2. ^{139}La chemical shift evolutions for (a) NaCl–$LaCl_3$ and (b) $MgCl_2$–$LaCl_3$, measured by in-situ HT-NMR as functions of composition and temperature.

2.5. DFT calculations

The Gauge Including Projector Augmented Waves (GIPAW) method [54] was executed via the CASTEP–NMR module [55,56] in Materials Studio 2024 to derive the chemical shielding and electric field gradient (EFG) tensors of the ^{139}La and ^{35}Cl nuclei in solid-state compounds and molten salt systems. The Perdew–Burke–Ernzerhof (PBE) functional [57] was used in the generalised gradient approximation (GGA) of the exchange-correlation energy. Ultrasoft pseudopotentials [58], generated by the "on-the-fly" generator (OTGF ultrasoft) in CASTEP, were used to describe the core-valence interactions.

For solid-state compounds, calculations were performed using the *cif* files of critically evaluated unit cell structures ($LaCl_3$ [59], K_2LaCl_5 [32], Cs_3LaCl_6 [33], LaI_3 [60], $LaBr_3$ [61], La_2O_3 [62], $LaNbO_4$ [63], $La(OH)_3$ [64], LaF_3 [65], $BaCl_2$ [66], CsCl [67], NH_4Cl [68], RbCl [69], KCl [70], LiCl [71], NaCl [72]). The electronic cutoff energies and sizes of the *k*-point mesh used for sampling the Brillouin zone were determined by the default *Ultra-fine* quality settings for NMR calculations. All calculations were performed using the *Energy* task module, with *Geometry Optimization* additionally applied to the intermediate compounds K_2LaCl_5 and Cs_3LaCl_6 (as the calculated parameters for these DFT-optimised structures showed better fit with experimental results). Our calculations returned the isotropic shielding (σ_{iso}), quadrupolar coupling constant (C_Q) and asymmetry parameter (η) of each distinct atom in the unit cell. The mapping of σ_{iso} to δ_{iso} was done using a linear regression analysis to correlate the calculated σ_{iso} and experimentally determined δ_{iso} of common lanthanum and chloride compounds [73–75] (**Figure S3**).

For liquids, DFT calculations were performed on ten distinct snapshots taken from the MD trajectories. To balance computational cost with accuracy, trajectories from the "small" box were used for these calculations. Snapshots were chosen based on their resemblance to the coordination environment in the "large" box (**Tables S8 and S9**), with a minimum of 200 ps between each snapshot to ensure they were uncorrelated. The electronic cutoff energy of 660.0 eV was adopted and a *k*-point mesh of 1 × 1 × 1 was used to sample the Brillouin zone [30]. Our calculations returned individual σ_{iso} values of each nucleus in the ensemble. The mean and standard deviation of σ_{iso} were calculated and the corresponding δ_{iso} values were derived via the best-fit linear correlation shown in **Figure S3**.

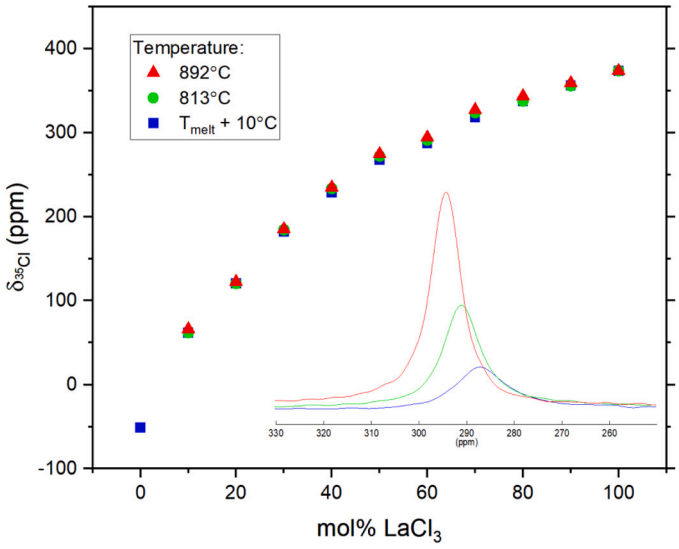

Fig. 3. ^{35}Cl chemical shift evolution for NaCl–$LaCl_3$, measured by in-situ HT-NMR as a function of composition and temperature. Measured peaks of the 50 mol% NaCl–50 mol% $LaCl_3$ at varying temperatures are given as an example in the bottom right of the figure. Note that while the changes in chemical shifts appear significant on the absolute scale, they remain small relative to the scale of the range of chemical shift evolutions.

3. Results and discussion

3.1. In-situ HT-NMR

The main results of this study focus on the effects of composition and temperature on the chemical shifts of the NaCl–$MgCl_2$–$LaCl_3$ molten salt system. Fig. 1 and Fig. 2 plot, respectively, the ^{35}Cl and ^{139}La chemical shifts measured by in-situ HT-NMR as a function of composition. Variations of the chemical shifts with temperature are provided for measurements involving ^{139}La nuclei only, since even with large temperature increments, ^{35}Cl chemical shifts are shown (Fig. 3) to exhibit very weak changes with respect to the range of chemical shift evolution and are therefore omitted. These observations are consistent with those of Hudry et al. [36] and Zhang and Farnan [76], who measured the ^{35}Cl chemical shifts of $LaCl_3$ and $CeCl_3$, respectively, in the LiCl–KCl binary eutectic salt and found limited changes in chemical shifts with temperature.

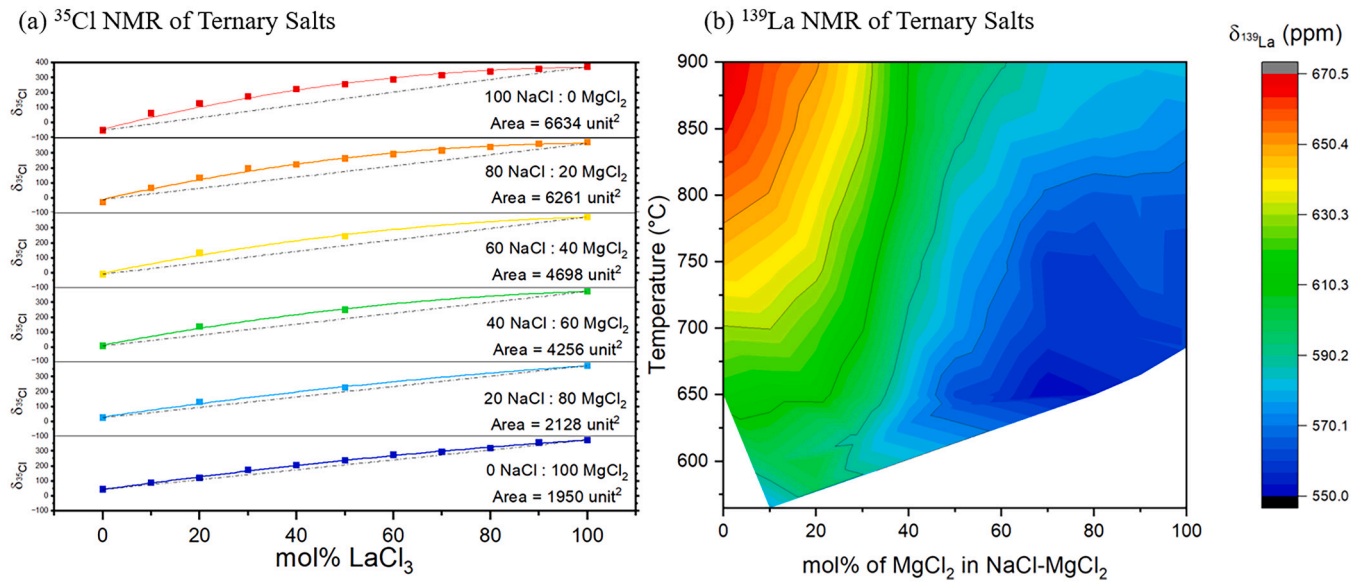

Fig. 4. (a) ^{35}Cl chemical shift evolutions of ternary salts at varying NaCl/$MgCl_2$ ratios measured at $T_m + 10$ °C of the respective salts (individual curves are offset for better visualisation); (b) ^{139}La chemical shift evolution of ternary salts with $LaCl_3$ fixed at 20 mol% as functions of temperature and NaCl:$MgCl_2$ ratio.

The ^{35}Cl chemical shift evolution shows a linear relationship with composition in the NaCl–$MgCl_2$ binary system; however, it exhibits non-linear behaviour in the NaCl–$LaCl_3$ and $MgCl_2$–$LaCl_3$ binaries. This can be attributed to the tendency for Cl^- ions to form bridges between two or more adjacent La^{3+} ions in the melt [77]. In NaCl–$MgCl_2$, Cl^- ions essentially exist as "free" ions; while in NaCl–$LaCl_3$ and $MgCl_2$–$LaCl_3$, Cl^- ions tend to be more tightly bound as they are shared between adjacent La^{3+} ions to maintain the large coordination number necessary for preserving local charge neutrality [78]. Corradini et al. quantified this phenomenon using the cage-correlation function analysis, showing that Cl^- ions exhibit longer lifetimes in the La^{3+} solvation shell in molten salts with increasing $LaCl_3$ content [79]. As we will discuss in later sections, bridging Cl^- ions tend to be more deshielded than non-bridging Cl^- ions, leading to more positive chemical shifts and deviating the curve further away from linearity. Moreover, the deviation from linearity is more marked in NaCl–$LaCl_3$ than in $MgCl_2$–$LaCl_3$, suggesting that chloride bridging may be more pronounced in the former system.

The ^{139}La chemical shift evolution reveals more complex spectra for analysis. Two linear fits were applied to the chemical shift evolution at lower and higher compositional fractions of the spectra at $T_m + 10$ °C. Notably, the intersections of these linear lines closely align with the eutectic compositions of the binary mixtures. Knowing that the ^{139}La chemical shift reflects the average La–Cl coordination number in chloride melts (as discussed later), this result suggests that, at the onset of melting, the coordination behaviour of La^{3+} ions is primarily governed by the La^{3+}-containing phase present between the solidus and liquidus temperatures at the respective compositions.

Additionally, the ^{139}La chemical shift range of NaCl–$LaCl_3$ is larger than that of $MgCl_2$–$LaCl_3$, implying a greater variation of the average La–Cl coordination number in NaCl–$LaCl_3$. Temperature further induces large, positive chemical shifts in the ^{139}La spectra, suggesting increased deshielding due to widened La–Cl distances and lower coordination with temperature. This explanation is consistent with the findings of Emerson et al. [80], who discovered through classical MD simulations that lower La–Cl coordination is preferred in NaCl–$LaCl_3$ melt at higher temperatures. In contrast, the Cl–La coordination remains relatively unchanged throughout a wide temperature range, explaining the inconsequentially small change in ^{35}Cl chemical shifts with temperature.

Building on our analysis of binary systems, we can now extend our investigation into ternary systems. To better reflect the desired MCFR fuel composition of 62 mol% NaCl–15 mol% $MgCl_2$–23 mol% (Pu,Am)Cl_3 [10], we measured the chemical shift evolution of ^{139}La and ^{35}Cl nuclei along the compositional variations of $(100-x)$ mol% $(NaCl)_{0.80}(MgCl_2)_{0.20} - x$ mol% $LaCl_3$ and 80 mol% $(NaCl)_{1-x}(MgCl_2)_x$ –20 mol% $LaCl_3$. Fig. 4(a) compares the ^{35}Cl chemical shift evolution at varying molar ratios of NaCl and $MgCl_2$. Here, the area between the parabolically fitted curve and the theoretical linear line is used as a measure of the deviation from linearity. The diagram shows that the curves generally deviate more from linearity when there is a higher NaCl/$MgCl_2$ ratio, supporting our previous claim that NaCl promotes more chloride bridging between La^{3+} ions than $MgCl_2$. A simple stoichiometric analysis supports this argument: since NaCl is monovalent and $MgCl_2$ is divalent, the lower supply of Cl^- ions from NaCl necessitates more sharing of Cl^- ions between adjacent La^{3+} ions to preserve local charge neutrality. Meanwhile, the higher supply of Cl^- ions from $MgCl_2$ augments the tendency for adjacent La^{3+} ions to exist as independent $[LaCl_n]^{3-n}$ complexes, forgoing chloride bridging in the process. Fig. 4(b) shows a contour plot of the ^{139}La chemical shift evolution as a function of temperature and the $MgCl_2$ fraction in the NaCl–$MgCl_2$ carrier salt, with $LaCl_3$ fraction fixed at 20 mol%. Consistent with the results of our measurements on binary systems, a higher proportion of $MgCl_2$ leads to smaller chemical shifts and a higher proportion of NaCl leads to larger chemical shifts; Increasing the temperature also results in greater chemical shifts. This result verifies our assertion that $MgCl_2$ promotes higher La–Cl coordination environments, while NaCl tends to lower La–Cl coordination environments.

In summary, in-situ HT-NMR provides exceptional insight into the structural dynamics of the NaCl–$MgCl_2$–$LaCl_3$ molten salt system: deviation from linearity in the ^{35}Cl chemical shift evolution curve indicates the degree of chloride bridging, while the ^{139}La chemical shift reflects the average La–Cl coordination number in the melt. In the subsequent sections, we perform more detailed and quantitative characterisation of the ^{35}Cl and ^{139}La chemical shifts by combining techniques such as SS-NMR, MD, and DFT Calculations.

3.2. *Interpreting HT-NMR data using SS-NMR, MD, & DFT*

SS-NMR measurements were performed to delineate the relationship between coordination numbers and chemical shifts. Unlike molten salts, solid salts usually exhibit consistent three-dimensional structure, characterised by the periodic and ordered geometry of ions which defines the crystalline arrangement of a Bravais lattice. As a result, solid salts

Table 1
Structural data of crystalline salts used in SS-NMR experiments.

Compound	La–Cl Bond Lengths (Å)	CN_{La-Cl}	CN_{Cl-La}	La sites	Cl sites	Ref
$LaCl_3$	2.95	9	3	1	1	[59]
K_2LaCl_5	2.81–2.89	7	1, 2*	1	4	[32]
Cs_3LaCl_6	La_1: 2.59–2.84 La_2: 2.67–2.92	6	1	2	6	[33]

* Three Cl sites are non-bridging, the multiplicity of these sites is 1, one Cl site is bridging, the multiplicity of this site is 2.

typically show minimal variation in bond lengths and fixed coordination numbers, such as those used in our experiments (Table 1).

However, SS-NMR spectra, especially those involving quadrupolar nuclei, tend to be very broad. This broadening arises from the effects of chemical shift anisotropy and quadrupolar coupling, which are not averaged out due to timescales of molecular tumbling/ion pair exchange on timescales much longer than that of NMR spectroscopy. In contrast, in liquid NMR, the rapid molecular tumbling and ion-pair exchange occur on much shorter timescales, effectively averaging out the effects of anisotropy and quadrupolar broadening. This leads to single, sharp Lorentzian peaks in molten salts.

Given that NMR is highly sensitive to subtle changes in bond lengths and coordination environments, the isotropic chemical shifts obtained from the SS-NMR of different compounds are expected to vary greatly, making them efficient indicators of trends in coordination chemistry. Fig. 5 depicts the ^{139}La NMR spectra from static and magic-angle spinning (MAS) measurements on the solid compounds, recorded under two magnetic fields: 17.6 and 20.0 T. The measured spectra were fitted using a consistent set of parameters (with slight adjustments for individual spectra) and compared to results from previous experiments [81] as well as our DFT calculations (Table 2).

For $LaCl_3$ and K_2LaCl_5, the fitted parameters closely align with the calculated values, affirming the reliability of our measurements. However, the fitted spectra do not fully capture all peaks observed in the measured spectra, a discrepancy particularly evident in the MAS spectra of K_2LaCl_5. These unaccounted peaks are attributed to the difference in orientation between the principal axis systems of the chemical shift tensor and quadrupolar moment (i.e., Euler angles). While fitting Euler angles is challenging, they do not significantly affect the main parameters discussed and are omitted from consideration herein.

In contrast, Cs_3LaCl_6 exhibits a notable divergence between the fitted and calculated parameters, with experimental linewidths appearing smaller than expected. This discrepancy may stem from dynamic effects not accounted for in the GIPAW calculations. Structurally, Cs_3LaCl_6 adopts a framework derived from the elpasolite structure [82]: at high temperatures, octahedral units of $[LaCl_6]^{3-}$ occupy ideal crystallographic positions; whereas, at low temperatures, these units are slightly deformed and are markedly rotated from their ideal orientations. Recent studies on analogous compounds, such as K_3AlF_6, Rb_3AlF_6 [83], and Rb_3ScF_6 [84], revealed that $[AlF_6]^{3-}$ or $[ScF_6]^{3-}$ octahedra undergo dynamic rotations in their high-temperature phase. This internal rotational motion causes spinning sidebands to vanish and significantly reduces quadrupolar broadening in ^{27}Al and ^{45}Sc NMR spectra. In our case, high-frequency MAS rotations are believed to induce frictional heating, incurring a transition of Cs_3LaCl_6 into its high-temperature phase. Consequently, the ^{139}La NMR spectra of Cs_3LaCl_6 also exhibit this peculiar absence of spinning sidebands under MAS conditions. Moreover, the presence of two distinct La sites contributes to broad, overlapping quadrupolar coupling signals, complicating spectral deconvolution for both static and MAS conditions.

Despite these difficulties, our results clearly show that higher La–Cl coordination numbers correspond to smaller δ_{iso} values and vice versa, substantiating our argument from the previous section. However, it should be noted that the calculated δ_{iso} from SS-NMR does not provide a

Table 2
^{139}La SS-NMR parameters obtained from line fitting and DFT calculations.

Compound	Method	δ_{iso} (ppm)	C_Q (MHz)	η
$LaCl_3$	SS-NMR	311 ± 3	15.85 ± 0.5	0.00
	SS-NMR [81]	305 ± 5	15.55	0.00
	DFT	286	15.10	0.00
K_2LaCl_5	SS-NMR	703 ± 20	30.14 ± 2.4	0.54 ± 0.1
	DFT	688	27.84	0.75
Cs_3LaCl_6	SS-NMR (Static spectra only)	La_1: 878 ± 3 La_2: 924 ± 3	La_1: 17.7 ± 0.3 La_2: 14.62 ± 0.4	La_1: 0.10 La_2: 0.78 ± 0.03
	DFT	La_1: 793 La_2: 851	La_1: 24.28 La_2: 18.98	La_1: 0.47 La_2: 0.57

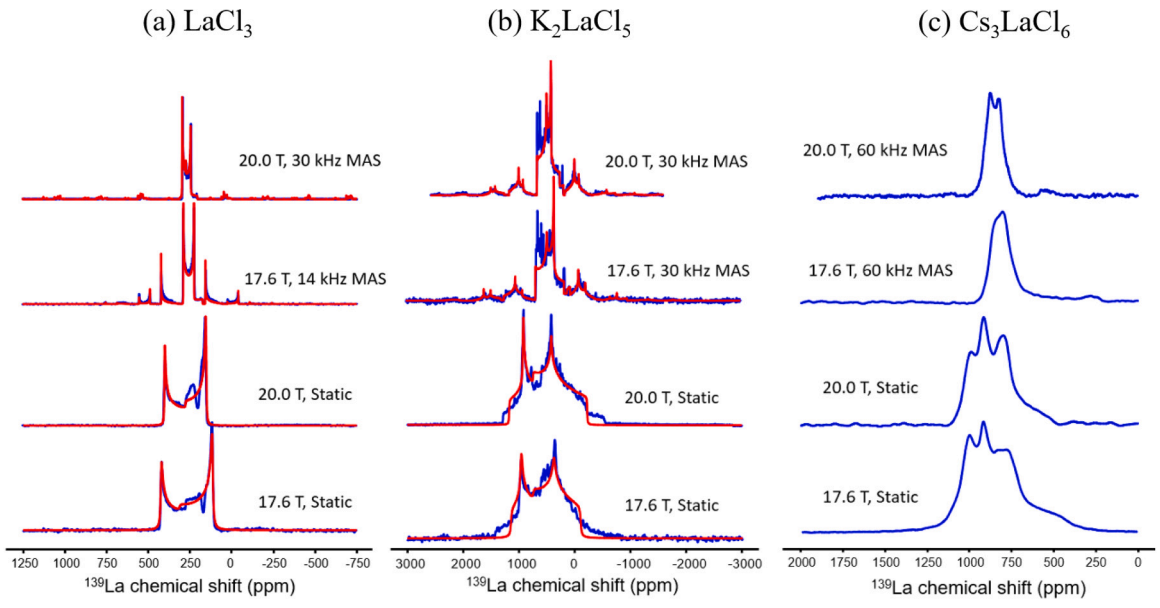

Fig. 5. ^{139}La SS-NMR spectra of (a) $LaCl_3$, (b) K_2LaCl_5 and (c) Cs_3LaCl_6. Measured spectra are given in blue and fitted spectra are given in red. Fitting for Cs_3LaCl_6 spectra is omitted for reasons discussed in the text.

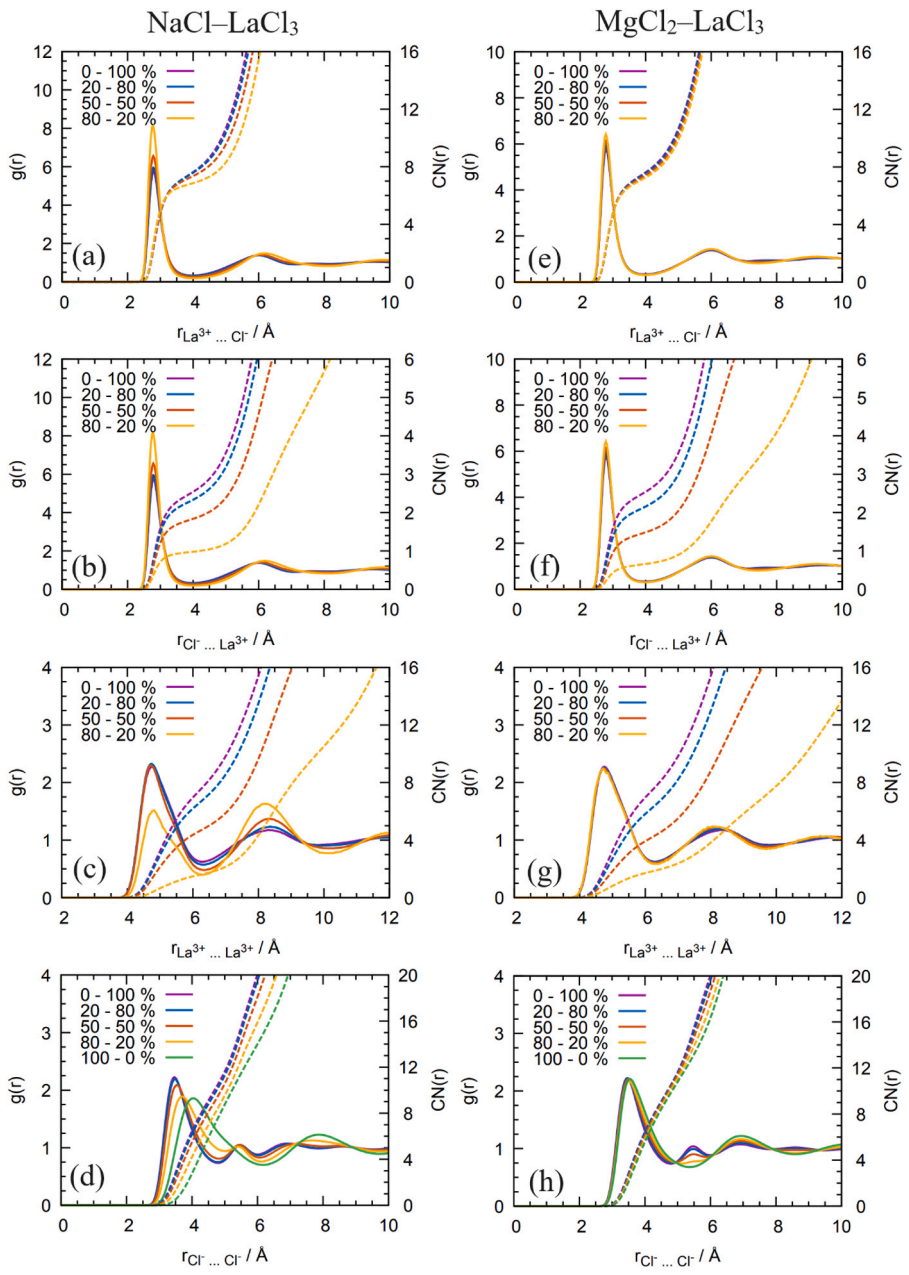

Fig. 6. Comparison of radial distribution functions, g(r), in solid lines, and coordination numbers, CN(r), in dotted lines, for key ion pairs in (a–d) $NaCl–LaCl_3$ and (e–h) $MgCl_2–LaCl_3$ binary molten salt systems at 1123 K.

quantitative representation of the chemical shifts in molten salts. This is because the radii of first coordination shells in liquids are considerably larger, and the presence of $K^+$and Cs^+ions in the second coordination sphere also influences the electron cloud density of La^{3+} ions.

Due to the strong overlap of several ^{35}Cl NMR signals, which exhibit large quadrupolar broadening from chlorine atoms in nonequivalent crystallographic positions, resolving the ^{35}Cl NMR spectra becomes significantly more challenging. **Figure S3** shows the static ^{35}Cl NMR spectra of the three solid compounds. While the ^{35}Cl NMR spectra of $LaCl_3$ can be easily extracted, those of K_2LaCl_5 and Cs_3LaCl_6 show superpositions of multiple lines from different Cl sites with broad quadrupolar coupling, making it nearly impossible to resolve them individually. To address this problem, the δ_{iso} values of each Cl site in the two compounds were derived from DFT calculations. Our results show that bridging Cl ions generally exhibit larger chemical shifts than non-bridging Cl ions. For example, in the case of K_2LaCl_5, the chemical shift in bridging Cl sites is calculated to be 256 ppm, while those of non-bridging Cl sites ranged from 193 to 236 ppm. This result supports our previous explanation that chloride bridging results in a positive deviation from linear behaviour in the ^{35}Cl NMR curve. Additionally, we found that a higher degree of chloride bridging results in higher chemical shifts. For instance, the triple-bridging Cl in $LaCl_3$ gives a chemical shift of 270 ppm, greater than the double-bridging Cl in K_2LaCl_5 at 256 ppm. However, caution should be exercised when directly comparing ^{35}Cl chemical shifts across different compounds, as the type of cation neighbours surrounding Cl^- anions may affect the observed chemical shifts.

To obtain deeper insight into the origins of the chemical shift evolution with compositional change, we explored the local structure of molten salt mixtures using classical MD simulations. Herein, we computed the radial distribution functions (RDF) using the ion trajectories generated from MD simulations. Fig. 6 shows the calculated RDF

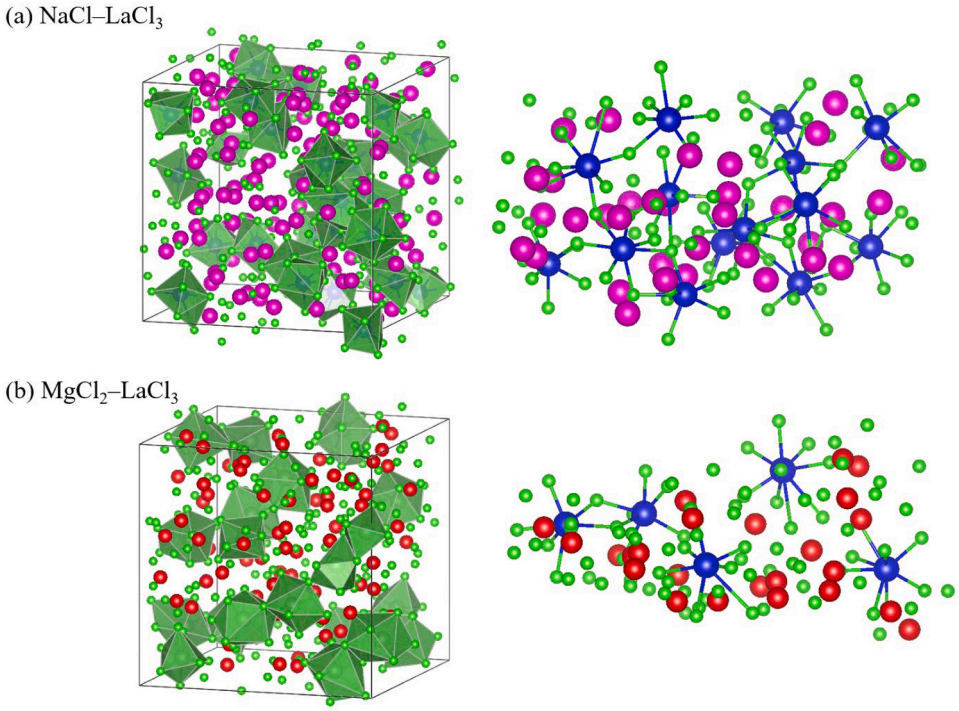

Fig. 7. Snapshots of (a) 80 mol% NaCl–20 mol% $LaCl_3$ and (b) 80 mol% $MgCl_2$–20 mol% $LaCl_3$ at 1123 K. Ions are represented based on colour: Na^+(violet), Mg^{2+}(red), La^{3+} (dark blue) and Cl^- (green). La–Cl coordination polyhedra are drawn around La^{3+} ions in the "full" screenshot to highlight the difference in network formation behaviour. The La–Cl bond length cutoff is set at 4.00 Å, based on the first minimum observed in the RDFs.

and the running coordination numbers (CN) of La^{3+}–Cl^-, Cl^-–La^{3+}, La^{3+}–La^{3+} and Cl^- –Cl^- pairs in NaCl–$LaCl_3$ and $MgCl_2$–$LaCl_3$ binary systems at 1123 K. These ion pairs were chosen because they adequately highlight the structural differences between NaCl–$LaCl_3$ and $MgCl_2$–$LaCl_3$.

For the La^{3+}– Cl^- ion pair, CN_{La-Cl} increases with $LaCl_3$ content in NaCl–$LaCl_3$, but remains roughly constant in the case of $MgCl_2$–$LaCl_3$. This finding complements the results of our HT-NMR measurements, whereby the range of chemical shifts for NaCl–$LaCl_3$ is conspicuously larger than for $MgCl_2$–$LaCl_3$ (Fig. 2), signifying that CN_{La-Cl} in NaCl–$LaCl_3$ is more sensitive to $LaCl_3$ content than CN_{La-Cl} in $MgCl_2$–$LaCl_3$. Moreover, for the Cl^-–La^{3+} ion pair, CN_{Cl-La} in their respective first solvation shells were calculated to be 0.96 for 80 mol% NaCl–20 mol% $LaCl_3$ and 0.65 for 80 mol% $MgCl_2$–20 mol% $LaCl_3$, supporting our claim that chloride ions exhibit a higher degree of bridging in NaCl–$LaCl_3$.

The RDF of La^{3+}– La^{3+} ion pairs shows that the primary-to-secondary peak ratio diminishes with decreasing $LaCl_3$ content in NaCl–$LaCl_3$, while this ratio remains constant for $MgCl_2$–$LaCl_3$, regardless of $LaCl_3$ content. Considering that Coulomb ordering induces an alternation of anionic and cationic shells around a given ion, this observation suggests that in the presence of Na^+ ions, La^{3+}ions are more likely to appear in the fourth coordination sphere than in the second coordination sphere of other La^{3+}ions. A plausible explanation may be that La_xCl_y complexes in NaCl–$LaCl_3$ are generally spaced by Na^+, creating local La^{3+}-depleted regions that align with the "spacer salt" concept proposed by Emerson et al. [80] $MgCl_2$ does not exhibit this "spacer salt" property and the mixing behaviour with $LaCl_3$ is more homogeneous [48]. From a thermodynamic perspective, the homogeneous mixing explanation complements the observation that NaCl–MCl_3 (where M is a trivalent lanthanide or actinide cation) mixtures often exhibit enthalpy of mixing (ΔH) values nearly a magnitude higher than $MgCl_2$−MCl_3 [14,15,37,38], indicating more ideal mixing behaviour in the latter.

The RDF of the Cl^- – Cl^- ion pair can further substantiate the idea of homogeneous mixing. The position of the first RDF peak shifts towards lower values with increasing $LaCl_3$ content for NaCl–$LaCl_3$, but remains almost unchanged for $MgCl_2$–$LaCl_3$. This result may be surprising as the mean La–Cl distance in molten $LaCl_3$ (2.82 Å) is closer to that of Na–Cl in molten NaCl (2.66 Å) than that of Mg–Cl in molten $MgCl_2$ (2.41 Å). A convenient method to address this discrepancy is to perform a simplified analysis based on the general coordination environment of the pure solid salts: $LaCl_3$ can be treated as a network of isotropic 9-fold coordination polyhedra, while NaCl and $MgCl_2$ are treated as networks of isotropic 6-fold octahedra. Despite different cation–anion bond lengths, the edge lengths (i.e. neighbouring Cl–Cl distances) of the $LaCl_3$ and $MgCl_2$ polyhedra are quite similar, around 3.4 Å [59,85]. This allows Mg^{2+} ions to be more seamlessly incorporated into the $LaCl_3$ network without significantly perturbing Cl^- ion positions, resulting in more "ideal" mixing. This explanation is further supported by the absence of peaks for the Cl^- –Cl^- RDF of pure $MgCl_2$ in the even-numbered peak positions of pure $LaCl_3$. These positions correspond to the Cl–Cl distances that exist in $LaCl_3$ but do not exist in $MgCl_2$, indicating similar anion spacings facilitate the ideal mixing of binary mixtures.

Fig. 7 illustrates the local structures of NaCl–$LaCl_3$ and $MgCl_2$–$LaCl_3$ with 20 mol% $LaCl_3$, using single-frame snapshots from MD-generated trajectories of the "small" box simulations. A close inspection reveals that 6-fold and 7-fold La–Cl coordinations are preferred in NaCl–$LaCl_3$, while 7-fold and 8-fold La–Cl coordinations are favoured in $MgCl_2$–$LaCl_3$. Additionally, chloride bridging is more prevalent in NaCl–$LaCl_3$ than in $MgCl_2$–$LaCl_3$. These findings align with the La and Cl coordination number analysis in **Tables S8 and S9**. Furthermore, Fig. 7 also exemplifies the tendency of Na^+ ions to form "spacer" layers between La_xCl_y complexes in NaCl–$LaCl_3$, a structural property not observed with Mg^{2+} ions in $MgCl_2$–$LaCl_3$. Instead, Mg^{2+} ions can even appear to act as an intermediary between two distinct, isolated $[LaCl_n]^{3-n}$ complexes. These observations align with the mixing homogeneity explanation discussed in the RDF analysis above.

RDF analysis of ternary systems supports our findings from binary systems. Fig. 8 compares the RDF and CN of key ion pairs between different salt compositions in the NaCl–$MgCl_2$–$LaCl_3$ ternary system.

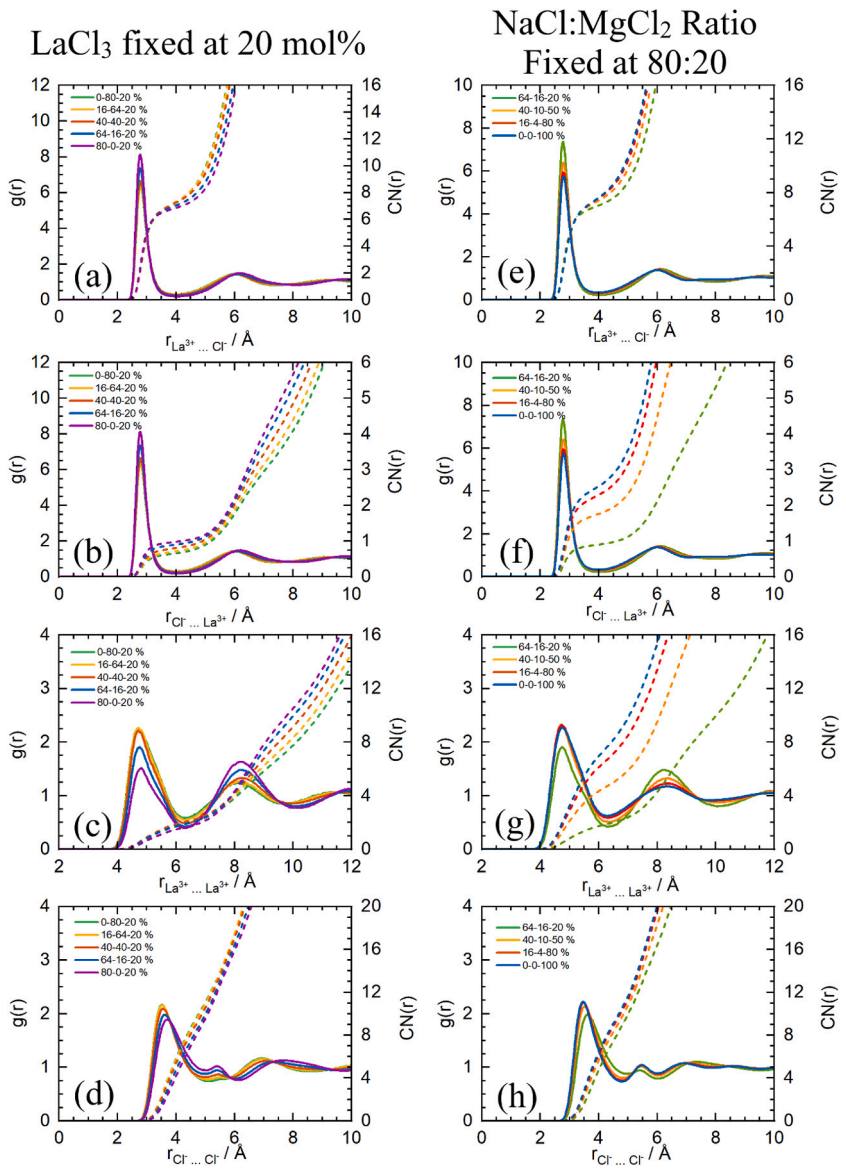

Fig. 8. Comparison of radial distribution functions, g(r), in solid lines, and coordination numbers, CN(r), in dotted lines, for key ion pairs in NaCl–$MgCl_2$–$LaCl_3$ with (a–d) $LaCl_3$ content fixed at 20 mol% and (e–h) NaCl/$MgCl_2$ ratio fixed at 80:20, at 1123 K.

With $LaCl_3$ fixed at 20 mol%, the La^{3+}–Cl^- RDF shows a marked increase in $CN_{La–Cl}$ from 6.94 to 7.25, while the Cl^-–La^{3+} RDF reveals a decrease in $CN_{Cl–La}$ from 0.99 to 0.66 as the $MgCl_2$ content rises. These results are consistent with our HT-NMR measurements of ternary systems (Fig. 4), upholding the role of $MgCl_2$ in enhancing La–Cl coordination and reducing chloride bridging. Furthermore, the shifting primary-to-secondary peak ratio in the La^{3+}–La^{3+} RDF reinforces the "spacer salt" effect present in NaCl but absent in $MgCl_2$. Additionally, the Cl^-–Cl^- ion pair RDF contrasts the mixing homogeneity induced by NaCl and $MgCl_2$; the secondary peak, indicative of the unique Cl–Cl distances in $LaCl_3$, diminishes with increasing $MgCl_2$ content, suggesting that Mg^{2+} ions can be more seamlessly incorporated into the La–Cl network than Na^+ ions. Meanwhile, when the NaCl/$MgCl_2$ ratio is fixed at 80:20, the RDFs exhibit similar behaviour as those in Fig. 6, albeit with characteristics reflecting both NaCl and $MgCl_2$.

Fig. 9 presents single-frame snapshots of ternary mixtures with varying NaCl/$MgCl_2$ ratios and a fixed $LaCl_3$ content of 20 mol%. As the NaCl/$MgCl_2$ ratio decreases, La^{3+} ions appear more evenly dispersed and higher-fold coordination becomes more prevalent. This may lead one to reason that the length of La_xCl_y chains decreases with increasing $MgCl_2$ content. However, polyhedral connectivity and polymer chain analyses on the simulated trajectories indicate a more nuanced behaviour (**Figure S5**). The number of sharing interactions between La–Cl polyhedra increases initially, peaking at a 1:1 NaCl/$MgCl_2$ ratio, before declining. Similarly, the average degree of polymerisation of La_xCl_y chains follows this trend. A closer examination of the polymer chain length distributions (**Figure S6**) indicates that binary systems exhibit a higher proportion of smaller polymer chains ($x < 8$) relative to ternary systems, while ternary systems exhibit a higher probability of longer chains ($x \geq 8$) when compared to binary systems. This behaviour likely stems from the dual role of $MgCl_2$ in NaCl–$LaCl_3$. While Na^+ ions act as a heterogeneous "spacer layer" that promotes the formation of longer La_xCl_y complexes, Mg^{2+} ions mix homogeneously with $LaCl_3$, disrupting the continuity of La–Cl polymer networks. Simultaneously, $MgCl_2$ contributes additional Cl^- ions into the system, creating more avenues for chloride bridging and network formation. While these opposing effects may explain the trends observed in MD simulations, the transient nature of these polymers—with lifetimes on the order of nanoseconds, far shorter than the millisecond timescales of NMR measurements—renders their formation undetectable in practice.

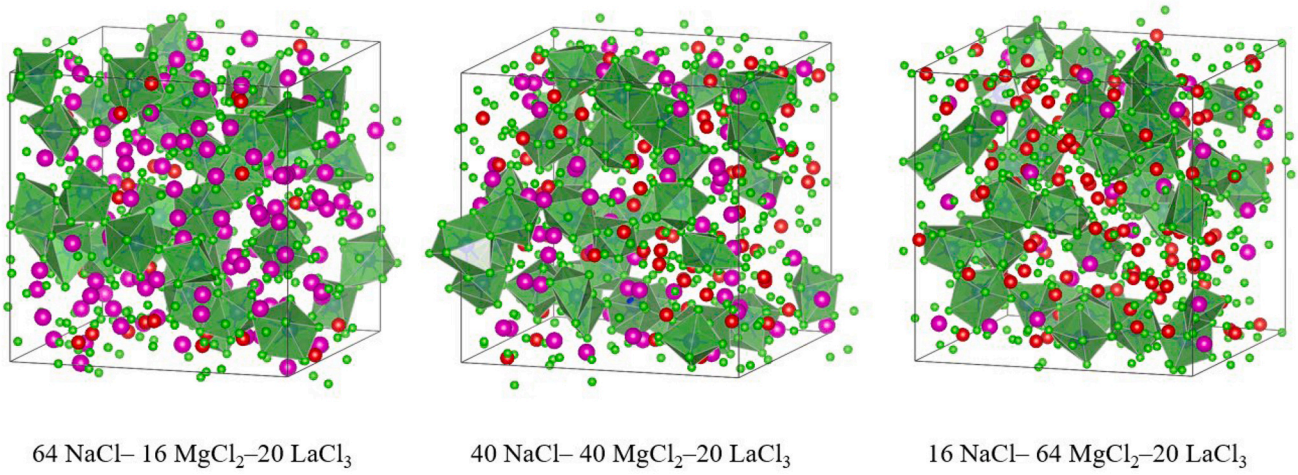

Fig. 9. Snapshots of NaCl–$MgCl_2$–$LaCl_3$ with varying NaCl/$MgCl_2$ ratios but fixed $LaCl_3$ content at 1123 K. Ions are represented based on colour: Na^+(violet), Mg^{2+}(red), La^{3+} (dark blue) and Cl^- (green). La–Cl coordination polyhedra are drawn around La^{3+} ions to highlight the difference in network formation behaviour. The La–Cl bond length cutoff is set at 4.00 Å, based on the first minimum observed in the RDFs.

To validate the accuracy of the MD simulations, we performed DFT calculations on the MD trajectories to assess whether the simulated chemical shifts aligned with experimental measurements. Specifically, the isotropic chemical shifts of all ^{139}La and ^{35}Cl atoms in selected snapshots of MD trajectories were calculated and the average of each species was taken as the simulated chemical shift.

Fig. 10 compares these simulated chemical shifts with the measured chemical shifts across different compositional variations. The simulated ^{35}Cl and ^{139}La chemical shifts markedly replicate the trends observed in the experimental data, albeit with a systematic error of approximately +30 ppm for ^{35}Cl and +90 ppm for ^{139}La. This discrepancy likely arises from the overestimation of La–Cl bond covalence by PBE functionals [86], uncertainties in the chemical shielding–shift correlation, finite-size effects of the simulation box, and absence of temperature effects in 0 K DFT calculations (as opposed to MD at finite temperatures). To remedy this error, we tried to recalibrate the chemical shielding–shift correlation by applying the DFT+*U* method. This approach involved shifting the empty 5d and 6s orbitals of La^{3+} to higher energies to reduce covalent interactions between La(5d,6s) and Cl(3p) orbitals [84,86]. While increasing orbital energy levels improved the correlation coefficient for ^{139}La nuclei (**Figure S7**), it simultaneously caused the corresponding ^{35}Cl chemical shifts to deviate further from the experimental values (**Table S8**). Consequently, we adopted to retain the default orbital energy levels defined by the ^{139}La pseudopotentials in CASTEP.

To elucidate the contribution of different coordination environments on the chemical shifts, we categorised the distribution of chemical shifts into smaller groups based on their CN, as shown in **Figures S9–S12**. The diagram reveals that chemical shifts in molten salts are not constant for a given CN, but instead follow a normal distribution. This variability arises from differences in interatomic distances and spatial configurations between ions, even when they share the same coordination environment.

Moreover, for ^{139}La nuclei, chemical shifts decrease as CN increases, consistent with our SS-NMR findings. However, the trends from SS-NMR do not always hold for ^{35}Cl in molten salts: In compositions with low $LaCl_3$ concentrations, ^{35}Cl chemical shifts increase with increasing coordination numbers, complying with SS-NMR trends; Yet, in $LaCl_3$-rich compositions, the opposite is observed—^{35}Cl chemical shifts decrease with increasing CN.

To address this inconsistency, we need to consider the deshielding effect of atoms in the first coordination sphere of La^{3+} and Cl^- ions in molten salts. For La^{3+}ions, which are always surrounded by Cl^- ions, an increase in the number of Cl^- neighbours enhances shielding, thereby lowering its chemical shift.

However, the situation is more nuanced for Cl^- ions, which can be coordinated by different cations. In general, La^{3+} ions exert a stronger deshielding effect than Na^+or Mg^{2+}, hence Cl^- ions involved in La–Cl–La interactions (i.e., bridging Cl^-) tend to exhibit larger chemical shifts than their non-bridging counterparts. Additionally, vacancies exercise a significant influence on chemical shifts. Unlike in crystalline solids where Cl^- are saturated with cation neighbours, Cl^- ions in molten salts may instead be adjacent to vacancy-like sites. These sites induce an even greater deshielding effect than La^{3+} ions. In $LaCl_3$-rich compositions, Cl^- ions with lower CN are more likely to be near these vacancies than Na^+ or Mg^{2+}, which increases deshielding and results in larger chemical shifts. This explains the counterintuitive trend observed in $LaCl_3$-rich compositions, where Cl^- ions with lower CN exhibit higher ^{35}Cl chemical shifts.

4. Conclusions

In this work, we employed in-situ HT-NMR to investigate the local structure of La^{3+} and Cl^- ions in molten NaCl–$MgCl_2$–$LaCl_3$ systems. Complementary techniques, such as SS-NMR, classical MD simulations, and DFT calculations, were also performed to interpret the chemical shifts obtained.

Our findings reveal that the average La–Cl coordination number tends to be lower in NaCl–$LaCl_3$ than in $MgCl_2$–$LaCl_3$ at comparable $LaCl_3$ concentrations. Moreover, chloride bridging occurs more frequently in NaCl–$LaCl_3$, resulting in more complex La–Cl–La networks; whereas, $MgCl_2$–$LaCl_3$ tend to form more isolated $[LaCl_n]^{3-n}$ units. These trends extend into the NaCl–$MgCl_2$–$LaCl_3$ ternary system; however, the polymerisation and polyhedral sharing interactions notably deviate from the expected behaviour, likely due to competing effects arising from the coexistence of NaCl and $MgCl_2$.

Our results suggest that in NaCl–$MgCl_2$–$LaCl_3$, NaCl takes on the role of a heterogeneous "spacer layer" that encourages the formation of larger continuous La–Cl–La networks, while $MgCl_2$ mixes homogeneously with $LaCl_3$, disrupting continuous La–Cl–La network formation. Extending this to MCFR fuel salts, the inclusion of $MgCl_2$ could potentially lower fuel viscosity. Another possible advantage may be the suppression of oxide precipitation, as the more isolated $[LaCl_n]^{3-n}$ units are expected to reduce the energy required to incorporate an oxygen atom between two adjacent La^{3+} ions [87,88], effectively making it more soluble.

By elucidating the structural dynamics at the atomic scale, our study

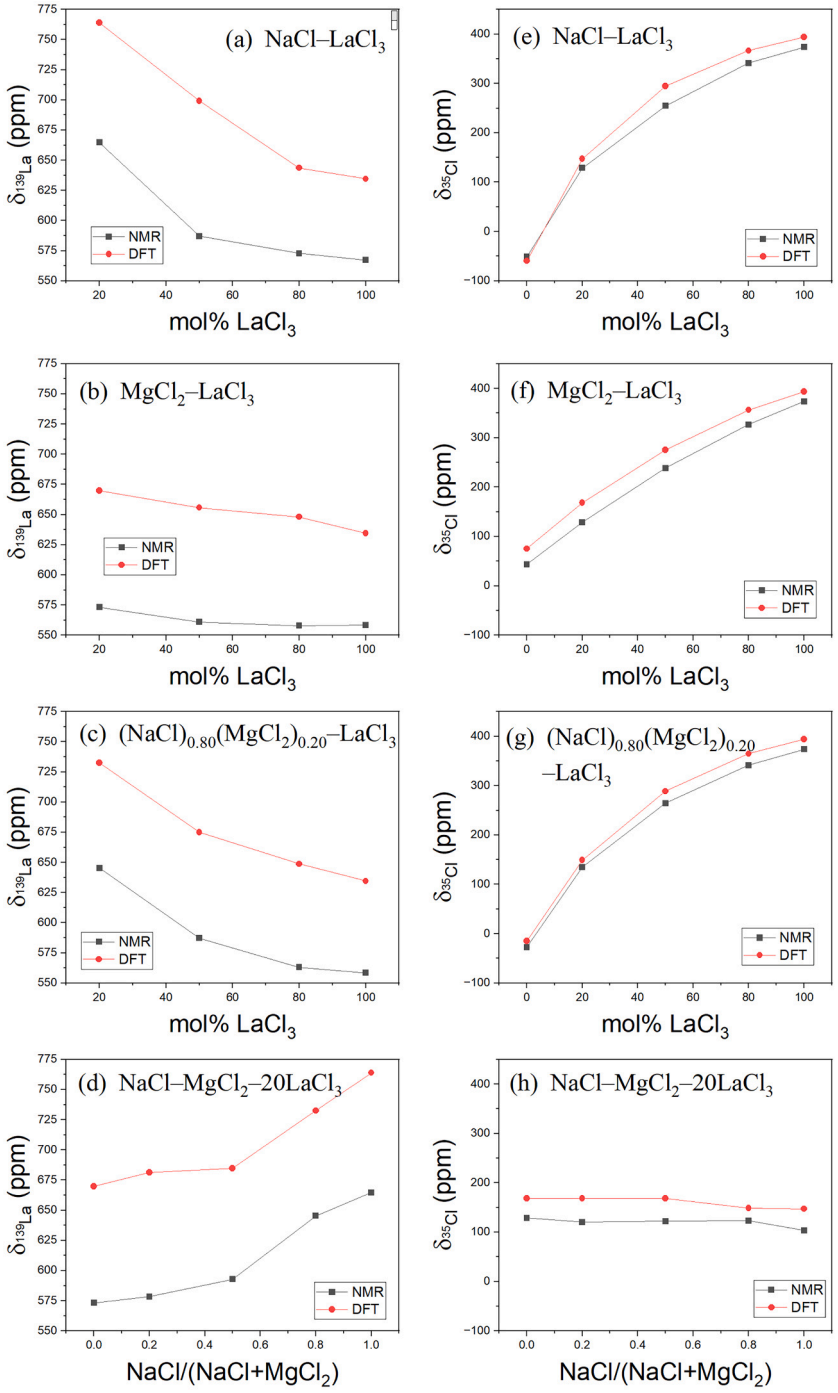

Fig. 10. Comparison of DFT-calculated (red circles) and HT-NMR-measured (black squares) chemical shifts for ^{139}La (a–d) and ^{35}Cl (e–f) nuclei across various molten salt compositions at 1123 K.

offers a deeper dive into the role of salt constituents and their impact on molten salt properties, which will be indispensable for the design and performance of MCFR fuel salts. Looking ahead, we plan to apply similar methods to study the effects of local structure on the viscosity and oxide solubility of molten salts. These insights could contribute to the advancement of molten salt reactors for civilian energy use.

Declaration of generative AI and AI-assisted technologies in the writing process

During the preparation of this work, the authors used ChatGPT-4o to improve the article's flow and readability. After using this tool/service, the authors reviewed and edited the content as needed and take full responsibility for the content of the published article.

CRediT authorship contribution statement

Woei Jer Ng: Data curation, Investigation, Methodology, Conceptualization, Formal analysis, Validation, Writing – original draft, Software, Visualization. **Aydar Rakhmatullin:** Writing – review & editing, Investigation, Resources, Validation, Methodology, Conceptualization, Supervision. **Kateryna Goloviznina:** Formal analysis, Software, Visualization, Data curation, Writing – review & editing, Conceptualization, Validation, Methodology. **Mathieu Salanne:** Validation, Software,

Writing – review & editing, Conceptualization, Methodology, Supervision. **Catherine Bessada:** Conceptualization, Project administration, Writing – review & editing, Funding acquisition, Supervision.

Declaration of competing interest

The authors declare that they have no known competing financial interests or personal relationships that could have appeared to influence the work reported in this paper.

Acknowledgements

This work was carried out as part of the ISAC (Innovative System for Actinide Conversion) project funded by the France 2030 government program. We extend our gratitude to SACADO (Service d'Aide au Calcul et à l'Analyse de DOnnées, Sorbonne Université) and CaSciMoDOT (Calcul Scientific et Modélisation Orléans Tours) for providing the computational resources necessary for our simulations. We also thank Dr F. Fayon and Dr D. Zanghi for the meaningful discussions. Financial support from the IR INFRANALYTICS FR2054 for conducting the research is gratefully acknowledged.

Supplementary materials

Supplementary material associated with this article can be found, in the online version, at doi:10.1016/j.jnucmat.2025.156056.

Data availability

Data will be made available on request.

References

[1] W.B. Cottrell, H.E. Hungerford, J.K. Leslie, and J.L. Meein, "Operation of the aircraft reactor experiment," 1955. doi: https://doi.org/10.2172/4237975.
[2] U.S. DOE Nuclear Energy Research Advisory Committee, A technology roadmap for generation IV nuclear energy systems, in: Generation-IV International Forum, 2002, 2002. Dec.
[3] G. Locatelli, M. Mancini, N. Todeschini, Generation IV nuclear reactors: current status and future prospects, Energy Policy 61 (2013) 1503–1520, https://doi.org/10.1016/j.enpol.2013.06.101.
[4] J.E. Kelly, Generation IV International Forum: a decade of progress through international cooperation, Prog. Nucl. Energy 77 (2014) 240–246, https://doi.org/10.1016/j.pnucene.2014.02.010.
[5] Global Nexus Initiative, "Nuclear power for the next generation: addressing energy, climate, and security challenges," 2017, [Online]. Available: http://globalnexusinitiative.org/wp-content/uploads/2017/04/GNI-Digital-Report-single.pdf.
[6] J. Serp, M. Allibert, O. Beneš, S. Delpech, O. Feynberg, V. Ghetta, D. Heuer, D. Holcomb, V. Ignatiev, J.L. Kloosterman, L. Luzzi, E. Merle-Lucotte, J. Uhlíř, R. Yoshioka, D. Zhimin, The molten salt reactor (MSR) in generation IV: overview and perspectives, Prog. Nucl. Energy 77 (2014) 308–319, https://doi.org/10.1016/j.pnucene.2014.02.014.
[7] L. He, S. Xia, J. Chen, G. Liu, J. Wu, Y. Zou, Th-U breeding performances in an optimized molten chloride salt fast reactor, Nucl. Sci. Eng. 195 (2) (2020) 185–202, https://doi.org/10.1080/00295639.2020.1798728.
[8] V. Pascal, P. Gauthé, E.M. Lopez, L. Matteo, Molten salt reactor technology: opportunities of Molten salt fuel for actinides management, in: Proceedings of a Technical Meeting, IAEA TECDOC Series, 2022.
[9] Rapport du Comité de Prospective en Énergie de l'Académie des sciences, "Les Réacteurs Nucléaires Modulaires de Faible Puissance (SMR): état des Lieux et Perspectives," 2022. [Online]. Available: https://www.academie-sciences.fr/pdf/rapport/20210614_avis_nucleaire.pdf.
[10] M.S. Chenaud, V. Pascal, C. Chabert-Koralewski, J. Serp, P. Laghoutaris, J. C. Garnier, F. Sudreau, B. Morel, I. Morales, O. Drouvot, S. David, E. Merle, J. M. Hamy, F. Botte, S. Takenouti, A. Sanna, The French R&D Collaborative Project ISAC on Fast MSR Dedicated to Actinides Transmutation, International Conference on the Management of Spent Fuel from Nuclear Power Plants (2024).
[11] M. Mascaron, T. le Meute, J. Martinet, V. Pascal, F. Bertrand, E. Merle, Study of the ARAMIS molten salt reactor behavior during unprotected transients. *ICAPP 2023*, ICAPP 2023 - 2023 International Congress on Advances in Nuclear Power Plants, in Conjunction with 38th Korea Atomic Power Annual Conference (ICAPP 2023 / KAP Conference) (2023) 2023200. https://cea.hal.science/cea-04399511.
[12] M. Mascaron, J. Martinet, V. Pascal, E. Merle, F. Bertrand, An approach to Molten Salt Reactor operation and control and its application to the ARAMIS actinide burner, Ann. Nucl. Energy 210 (2025), https://doi.org/10.1016/j.anucene.2024.110888. Jan.
[13] J.A. Ocádiz Flores, R.J.M. Konings, A.L. Smith, Using the quasi-chemical formalism beyond the phase diagram: density and viscosity models for molten salt fuel systems, J. Nucl. Mater. 561 (2022) 153536, https://doi.org/10.1016/j.jnucmat.2022.153536.
[14] O. Beneš, R.J.M. Konings, Thermodynamic evaluation of the NaCl-$MgCl_2$-UCl_3-$PuCl_3$ system, J. Nucl. Mater. 375 (2) (2008) 202–208, https://doi.org/10.1016/j.jnucmat.2008.01.007.
[15] W.J. Ng, H.J. Ryu, Effects of base salt additives on NaCl–UCl_3–$PuCl_3$ fuel systems: insights from CALPHAD simulations, J. Mol. Liq. 379 (2023), https://doi.org/10.1016/j.molliq.2023.121649. Jun.
[16] Y. Li, X. Xu, X. Wang, P. Li, Q. Hao, B. Xiao, Survey and evaluation of equations for thermophysical properties of binary/ternary eutectic salts from NaCl, KCl, $MgCl_2$, $CaCl_2$, $ZnCl_2$ for heat transfer and thermal storage fluids in CSP, Sol. Energy 152 (2017) 57–79, https://doi.org/10.1016/j.solener.2017.03.019.
[17] K. Hanson, K.M. Sankar, P.F. Weck, J.K. Startt, R. Dingreville, C.S. Deo, J.D. Sugar, P.M. Singh, Effect of excess Mg to control corrosion in molten $MgCl_2$ and KCl eutectic salt mixture, Corros. Sci. 194 (2022), https://doi.org/10.1016/j.corsci.2021.109914.
[18] C.W. Forsberg, "Thermal-and fast-spectrum molten salt reactors for actinide burning and fuel production thermal-and fast-spectrum molten salt reactors for actininde burning and fuel production," 2007.
[19] M.A. Rose, L.D. Gardner, T.T. Lichtenstein, S.A. Thomas, and E. Wu, "Property measurements of NaCl-UCl 3 and NaCl-KCl-UCl 3 molten salts prepared by," 2023. [Online]. Available: http://www.osti.gov/.
[20] T.Y. Karlsson, S.C. Middlemas, M.T. Nguyen, M.E. Woods, K.R. Tolman, V. A. Glezakou, S.D. Herrmann, J. Schorne-Pinto, R.D. Johnson, S.E. Reddish, S. A. Warmann, P.D. Paviet, Synthesis and thermophysical property determination of NaCl-PuCl3 salts, J. Mol. Liq. 387 (2023), https://doi.org/10.1016/j.molliq.2023.122636.
[21] M. Salanne and P.A. Madden, "Polarization effects in ionic solids and melts," Oct. 10, 2011. doi: 10.1080/00268976.2011.617523.
[22] B. Li, S. Dai, D. en Jiang, Molecular dynamics simulations of structural and transport properties of molten NaCl-UCl_3 using the polarizable-ion model, J. Mol. Liq. 299 (2020), https://doi.org/10.1016/j.molliq.2019.112184.
[23] H. Kim, C. Kwon, S. Ham, J. Lee, S.J. Kim, S. Kim, Physical properties of KCl-UCl_3 molten salts as potential fuels for molten salt reactors, J. Nucl. Mater. 577 (2023), https://doi.org/10.1016/j.jnucmat.2023.154329. Apr.
[24] M. Simoes Santos, M. Salanne, T. Kooyman, D. Lambertin, Structural and transport properties of the molten salt NaCl-KCl-UCl_3 using the polarizable ion model, J. Nucl. Mater. 597 (2024), https://doi.org/10.1016/j.jnucmat.2024.155125. Aug.
[25] B. Li, S. Dai, D. en Jiang, Adding $MgCl_2$ to Molten NaCl−UCl_n (n=3, 4): insights from First-principles Molecular dynamics, Chemphyschem. 23 (11) (2022), https://doi.org/10.1002/cphc.202200078.
[26] S. Delpech, C. Carrière, A. Chmakoff, L. Martinelli, D. Rodrigues, C. Cannes, Corrosion mitigation in molten salt environments, Mater. (Basel) 17 (3) (2024), https://doi.org/10.3390/ma17030581. Feb.
[27] K.A. Pace, V.V. Klepov, A.A. Berseneva, H.C. zur Loye, Covalency in actinide compounds, Chem. - Eur. J. 27 (19) (2021) 5835–5841, https://doi.org/10.1002/chem.202004632. Apr.
[28] D.S. Maltsev, D.M. Driscoll, Y. Zhang, J.C. Neuefeind, B. Reinhart, C. Agca, D. Ray, P.W. Halstenberg, M. Aziziha, J. Schorne-Pinto, T.M. Besmann, V.S. Bryantsev, S. Dai, S. Roy, A.S. Ivanov, Transient covalency in molten uranium(III) chloride, J. Am. Chem. Soc. 146 (31) (2024) 21220–21224, https://doi.org/10.1021/jacs.4c05765.
[29] S. Jiang, Y. Liu, L. Wang, Z. Chai, W.Q. Shi, The Coordination Chemistry of F-Block Elements in Molten Salts, John Wiley and Sons Inc., 2022, https://doi.org/10.1002/chem.202201145. Oct. 26.
[30] K. Machado, D. Zanghi, M. Salanne, C. Bessada, Structural, dynamic, and thermodynamic study of KF-AlF3 melts by combining high-temperature NMR and molecular dynamics simulations, J. Phys. Chem. C 123 (4) (2019) 2147–2156, https://doi.org/10.1021/acs.jpcc.8b11907. Jan.
[31] A. Rakhmatullin, K. Machado, D. Zanghi, I.B. Polovov, R. Bakirov, K. V. Maksimtsev, C. Bessada, Study of the NaF-ScF_3 system as a molten bath for production of Sc alloys: acombination of NMR and molecular dynamics simulations, J. Alloys Comp. 786 (2019) 953–959.
[32] C.M. Schurz, T. Schleid, G. Meyer, K_2LaCl_5, Acta Crystallogr Struct Rep Online 66 (12) (2010), https://doi.org/10.1107/S1600536810045198. Dec.
[33] H.J. Seifert, H. Fink, B. Baumgartner, Structure and stability of the low-temperature modification of compounds Cs3LnCl6 (Ln = La–Gd), J. Solid. State Chem. 107 (1993) 19–26.
[34] L. Bonafous, B. Ollivier, Y. Auger, H. Chaudret, C. Bessada, D. Massiot, I. Farnan, J. P. Coutures, High temperature NMR observation of mobile phases up to 1500°C, J. Chim. Phys. 92 (1995) 1867–1870.
[35] V. Lacassagne, C. Bessada, P. Florian, S. Bouvet, B. Ollivier, J.P. Coutures, D. Massiot, Structure of high-temperature NaF-AlF_3-Al_2O_3 melts: a multinuclear NMR study, J. Phys. Chem. B. 106 (8) (2002) 1862–1868.
[36] D. Hudry, A. Rakhmatullin, C. Bessada, I. Bardez, F. Bart, S. Jobic, P. Deniard, Reactivity of $NH_4H_2PO_4$ toward $LaCl_3$ in LiCl-KCl melt flux. Step by step formation of monazite-like $LaPO_4$, Inorg. Chem. 48 (15) (2009) 7141–7150, https://doi.org/10.1021/ic9003142.
[37] K. Igarashi, H. Ohtani, J. Mochinaga, Phase diagram of the system $LaCl_3$-$CaCl_2$-NaCl, Z. Naturforsch 42 (1987) 1421–1424.
[38] Y. Wang, X. Hu, T. Huang, C. Tian, Thermodynamic optimization and calculation of $LaCl_3$-$MgCl_2$ system, Asian J. Chem. 26 (6) (2014) 1655–1657, https://doi.org/10.14233/ajchem.2014.17315.

[39] A.D. Pelton, S.A. Degterov, G. Eriksson, C. Robelin, Y. Dessureault, The modified quasichemical model I - Binary solutions, Metall. Mater. Trans. B: Process Metall. Mater. Process. Sci. 31 (4) (2000) 651–659, https://doi.org/10.1007/s11663-000-0103-2.

[40] A.D. Pelton, P. Chartrand, The modified quasi-chemical model: part II. Multicomponent solutions, Met. Mater Trans Phys Met. Mater Sci. 32 (6) (2001) 1355–1360, https://doi.org/10.1007/s11661-001-0226-3.

[41] C.W. Bale, E. Bélisle, P. Chartrand, S.A. Decterov, G. Eriksson, A.E. Gheribi, K. Hack, I.H. Jung, Y.B. Kang, J. Melançon, A.D. Pelton, S. Petersen, C. Robelin, J. Sangster, P. Spencer, M.A. van Ende, FactSage thermochemical software and databases, 2010-2016, CALPHAD 54 (2016) 35–53, https://doi.org/10.1016/j.calphad.2016.05.002.

[42] E.L. Hahn, Spin Echoes, Phys. Rev. 80 (4) (1950) 580–594.

[43] S. Meiboom, D. Gill, Modified spin-echo method for measuring nuclear relaxation times, Rev. Sci. Instrum. 29 (8) (1958) 688–691, https://doi.org/10.1063/1.1716296.

[44] D. Massiot, I. Farnan, N. Gautier, D. Trumeau, A. Trokiner, J.P. Coutures, ^{71}Ga and ^{69}Ga nuclear magnetic resonance study of β-Ga_2O_3: resolution of four- and six-fold coordinated Ga sites in static conditions, Solid State Nucl. Magn. Reson. 4 (1995) 241–248.

[45] D. Massiot, F. Fayon, M. Capron, I. King, S. le Calvé, B. Alonso, J.O. Durand, B. Bujoli, Z. Gan, G. Hoatson, Modelling one- and two-dimensional solid-state NMR spectra, Magn. Reson. Chem. 40 (1) (2002) 70–76, https://doi.org/10.1002/mrc.984.

[46] A. Marin-Laflèche, M. Haefele, L. Scalfi, A. Coretti, T. Dufils, G. Jeanmairet, S. Reed, A. Serva, R. Berthin, C. Bacon, S. Bonella, B. Rotenberg, P. Madden, M. Salanne, MetalWalls: a classical molecular dynamics software dedicated to the simulation of lectrochemical systems, J. Open Source Softw. 5 (53) (2020) 2373, https://doi.org/10.21105/joss.02373.

[47] Y. Ishii, S. Kasai, M. Salanne, N. Ohtori, Transport coefficients and the Stokes-Einstein relation in molten alkali halides with polarisable ion model, Mol. Phys. 113 (17–18) (2015) 2442–2450, https://doi.org/10.1080/00268976.2015.1046527. Sep.

[48] M.S. Emerson, A.S. Ivanov, L.C. Gallington, D.S. Maltsev, P. Halstenberg, S. Dai, S. Roy, V.S. Bryantsev, C.J. Margulis, Heterogeneous structure, mechanisms of counterion exchange, and the spacer salt effect in complex molten salt mixtures including $LaCl_3$, J. Phys. Chem. B. 128 (16) (2024) 3972–3980, https://doi.org/10.1021/acs.jpcb.4c01429.

[49] K. Goloviznina, M.C. Notarangelo, J. Tranchida, E. Bourasseau, M. Salanne, DFT-based polarizable ion models for molten rare-earth chlorides: from lanthanum to europium, J. Phys. Chem. B 129 (3) (2025) 1016–1025, https://doi.org/10.1021/acs.jpcb.4c07931.

[50] L. Martinez, R. Andrade, E.G. Birgin, J.M. Martínez, PACKMOL: a package for building initial configurations for molecular dynamics simulations, J. Comput. Chem. 30 (13) (2009) 2157–2164, https://doi.org/10.1002/jcc.21224.

[51] M. Brehm, B. Kirchner, TRAVIS - A free analyzer and visualizer for monte carlo and molecular dynamics trajectories, J. Chem. Inf. Model. 51 (8) (2011) 2007–2023, https://doi.org/10.1021/ci200217w. Aug.

[52] M. Brehm, M. Thomas, S. Gehrke, B. Kirchner, TRAVIS—A Free Analyzer For Trajectories from Molecular Simulation, American Institute of Physics Inc., 2020, https://doi.org/10.1063/5.0005078. Apr. 30.

[53] K. Momma, F. Izumi, VESTA 3 for three-dimensional visualization of crystal, volumetric and morphology data, J. Appl. Crystallogr. 44 (6) (2011) 1272–1276, https://doi.org/10.1107/S0021889811038970. Dec.

[54] C.J. Pickard and F. Mauri, "All-electron magnetic response with pseudopotentials: NMR chemical shifts," 2001.

[55] S.J. Clark, M.D. Segall, C.J. Pickard, P.J. Hasnip, M.I.J. Probert, K. Refson, M. C. Payne, First principles methods using CASTEP, Z. Kristallogr. (2005) 220.

[56] M.D. Segall, P.J.D Lindan, C.J. Pickard, P. Hasnip, and S.J. Clark, "First-principles simulation: ideas, illustrations and the CASTEP code," 2002.

[57] J.P. Perdew, K. Burke, and M. Ernzerhof, "Generalized gradient approximation made simple," 1996.

[58] J.R. Yates, C.J. Pickard, F. Mauri, Calculation of NMR chemical shifts for extended systems using ultrasoft pseudopotentials, Phys. Rev. B Condens. Matter. Mater. Phys. 76 (2) (2007), https://doi.org/10.1103/PhysRevB.76.024401. Jul.

[59] B. Morosi, Crystal structures of anhydrous rare-earth chlorides, J. Chem. Phys. 49 (7) (1968) 3007–3012, https://doi.org/10.1063/1.1670543.

[60] D. Kato, P. Song, H. Ubukata, H. Taguro, C. Tassel, K. Miyazaki, T. Abe, K. Nakano, K. Hongo, R. Maezono, H. Kageyama, Evolutionary algorithm directed synthesis of mixed anion compounds LaF_2X (X=Br, I) and $LaFI_2$, Angew. Chem. Int. Ed. 62 (30) (, 2023), https://doi.org/10.1002/anie.202301416.

[61] K. Krämer, T. Schleid, M. Schulze, W. Urland, G. Meyer, Three bromides of Lanthanum: laBr_2, La_2Br_5, and $LaBr_3$, ZAAC - J. Inorg. Gen. Chem. 575 (1) (1989) 61–70, https://doi.org/10.1002/zaac.19895750109.

[62] C. Gökhan Ünlü, M. Burak Kaynar, T. Şimşek, A. Tekgül, B. Kalkan, Ş. Özcan, Structure and magnetic properties of $(La_{1-x}Fe_x)FeO_3$ (x = 0, 0.25, 0.50) perovskite, J. Alloys. Compd. 784 (2019) 1198–1204, https://doi.org/10.1016/j.jallcom.2019.01.047. May.

[63] S. Tsunekawa, T. Kamiyama, K. Sasaki, H. Asano, T. Fukuda, Precise structure analysis by neutron diffraction for $RNbO_4$ and distortion of NbO_4 tetrahedra, Acta Crystallogr. A 49 (4) (1993) 595–600, https://doi.org/10.1107/S0108767392013035.

[64] I. Khidirov, V.T. Om, Localization of hydrogen atoms in rare earth metal trihydroxides $R(OH)_3$, phys. status solidi (a) 140 (2) (1993) K59–K62, https://doi.org/10.1002/pssa.2211400231.

[65] A. Zalkin and D.H. Templeton, "Refinement of the trigonal crystal structure of Lanthanum trifluoride with neutron diffraction data," 1984.

[66] S. Hull, S.T. Norberg, I. Ahmed, S.G. Eriksson, C.E. Mohn, High temperature crystal structures and superionic properties of $SrCl_2$, $SrBr_2$, $BaCl_2$ and $BaBr_2$, J. Solid. State Chem. 184 (11) (2011) 2925–2935, https://doi.org/10.1016/j.jssc.2011.09.004. Nov.

[67] M. Sist, K.F.F. Fischer, H. Kasai, B.B. Iversen, Low-temperature anharmonicity in cesium chloride (CsCl), Angew. Chem. 129 (13) (2017) 3679–3683, https://doi.org/10.1002/ange.201700638. Mar.

[68] Y.V. Nelyubina, A.A. Korlyukov, K.A. Lyssenko, Experimental charge density evidence for pnicogen bonding in a crystal of ammonium chloride, Chemphyschem. 16 (3) (2015) 676–681, https://doi.org/10.1002/cphc.201402673. Feb.

[69] F.F.Y. Wang, D.E. Cox, The coherent neutron scattering amplitude of Rb: a neutron diffraction study of RbCl, Acta Crystallogr. A 26 (3) (1970) 377–379, https://doi.org/10.1107/S0567739470000906.

[70] V.L. Cherginets, V.N. Baumer, S.S. Galkin, L.V. Glushkova, T.P. Rebrova, Z. V. Shtitelman, Solubility of Al_2O_3 in some chloride-fluoride melts, Inorg. Chem. 45 (18) (2006) 7367–7371, https://doi.org/10.1021/ic060181r. Sep.

[71] A. Ievinš, M. Straumanis, and K. Karlsons, "Präzisionsbestimmung von Gitterkonstanten hygroskopischer verbindungen (LiCl, NaBr)," 1936.

[72] S. Lee, H. Xu, H. Xu, J. Neuefeind, Crystal structure of moganite and its anisotropic atomic displacement parameters determined by synchrotron x-ray diffraction and x-ray/neutron pair distribution function analyses, Minerals 11 (3) (2021) 1–12, https://doi.org/10.3390/min11030272. Mar.

[73] K.J. Ooms, K.W. Feindel, M.J. Willans, R.E. Wasylishen, J.V. Hanna, K.J. Pike, M. E. Smith, Multiple-magnetic field ^{139}La NMR and density functional theory investigation of the solid lanthanum(III) halides, "Solid State Nucl. Magn. Reson. 28 (2–4) (2005) 125–134, https://doi.org/10.1016/j.ssnmr.2005.07.002.

[74] L. Spencer, E. Coomes, E. Ye, V. Terskikh, A. Ramzy, V. Thangadurai, G.R. Goward, Structural analysis of lanthanum-containing battery materials using ^{139}La solid-state NMR, Can. J. Chem. 89 (9) (2011) 1105–1117, https://doi.org/10.1139/v11-049.

[75] C.M. Widdifield, R.P. Chapman, and D.L. Bryce, "Chapter 5 chlorine, bromine, and iodine solid-State NMR spectroscopy," 2009. doi: 10.1016/S0066-4103(08)00405-5.

[76] H. Zhang, I. Farnan, High temperature 35Cl nuclear magnetic resonance study of the LiCl-KCl system and the effect of CeCl3 dissolution, Faraday Discuss. 190 (2016) 367–385, https://doi.org/10.1039/c6fd00003g.

[77] F. Hutchinson, A.J. Rowley, M.K. Walters, M. Wilson, P.A. Madden, J.C. Wasse, P. S. Salmon, *Structure of molten MCl_3 systems from a polarizable ion simulation model.* http://ojps.aip.org/jcpo/jcpcr.jsp.

[78] A.L. Rollet, S. Godier, C. Bessada, High temperature NMR study of the local structure of molten LaF_3-AF (A = Li, Na, K and Rb) mixtures, Phys. Chem. Chem. Phys. 10 (22) (2008) 3222–3228, https://doi.org/10.1039/b719158h.

[79] D. Corradini, P.A. Madden, M. Salanne, Coordination numbers and physical properties in molten salts and their mixtures, Faraday Discuss. 190 (2016) 471–486, https://doi.org/10.1039/c5fd00223k.

[80] M.S. Emerson, S. Sharma, S. Roy, V.S. Bryantsev, A.S. Ivanov, R. Gakhar, M. E. Woods, L.C. Gallington, S. Dai, D.S. Maltsev, C.J. Margulis, Complete description of the $LaCl_3$–NaCl melt structure and the concept of a spacer salt that causes structural heterogeneity, J. Am. Chem. Soc. (2022), https://doi.org/10.1021/jacs.2c09987.

[81] K.J. Ooms, K.W. Feindel, M.J. Willans, R.E. Wasylishen, J.V. Hanna, K.J. Pike, M. E. Smith, Multiple-magnetic field ^{139}La NMR and density functional theory investigation of the solid lanthanum(III) halides, Solid State Nucl. Magn. Reson. 28 (2–4) (2005) 125–134, https://doi.org/10.1016/j.ssnmr.2005.07.002.

[82] I.N. Flerov, M.V. Gorev, K.S. Aleksandrov, A. Tressaud, J. Grannec, M. Couzi, Phase transitions in elpasolites (ordered perovskites), Mater. Sci. Eng. 24 (1998) 81–151.

[83] A. Rakhmatullin, F. Šimko, E. Véron, M. Allix, C. Martineau-Corcos, A. Fitch, F. Fayon, R.A. Shakhovoy, K. Okhotnikov, V. Sarou-Kanian, M. Korenko, Z. Netriová, I.B. Polovov, C. Bessada, X-ray diffraction, NMR studies, and DFT calculations of the room and high temperature structures of rubidium cryolite, Rb_3AlF_6, In. Chem. 59 (9) (2020) 6308–6318.

[84] A. Rakhmatullin, M.S. Molokeev, G. King, I.B. Polovov, K.V. Maksimtsev, E. Chesneau, E. Suard, R. Bakirov, F. Šimko, C. Bessada, M. Allix, Polymorphs of Rb_3ScF_6: X-ray and neutron diffraction, solid-state NMR, and density functional theory calculations study, In. Chem. 60 (8) (2021) 6016–6026, https://doi.org/10.1021/acs.inorgchem.1c00485.

[85] D.E. Partin and M. O'Keeffe, "The structures and crystal chemistry of magnesium chloride and cadmium chloride," 1991.

[86] A. Sadoc, M. Body, C. Legein, M. Biswal, F. Fayon, X. Rocquefelte, F. Boucher, NMR parameters in alkali, alkaline earth and rare earth fluorides from first principle calculations, Physi. Chem. Chem. Phy. 13 (41) (2011) 18539–18550, https://doi.org/10.1039/c1cp21253b.

[87] A.L. Rollet, E. Veron, C. Bessada, Fission products behavior in molten fluoride salts: speciation of La^{3+} and Cs^+ in melts containing oxide ions, J. Nucl. Mater. 429 (1–3) (2012) 40–47, https://doi.org/10.1016/j.jnucmat.2012.05.010. Oct.

[88] X. Song, S. Li, S. Liu, Y. Fan, J. He, J. Song, Coordination States of Metal Ions in Molten Salts and Their Characterization Methods, University of Science and Technology Beijing, 2023, https://doi.org/10.1007/s12613-023-2608-7. Jul. 01.

THE JOURNAL OF PHYSICAL CHEMISTRY B
A JOURNAL OF THE AMERICAN CHEMICAL SOCIETY

pubs.acs.org/JPCB

Article

Effect of Mg^{2+} Ions on Transport Properties in Molten Chloride Fast Reactor Fuels

Woei Jer Ng,* Kateryna Goloviznina, Vincent Sarou-Kanian, Mathieu Salanne, and Aydar Rakhmatullin

Cite This: *J. Phys. Chem. B* 2026, 130, 2270−2277

Read Online

ACCESS | Metrics & More | Article Recommendations | Supporting Information

ABSTRACT: Molten chloride fast reactors (MCFRs) are emerging as a promising class of molten salt reactor (MSR) designs due to their ability to dissolve large amounts of major actinides while keeping low melting points and sustaining a hard neutron spectrum. In this context, understanding the transport properties of molten salts—such as viscosity and self-diffusivity—is essential for the design and optimization of MSRs with efficient heat transfer. However, an important gap remains in the literature regarding the transport properties in molten chlorides. In this work, we performed classical molecular dynamics (MD) simulations with the polarizable ion model (PIM) to evaluate the viscosities and self-diffusion coefficients of molten NaCl−$MgCl_2$−$LaCl_3$, which was used in our previous work as a simulant for the ARAMIS-A reactor fuel. To validate the accuracy of our approach, calculated transport properties for the NaCl−$LaCl_3$ binary system were benchmarked against capillary viscometry measurements from the literature and our own pulsed-field gradient nuclear magnetic resonance (PFG−NMR) experiments. Our study compares the roles of NaCl and $MgCl_2$ on the transport properties of MCFR fuels. Interestingly, we observe that $MgCl_2$ does not affect $LaCl_3$-poor and $LaCl_3$-rich melts in the same way due to the competition between multivalent ions for chloride ions in their first coordination shells and their ability to form cluster species.

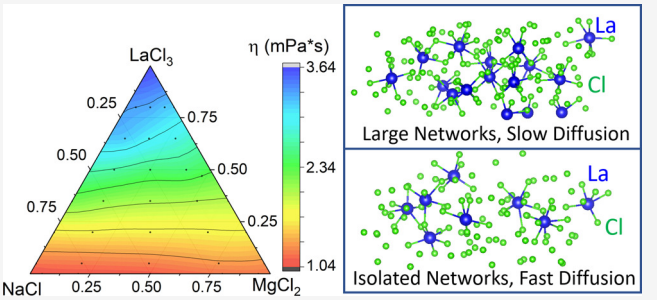

Downloaded via BIBCNRS INC on April 24, 2026 at 14:00:28 (UTC).
See https://pubs.acs.org/sharingguidelines for options on how to legitimately share published articles.

1. INTRODUCTION

Chloride salts have garnered renewed interest as fuel candidates for molten salt reactors (MSRs).[1] In the United States, the Molten Chloride Reactor Experiment utilizes the binary eutectic mixture of NaCl−UCl_3 to investigate key performance characteristics of molten chloride fast reactors (MCFRs), such as fuel salt chemistry, instrumentation, thermal hydraulics, corrosion behavior, and fuel handling techniques.[2,3] In Canada, the Stable Salt Reactor−Wasteburner concept proposes an innovative MSR design in which actinide trichloride fuel salts are loaded in fuel assemblies similar to those of light water reactors and cooled by a surrounding pool of liquid salt.[4] In France, the ARAMIS-A actinide burner reactor design employs NaCl−$MgCl_2$−$PuCl_3$−$AmCl_3$ fuel salt as part of a long-term strategy to reduce its high-level radioactive waste inventory.[5]

Being a thermal power system, efficient heat transfer is central to the design and engineering of MSRs. In this context, Bonilla's Figures of Merit (FOMs)[6] are widely used to assess the heat transfer efficiency of MSRs. Quantification of the FOMs typically requires five key thermophysical parameters: thermal expansivity, density, heat capacity, viscosity, and thermal conductivity. Among these, viscosity—along with its complementary property of ion diffusivity—stands out as a property that is particularly challenging to measure and verify. This can be attributed to several factors: (1) high operating temperatures and the corrosive nature of molten salts necessitate the use of specialized and robust equipment; (2) low flow resistance makes viscosity measurements susceptible to minor temperature fluctuations and mechanical vibrations, therefore requiring instruments with high sensitivity and precision; (3) susceptibility to moisture and oxygen impurities often reduces the reproducibility of measurements; (4) radiotoxicity of actinide salts poses additional safety and handling concerns.

Due to these challenges, progress in measuring the viscosity of actinide chlorides has been limited. Early work by Desyatnik et al. used a torsional oscillation viscometer to study NaCl−UCl_3 melts.[7] This was followed by Katyshev et al., who extended this technique to the KCl−UCl_3−UCl_4 system.[8] More recently, Kim et al. developed a custom high-temperature falling ball viscometer to evaluate the viscosities of the $(LiCl−KCl)_{eut}$−UCl_3−$NdCl_3$−$LaCl_3$−$CeCl_3$ molten salt system at 773 K.[9] Using a similar setup, Jung et al. measured the viscosity of the NaCl−$MgCl_2$−UCl_3 molten salt between 877 and 941 K, reporting good reproducibility of data with an

Received: December 2, 2025
Revised: January 16, 2026
Accepted: February 2, 2026
Published: February 5, 2026



ACS Publications

© 2026 The Authors. Published by American Chemical Society

https://doi.org/10.1021/acs.jpcb.5c08179
J. Phys. Chem. B 2026, 130, 2270−2277

experimental error of less than 3%.[10] The most recent advancements came from Oak Ridge National Laboratory, where rolling ball viscometry and high-purity salts were used to reassess the viscosities of 63 mol % NaCl−37 mol % UCl_3, yielding improved accuracy over previous results.[11]

In contrast to the limited experimental data, many of the currently available assessments of MCFR fuel viscosities are purely computational. Paul et al. used semiempirical models to evaluate the impact of transmutation products on the viscosity of NaCl−UCl_3.[12] Ocádiz Flores et al. demonstrated the use of advanced CALPHAD models to predict viscosities of the NaCl−UCl_3 binary system.[13] Classical molecular dynamics (MD) simulations based on the polarizable ion model (PIM) have been used extensively to compute the viscosities of various fuel salt compositions, including NaCl−UCl_3,[14] NaCl−$PuCl_3$,[15] KCl−UCl_3,[16] and NaCl−KCl−UCl_3.[17] First-principle molecular dynamics simulations have also been applied to investigate the viscosities and ion diffusivities of NaCl−UCl_3,[11] NaCl−$PuCl_3$,[18] and LiCl−KCl−UCl_3.[19]

Building on our previous work on NaCl−$MgCl_2$−$LaCl_3$ as a surrogate for the ARAMIS-A reactor fuel,[20] in this study, we bridge the gap between computational insights and experimental data by calculating the viscosities and ion diffusion coefficients of the NaCl−$LaCl_3$ binary system from MD trajectories, subsequently benchmarking them against experimental measurements from capillary viscometry and pulsed field gradient nuclear magnetic resonance (PFG−NMR). Our MD simulations produce well-converged transport properties with minimal statistical noise, showing excellent agreement with experimental data. Furthermore, we investigate the variation of these transport properties with the addition of $MgCl_2$, interpreting the trends from the perspective of structural dynamics and local coordination environments. Our results not only reinforce the foundations for accurate thermophysical modeling of MSR fuel salts but also offer invaluable insights for the design and optimization of pyroprocessing technologies.

2. METHODOLOGY

2.1. Classical MD Simulations

Ion trajectories of molten chloride systems were simulated using the MetalWalls code[21,22] which implements the PIM.[23] All force field parameters and interatomic potentials are documented in Tables S1−S3, which are the same values from our previous work.[20] Cubic periodic simulation boxes containing 2000−4000 atoms were constructed for each target composition (Table S4), with the initial configurations generated using PACKMOL.[24] Simulations were performed with a 1.0 fs time step following this protocol: (1) nonpolarizable *NPT* equilibration of 0.2 ns, (2) polarizable *NPT* equilibration of 0.5 ns, and (3) polarizable *NVT* production of 10.0 ns. During the final step, stress tensors and ion trajectories were recorded at 10.0 fs and 1.0 ps intervals, respectively. The simulation temperature was regulated using Nosé−Hoover thermostats (1123 K for standard calculations and 1200 K for direct comparison with experimental viscosities), and an external pressure was fixed at 1 bar for NPT simulations. A cutoff of 10.6 Å was used for nonbonded interactions, with a tail correction included for energy and pressure. Long-range Coulomb interactions were treated using the Ewald summation method with a tolerance of 10^{-7}.

Viscosities, η, were computed using the Green−Kubo formalism, which relates viscosity to the time integral of the autocorrelation function of the off-diagonal components of the stress tensor:

$$\eta = \frac{V}{k_B T}\int_0^\infty \mathrm{d}t' \langle \tau_{\alpha\beta}(t')\cdot\tau_{\alpha\beta}(0)\rangle \tag{1}$$

where V is the volume of the simulation box, k_B is the Boltzmann constant, T is the absolute temperature, and $\tau_{\alpha\beta}$ denotes an off-diagonal element of the stress tensor (xy, xz, or yz). To eliminate statistical noise and improve convergence of the integral, a cepstral filter[25] was applied, following the methodology outlined in ref 26.

Self-diffusion coefficients, D_i, were derived from ion trajectories using Einstein's relation for mean-squared displacement:

$$D_i = \frac{1}{6}\lim_{t\to\infty}\frac{d}{dt}\left\langle \frac{1}{N}\sum_{k=1}^{N} |r_{i,k}(t) - r_{i,k}(0)|^2 \right\rangle \tag{2}$$

where N is the number of ions of species i and $r_{i,k}(t)$ is the position of the kth ion of species i at time t. To correct for finite-size effects in periodic simulation cells, the Yeh−Hummer correction[27,28] was applied

$$D_{i,\infty} = D_i + \frac{2.837298 k_B T}{6\pi\eta L} \tag{3}$$

where $D_{i,\infty}$ is the self-diffusion coefficient in infinite systems and L is the edge length of the cubic simulation box.

2.2. PFG−NMR Experiments

NaCl (Merck Suprapur, ≥99.5%) and $LaCl_3$ (AnhydroBeads, ≥99.99%) salts were used as received without further purification. All sample preparation was conducted inside an argon-filled glovebox, with moisture and oxygen levels maintained below 0.3 and 1.0 ppm, respectively. The salts were carefully weighed using an electronic balance and homogenized using a mortar and pestle to obtain the desired salt compositions.

For each measurement, three small fragments of boron nitride (measuring <3 mm on each dimension) were inserted into a high-purity boron nitride crucible (6 mm diameter × 14 mm height). The crucible was subsequently filled with the prepared salt mixtures. These boron nitride inserts serve to suppress the convection currents of molten salts, ensuring that the measured transport phenomena arise solely from ion diffusion.[29]

PFG−NMR measurements were carried out following the protocol established in ref 29, with the sole modification of using 16 gradient steps instead of 8 to improve precision. Additionally, each measurement was also repeated over a range of time parameters—including the diffusion time (Δ), gradient pulse length (δ), and the interval between successive $\pi/2$-pulses (τ)—to verify that the measured diffusivities were consistent and free of convection artifacts. As the pulse sequence is highly sensitive to nuclear relaxation properties, the T_1 and T_2 relaxation times of ^{23}Na, ^{139}La, and ^{35}Cl were measured beforehand (Table 1). Given that reliable self-diffusion coefficient measurements require T_1 and T_2 values greater than 5 ms, only ^{23}Na exhibited sufficiently long relaxation times, and thus, measurements were limited to this nucleus.

https://doi.org/10.1021/acs.jpcb.5c08179
J. Phys. Chem. B 2026, 130, 2270−2277

Table 1. Measured T_1 and T_2 Relaxation Times of Molten NaCl−$LaCl_3$ Binary Compositions at 1123 K and a Magnetic Field of 9.4 T

$LaCl_3$ mole fraction, x_{LaCl3}	T_1 relaxation times (ms)			T_2 relaxation times (ms)		
	^{23}Na	^{139}La	^{35}Cl	^{23}Na	^{139}La	^{35}Cl
0	1120	–	137	5.93	–	2.48
0.20	78.0	0.426	2.57	32.7	0.693	2.31
0.50	70.2	0.355	0.402	29.7	0.211	0.937
0.80	45.5	0.0744	0.662	13.1	0.109	0.702

3. RESULTS AND DISCUSSION

3.1. NaCl−$LaCl_3$

Figure 1 compares the dynamic viscosities of NaCl−$LaCl_3$ binary melts obtained from our MD simulations with available experimental data. To the best of our knowledge, the only reported measurements of this binary system are from Kim,[30,31] who used capillary viscometry at 1200 K. To supplement our comparison, reference viscosities of pure NaCl and $LaCl_3$ melts have been included. For NaCl, we used values recommended by Janz[32] and Brockner et al.,[33] obtained using torsional oscillation viscometry between 1080 and 1300 K. For $LaCl_3$, we used capillary viscometry data by Potapov and Sato[34] in the temperature range of 1140−1196 K.

Molten salt viscosities follow Arrhenius behavior, where relatively small temperature changes can lead to sharp drops in viscosity. For example, NaCl melts experience a 16.3% reduction in viscosity from 1123 to 1200 K, while $LaCl_3$ melts exhibit a 20.3% drop from 1140 to 1196 K. Consequently, our initial MD results at 1123 K showed a sizable discrepancy from Kim's measurements at 1200 K. To enable a direct comparison, we performed additional viscosity calculations at 1200 K. The MD-calculated viscosity data points at 1123 and 1200 K are provided in Table S5. Our calculations show excellent agreement with the experimental data, with a minor overprediction of <0.2 mPa·s for compositions with <80 mol % $LaCl_3$ and a slight underprediction of <0.4 mPa·s at higher $LaCl_3$ content. This composition-dependent transition from slight overprediction to underprediction may arise from the finite size of our simulation box relative to the increasingly interdigitated La−Cl−La networks at high $LaCl_3$ content.

Another notable trend is the steep increase in viscosity with increasing $LaCl_3$ content. Previous structural dynamics analyses of NaCl−$LaCl_3$ melts[20,35] have shown that $LaCl_3$ tends to form extended La−Cl−La chains and large $[La_xCl_y]^{3x-y}$ complexes in NaCl−$LaCl_3$, with this behavior becoming increasingly prevalent at higher $LaCl_3$ concentrations. On a microscopic scale, these large, interconnected units impede flow by increasing internal resistance to deformation and raising the shear stress required to sustain motion, thereby elevating viscosity.

While viscosity elucidates the resistance of the melt to flow, the self-diffusivity was also investigated as a complementary measure of how individual ions move through the ionic network. Figure 2a compares the sodium ion diffusivities across NaCl−$LaCl_3$ binary compositions obtained from PFG−NMR measurements and MD simulations at 1123 K. Values of the measured and calculated diffusion coefficients are provided in Tables S6 and S7, respectively. Diffusivity data for pure NaCl by Janz and Bansal[36] are included to provide an additional reference for benchmarking. The close agreement between our MD calculations and the experimental results corroborates our computational approach. As $LaCl_3$ content increases, we observe a marked decrease in sodium ion diffusivities. A similar trend is observed for the calculated diffusivities of La^{3+}

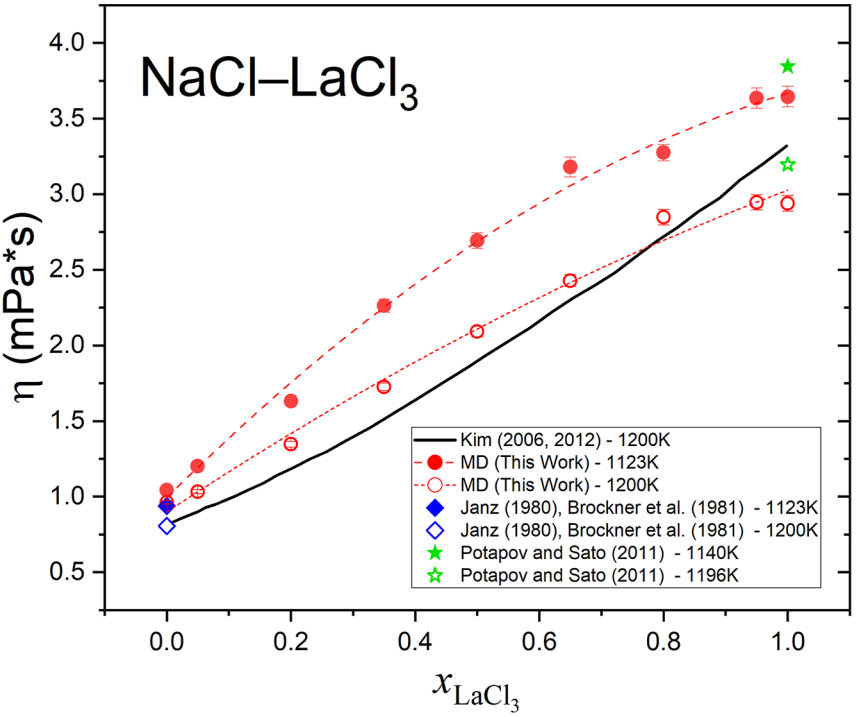

Figure 1. Comparison between the dynamic viscosities of NaCl−$LaCl_3$ binary melts. The MD-calculated data were fitted using single-exponential decay functions of the form $y = a + b \exp(-kx)$.

https://doi.org/10.1021/acs.jpcb.5c08179
J. Phys. Chem. B 2026, 130, 2270−2277

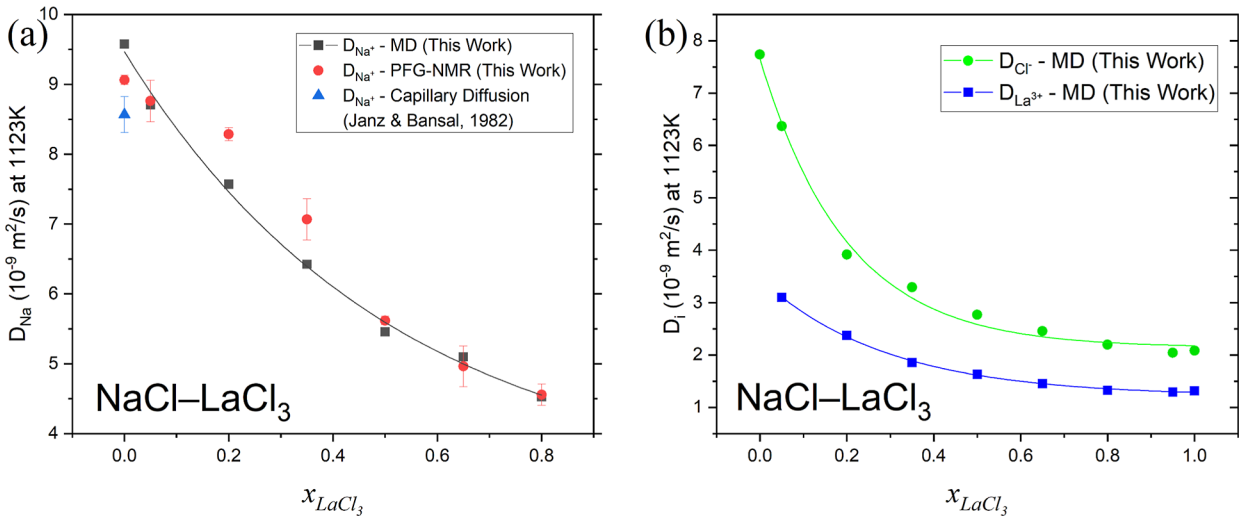

Figure 2. (a) Calculated and measured Na^+ self-diffusion coefficients in NaCl–$LaCl_3$ binary melts at 1123 K; (b) calculated La^{3+} and Cl^- self-diffusion coefficients in NaCl–$LaCl_3$ binary melts at 1123 K. The MD-calculated data were fitted using single-exponential decay functions of the form $y = a + b\ \exp(-kx)$.

and Cl^- ions, which also decrease rapidly with increasing $LaCl_3$ concentration (Figure 2b).

A useful metric to evaluate this flow behavior is the hydrodynamic radius, r_H, defined via the Stokes–Einstein–Sutherland relation:

$$r_{H,i} = \frac{k_B T}{c' \pi \eta D_{i,\infty}} \tag{4}$$

where c' is a constant that depends on boundary conditions ($c' = 4$ for "slip" and $c' = 6$ for "stick"). Tables S8 ("slip") and S9 ("stick") document the simulated hydrodynamic radii of ions for all molten salt compositions assessed in this study. Under "slip" boundary conditions, the hydrodynamic radii for Na^+ and Cl^- ions closely resemble their Shannon crystal radii (Table S10).[37] In the framework of previously established hydrodynamic interpretation of alkali halide melts bearing trivalent metal cations,[38] this suggests that Na^+ and Cl^- ions behave as nearly spherical diffusing particles that "slip" past surrounding fluids with little tangential drag. Nonetheless, because the Shannon radii of Na^+ (1.16 Å) and Cl^- (1.67 Å) differ substantially, the "slip" designation—which is more commonly applied to diffusing entities of comparable sizes—should be understood phenomenologically in this context: it reflects that the Na–Cl coordination shell relaxes faster than momentum is transferred to the surrounding melt,[38] rather than implying that the ions themselves diffuse strictly at their crystallographic radii.

In contrast, both "slip" and "stick" hydrodynamic radii for La^{3+} ions are substantially larger than the corresponding bare crystal radii, indicating that La^{3+} transport couples strongly to the surrounding fluid. This behavior is consistent with La^{3+} ions diffusing as part of interdigitated $[La_xCl_y]^{3x-y}$ complexes.[38] These anisotropic clusters act like "sticky" hydrodynamic objects that transfer tangential momentum to the surrounding melt, thereby increasing viscous dissipation. Taken together, this hydrodynamic analysis reinforces prior findings that lanthanide and actinide trichlorides markedly increase the viscosity of molten salt systems.

3.2. Effects of $MgCl_2$ Addition

Unfortunately, PFG–NMR measurements could not be performed on molten salts containing $MgCl_2$ due to material compatibility issues with boron nitride. In this context, $MgCl_2$ exhibited strong surface interactions with BN inserts, resulting in an anomalous peak splitting. Moreover, we noticed the creeping of molten $MgCl_2$ along the walls of the BN crucibles, resulting in profuse leakage during heating and consequently poor measurements. These limitations underline the need for alternative crucibles and insert materials to enable reliable diffusion measurements in molten salts containing $MgCl_2$. In light of these challenges, the influence of $MgCl_2$ on the viscosities and diffusion coefficients of NaCl–$LaCl_3$ melts was evaluated solely through classical MD simulations.

Figure 3 presents the calculated dynamic viscosities of the NaCl–$MgCl_2$–$LaCl_3$ ternary system at 1123 K. Viscosities were assessed at 41 distinct compositions using eq 1 and interpolated with a complementary smoothing algorithm to

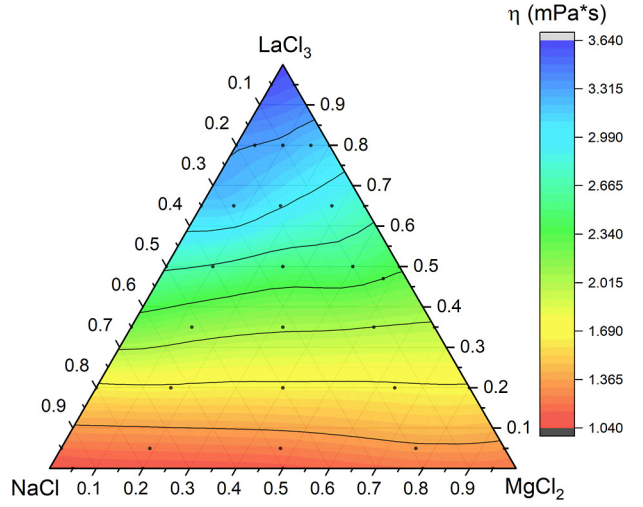

Figure 3. Calculated dynamic viscosities of the NaCl–$MgCl_2$–$LaCl_3$ ternary system at 1123 K. Black dots indicate the 41 reference compositions used in the interpolation.

https://doi.org/10.1021/acs.jpcb.5c08179
J. Phys. Chem. B 2026, 130, 2270–2277

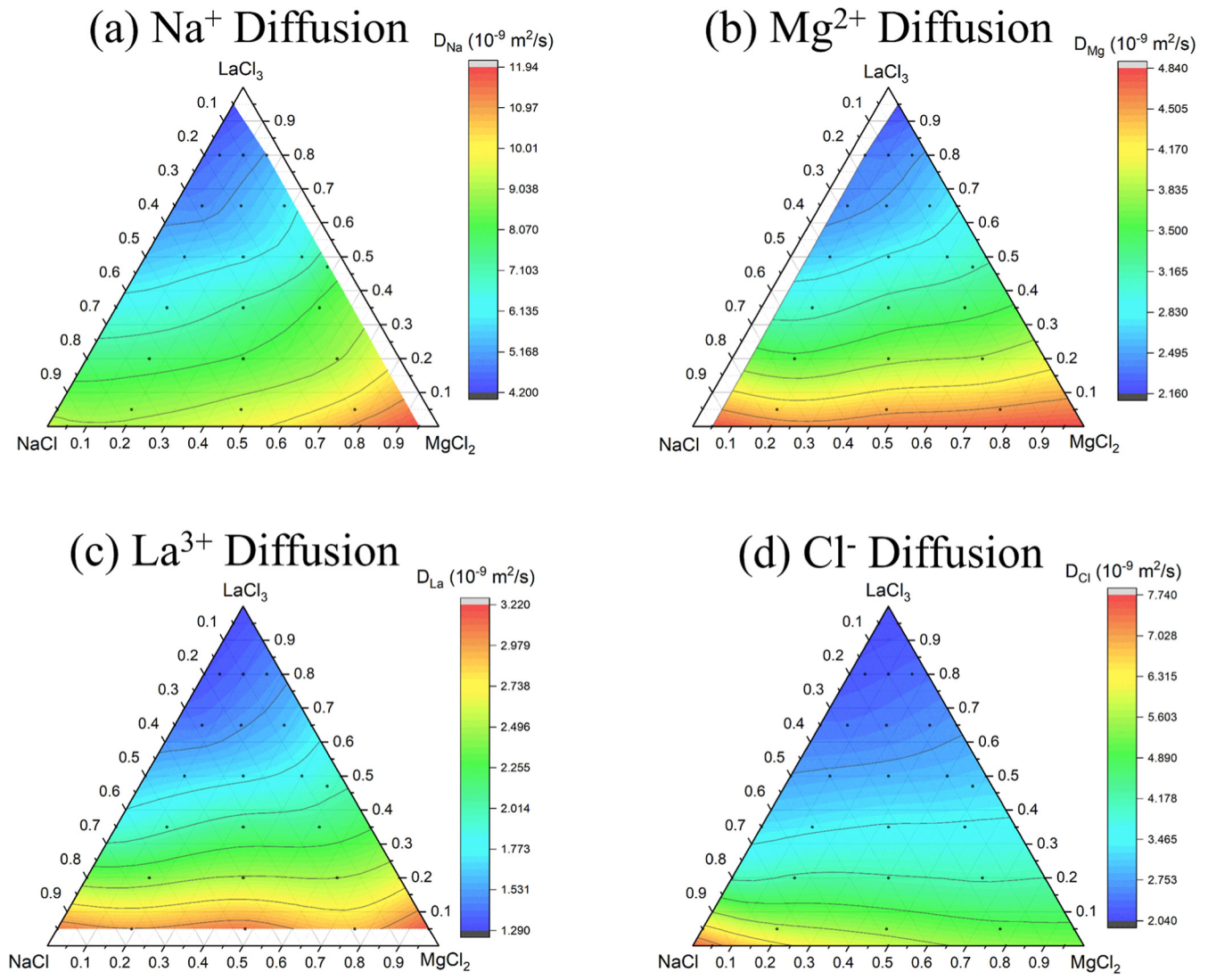

Figure 4. Calculated self-diffusion coefficients of (a) Na^+, (b) Mg^{2+}, (c) La^{3+}, and (d) Cl^- ions in the $NaCl–MgCl_2–LaCl_3$ ternary system at 1123 K. Black dots indicate the 41 reference compositions used in the interpolation.

produce a continuous contour map. The raw viscosity data points are given in Table S7.

At first glance, it is evident that the $LaCl_3$ concentration exerts the largest effect on melt viscosities: as the $LaCl_3$ content increases, the melt becomes significantly more viscous. As discussed earlier, this corresponds directly to the formation of large $[La_xCl_y]^{3x-y}$ clusters that hinder ion mobility and impede flow.

In contrast, the effects of the $MgCl_2$ addition are more nuanced. At higher $LaCl_3$ concentrations (>20 mol %), increasing $MgCl_2$ content results in a noticeable reduction of melt viscosities. This is attributable to the role of $MgCl_2$ in disrupting the formation of extensive La−Cl−La networks, leading to smaller and more isolated $[La_xCl_y]^{3x-y}$ units.[20,39] Under this less rigid framework, ions experience fewer barriers to mobility and less internal resistance to flow, thus leading to lower viscosities. However, below the threshold of 20 mol % $LaCl_3$, the impact of $MgCl_2$ appears less pronounced—and conversely, the melt viscosities tend to increase slightly with $MgCl_2$. In these more dilute regimes, the formation of $[La_xCl_y]^{3x-y}$ clusters is less prominent. Consequently, melt viscosities become more dependent on the intrinsic mobilities of the constituent ions in NaCl and $MgCl_2$.

To further elucidate these trends, Figure 4 depicts the self-diffusion coefficients of Na^+, Mg^{2+}, La^{3+}, and Cl^- ions across the same compositional spectrum. Here, the color scheme is chosen to mirror that of the viscosity contour plot, accentuating ion mobility instead of absolute diffusivity values. It is worth noting that the magnitude of ion diffusivities consistently decreases in the order $Na^+ > Cl^- > Mg^{2+} > La^{3+}$ across all compositions, mirroring the trend of increasing hydrodynamic radii. This correspondence highlights the utility of the hydrodynamic radius as a metric for evaluating relative ion mobilities.

As expected, all ion diffusivities decline sharply with increasing $LaCl_3$ concentration, reflecting the dominant effect of $[La_xCl_y]^{3x-y}$ clusters in retarding the ion mobility. Within this overall trend, cations and anions behave differently. Cation diffusivities are enhanced by increasing the $MgCl_2$-to-NaCl ratio at all $LaCl_3$ concentrations, consistent with the role of $MgCl_2$ in disrupting the La−Cl−La network formation. Anions, by contrast, show diffusivity trends more akin to that of viscosity: at high $LaCl_3$ concentrations, Cl^- diffusion

https://doi.org/10.1021/acs.jpcb.5c08179
J. Phys. Chem. B 2026, 130, 2270−2277

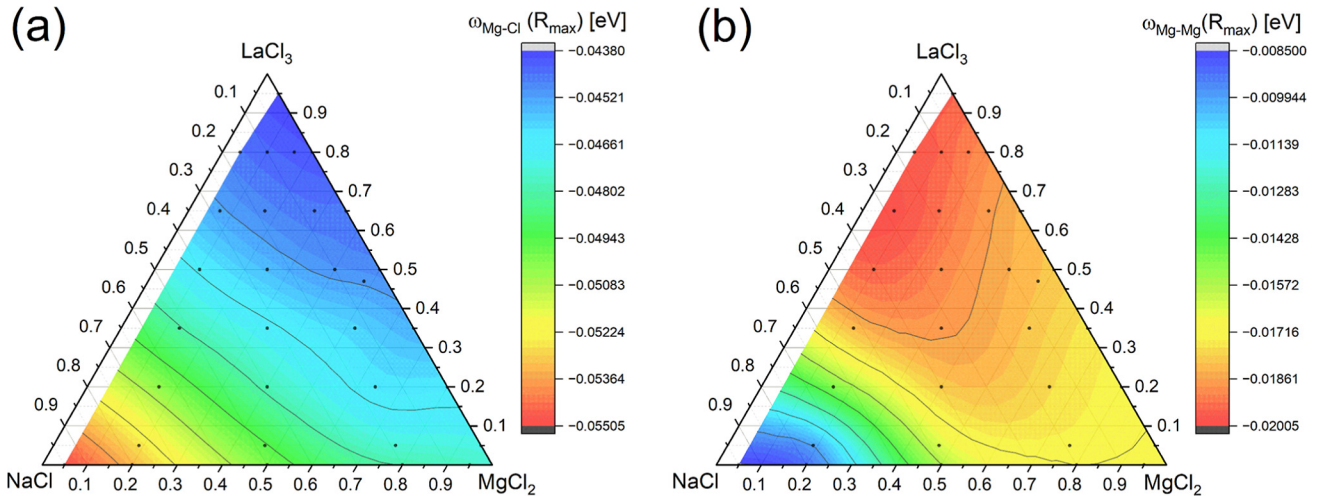

Figure 5. Potential of mean force (PMF) for (a) Mg^{2+}−Cl^- and (b) Mg^{2+}−Mg^{2+} ion pairs across all compositions. All PMFs here are evaluated at the first RDF maximum of each composition, R_{max}. Black dots indicate the 41 reference compositions used in the interpolation.

increases with $MgCl_2$ content because smaller, more isolated $[La_xCl_y]^{3x-y}$ complexes reduce Cl^- ion confinement to bridging interactions within clusters;[20] at lower $LaCl_3$ concentrations, Cl^- ion diffusivity decreases slightly with $MgCl_2$, reflecting a more complex role of $MgCl_2$ under dilute $LaCl_3$ conditions.

To rationalize these behaviors, we examine the free energy profile between ion pairs, described by the potential of mean force (PMF), ω_{ij}, defined in eq 5:

$$\omega_{ij}(r) = -k_B T \ln g_{ij}(r) \tag{5}$$

where $g_{ij}(r)$ is the radial distribution function (RDF) for an i−j ion pair. In this work, we specifically evaluate ω_{ij} at the first RDF maximum, R_{max}. RDFs of Mg^{2+}−Cl^- and Mg^{2+}−Mg^{2+} ion pairs for several representative molten salt compositions are shown in Figure S1, while Figure 5 presents the corresponding PMFs across all compositions.

The Mg^{2+}−Cl^- PMF indicates the strongest correlations in NaCl-rich compositions, which weaken as the $MgCl_2$ content rises and are the weakest in the $LaCl_3$-rich region. This trend reflects competition between cations of differing charge densities for Cl^- coordination. At low $LaCl_3$ concentrations, stronger Mg^{2+}−Cl^- electrostatic interactions slow down Cl^- motion (relative to Na^+−Cl^-), therefore reducing its diffusivity.

Another plausible explanation for the reduced Cl^- mobility in $MgCl_2$-rich compositions involves the formation of $[Mg_xCl_y]^{2x-y}$ complexes. In this compositional region, the Mg^{2+}−Mg^{2+} PMF reveals enhanced correlations, consistent with the formation of interconnected Mg−Cl−Mg networks. In low-$LaCl_3$ melts, these $[Mg_xCl_y]^{2x-y}$ complexes act as the primary "sticky" hydrodynamic units that impede flow, leading to greater viscous dissipation. This explanation parallels the intermediate-ranged ordering of $MgCl_2$ previously observed in molten KCl−$MgCl_2$.[40] The large discrepancy between Mg^{2+} hydrodynamic and Shannon radii (Tables S8−S10) further supports this picture. Because Cl^- anions are the nearest neighbors of Mg^{2+}, their diffusivity in low-$LaCl_3$ concentration regimes is strongly influenced by $[Mg_xCl_y]^{2x-y}$ clustering, whereas this clustering effect on the mobility of secondary-neighbor cations is less pronounced.

In short, the dual role of $MgCl_2$ reconciles the contrasting diffusivity trends: In $LaCl_3$-rich compositions, $MgCl_2$ acts as a La−Cl−La network disruptor that improves ion diffusivity, whereas at low $LaCl_3$ concentrations, $MgCl_2$ forms "sticky" hydrodynamic complexes that hinder ion mobility. Given that Cl^- ions constitute a majority species in NaCl−$MgCl_2$−$LaCl_3$, these competing effects also explain why the viscosity landscape most closely mirrors Cl^- diffusivity.

4. CONCLUSIONS

In this work, we employed classical MD simulations with PIM to evaluate viscosities and self-diffusion coefficients across the NaCl−$MgCl_2$−$LaCl_3$ compositional space. The accuracy of our simulations for NaCl−$LaCl_3$ binary compositions was validated against capillary viscometry data from Kim[30,31] and our own PFG−NMR measurements. To the best of our knowledge, viscosity measurements on the $MgCl_2$−$LaCl_3$ binary system are unavailable in the literature, and PFG−NMR measurements could not be performed due to compatibility issues between molten $MgCl_2$ and BN crucibles.

Overall, we discovered that $MgCl_2$ reduces molten salt viscosity when $LaCl_3$ concentrations exceed 20 mol %, primarily due to its ability to disrupt the formation of large $[La_xCl_y]^{3x-y}$ clusters and thereby enhance ion mobility. Below this threshold, however, NaCl contributes to viscosities slightly lower than those of $MgCl_2$. This is attributed to the tendency of $MgCl_2$ to form $[Mg_xCl_y]^{2x-y}$ complexes in $LaCl_3$-deficient regimes, thereby impeding the ion mobility. The excellent agreement between simulation results and experimental data confirms the reliability of our interatomic potentials in accurately capturing the atomic-scale structure and transport of molten salts. Additionally, the smooth continuity of our calculated values throughout the ternary composition space demonstrates the consistency of our simulation protocol and shows that converged transport properties can be obtained using moderate box sizes (<5000 atoms) and relatively short simulation time scales (~10 ns).

In short, our work highlights the feasibility of computationally efficient and precise modeling of molten salt transport properties. Our results offer valuable insights and benchmarks for the advancement of molten salt R&D, not only limited to MSR technology but also for other energy and industrial applications, such as pyroprocessing, concentrated solar power, and electrorefining.

https://doi.org/10.1021/acs.jpcb.5c08179
J. Phys. Chem. B 2026, 130, 2270−2277

■ ASSOCIATED CONTENT

Supporting Information

The Supporting Information is available free of charge at https://pubs.acs.org/doi/10.1021/acs.jpcb.5c08179.

PIM interatomic potentials for NaCl−$MgCl_2$−$LaCl_3$, number of ions used for MD simulations, raw data of calculated and measured transport properties, calculated "slip" and "stick" hydrodynamic radii of individual ions, and RDF of Mg^{2+}−Cl^- and Mg^{2+}−Mg^{2+} ion pairs for representative compositions (PDF)

■ AUTHOR INFORMATION

Corresponding Author

Woei Jer Ng − *CEMHTI UPR3079 CNRS, Université d'Orléans, F-45071 Orléans, France;* orcid.org/0000-0002-1388-9211; Email: woei-jer.ng@cnrs-orleans.fr

Authors

Kateryna Goloviznina − *Sorbonne Université, CNRS, Physicochimie des Électrolytes et Nanosystèmes Interfaciaux, F-75005 Paris, France;* orcid.org/0000-0001-9913-4938

Vincent Sarou-Kanian − *CEMHTI UPR3079 CNRS, Université d'Orléans, F-45071 Orléans, France;* orcid.org/0000-0001-9611-8377

Mathieu Salanne − *Sorbonne Université, CNRS, Physicochimie des Électrolytes et Nanosystèmes Interfaciaux, F-75005 Paris, France; CNRS@CREATE, Singapore 138601, Singapore;* orcid.org/0000-0002-1753-491X

Aydar Rakhmatullin − *CEMHTI UPR3079 CNRS, Université d'Orléans, F-45071 Orléans, France*

Complete contact information is available at: https://pubs.acs.org/10.1021/acs.jpcb.5c08179

Notes

The authors declare no competing financial interest.

■ ACKNOWLEDGMENTS

This work was carried out as part of the ISAC (Innovative System for Actinides Conversion) project funded by the France 2030 government program. We extend our gratitude to SACADO (Service d'Aide au Calcul et à l'Analyse de DOnnées, Sorbonne Université) for providing the computational resources necessary for our simulations.

■ REFERENCES

(1) Serp, J.; Allibert, M.; Beneš, O.; Delpech, S.; Feynberg, O.; Ghetta, V.; Heuer, D.; Holcomb, D.; Ignatiev, V.; Kloosterman, J. L.; Luzzi, L.; Merle-Lucotte, E.; Uhlíř, J.; Yoshioka, R.; Zhimin, D. The Molten Salt Reactor (MSR) in Generation IV: Overview and Perspectives. *Prog. Nucl. Energy* **2014**, *77*, 308−319.

(2) Krepel, J.; Kramer, K. J. TerraPower Fast Chloride Reactor. In *Molten Salt Reactors and Thorium Energy*; Elsevier, 2024; pp 953−972.

(3) *Molten Chloride Reactor Experiment*. https://inl.gov/nuclear-energy/molten-salt-research/ (accessed 2025−11−24).

(4) Taylor, T.; Gregoire, O.; Haigh, P.; Boddington, S.; O'Sullivan, R. Waste burning performance of the moltex SSR-W. In *5th Generation IV and Small Reactors (G4SR) Conference*: Ottawa, ON, Canada, 2024.

(5) Mascaron, M.; Martinet, J.; Pascal, V.; Merle, E.; Bertrand, F. An Approach to Molten Salt Reactor Operation and Control and Its Application to the ARAMIS Actinide Burner. *Ann. Nucl. Energy* **2025**, *210*, 110888.

(6) Bonilla, C. F. *Nuclear Engineering Handbook*; McGraw-Hill: New York, 1958; pp 9−90.

(7) Desyatnik, V. N.; Katyshev, S. F.; Raspopin, S. P.; Chervinskii, Y. F. Density, Surface Tension, and Viscosity of Uranium Trichloride-Sodium Chloride Melts. *Sov. Atom. Energy* **1975**, *39* (1), 649−651.

(8) Katyshev, S. F.; Chervinskii, Y. F.; Desyatnik, V. N. Density and Viscosity of Fused Mixtures of Uranium Chlorides and Potassium Chloride. *Sov. Atom. Energy* **1982**, *53* (2), 565−566.

(9) Kim, J. Y.; Bae, S. E.; Kim, D. H.; Choi, Y. S.; Yeon, J. W.; Song, K. High-Temperature Viscosity Measurement of LiCl-KCl Molten Salts Comprising Actinides and Lanthanides. *Bull. Korean Chem. Soc.* **2012**, *33* (11), 3871−3874.

(10) Jung, C.-Y.; Lee, E.; Kim, T.-H.; Kim, J.-Y. Viscosity of Molten Salt Systems: NaCl-$MgCl_2$ and NaCl-$MgCl_2$-UCl_3. In *Abstracts of Proceedings of the Korean Radioactive Waste Society*, 2023, p 474.

(11) Termini, N.; Birri, A.; Smith, B.; Chesser, R.; Numbers, J.; Garland, K.; Wilgocki, E.; Gray, C.; Glezakou, V. *FY24 Progress Report on Viscosity and Thermal Conductivity Measurements of Nuclear Industry-Relevant Chloride Salts: An Experimental and Computational Study*; 2024. https://www.osti.gov/(accessed 2025−11−24).

(12) Paul, S.; Attarian, S.; Fratoni, M.; Morgan, D.; Szlufarska, I. Influence of Transmutation Products on the Thermophysical Properties of Eutectic NaCl-UCl_3 Fuel Salt in a Fast-Spectrum Molten Salt Reactor. *J. Nucl. Mater.* **2025**, *605*, 155572.

(13) Ocádiz Flores, J. A.; Konings, R. J. M.; Smith, A. L. Using the Quasi-Chemical Formalism beyond the Phase Diagram: Density and Viscosity Models for Molten Salt Fuel Systems. *J. Nucl. Mater.* **2022**, *561*, 153536.

(14) Li, B.; Dai, S.; Jiang, D. en. Molecular Dynamics Simulations of Structural and Transport Properties of Molten NaCl-UCl_3 Using the Polarizable-Ion Model. *J. Mol. Liq.* **2020**, *299*, 112184.

(15) Goloviznina, K.; Salanne, M. What Is a Good Simulant for Plutonium(III) in Molten Chloride Salts? *J. Phys. Chem. B* **2025**, *129* (30), 7826−7830.

(16) Kim, H.; Kwon, C.; Ham, S.; Lee, J.; Kim, S. J.; Kim, S. Physical Properties of KCl-UCl_3 Molten Salts as Potential Fuels for Molten Salt Reactors. *J. Nucl. Mater.* **2023**, *577*, 154329.

(17) Simoes Santos, M.; Salanne, M.; Kooyman, T.; Lambertin, D. Structural and Transport Properties of the Molten Salt NaCl-KCl-UCl_3 Using the Polarizable Ion Model. *J. Nucl. Mater.* **2024**, *597*, 155125.

(18) Duemmler, K.; Andersson, D.; Beeler, B. First-Principles Investigation of the Thermophysical Properties of NaCl, $PuCl_3$, and NaCl-$PuCl_3$ Molten Salts. *J. Nucl. Mater.* **2024**, *591*, 154902.

(19) Kwon, C.; Kang, J.; Kang, W.; Kwak, D.; Han, B. First Principles Study of the Thermodynamic and Kinetic Properties of U in an Electrorefining System Using Molybdenum Cathode and LiCl-KCl Eutectic Molten Salt. *Electrochim. Acta* **2016**, *195*, 216−222.

(20) Ng, W. J.; Rakhmatullin, A.; Goloviznina, K.; Salanne, M.; Bessada, C. Structural Dynamics of Molten NaCl−$MgCl_2$−$LaCl_3$: A Proxy for Molten Chloride Fast Reactor Fuels. *J. Nucl. Mater.* **2025**, *616*, 156056.

(21) Marin-Laflèche, A.; Haefele, M.; Scalfi, L.; Coretti, A.; Dufils, T.; Jeanmairet, G.; Reed, S.; Serva, A.; Berthin, R.; Bacon, C.; Bonella, S.; Rotenberg, B.; Madden, P.; Salanne, M. MetalWalls: A Classical Molecular Dynamics Software Dedicated to the Simulation of Electrochemical Systems. *J. Open Source Softw.* **2020**, *5* (53), 2373.

(22) Coretti, A.; Bacon, C.; Berthin, R.; Serva, A.; Scalfi, L.; Chubak, I.; Goloviznina, K.; Haefele, M.; Marin-Laflèche, A.; Rotenberg, B.; Bonella, S.; Salanne, M. MetalWalls: Simulating Electrochemical Interfaces between Polarizable Electrolytes and Metallic Electrodes. *J. Chem. Phys.* **2022**, *157* (18), 184801.

(23) Salanne, M.; Madden, P. A. Polarization Effects in Ionic Solids and Melts. *Mol. Phys.* **2011**, *109* (19), 2299−2315.

(24) Martinez, L.; Andrade, R.; Birgin, E. G.; Martínez, J. M. PACKMOL: A Package for Building Initial Configurations for Molecular Dynamics Simulations. *J. Comput. Chem.* **2009**, *30* (13), 2157−2164.

(25) Ercole, L.; Bertossa, R.; Bisacchi, S.; Baroni, S. SporTran: A Code to Estimate Transport Coefficients from the Cepstral Analysis of (Multivariate) Current Time Series. *Comput. Phys. Commun.* **2022**, *280*, 108470.
(26) Goloviznina, K.; Notarangelo, M. C.; Tranchida, J.; Bourasseau, E.; Salanne, M. DFT-Based Polarizable Ion Models for Molten Rare-Earth Chlorides: From Lanthanum to Europium. *J. Phys. Chem. B* **2025**, *129* (3), 1016−1025.
(27) Yeh, I. C.; Hummer, G. System-Size Dependence of Diffusion Coefficients and Viscosities from Molecular Dynamics Simulations with Periodic Boundary Conditions. *J. Phys. Chem. B* **2004**, *108* (40), 15873−15879.
(28) Maginn, E. J.; Messerly, R. A.; Carlson, D. J.; Roe, D. R.; Elliot, J. R. Best Practices for Computing Transport Properties 1. Self-Diffusivity and Viscosity from Equilibrium Molecular Dynamics [Article v1.0]. *Living J. Comput. Mol. Sci.* **2018**, *1* (1), 6324.
(29) Rollet, A. L.; Sarou-Kanian, V.; Bessada, C. Self-Diffusion Coefficient Measurements at High Temperature by PFG NMR. *C. R. Chim.* **2010**, *13* (4), 399−404.
(30) Kim, K. Viscosities of $LaCl_3$-NaCl Binary Melts. *J. Korean Inst. Surf. Eng.* **2006**, *39* (6), 282−287.
(31) Kim, K. Viscosities of $LaCl_3$-CsCl Binary Melts. *J. Korean Inst. Surf. Eng.* **2013**, *46* (2), 87−92.
(32) Janz, G. J. Molten Salts Data as Reference Standards for Density, Surface Tension, Viscosity, and Electrical Conductance: KNO_3 and NaCl. *J. Phys. Chem. Ref. Data* **1980**, *9* (4), 791−830.
(33) Brockner, W.; Toerklep, K.; Oeye, H. A. Viscosity of Molten Alkali Chlorides. *J. Chem. Eng. Data* **1981**, *26*, 250−253.
(34) Potapov, A.; Sato, Y. Viscosity of Molten Rare Earth Metal Trichlorides II. Cerium Subgroup. *Z. Naturforsch.* **2011**, *66* (10−11), 649−655.
(35) Emerson, M. S.; Sharma, S.; Roy, S.; Bryantsev, V. S.; Ivanov, A. S.; Gakhar, R.; Woods, M. E.; Gallington, L. C.; Dai, S.; Maltsev, D. S.; Margulis, C. J. Complete Description of the $LaCl_3$-NaCl Melt Structure and the Concept of a Spacer Salt That Causes Structural Heterogeneity. *J. Am. Chem. Soc.* **2022**, *144* (47), 21751−21762.
(36) Janz, G. J.; Bansal, N. P. Molten Salts Data: Diffusion Coefficients in Single and Multi-Component Salt Systems. *J. Phys. Chem. Ref. Data* **1982**, *11* (3), 505−693.
(37) Shannon, R. D. Revised Effective Ionic Radii and Systematic Studies of Interatomic Distances in Halides and Chalcogenides. *Acta Crystallogr.* **1976**, *A32*, 751−767.
(38) Brookes, R.; Davies, A.; Ketwaroo, G.; Madden, P. A. Diffusion Coefficients in Ionic Liquids: Relationship to the Viscosity. *J. Phys. Chem. B* **2005**, *109* (14), 6485−6490.
(39) Emerson, M. S.; Ivanov, A. S.; Gallington, L. C.; Maltsev, D. S.; Halstenberg, P.; Dai, S.; Roy, S.; Bryantsev, V. S.; Margulis, C. J. Heterogeneous Structure, Mechanisms of Counterion Exchange, and the Spacer Salt Effect in Complex Molten Salt Mixtures Including $LaCl_3$. *J. Phys. Chem. B* **2024**, *128* (16), 3972−3980.
(40) Wu, F.; Sharma, S.; Roy, S.; Halstenberg, P.; Gallington, L. C.; Mahurin, S. M.; Dai, S.; Bryantsev, V. S.; Ivanov, A. S.; Margulis, C. J. Temperature Dependence of Short and Intermediate Range Order in Molten $MgCl_2$ and Its Mixture with KCl. *J. Phys. Chem. B* **2020**, *124* (14), 2892−2899.



https://doi.org/10.1021/acs.jpcb.5c08179
J. Phys. Chem. B 2026, 130, 2270−2277

Inorganic Chemistry

pubs.acs.org/IC

Featured Article

$MgCl_2$-Mediated Mechanisms of Oxygen Solubility in Molten Chlorides

Woei Jer Ng,* Kateryna Goloviznina, František Šimko, Mathieu Salanne,* and Aydar Rakhmatullin

Cite This: https://doi.org/10.1021/acs.inorgchem.6c01882

Read Online

ACCESS | Metrics & More | Article Recommendations | Supporting Information

ABSTRACT: In molten salt reactors, oxygen impurities accelerate structural material corrosion. Moreover, the ingress of oxide species may promote the formation of insoluble actinide oxychlorides or oxides, potentially raising safety concerns. To limit the undesired precipitation of such phases, $MgCl_2$ has been proposed as a complementary fuel component to sequester oxygen by enhancing the solubility of actinide oxide species. In this study, we provide direct, molecular-level evidence of an $MgCl_2$-mediated oxygen solubility mechanism. This was achieved through high-temperature ^{17}O nuclear magnetic resonance spectroscopy on NaCl−$MgCl_2$−$LaCl_3$ melts with various amounts of dissolved ^{17}O-enriched LaOCl, corroborated by classical molecular dynamics with the polarizable ion model and first-principles NMR calculations. Experiment and simulation both show that adding $MgCl_2$ promotes the sharing of O^{2-} coordination between Mg^{2+} and La^{3+} ions, disrupting La−O clustering that facilitates oxide precipitation. Altogether, these results establish a mechanistic framework for tuning oxygen speciation and solubility through compositional design in high-temperature molten salt systems.

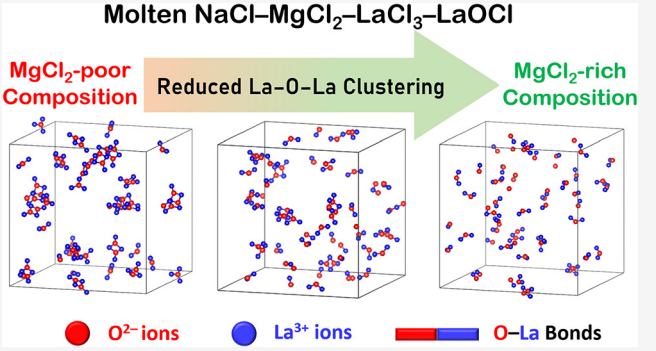

Downloaded via BIBCNRS INC on July 15, 2026 at 12:20:08 (UTC).
See https://pubs.acs.org/sharingguidelines for options on how to legitimately share published articles.

1. INTRODUCTION

Molten salts are drawing renewed attention due to their unique physicochemical properties and broad utility in various applications, including nanocrystal synthesis,[1,2] metal production and electrochemical processing,[3] waste recycling,[4,5] thermal energy storage,[6,7] and nuclear technologies such as spent fuel reprocessing[8,9] and molten salt reactors (MSRs).[10] In the context of MSRs, numerous designs and concepts have been proposed—most prominently fluoride-based reactors such as the Chinese Thorium Molten Salt Reactor (TMSR)[11] and Russian MOlten Salt Actinide Recycler and Transmuter (MOSART) system,[12,13] and more recently chloride-based reactors such as TerraPower's Molten Chloride Fast Reactor (MCFR),[14] Moltex Energy's Stable Salt Reactor−Wasteburner (SSR−W),[15] and France's Advanced Reactor of Actinide Management In Salt (ARAMIS-A).[16]

Notwithstanding this progress, the corrosive nature of molten salts remains a critical barrier to the widespread deployment of MSR technology. Concerted efforts to extend reactor lifetimes have focused on developing corrosion-resistant structural alloys,[17−20] studying the redox potential of fuel salts,[21−23] developing in situ monitoring tools,[24] and refining purification methods.[25−27] The current scientific consensus holds that salt impurities—such as H_2O and oxygen—are the main driving factor in accelerating the oxidation of alloying elements, thereby intensifying corrosion and limiting reactor lifetimes.[28,29]

Historically, ZrF_4 was used as an oxygen absorber during the pilot Molten Salt Reactor Experiments.[30] Similarly, in chloride-based reactors, $MgCl_2$ has been proposed as a fuel salt component to sequester oxygen and limit the formation of insoluble oxide phases,[31] a role motivated by prior observations that its presence facilitates MgO dissolution in $MgCl_2$−$NdCl_3$ melts for the electrowinning of magnesium metal.[32] Beyond this, $MgCl_2$ also contributes to lowering fuel melting temperatures,[33] reducing viscosity,[34] and controlling redox potential.[23]

Despite these advantages, the precise mechanism of $MgCl_2$-mediated oxygen solubility remains insufficiently understood. Structural studies using X-ray diffraction and Raman spectroscopy[35] suggested that the formation of $Mg_xNd_yOCl_{2x+3y-2}$ networks promotes oxygen solubility in liquid mixtures of $NdCl_3$−$MgCl_2$−MgO. Bulk solubility measurements by EDTA volumetric analysis[36] indicated that increasing $MgCl_2$ and $NdCl_3$ concentrations similarly improve MgO solubility, likely via the formation of soluble NdOCl. Preliminary unpublished electrochemical data[37] indicate slower oxide precipitation in

Received: April 13, 2026
Revised: July 3, 2026
Accepted: July 9, 2026

© XXXX American Chemical Society

lanthanide trichloride melts containing $MgCl_2$, consistent with the formation of soluble lanthanide oxychloride species. Extending beyond chloride systems, studies on other molten fluorides containing transition metals or lanthanides[38−44] likewise support the formation of complex oxyhalide species, such as $NbOF_5^{2-}$/$NbO_2F_4^{3-}$/$NbO_4F_2^{5-}$, $TaOF_5^{2-}$/$TaOF_6^{3-}$/$TaO_2F_2^{-}$/$TaO_2F_3^{2-}$, $NdOF_4^{3-}$/$NdOF_5^{4-}$/$Nd_2OF_8^{4-}$/$Nd_2OF_{10}^{6-}$, $ZrOF_5^{3-}$, $HfOF_5^{3-}$, $Lu_2OF_8^{4-}$/ $Lu_2O_2F_4^{2-}$/$Lu_2O_2F_6^{4-}$, and $LaO_xF_y^{3-x-y}$.

In this study, we provide direct evidence for the oxygen solubility mechanism using high-temperature (HT) ^{17}O nuclear magnetic resonance (NMR) measurements of molten NaCl−$MgCl_2$−$LaCl_3$ containing varying amounts of dissolved ^{17}O-enriched LaOCl. As in earlier studies,[45] this salt system was selected as a surrogate for the ARAMIS-A reactor fuel (NaCl−$MgCl_2$−$PuCl_3$−$AmCl_3$) because it preserves the key physicochemical properties of the fuel while avoiding the handling of highly radioactive Pu and Am.

While HT ^{17}O NMR has been previously applied[46−48] to study oxyfluoride speciation in Al−O−F melts relevant for the aluminum industry, those studies typically reported only negligible variations in chemical shift. A notable exception[49] showed a measurable shift in ^{17}O chemical shifts with composition, attributed to changes in the number of oxygen bridges. Herein, our measurements reveal pronounced and systematic variations in ^{17}O chemical shifts that directly reflect the diversification of oxygen coordination environments in chloride melts. To substantiate these findings, we combine molecular dynamics (MD) simulations performed with the polarizable ion model (PIM) and first-principles NMR calculations to provide a robust theoretical framework for our experimental results. Together, these results provide the first molecular-level mechanistic picture of $MgCl_2$-mediated oxygen solubility in molten chlorides, with implications for high-temperature molten salt chemistry across nuclear, metallurgical, and electrochemical systems.

2. METHODOLOGY

2.1. Materials and Synthesis

NaCl (Merck Suprapur, ≥ 99.5%), $MgCl_2$ (Thermo Scientific Chemicals, ≥ 98%), $LaCl_3$ (AnhydroBeads, ≥ 99.99%), and 90 at% ^{17}O-enriched water (CortecNet) were purchased and used without further purification. All chemicals were stored and handled in an argon-filled glovebox maintained at <0.3 ppm moisture and <1.0 ppm oxygen.

To enable ^{17}O NMR measurements, ^{17}O-labeled LaOCl was synthesized by hydrating 1.0 g of fine $LaCl_3$ powder with an excess of 90 at% ^{17}O-enriched water in an argon-filled glovebox. Hydration was performed gradually due to the extremely exothermic nature of the reaction. The resulting slurry was continuously mixed using a mortar and pestle to ensure homogeneity and complete conversion. Subsequently, the reaction product was transferred to an open-sided alumina crucible and dried in an argon-filled tube furnace at 650 °C overnight.[50] Powdered X-ray diffraction (XRD) analysis on the dried product under ambient conditions (Figure S1) showed that all measured peaks matched those of the reference PDF card (04−008−5087), with no detectable $LaCl_3$ or $LaCl_3·6H_2O$ impurities, confirming that the synthesized LaOCl is phase-pure and stable.

2.2. Sample Preparation

Before HT NMR measurements, all samples were prepared inside an argon-filled glovebox. Finely ground powders of NaCl, $MgCl_2$, $LaCl_3$, and LaOCl were weighed according to the desired molar composition using an electronic balance. The samples were thoroughly mixed using a mortar and pestle, then ∼60 mg of the homogenized mixture was transferred into a high-purity boron nitride (BN) crucible (0.9 cm diameter × 1.4 cm height) and tightly sealed with a screw cap.

2.3. NMR Spectroscopy

In-situ HT NMR measurements were performed on a Bruker AVANCE I spectrometer operating at 9.4 T. BN crucibles containing our samples were placed inside a modified axial NMR probehead, with uniform heating achieved by irradiating the crucibles from both top and bottom using two CO_2 lasers, each operating at 250 W. Sample temperatures were determined indirectly from laser power, which was calibrated against the known melting temperatures of benchmark fluoride salts and their mixtures (Figure S2). To minimize crucible oxidation, a continuous argon flow of 1.9 cm^3/s was maintained inside the probe before and during laser irradiation.

0.1 M $LaCl_3$, 1.0 M NaCl solutions, and tap water were used for the reference chemical shifts for the ^{139}La, ^{35}Cl, and ^{17}O nuclei, respectively. $\pi/2$ pulses were used for all measurements: ^{139}La and ^{35}Cl NMR were acquired at 850 °C; ^{17}O NMR was collected at 1000 °C to enhance signal strength. Acquisition parameters for the three nuclei are given in Table S1.

2.4. MD Simulations

Ion trajectories of the NaCl−$MgCl_2$−$LaCl_3$−LaOCl system were simulated using the MetalWalls code[51,52] with PIM. The PIM force field has been extensively validated for a wide range of molten chlorides[34,45,53,54] as well as oxides in molten,[55] glassy,[56] and crystalline[57] states, and is known for its high transferability based on strong physical foundations.[58] However, its application to systems containing mixtures of oxides with other anionic species remains underexplored. Accordingly, interaction potential parameters were either obtained from the literature or derived from scratch using the force-fitting procedure described in Section 1.3 of the ESI. A complete set of parameters used is provided in Tables S2−S4.

Two sets of simulations were performed for each target composition: (i) NPT ensemble simulations of "large boxes" containing 2350 to 3200 atoms (Table S5) and (ii) NPT ensemble simulations of "small boxes" containing 235 to 320 atoms (Table S6). "Large box" simulations were used for visualizing oxygen clustering behavior using the VESTA software[59] and analyzing radial distribution functions (RDFs) using the TRAVIS code.[60] "Small box" simulations were used for subsequent first-principles NMR calculations.

Initial configurations of the cubic periodic simulation boxes were generated with the Packmol utility.[61] Each simulation was performed in the following order: a 0.2 ns nonpolarizable equilibration step, a 0.5 ns polarizable equilibration step, and a 5.0 ns polarizable production step, all with a 1.0 fs time step. Ion trajectories were recorded at regular 1.0 ps intervals. The temperature of all simulations was regulated at 850 °C using Nosé−Hoover thermostats, and a pressure of 1 bar was considered for NPT simulations. Cutoff radii of 10.6 Å ("large box") and 6.0 Å ("small box") were used for nonbonded interactions, with a tail correction included for energy and

https://doi.org/10.1021/acs.inorgchem.6c01882
Inorg. Chem. XXXX, XXX, XXX−XXX

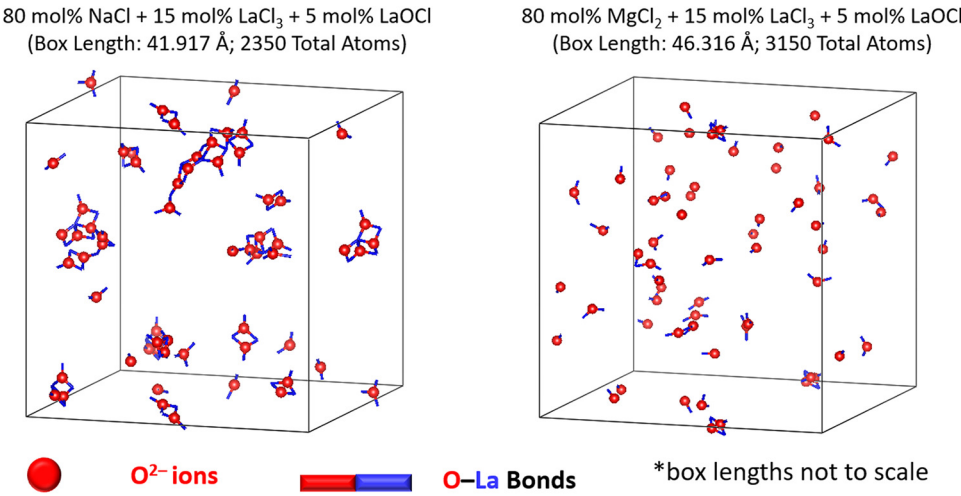

Figure 1. Visualization of O−La bond distribution inside a simulation cell of 80 NaCl−15 $LaCl_3$−5 LaOCl and 80 $MgCl_2$−15 $LaCl_3$−5 LaOCl (both in mol %) at 850 °C. The La−O bond length cutoff is set at 3.38 Å to reflect the first coordination sphere of oxygen. For better visibility of the O−La clustering behavior, only O^{2-} ions and O−La bonds are shown; all other ions and bonds are omitted.

Table 1. Percentage of O^{2-} Ions in O−La Polymers of Chain Length *n* for Different Molten Salt Compositions at 850 °C, Calculated from "Large Box" MD Trajectories

	percentage of O^{2-} ions in $-(O-La)_n-$ polymer (%)			
molten salt mixture (in mol %)	*n* = 1	*n* = 2	*n* = 3	*n* > 4
80 NaCl−15 $LaCl_3$−5 LaOCl	17.4	46.0	10.6	26.0
64 NaCl−16 $MgCl_2$−15 $LaCl_3$−5 LaOCl	46.4	39.5	9.21	4.91
40 NaCl−40 $MgCl_2$−15 $LaCl_3$−5 LaOCl	59.3	35.6	2.52	2.60
16 NaCl−64 $MgCl_2$−15 $LaCl_3$−5 LaOCl	71.2	25.0	2.78	0.99
80 $MgCl_2$−15 $LaCl_3$−5 LaOCl	78.8	20.4	0.85	0.00

pressure. Long-range Coulomb interactions were treated using the Ewald summation method with a tolerance of 10^{-7}.

2.5. First-Principles NMR Calculations

The Vienna Ab-initio Simulation Package (VASP)[62] was used to calculate chemical shieldings for both the solid- and molten-state compounds. The Perdew−Burke−Ernzerhof (PBE) functional was used for the Generalized Gradient Approximation (GGA) of the exchange-correlation energy.[63] No dispersion corrections were applied. The Projector Augmented Wave (PAW) formalism was employed throughout, using the recommended GW data sets,[64] e.g., *Na_sv_GW*, *Mg_sv_GW*, *La_GW*, *Cl_GW*, *O_GW*.

For solid-state compounds, crystallographic information files (CIF) were obtained from the ICSD database and converted into VASP POSCAR format. A Gaussian smearing scheme (ISMEAR = 0) with a width of SIGMA = 0.01 eV was applied. The plane wave cutoff energy was set to ENCUT = 600 eV, exceeding the ENAMX among all pseudopotentials used. The electronic self-consistent loop was converged to EDIFF = 10^{-8} eV. Regular Monkhorst−Pack k-point meshes ($n \times n \times n$) were determined individually for each compound by performing convergence tests on total energy with respect to k-point density until changes were below 1 meV/atom. The LEFG and LCHIMAG tags were enabled to calculate electric field gradients and magnetic shielding parameters.

The resultant isotropic chemical shieldings (σ_{iso}) of reference solid-state compounds were benchmarked against experimentally reported[45,65−68] isotropic chemical shifts (δ_{iso}) of ^{35}Cl, ^{17}O, and ^{139}La to establish a calibration curve of δ_{iso} versus σ_{iso} (Figure S4). For La-containing compounds, a Hubbard correction[69] of U = +6 eV was applied to the La-4*f* orbitals to improve the accuracy of chemical shift predictions; this approach is discussed further in Section 1.5 of the ESI and the Results and Discussions section.

For molten-state calculations, regularly spaced snapshots from the "small box" MD trajectories were converted into VASP POSCAR format. Because the primary objective of this study is to quantify ^{17}O chemical shifts, the number of snapshots was chosen such that at least 50 oxygen atoms were evaluated for each composition. The same smearing settings were retained (ISMEAR = 0 and SIGMA = 0.01 eV), while other parameters were relaxed to improve computation efficiency: ENCUT = 450 eV (slightly above the ENAMX of all PAW data sets), EDIFF = 10^{-6}, Γ-point sampling, and a real-space solution of the Hamiltonian (LREAL = .True.). The output σ_{iso} values for individual nuclei in the molten salt snapshots were converted to δ_{iso} using the δ_{iso}-to-σ_{iso} calibration curves in Figure S4, and the ensemble average was taken as the predicted chemical shift for each composition.

3. RESULTS AND DISCUSSION

Our study employs the (80-α) NaCl−α $MgCl_2$−(20-x) $LaCl_3$−x LaOCl mixture (compositions given in mol %; α = 0−80; x = 0−5) to simulate the replacement of two Cl^- ions by one O^{2-} ion in an idealized MSR fuel contamination framework. Here, LaOCl was selected over more conventional options such as La_2O_3 and MgO because it is more straightforward for isotope labeling, preserves the lanthanum stoichiometry, and has higher solubility in chloride melts.[70,71] LaOCl as a simulated contaminant most closely mimics

https://doi.org/10.1021/acs.inorgchem.6c01882
Inorg. Chem. XXXX, XXX, XXX−XXX

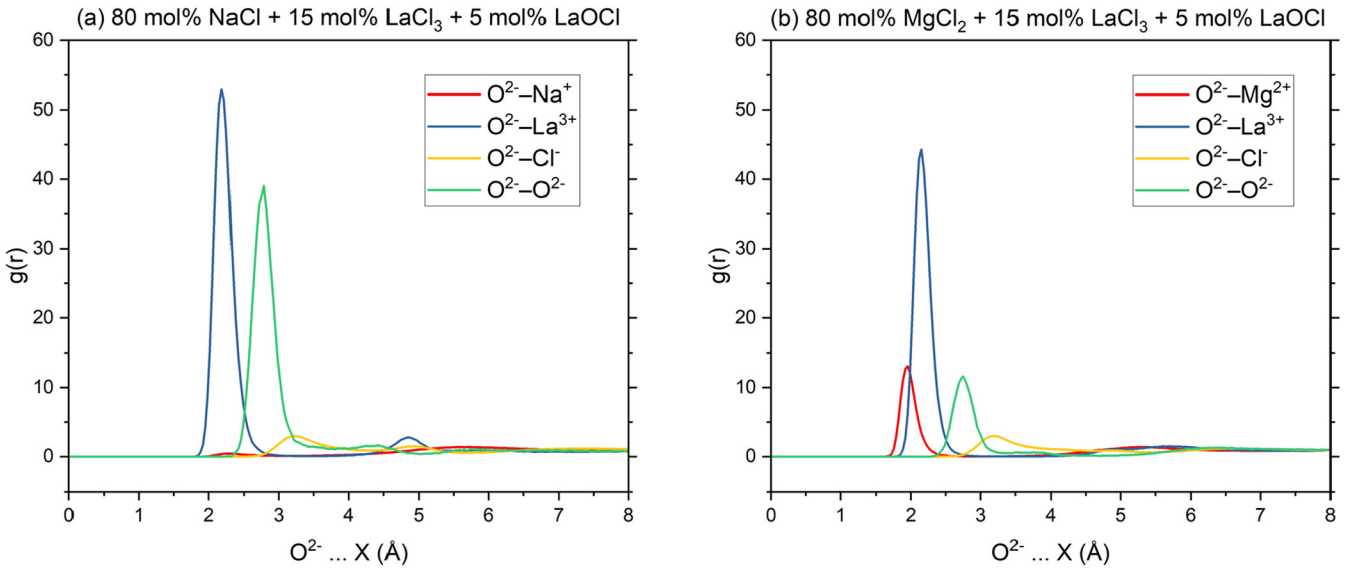

Figure 2. RDFs of O^{2-} with its neighboring ions for (a) 80 NaCl−15 $LaCl_3$−5 LaOCl and (b) 80 $MgCl_2$−15 $LaCl_3$−5 LaOCl at 850 °C, calculated from "large box" MD trajectories.

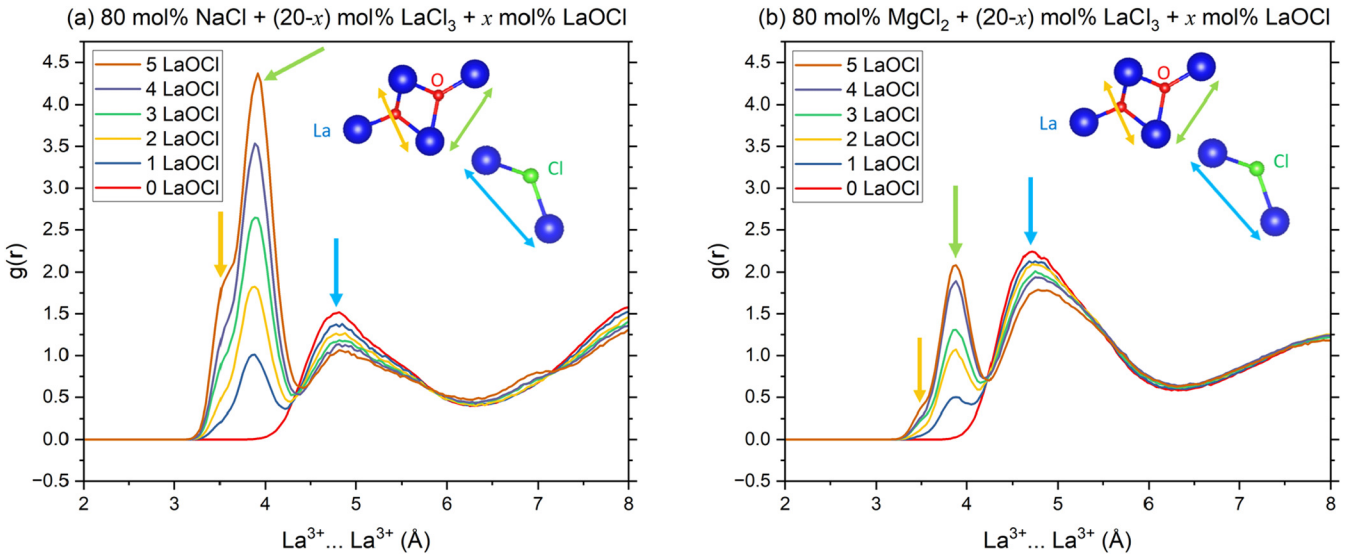

Figure 3. La^{3+}−La^{3+} RDFs for (a) 80 NaCl−(20-*x*) $LaCl_3$−*x* LaOCl and (b) 80 $MgCl_2$−(20-*x*) $LaCl_3$−*x* LaOCl (*x* = 0−5) at 850 °C, calculated from "large box" MD trajectories. Arrows mark characteristic La spacings corresponding to La−Cl−La (blue), La−O−La (green), and double oxygen-bridged La (orange) linkages.

inadequately purified actinide trichlorides ($AnCl_3$) in fresh MSR fuels, which typically present as partially hydrated ($AnCl_3{\cdot}xH_2O$) or oxychloride (AnOCl) species. It also approximates unintended O_2 or H_2O ingress during MSR operation, where oxygen preferentially coordinates with actinide species in the melt. We note, however, that H_2O ingress scenarios involve HCl evolution from chloride hydrolysis—a well-established corrosion pathway[27]—which is not captured in our present contamination framework.

To probe the behavior of oxygen in chloride melts, we first examined its local coordination environments in NaCl−$MgCl_2$−$LaCl_3$−LaOCl using classical MD with PIM. Figure 1 compares the MD snapshots of the 80 NaCl−15 $LaCl_3$−5 LaOCl and the 80 $MgCl_2$−15 $LaCl_3$−5 LaOCl systems at 850 °C. In the NaCl-based system, oxygen atoms are observed to cluster around lanthanum; whereas, in the $MgCl_2$-based system, they appear more evenly distributed in the matrix. Analysis of the O−La polymer chain lengths (Table 1), using the same methods as in the references,[46,72] confirms this trend: NaCl-rich melts favor longer O−La chains; whereas, $MgCl_2$-rich melts prefer shorter O−La chains. These results suggest that Mg^{2+} disrupts O−La clustering by promoting a mixture of O−Mg and O−La coordination environments in the melt. Thermodynamically, these insights are also consistent with the unfavorable O−Na and favorable O−Mg/O−La interactions shown in Figure S5, which promote a multiplicity of coordination motifs in the latter system.

To better quantify these coordination trends, we performed RDF analysis of O^{2-} and its neighboring ions. Figure 2 compares the RDF for the same two systems as in Figure 1. The O−Na peak is nearly absent compared to the O−Mg peak, confirming the thermodynamically unfavorable nature of the O−Na interaction. Additionally, the stronger O−O

https://doi.org/10.1021/acs.inorgchem.6c01882
Inorg. Chem. XXXX, XXX, XXX−XXX

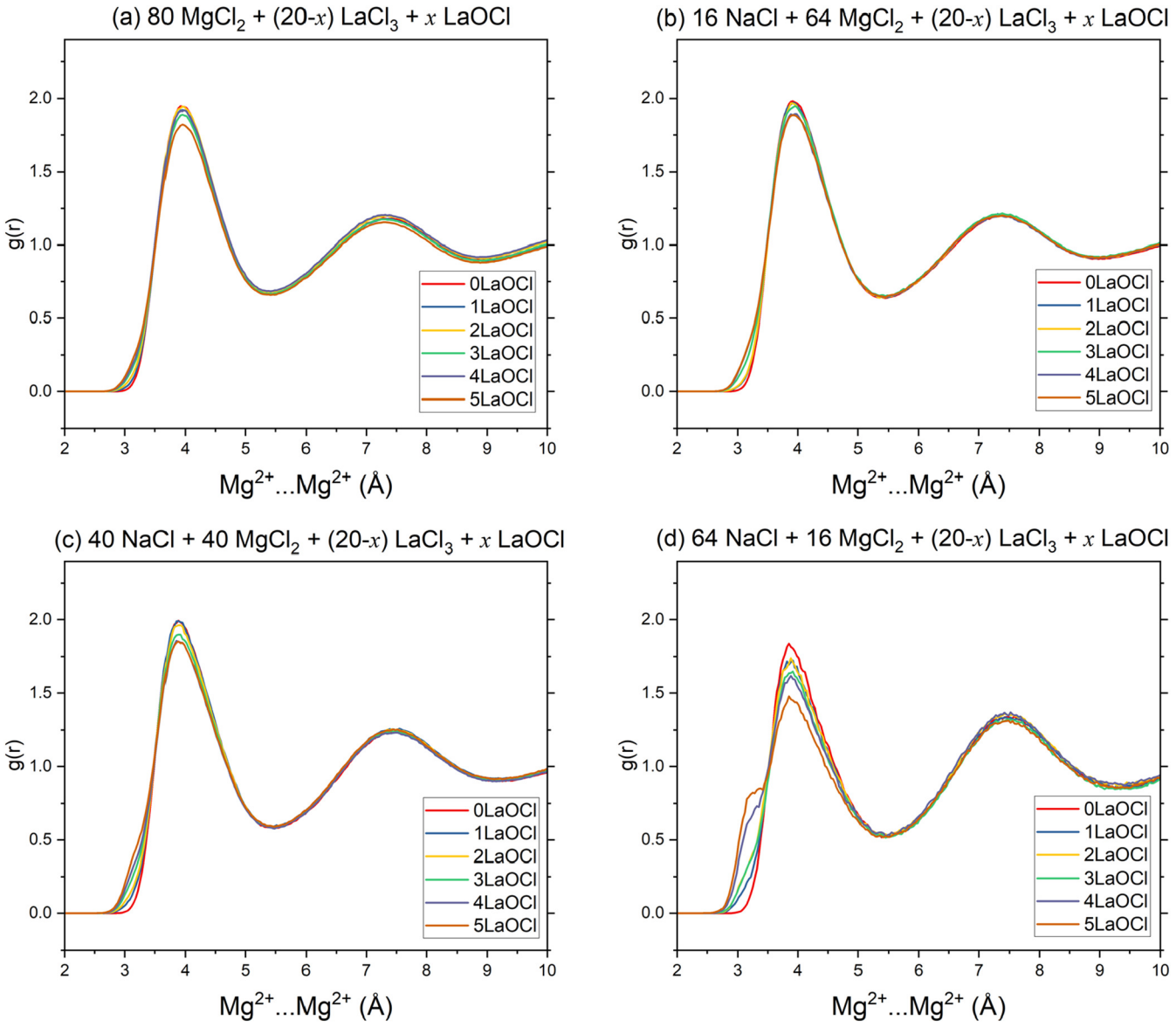

Figure 4. Mg^{2+}–Mg^{2+} RDFs of (80-α) NaCl–α $MgCl_2$–(20-x) $LaCl_3$–x LaOCl (in mol %, x = 0–5) for (a) α = 80, (b) α = 64, (c) α = 40, and (d) α = 16. All the RDFs are calculated from "large box" MD trajectories, with simulation temperatures regulated at 850 °C.

correlation in the NaCl-based system corroborates the oxygen clustering around La^{3+} observed in Figure 1.

To further assess clustering, we compared the La^{3+}–La^{3+} RDFs for NaCl–(20-x) $LaCl_3$–x LaOCl and $MgCl_2$–(20-x) $LaCl_3$–x LaOCl systems (x = 0–5) (Figure 3). Here, three characteristic peaks emerge: (i) the broad peak at 4.8 Å from La–Cl–La linkages, which has been well characterized in the case of pure molten chlorides,[73] (ii) a sharp peak at 3.9 Å corresponding to La^{3+} ions bridged by a single O^{2-} ion, and (iii) a shoulder peak at 3.5 Å associated with multiple O^{2-} bridges. A quasi-isosbestic point at approximately 4.4 Å separates peak (i) from peaks (ii) and (iii). With increasing LaOCl concentration, peaks (ii) and (iii) intensify at the expense of peak (i) in both systems. Nonetheless, the magnitudes of peaks (ii) and (iii) are significantly diminished in the $MgCl_2$-based system, evidencing a marked reduction in La–O clustering.

The role of $MgCl_2$ in mitigating La–O clustering is further supported by Mg^{2+}–Mg^{2+} RDFs of (80-α) NaCl–α $MgCl_2$–(20-x) $LaCl_3$–x LaOCl (α = 16–80; x = 0–5). The RDFs, shown in Figure 4, exhibit two major humps at 4.0 and 7.3 Å, characteristic of the Mg–Mg spacings in Mg–Cl–Mg–Cl–Mg.[74] Additional shoulders appearing at ∼3.3 Å correspond to Mg–O–Mg linkages. The intensity of these shoulders increases with (1) higher LaOCl concentration and (2) lower $MgCl_2$ content, highlighting the role of Mg^{2+} in binding and evenly dispersing O^{2-} ions within the molten salt matrix. In practical MSR settings, this suggests that $MgCl_2$ may enhance the solubility of oxide species in chloride fuels by mitigating the clustering and subsequent precipitation of actinide-rich oxide phases. Effectively, this $MgCl_2$-assisted mechanism curbs a prominent pathway for oxide deposition, thereby lowering the risk of deposit-induced corrosion of MSR structural surfaces.

Based on our MD analysis of O–Na and O–Mg coordination preferences, we can predict the expected ^{17}O NMR chemical shifts in our molten salt systems. Solid-state ^{17}O NMR of the corresponding oxides provides useful

https://doi.org/10.1021/acs.inorgchem.6c01882
Inorg. Chem. XXXX, XXX, XXX–XXX

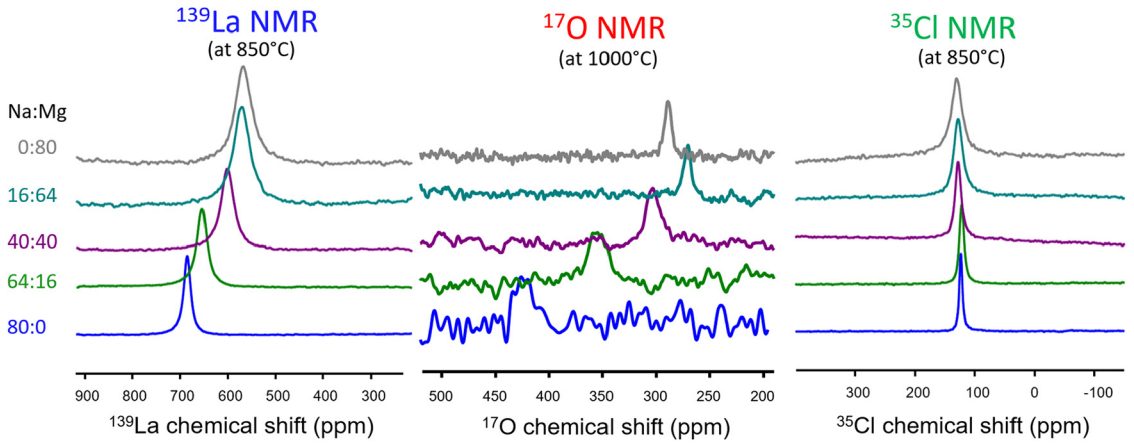

Figure 5. Measured ^{139}La, ^{17}O, and ^{35}Cl NMR spectra of the (80-α) NaCl–α $MgCl_2$–15 $LaCl_3$–5 LaOCl (α = 0–80) system. ^{139}La and ^{35}Cl spectra were acquired at 850 °C; ^{17}O spectra were collected at 1000 °C to enhance signal quality.

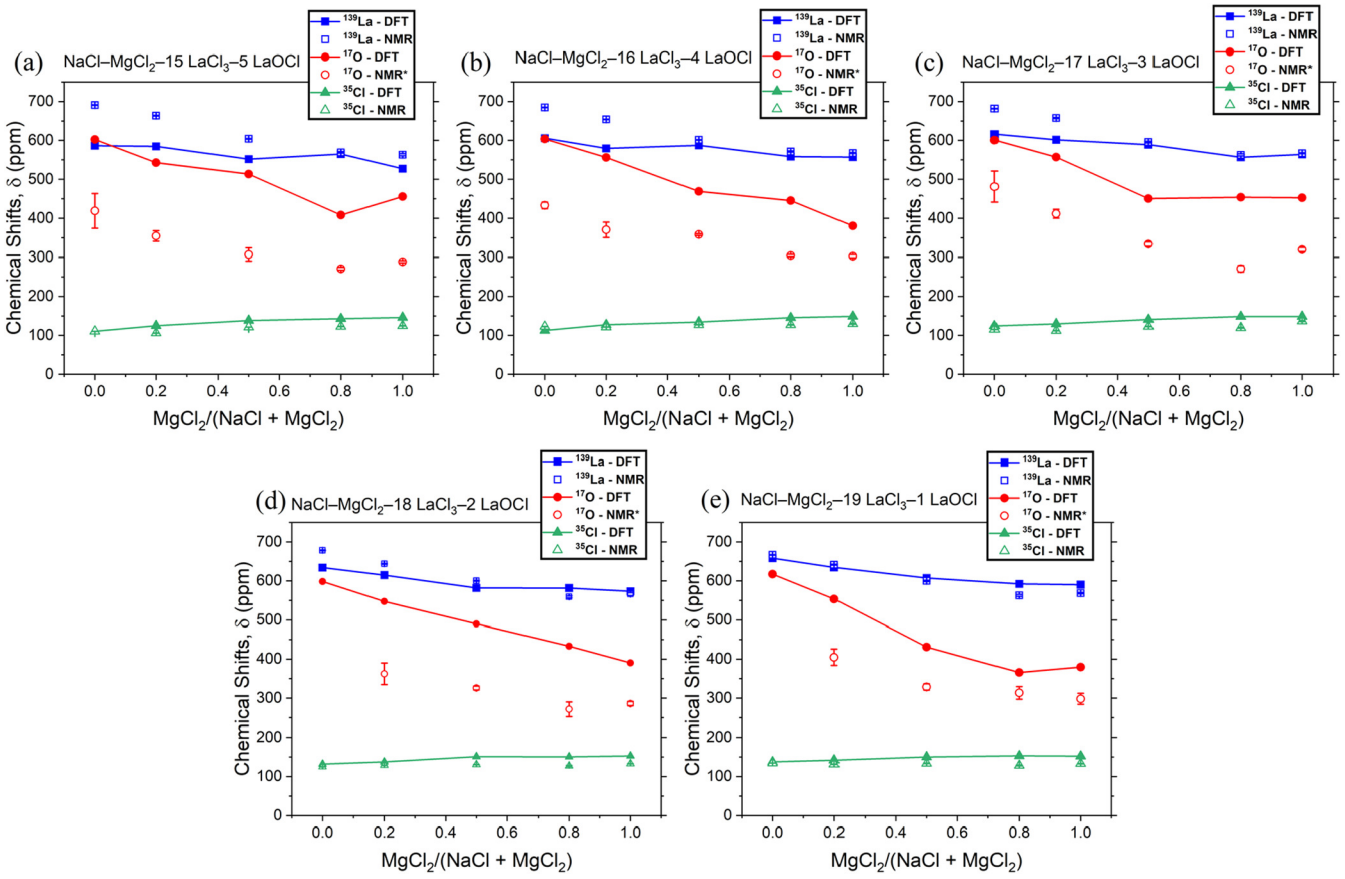

Figure 6. Comparisons between NMR-measured and DFT-calculated chemical shifts of the NaCl–$MgCl_2$–(20-x) $LaCl_3$–x LaOCl compositions, for (a) x = 5, (b) x = 4, (c) x = 3, (d) x = 2, and (e) x = 1. DFT calculations were performed on MD snapshots at 850 °C; ^{139}La and ^{35}Cl NMR were measured at 850 °C, while ^{17}O NMR was measured at 1000 °C. No measurable ^{17}O NMR signal was obtained for the compositions of 80 NaCl–18 $LaCl_3$–2 LaOCl and 80 NaCl–19 $LaCl_3$–1 LaOCl. Error bars in NMR measurements correspond to the one-sigma uncertainties from spectral fitting.

benchmarks: La_2O_3 (*P3m1* symmetry) has two oxygen sites, with reported chemical shifts of 469 and 590 ppm;[66] Na_2O and MgO only have a single oxygen site each,[75,76] with first-principles calculations using VASP predicting chemical shifts of 11.8 and 24.2 ppm, respectively (Figure S4b). The much larger chemical shifts in La_2O_3 indicate that oxygen bound exclusively to La^{3+} will return high ^{17}O chemical shift values. Therefore, in NaCl–$LaCl_3$ melts, since oxygen coordinates only with La^{3+}, large chemical shift values are expected. By gradually replacing NaCl with $MgCl_2$, oxygen increasingly interacts with Mg^{2+} as well as La^{3+}, and the corresponding ^{17}O chemical shift values are projected to decrease accordingly.

Figure 5 shows ^{139}La, ^{17}O, and ^{35}Cl NMR signals measured on the molten (80-α) NaCl–α $MgCl_2$–15 $LaCl_3$–5 LaOCl (α = *0–80*) system. In these measurements, ^{17}O NMR provides direct insight into the oxygen coordination environment,

https://doi.org/10.1021/acs.inorgchem.6c01882
Inorg. Chem. XXXX, XXX, XXX–XXX

whereas the ^{139}La and ^{35}Cl spectra serve as internal benchmarks for comparisons with VASP calculations discussed later. At 850 °C, ^{139}La and ^{35}Cl NMR measurements yielded strong, low-noise signals with sharp peaks, whereas ^{17}O NMR returned weak, noisy signals—and no detectable signal at all for the 80 NaCl−15 $LaCl_3$−5 LaOCl and 64 NaCl−16 $MgCl_2$−15 $LaCl_3$−5 LaOCl compositions. Nevertheless, it should be noted that weak or absent ^{17}O NMR signals do not necessarily imply oxygen insolubility at 850 °C, as the detectability of NMR signals is nucleus-dependent and governed by relaxation behavior that is distinct from thermodynamic solubility.

For these reasons, ^{17}O NMR measurements were performed at 1000 °C to increase ion mobility and obtain measurable signals. Despite elevated temperatures and a greater number of accumulated scans (Table S1), the ^{17}O NMR signals remained comparatively weak, broadened, and exhibited noisy baselines. The origins of these artifacts were investigated using a combination of differential scanning calorimetry (DSC, Figure S6), thermogravimetric−differential thermal analysis (TG−DTA, Figure S7), and ex-situ powdered XRD (Figure S8). The combined analyses indicated that LaOCl does not dissociate into insoluble La_2O_3 in the chloride melt, and that oxygen-containing species dissolved completely by 770 °C, even in the theoretically least soluble 80 NaCl−15 $LaCl_3$−5 LaOCl composition. The observed ^{17}O NMR peak broadening is ascribed to the volatilization of chloride species during prolonged high-temperature acquisitions, which progressively alters the melt composition. These time-dependent compositional changes induce gradual shifts in the ^{17}O resonance frequency, resulting in broadened signals in the accumulated spectra. Moreover, the inherently low concentration of ^{17}O-containing species in the melt further contributes to the weak signals and noisy baselines.

Despite these challenges, clear trends are observed: the ^{17}O chemical shifts progressively decrease with increasing $MgCl_2$ concentration up to a 1:1 NaCl-to-$MgCl_2$ ratio, after which no more systematic decrease is observed. Moreover, ^{17}O resonances are visibly sharper at higher $MgCl_2$ content. This behavior arises because a good signal quality can be achieved within comparatively short acquisition times (∼10 min) in these $MgCl_2$-rich compositions, limiting chloride volatilization. These observations also provide qualitative evidence for enhanced oxygen solubility in the presence of $MgCl_2$.

To corroborate the agreement between MD-generated structures and HT NMR experiments, VASP−NMR calculations were performed on regular-interval MD snapshots of all studied compositions, and ensemble averages were used to predict ^{139}La, ^{17}O, and ^{35}Cl chemical shifts. Figure 6 compares the simulated values with experimental NMR measurements. ^{17}O NMR signals for 80 NaCl−(20-x) $LaCl_3$−x LaOCl (x = 1,2) systems could not be resolved experimentally and are therefore omitted.

Both experiment and simulation show the same overall trend: ^{17}O chemical shifts decrease with increasing $MgCl_2$ content, consistent with our MD analysis that Mg^{2+} mitigates exclusive O−La coordination by diversifying the local oxygen coordination environment. Beyond a 1:1 $MgCl_2$-to-NaCl ratio, the measured and simulated chemical shifts level off and fluctuate. One possible reason is that, under these conditions, the O^{2-} coordination sphere becomes saturated with Mg^{2+}, consequently, and the large number of accessible coordination permutations averages out without producing further systematic changes in ^{17}O chemical shifts.

Nonetheless, the VASP−NMR calculations systematically overpredict experimental ^{17}O chemical shifts by ∼150 ppm. We attribute this offset to two factors. First, the limited treatment of finite-temperature effects in the simulations. Although we averaged our density functional theory (DFT) shieldings over an ensemble of MD snapshots, these static electronic-structure calculations of frozen snapshots only partially account for thermal motion and structural disorder via configurational diversity. They cannot fully reproduce other finite-temperature effects, such as anharmonic vibrations[77] and dielectric screening.[78] While there is also a nominal temperature mismatch between our ^{17}O NMR measurements at 1000 °C and the calculations performed at 850 °C, repeating the simulations at 1000 °C showed no significant difference in the predicted shifts and local structure (Table S7, Figures S9,S10). Second, the electronic structure model itself is limited. Even though a Hubbard shift of +6 eV was added to La-4f states to fit the ^{17}O and ^{35}Cl chemical shifts of La_2O_3 and $LaCl_3$ to calibration data (Figure S4), the calibration was derived from crystalline phases and does not capture the enhanced bond delocalization and anharmonic vibrations of La−O at elevated temperatures and in the molten state.[79] Taken together, these omissions leave the computed shifts too high, which manifests as a large systematic offset. Notwithstanding, the agreement between the trends in calculated and measured chemical shifts validates the role of Mg^{2+} as an additional oxygen coordination site to La^{3+}.

Since La^{3+} is a primary neighbor of O^{2-}, ^{139}La NMR can also probe oxygen coordination environments. As shown in Figure 6, both calculated and experimental ^{139}La chemical shifts decrease with $MgCl_2$ content. However, because oxide species only constitute a minority of the anionic neighbors of La^{3+}, this decreasing trend primarily reflects changes in La−Cl coordination number when NaCl is substituted with $MgCl_2$.[45] Moreover, the calculated ^{139}La chemical shifts are systematically underpredicted for NaCl-rich compositions but show improved agreement with experimental values in $MgCl_2$-rich compositions. We attribute this behavior to the limited ability of the standard PBE−GGA exchange-correlation functional[63] in describing the delocalized electronic structure of La−O bonds.[80] As shown in Figure S4d, the calculated La_2O_3 reference point deviates markedly from the calibration curve even with a Hubbard shift of +6 eV on La-4f orbitals, indicating a severe underestimation of the ^{139}La shift in La_2O_3. In contrast, the deviation for $LaCl_3$ is substantially smaller. This discrepancy originates from the fundamentally different bonding characters of La−O−La and La−Cl−La linkages, which give rise to contrasting heavy-atom-on-heavy-atom (HAHA) effects on the calculated ^{139}La shielding. In La−Cl−La environments, ^{139}La nuclei behave as electronically isolated, closed-shell heavy atoms with large HOMO−LUMO gaps,[80] such that their shielding is dominated by ground-state electrostatic contributions that are well captured by static DFT. By contrast, in polar covalent La−O−La networks, ^{139}La nuclei are strongly electronically coupled through oxygen, rendering the ^{139}La shift a HAHA-dominated property that lies beyond the scope of static DFT. As a result, in $MgCl_2$-rich compositions—where La−O coordination is less prevalent—the predicted shifts show closer agreement with experimental values.

https://doi.org/10.1021/acs.inorgchem.6c01882
Inorg. Chem. XXXX, XXX, XXX−XXX

Unlike ^{17}O and ^{139}La, ^{35}Cl NMR does not directly probe oxygen coordination environments, as Cl^- does not coordinate directly with O^{2-} in these molten salt mixtures. Consequently, ^{35}Cl serves primarily as a benchmark for comparing simulations and experiments. The measured ^{35}Cl chemical shifts vary only slightly between 110 and 130 ppm across all compositions, and VASP calculations reproduced these trends accurately. This minimal variation arises because La^{3+} exerts the dominant influence on ^{35}Cl shifts.[45] Even though the Na^+/Mg^{2+} ratio changes across compositions, the cationic fraction of La^{3+} was fixed at 0.2, keeping the ^{35}Cl shifts largely constant. Importantly, despite the same temperature mismatch affecting ^{17}O, no pronounced systematic offset was observed here. This difference arises from the bonding character: La−Cl is largely ionic, resulting in smaller temperature-dependent distortions of electrons in the La−Cl molecular orbitals; whereas, La−O leans toward polar covalency, making finite-temperature considerations of bond polarization critical for accurately predicting ^{17}O shifts.

To further substantiate the explanations proposed above for the discrepancies between predicted and measured chemical shifts, additional NMR calculations were performed for crystalline LaOCl,[81] and compared with solid-state NMR (SS NMR) measurements of the synthesized LaOCl under ambient conditions. The results are summarized in Figure S11 and Table S8. For all nuclei, the predicted electric field gradient parameters (C_Q and η) show close agreement with experiment, indicating that the local coordination geometries are well captured by the calculations. In contrast, varying degrees of discrepancy are observed for the predicted isotropic chemical shifts (δ_{iso}): VASP vastly underpredicts the ^{139}La shifts by 100 ppm, modestly underpredicts the ^{17}O shifts by 20 ppm, and reproduces the ^{35}Cl shifts with an error of only 1 ppm. While the discrepancies in ^{139}La and ^{35}Cl shifts have been addressed above, the 20 ppm underprediction of ^{17}O shifts in the solid state stands in clear contrast to the ∼150 ppm overprediction in the molten state. This difference is most likely attributed to the following two factors: (1) finite-temperature effects that are not fully captured in the ensemble-averaged DFT calculations of MD snapshots (as discussed above), and (2) limitations of the MD model in accurately reproducing the average La−O distances in the molten state.

With respect to the second point, it was recently shown using *ab initio* MD that transient covalent U−Cl interactions in molten UCl_3 are not adequately captured by the PIM.[82] This limitation was attributed to the participation of partially occupied U-5f orbitals, and is therefore unlikely to apply to La^{3+}, whose 4f shell is empty. Nevertheless, to assess whether deficiencies in the classical MD model could affect the predicted La−O coordination in the molten state, we performed additional DFT calculations to verify if the classical MD-generated structures correspond to the structural motifs at the DFT level.

Accordingly, geometry optimization operations were carried out using VASP on representative MD snapshots of the 80 NaCl−15 $LaCl_3$−5 LaOCl molten salt composition. Upon relaxation, the average La−O bond lengths increased from approximately 2.18 to 2.30 Å, while the distribution became narrower (Figure S12b). This change is accompanied by an enhanced preference for La−O−La bond angles near 109° and 120°, consistent with symmetric $[La_4O]^{10+}$ and $[La_3O]^{7+}$ coordination motifs (Figure S12c). Subsequent NMR calculations of the relaxed structures yielded ^{17}O shifts that were only slightly lower (<10 ppm) than those obtained from the unrelaxed MD snapshots (Figure S12d).

These results indicate that the MD-generated configurations are structurally consistent with first-principles relaxed geometries, while additionally capturing thermal disorder inherent to the molten state. As such, inaccuracies in the MD-generated ionic configurations are unlikely to be the primary source of the large discrepancy between calculated and experimental ^{17}O chemical shifts. Instead, the error is attributed to the intrinsic limitations of static, ground-state DFT in describing temperature-dependent bond aharmonicity and dielectric screening in polar covalent La−O bonds under molten conditions. In principle, more advanced exchange-correlation functionals (such as PBE0, PW31, B3LYP), which have been shown to improve the description of heavy-atom effects in solid-state systems,[83−85] may offer a more accurate treatment of these effects, albeit at substantially higher computational cost.

Despite these limitations in absolute shift prediction, the strong correlation between oxygen coordination environments and calculated ^{17}O chemical shifts remains robust. Accordingly, the trends in ^{17}O chemical shifts across the (80-α) NaCl−α $MgCl_2$−15 $LaCl_3$−5 LaOCl (α=0−80) series can be rationalized by decomposing the predicted shifts into contributions from individual O^{2-} environments. As shown in Figure 7, each vertical line at the bottom represents the chemical shift of a single O^{2-} ion calculated from the MD snapshots, with the resulting distributions plotted as normal curves. The spread of each curve reflects the diversity of local oxygen coordination environments in a given composition. To aid interpretation, chemical shift ranges associated with distinct

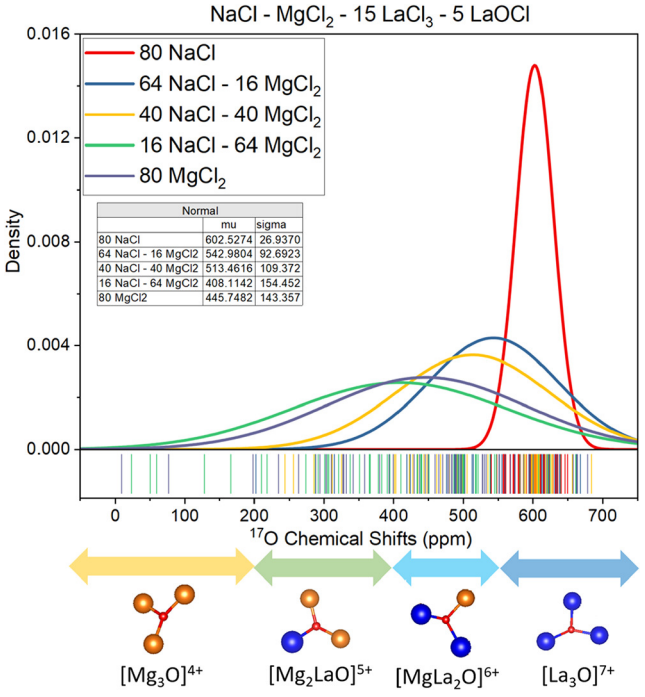

Figure 7. Distribution of predicted ^{17}O chemical shifts from individual O^{2-} environments in (80-α) NaCl−α $MgCl_2$−15 $LaCl_3$−5 LaOCl (α = 0−80). Chemical shift ranges for representative oxide species (considering only the three nearest neighbors) are shown below the *x*-axis. O^{2-}, Mg^{2+}, and La^{3+} ions are represented by red, orange, and blue spheres, respectively. All DFT calculations were performed on sampled "small box" MD trajectories.

https://doi.org/10.1021/acs.inorgchem.6c01882
Inorg. Chem. XXXX, XXX, XXX−XXX

oxide species are indicated below the distribution plots. For simplicity, these ranges were derived by considering only the first coordination shell, where each O^{2-} ion is coordinated by three cations (a combination of Mg^{2+} and La^{3+}). The ranges represent a span in which ~90% of the predicted shifts for each oxide species fall. Corresponding plots for systems with lower LaOCl concentrations are provided in Figure S13.

Across all compositions, purely NaCl-based systems exhibit the narrowest distribution. This arises because O^{2-} ions coordinate almost exclusively with La^{3+}, resulting in the predicted shifts being large but narrowly confined (550−700 ppm). With the introduction of $MgCl_2$, the predicted shifts gravitate toward smaller values and the distributions broaden, reflecting the increasing prevalence of mixed-species environments such as $[MgLa_2O]^{6+}$ and $[Mg_2LaO]^{5+}$. Beyond a 1:1 $MgCl_2$-to-NaCl ratio, however, the distributions no longer broaden, and the predicted shifts fluctuate without a systematic trend. As discussed earlier, this behavior reflects the saturation of Mg^{2+} coordination: with Mg^{2+} dominating the local environment, additions of $MgCl_2$ no longer appreciably alter the oxide speciation landscape.

Overall, our speciation analysis systematically addresses the experimental observations: NaCl-rich systems yield large ^{17}O shifts because O^{2-} coordinates exclusively with La^{3+}, whereas increasing $MgCl_2$ content reduces the average shift by promoting diverse mixed-coordination environments. In the context of oxygen solubility, these mixed coordination environments mitigate La−O clustering, thereby enhancing oxygen solubility and preventing the deposition of oxide precipitates.

4. CONCLUSIONS

In this study, we examined the $MgCl_2$-mediated solubility mechanism of oxygen in molten chlorides by performing ^{17}O NMR on NaCl−$MgCl_2$−$LaCl_3$−LaOCl and validating the results using MD and DFT calculations. Here, minor quantities of 90 at% ^{17}O-enriched LaOCl were progressively added to simulate oxygen contamination in NaCl−$MgCl_2$−$LaCl_3$, a proxy for the ARAMIS-A fuel composition of NaCl−$MgCl_2$−$PuCl_3$−$AmCl_3$.

Our results show that $MgCl_2$ inclusion lowers ^{17}O chemical shifts, indicating Mg^{2+} disrupts La−O clustering by promoting mixed coordination environments such as $[MgLa_2O]^{6+}$ and $[Mg_2LaO]^{5+}$. This mechanistic insight demonstrates how the incorporation of divalent Mg^{2+} cations enhances oxygen solubility and modifies oxide speciation in molten chlorides containing heavy lanthanide or actinide ions. In MSR-relevant compositions, such behavior provides the added benefit of sequestering oxygen contaminants, mitigating the deposition of actinide-rich oxide precipitates on MSR structural surfaces and suppressing a prominent pathway for deposit-induced corrosion. It should be noted, however, that these insights from the La-based surrogate system may not extend directly to actinide-bearing systems, where more complex bonding and redox chemistry could alter the relevant speciation behavior.

At the same time, the strong affinity for oxygen implies that $MgCl_2$ can also act as an impurity carrier if it is not sufficiently purified. This caveat underscores the importance of rigorous salt purification to harness the oxygen-sequestering capability of $MgCl_2$ without introducing additional impurities.

Altogether, our study lays out a molecular-level framework for tuning oxygen speciation in molten salts through compositional design, offering critical insight for the development of advanced high-temperature molten salt technologies.

■ ASSOCIATED CONTENT

Data Availability Statement

All experimental and computational data will be made available by the corresponding authors upon reasonable request.

Supporting Information

The Supporting Information is available free of charge at https://pubs.acs.org/doi/10.1021/acs.inorgchem.6c01882.

XRD of synthesized LaOCl; acquisition parameters for HT NMR measurements; laser-power-to-temperature calibration curve; PIM force field development, interatomic potential parameters; MD simulation details; chemical-shielding-to-shift calibration curves; Hubbard shift optimization strategy; thermodynamic stability diagrams; DSC curves; TG−DTA measurements; ex-situ XRD spectroscopy; calculated chemical shifts; RDFs, and O−La polymer chain lengths at 1000 °C; solid state NMR of LaOCl under ambient conditions; changes in MD-simulated molten salt structure after geometric relaxation at the DFT level; and distribution of predicted ^{17}O chemical shifts from individual O^{2-} environments in different molten salt compositions (PDF)

■ AUTHOR INFORMATION

Corresponding Authors

Woei Jer Ng − *CEMHTI UPR3079 CNRS, Université d'Orléans, F-45071 Orléans, France;* orcid.org/0000-0002-1388-9211; Email: woei-jer.ng@cnrs-orleans.fr

Mathieu Salanne − *Sorbonne Université, CNRS, Physicochimie des Électrolytes et Nanosystèmes Interfaciaux, F-75005 Paris, France; CNRS@CREATE, Singapore 138601, Singapore;* orcid.org/0000-0002-1753-491X; Email: mathieu.salanne@sorbonne-universite.fr

Authors

Kateryna Goloviznina − *Sorbonne Université, CNRS, Physicochimie des Électrolytes et Nanosystèmes Interfaciaux, F-75005 Paris, France; ICSM, University of Montpellier, CEA, CNRS, ENSCM, 30207 Bagnols-Sur-Cèze, France;* orcid.org/0000-0001-9913-4938

František Šimko − *Institute of Inorganic Chemistry, Slovak Academy of Sciences, 84104 Bratislava, Slovakia*

Aydar Rakhmatullin − *CEMHTI UPR3079 CNRS, Université d'Orléans, F-45071 Orléans, France;* orcid.org/0000-0002-7328-5081

Complete contact information is available at: https://pubs.acs.org/10.1021/acs.inorgchem.6c01882

Author Contributions

W.J.N. and A.R. conceived and designed the project. W.J.N. performed the synthesis experiments with assistance from A.R.. W.J.N. and A.R. conducted the NMR experiments. K.G. and M.S. developed the PIM force fields for MD simulations. W.J.N. and K.G. carried out the MD simulations and postanalysis under the supervision of M.S.. W.J.N. performed the DFT calculations of NMR parameters under the supervision of M.S.. F.Š. performed the TG−DTA measure-

https://doi.org/10.1021/acs.inorgchem.6c01882
Inorg. Chem. XXXX, XXX, XXX−XXX

ments. W.J.N. wrote the original draft of this manuscript with contributions from all coauthors.

Notes

The authors declare no competing financial interest.

■ ACKNOWLEDGMENTS

This work was carried out as part of the ISAC (Innovative System for Actinide Conversion) project funded by the France 2030 government program. We extend our gratitude to SACADO (Service d'Aide au Calcul et à l'Analyse de DOnnées, Sorbonne Université) for providing the computational resources necessary for our simulations. We extend our gratitude to S. Ory for helping us with the DSC measurements. We thank Dr. J. Serp and Dr. A.H. Meskine for the meaningful discussions on oxygen solubility in chloride melts. We also thank Dr. T. Charpentier for the valuable advice and recommendations on performing DFT calculations.

■ REFERENCES

(1) Zhang, H.; Dasbiswas, K.; Ludwig, N. B.; Han, G.; Lee, B.; Vaikuntanathan, S.; Talapin, D. V. Stable Colloids in Molten Inorganic Salts. *Nature* **2017**, *542* (7641), 328−331.
(2) Song, Y.; Ghoridi, A.; Saldaña, F. I.; Gómez-Recio, I.; Janisch, D.; de Rolland Dalon, E.; Thiaudière, D.; Ruiz-González, M. L.; González-Calbet, J. M.; Lassalle-Kaiser, B.; Zitolo, A.; Laberty-Robert, C.; Portehault, D. In and Out: Shuttling Atoms in Covalent Nanocrystals, from Synthesis in Molten Salts to Water-Splitting Electrocatalysis. *J. Am. Chem. Soc.* **2025**, *147* (24), 20878−20887.
(3) Mohandas, K. S. Direct Electrochemical Conversion of Metal Oxides to Metal by Molten Salt Electrolysis: A Review. *Miner. Process. Extr. Metall.* **2013**, *122*, 195−212.
(4) Flandinet, L.; Tedjar, F.; Ghetta, V.; Fouletier, J. Metals Recovering from Waste Printed Circuit Boards (WPCBs) Using Molten Salts. *J. Hazard. Mater.* **2012**, *213*−*214*, 485−490.
(5) Gao, S.; Chen, X.; Qu, J.; Guo, Y.; Shi, H.; Pang, F.; Guo, L.; Qu, X.; Wang, D.; Yin, H. Recycling of Silicon Solar Panels through a Salt-Etching Approach. *Nat. Sustainability* **2024**, *7* (7), 920−930.
(6) Caraballo, A.; Galán-Casado, S.; Caballero, A.; Serena, S. Molten Salts for Sensible Thermal Energy Storage: A Review and an Energy Performance Analysis. *Energies* **2021**, *14* (4), No. 1197.
(7) Bhatnagar, P.; Siddiqui, S.; Sreedhar, I.; Parameshwaran, R. Molten Salts: Potential Candidates for Thermal Energy Storage Applications. *Int. J. Energy Res.* **2022**, *46* (13), 17755−17785.
(8) Mirza, M.; Abdulaziz, R.; Maskell, W. C.; Wilcock, S.; Jones, A. H.; Woodall, S.; Jackson, A.; Shearing, P. R.; Brett, D. J. L. Electrochemical Processing in Molten Salts - a Nuclear Perspective. *Energy Environ. Sci.* **2023**, *16* (3), 952−982.
(9) Im, S.; Varnell, K. E.; Pandey, A. K.; Asghari-Rad, P.; Yoo, T. S.; Kim, H. Effect of Fluoride Anions on Nd(III) Electrode Processes and Nd Metal Recovery in LiCl−KCl−$NdCl_3$. *J. Am. Chem. Soc.* **2025**, *147* (51), 47289−47298.
(10) Roper, R.; Harkema, M.; Sabharwall, P.; Riddle, C.; Chisholm, B.; Day, B.; Marotta, P. Molten Salt for Advanced Energy Applications: A Review. *Ann. Nucl. Energy* **2022**, *169*, No. 108924.
(11) Dai, Z. Thorium Molten Salt Reactor Nuclear Energy System (TMSR). In *Molten Salt Reactors and Thorium Energy* 2017; pp 803−814.
(12) Ignatiev, V. V.; Feynberg, O.; Zagnitko, A. V.; Afonichkin, V.; Ignatiev, V.; Merzlyakov, A.; Surenkov, A.; Zagnitko, A.; Bovet, A.; Khokhlov, V.; Subbotin, V.; Fazilov, R.; Gordeev, M.; Panov, A.; Toropov, A. Progress in Development of MOSART Concept with Th Support. In *Proceedings of ICAPP '12; Chicago, USA*; Chicago: USA, 2012; pp 943−952.
(13) Ignatiev, V. Molten Salt Reactor for the Management of Minor from VVER 1000/1200 Used Fuel *International Conference on the Management of Spent Fuel from Nuclear Power Reactors 2019: Learning from the Past, Enabling the Future;* 2019.
(14) Krepel, J.; Kramer, K. J. TerraPower Fast Chloride Reactor. In *Molten Salt Reactors and Thorium Energy*; Elsevier, 2024; pp 953−972.
(15) Taylor, T.; Gregoire, O.; Haigh, P.; Boddington, S.; O'Sullivan, R. Waste Burning Performance of the Moltex SSR-W *5th Generation IV and Small Reactors (G4SR) Conference; Ottawa, ON, Canada,* 2024.
(16) Mascaron, M.; Martinet, J.; Pascal, V.; Merle, E.; Bertrand, F. An Approach to Molten Salt Reactor Operation and Control and Its Application to the ARAMIS Actinide Burner. *Ann. Nucl. Energy* **2025**, *210*, No. 110888.
(17) Harinath, Y. V.; Mohan, T. V. K.; Rangarajan, S.; Albert, S. K. Structural Materials for Molten Salt Reactors. In *In A Treatise on Corrosion Science, Engineering, and Technology. Indian Institute of Metals Series*; Springer: Singapore, 2022; pp 169−191.
(18) Wright, R. N.; Sham, T.-L. Status of Metallic Structural Materials for Molten Salt Reactors 2018 http://www.inl.gov (accessed October 11, 2025).
(19) Zheng, G.; Sridharan, K. Corrosion of Structural Alloys in High-Temperature Molten Fluoride Salts for Applications in Molten Salt Reactors. *JOM* **2018**, *70* (8), 1535−1541.
(20) Surenkov, A. I.; Abalin, S. S.; Ivliev, P. N.; Ignatiev, V. V.; Klimov, K. S.; Subbotin, A. S.; Trunkin, I. N.; Uglov, V. S. Experimental Study of Corrosion Resistance of Nickel-Molybdenum Alloys in the Melt of Lithium and Beryllium Fluoride Salts. *Phys. At. Nucl.* **2024**, *87* (8), 1176−1186.
(21) Zhang, J.; Forsberg, C. W.; Simpson, M. F.; Guo, S.; Lam, S. T.; Scarlat, R. O.; Carotti, F.; Chan, K. J.; Singh, P. M.; Doniger, W.; Sridharan, K.; Keiser, J. R. Redox Potential Control in Molten Salt Systems for Corrosion Mitigation. *Corros. Sci.* **2018**, *144*, 44−53.
(22) Walker, S. A.; Tano, M. E.; Abou-Jaoude, A.; Calvin, O. Depletion-Driven Thermochemistry of Molten Salt Reactors: Review, Method, and Analysis. *Front. Nucl. Eng.* **2023**, *2*, No. 1214727.
(23) Delpech, S.; Carrière, C.; Chmakoff, A.; Martinelli, L.; Rodrigues, D.; Cannes, C. Corrosion Mitigation in Molten Salt Environments. *Materials* **2024**, *17* (3), No. 581.
(24) Kim, C.; Couet, A. In Situ Monitoring of Molten Chloride Salt Chemistry and Corrosion Using a Microelectrode. *J. Am. Chem. Soc.* **2025**, *147* (22), 19013−19025.
(25) Xu, H. Thorium Energy and Molten Salt R&D in China. *Thorium Energy World* **2016**, 37−44.
(26) Mayes, R. T.; Kurley, J. M.; Halstenberg, P. W.; Mcalister, A.; Sulejmanovic, D.; Raiman, S.; Dai, S.; Pint, B. Purification of Chloride Salts for Concentrated Solar Power Applications 2018 www.osti.gov (accessed October 01, 2025).
(27) Burak, A.; Raiman, S. Parametric Study of Metallothermic Purification of Chloride Salts. *ACS Omega* **2025**, *10*, 41247−41259.
(28) Raiman, S. S.; Lee, S. Aggregation and Data Analysis of Corrosion Studies in Molten Chloride and Fluoride Salts. *J. Nucl. Mater.* **2018**, *511*, 523−535.
(29) Kurley, J. M.; Halstenberg, P. W.; McAlister, A.; Raiman, S.; Dai, S.; Mayes, R. T. Enabling Chloride Salts for Thermal Energy Storage: Implications of Salt Purity. *RSC Adv.* **2019**, *9* (44), 25602−25608.
(30) Haubenreich, P. N.; Engel, J. R. Experience with the Molten-Salt Reactor Experiment. *Nucl. Appl. Technol.* **1970**, *8* (2), 118−136.
(31) Chenaud, M. S.; Pascal, V.; Chabert-Koralewski, C.; Serp, J.; Laghoutaris, P.; Garnier, J. C.; Sudreau, F.; Morel, B.; Morales, I.; Drouvot, O.; David, S.; Merle, E.; Hamy, J. M.; Botte, F.; Takenouti, S.; Sanna, A. The French R&D Collaborative Project ISAC on Fast MSR Dedicated to Actinides Transmutation. In *International Conference on the Management of Spent Fuel from Nuclear Power Plants*; International Atomic Energy Agency (IAEA): Vienna, 2024.
(32) Cathro, K. J.; Deutscher, R. L.; Sharma, R. A. Electrowinning Magnesium from Its Oxide in a Melt Containing Neodymium Chloride. *J. Appl. Electrochem.* **1997**, *27*, 404−413.
(33) Beneš, O.; Konings, R. J. M. Thermodynamic Evaluation of the NaCl−$MgCl_2$−UCl_3−$PuCl_3$ System. *J. Nucl. Mater.* **2008**, *375* (2), 202−208.

https://doi.org/10.1021/acs.inorgchem.6c01882
Inorg. Chem. XXXX, XXX, XXX−XXX

(34) Ng, W. J.; Goloviznina, K.; Sarou-Kanian, V.; Salanne, M.; Rakhmatullin, A. Effect of Mg^{2+} Ions on Transport Properties in Molten Chloride Fast Reactor Fuels. *J. Phys. Chem. B* **2026**, *130*, 2270−2277.
(35) Mediaas, H.; Tkatcheva, O.; Dracopoulos, V.; Papatheodorou, G. N.; Kipouros, G. J.; Østvold, T. Solubilities and Raman Spectra of NdOCl in Some Chloride Melts of Interest for the Electrowinning of Magnesium from Its Oxide. *Metall. Mater. Trans. B* **2000**, *31*, 631−639.
(36) Li, B.; Li, J.; Chen, J.; Yu, J. Solubility of MgO in Chloride Melts Containing NdCl3 or LaCl3. *Nat. Resour. Environ. Issues* **2009**, *15*, 209−213.
(37) Meskine, H.; Serp, J. Rôle de MgCl2. *ISAC Internal Presentation - Unpublished Work*. 2024.
(38) Song, X.; Li, S.; Liu, S.; Fan, Y.; He, J.; Song, J. Coordination States of Metal Ions in Molten Salts and Their Characterization Methods. *Int. J. Miner. Metall. Mater.* **2023**, *30* (7), 1261−1277.
(39) Vik, A. F.; Dracopoulos, V.; Papatheodorou, G. N.; Østvold, T. Solubility and Raman Spectra of Nb(V) in LiF−NaF−KF−Na_2O Melts. *J. Alloys Compd.* **2001**, *321* (2), 284−299.
(40) Liu, X.; Wang, B.; Fu, H.; Wang, C. Raman Spectroscopic and Theoretical Studies on the Structure of Ta (V) Fluoro and Oxofluoro Complexes in Molten FLiNaK. *J. Mol. Liq.* **2021**, *337*, No. 116409.
(41) Stefanidaki, E.; Photiadis, G. M.; Kontoyannis, C. G.; Vik, A. F.; Østvold, T. Oxide Solubility and Raman Spectra of NdF_3−LiF−KF−MgF_2-Nd_2O_3 Melts. *J. Chem. Soc., Dalton Trans.* **2002**, No. No.11, 2302−2307.
(42) Chen, X.; Fu, H.; Wang, C. Influence of Oxide Ions on the Speciation in Molten KF−ZrF_4 and KF−HfF_4: A Raman Spectroscopic and Theoretical Investigation. *J. Mol. Liq.* **2021**, *342*, No. 117476.
(43) Liu, X.; Li, Y.; Wang, B.; Wang, C. Raman and Density Functional Theory Studies of Lutecium Fluoride and Oxyfluoride Structures in Molten FLiNaK. *Spectrochim. Acta A Mol. Biomol. Spectrosc.* **2021**, *251*, No. 119435.
(44) Rollet, A. L.; Matsuura, H.; Bessada, C. An in Situ Spectroscopic Study of the Local Structure of Oxyfluoride Melts: NMR Insights into the Speciation in Molten LiF−LaF_3−Li_2O Systems. *Dalton Trans.* **2015**, *44* (2), 522−529.
(45) Ng, W. J.; Rakhmatullin, A.; Goloviznina, K.; Salanne, M.; Bessada, C. Structural Dynamics of Molten NaCl−$MgCl_2$−$LaCl_3$: A Proxy for Molten Chloride Fast Reactor Fuels. *J. Nucl. Mater.* **2025**, *616*, No. 156056.
(46) Machado, K.; Zanghi, D.; Salanne, M.; Stabrowski, V.; Bessada, C. Anionic Structure in Molten Cryolite-Alumina Systems. *J. Phys. Chem. C* **2018**, *122* (38), 21807−21816.
(47) Keppert, M.; Rakhmatullin, A.; Simko, F.; Deschamps, M.; Haarberg, G. M.; Bessada, C. Multi-Nuclear Magnetic Resonance Study of Na_3AlF_6-$AlPO_4$ Molten and Solidified Mixtures. *Magn. Reson. Chem.* **2008**, *46* (9), 803−810.
(48) Rakhmatullin, A.; Michel, R.; Bessada, C. Structural Characterization and Chemistry of LiF−AlF_3 Melts with Addition of MgO and MgF_2. *J. Fluor. Chem.* **2021**, *241*, No. 109678.
(49) Rakhmatullin, A.; Keppert, M.; Šimko, F.; Bessada, C. Aluminium Phosphate Behaviour in Na_3AlF_6-Al_2O_3 Melts: A New Insight from in Situ High Temperature NMR Measurements. *New J. Chem.* **2016**, *40* (2), 1737−1741.
(50) Wendlandt, W. W. The Thermal Decomposition of Yttrium, Scandium, and Some Rare-Earth Chloride Hydrates. *J. Inorg. Nucl. Chem.* **1957**, *5*, 118−122.
(51) Marin-Laflèche, A.; Haefele, M.; Scalfi, L.; Coretti, A.; Dufils, T.; Jeanmairet, G.; Reed, S.; Serva, A.; Berthin, R.; Bacon, C.; Bonella, S.; Rotenberg, B.; Madden, P.; Salanne, M. MetalWalls: A Classical Molecular Dynamics Software Dedicated to the Simulation of Electrochemical Systems. *J. Open Source Software* **2020**, *5* (53), No. 2373.
(52) Coretti, A.; Bacon, C.; Berthin, R.; Serva, A.; Scalfi, L.; Chubak, I.; Goloviznina, K.; Haefele, M.; Marin-Laflèche, A.; Rotenberg, B.; Lafi, A. M.; Bonella, S.; Salanne, M. MetalWalls: Simulating Electrochemical Interfaces between Polarizable Electrolytes and Metallic Electrodes. *J. Chem. Phys.* **2022**, *157* (18), No. 184801.
(53) Pireddu, G.; Santos, M. S.; Lambertin, D.; Kooyman, T. Molecular Dynamics Simulations for the Prediction of Thermophysical Properties of Plutonium-Based Molten Salts. *J. Nucl. Mater.* **2024**, *597*, No. 155124.
(54) Pireddu, G.; Salcedo, A.; Sauzet, H.; Delpech, S.; Lambertin, D.; Kooyman, T. Polarizable Force Fields for the Structural and Thermophysical Properties of Molten Actinide Chlorides. *J. Nucl. Mater.* **2025**, *612*, No. 155822.
(55) Aguado, A.; Madden, P. A. New Insights into the Melting Behavior of MgO from Molecular Dynamics Simulations: The Importance of Premelting Effects. *Phys. Rev. Lett.* **2005**, *94* (6), No. 068501.
(56) Pacaud, F.; Salanne, M.; Charpentier, T.; Cormier, L.; Delaye, J. M. Structural Study of Na_2O−B_2O_3−SiO_2−La_2O_3 Glasses from Molecular Simulations Using a Polarizable Force Field. *J. Non. Cryst. Solids* **2018**, *499*, 371−379.
(57) Burbano, M.; Carlier, D.; Boucher, F.; Morgan, B. J.; Salanne, M. Sparse Cyclic Excitations Explain the Low Ionic Conductivity of Stoichiometric $Li_7La_3Zr_2O_{12}$. *Phys. Rev. Lett.* **2016**, *116* (13), No. 135901.
(58) Madden, P. A.; Wilson, M. "Covalent" Effects in "Ionic" Systems. *Chem. Soc. Rev.* **1996**, *25*, 339−359.
(59) Momma, K.; Izumi, F. VESTA 3 for Three-Dimensional Visualization of Crystal, Volumetric and Morphology Data. *J. Appl. Crystallogr.* **2011**, *44* (6), 1272−1276.
(60) Brehm, M.; Thomas, M.; Gehrke, S.; Kirchner, B. TRAVIS—A Free Analyzer for Trajectories from Molecular Simulation. *J. Chem. Phys.* **2020**, *152* (16), No. 164105.
(61) Martínez, L.; Andrade, R.; Birgin, E. G.; Martínez, J. M. PACKMOL: A Package for Building Initial Configurations for Molecular Dynamics Simulations. *J. Comput. Chem.* **2009**, *30* (13), 2157−2164.
(62) Hafner, J. Ab-Initio Simulations of Materials Using VASP: Density-Functional Theory and Beyond. *J. Comput. Chem.* **2008**, *29* (13), 2044−2078.
(63) Perdew, J. P.; Burke, K.; Ernzerhof, M. Generalized Gradient Approximation Made Simple. *Phys. Rev. Lett.* **1996**, *77* (18), 3865−3868.
(64) Choosing pseudopotentials. https://www.vasp.at/wiki/Choosing_pseudopotentials (accessed February 09, 2026).
(65) Widdifield, C. M.; Chapman, R. P.; Bryce, D. L. Chapter 5 Chlorine, Bromine, and Iodine Solid-State NMR Spectroscopy. In *Annual Reports on NMR Spectroscopy* 2009 *Vol. 66*, pp 195−326.
(66) Bastow, T. J.; Stuart, S. N. ^{17}O NMR in Simple Oxides. *Chem. Phys.* **1990**, *143* (3), 459−467.
(67) Ooms, K. J.; Feindel, K. W.; Willans, M. J.; Wasylishen, R. E.; Hanna, J. V.; Pike, K. J.; Smith, M. E. Multiple-Magnetic Field ^{139}La NMR and Density Functional Theory Investigation of the Solid Lanthanum(III) Halides. *Solid State Nucl. Magn. Reson.* **2005**, *28* (2−4), 125−134.
(68) Spencer, L.; Coomes, E.; Ye, E.; Terskikh, V.; Ramzy, A.; Thangadurai, V.; Goward, G. R. Structural Analysis of Lanthanum-Containing Battery Materials Using ^{139}La Solid-State NMR. *Can. J. Chem.* **2011**, *89* (9), 1105−1117.
(69) Dudarev, S. L.; Botton, G. A.; Savrasov, S. Y.; Humphreys, C. J.; Sutton, A. P. Electron-Energy-Loss Spectra and the Structural Stability of Nickel Oxide: An LSDA+U Study. *Phys. Rev. B* **1998**, *57* (3), No. 1505.
(70) Park, S.; Yun, J. Il. An In-Situ Raman Spectroscopic Study on Potential-P_{O2}- Phase Diagram of Lanthanum in LiCl−KCl Eutectic Melt. *J. Rare Earths* **2020**, *38* (7), 793−800.
(71) Smolenski, V.; Novoselova, A. Thermodynamic Properties and the Solubility of the Oxide Lanthanum Compounds in Fused 0.36NaCl−0.64CsCl Eutectic. *J. Chem. Thermodyn.* **2021**, *163*, No. 106583.

https://doi.org/10.1021/acs.inorgchem.6c01882
Inorg. Chem. XXXX, XXX, XXX−XXX

(72) Salanne, M.; Simon, C.; Turq, P.; Madden, P. A. Conductivity-Viscosity-Structure: Unpicking the Relationship in an Ionic Liquid. *J. Phys. Chem. B* **2007**, *111* (18), 4678−4684.
(73) Emerson, M. S.; Sharma, S.; Roy, S.; Bryantsev, V. S.; Ivanov, A. S.; Gakhar, R.; Woods, M. E.; Gallington, L. C.; Dai, S.; Maltsev, D. S.; Margulis, C. J. Complete Description of the $LaCl_3$−NaCl Melt Structure and the Concept of a Spacer Salt That Causes Structural Heterogeneity. *J. Am. Chem. Soc.* **2022**, *144* (47), 21751−21762.
(74) Duemmler, K.; Woods, M.; Karlsson, T.; Gakhar, R.; Beeler, B. An Ab Initio Molecular Dynamics Investigation of the Thermophysical Properties of Molten NaCl−$MgCl_2$. *J. Nucl. Mater.* **2022**, *570*, No. 153916.
(75) Wu, X.; Zhang, Y.; Zhang, J.; Liu, R.; Yang, J.; Yang, B.; Xu, H.; Ma, Y. High Pressure X-Ray Diffraction Study of Sodium Oxide (Na_2O): Observations of Amorphization and Equation of State Measurements to 15.9 GPa. *J. Alloys Compd.* **2020**, *823*, No. 153793.
(76) Tsirelson, V. G.; Avilov, A. S.; Abramov, Y. A.; Belokoneva, E. L.; Io'raneh, R.; Feil, A. D. X-Ray and Electron Diffraction Study of MgO. *Acta Crystallogr.* **1998**, *54*, 8−17.
(77) Monserrat, B.; Needs, R. J.; Pickard, C. J. Temperature Effects in First-Principles Solid State Calculations of the Chemical Shielding Tensor Made Simple. *J. Chem. Phys.* **2014**, *141* (13), No. 134113.
(78) Han, Z.; Lee, C.; Song, J.; Wang, H.; Bermel, P.; Ruan, X. Temperature-Dependent Full Spectrum Dielectric Function of Semiconductors from First Principles. *Phys. Rev. B* **2023**, *107* (20), No. L201202.
(79) Barrett, N. T.; Greaves, G. N.; Willis, T. M.; Antoninill, G. M.; Thornley, F. R. Anharmonic Vibrations in UO_2, as Determined by EXAFS. *J. Phys. C: Solid State Phys.* **1988**, *21*, 791−796.
(80) Vicha, J.; Novotny, J.; Komorovsky, S.; Straka, M.; Kaupp, M.; Marek, R. Relativistic Heavy-Neighbor-Atom Effects on NMR Shifts: Concepts and Trends across the Periodic Table. *Chem. Rev.* **2020**, *120* (15), 7065−7103.
(81) Hölsä, J.; Lastusaari, M.; Valkonen, J. X-Ray Powder Diffraction Study of the Stability of Solid Solutions in $LaO(Cl_{1-x}Br_x)$. *J. Alloys Compd.* **1997**, *262*−*263*, 299−304.
(82) Maltsev, D. S.; Driscoll, D. M.; Zhang, Y.; Neuefeind, J. C.; Reinhart, B.; Agca, C.; Ray, D.; Halstenberg, P. W.; Aziziha, M.; Schorne-Pinto, J.; Besmann, T. M.; Bryantsev, V. S.; Dai, S.; Roy, S.; Ivanov, A. S. Transient Covalency in Molten Uranium(III) Chloride. *J. Am. Chem. Soc.* **2024**, *146* (31), 21220−21224.
(83) Cho, H.; De Jong, W. A.; Soderquist, C. Z. Probing the Oxygen Environment in UO_2^{2+} by Solid-State O^{17} Nuclear Magnetic Resonance Spectroscopy and Relativistic Density Functional Calculations. *J. Chem. Phys.* **2010**, *132* (8), No. 084501.
(84) Smiles, D. E.; Wu, G.; Hrobárik, P.; Hayton, T. W. Use of ^{77}Se and ^{125}Te NMR Spectroscopy to Probe Covalency of the Actinide-Chalcogen Bonding in $[Th(E_n)\{N(SiMe_3)_2\}_3]-$ (E = Se, Te; n = 1, 2) and Their Oxo-Uranium(VI) Congeners. *J. Am. Chem. Soc.* **2016**, *138* (3), 814−825.
(85) Reta, D.; Ortu, F.; Randall, S.; Mills, D. P.; Chilton, N. F.; Winpenny, R. E. P.; Natrajan, L.; Edwards, B.; Kaltsoyannis, N. The Performance of Density Functional Theory for the Description of Ground and Excited State Properties of Inorganic and Organometallic Uranium Compounds. *J. Organomet. Chem.* **2018**, *857*, 58−74.

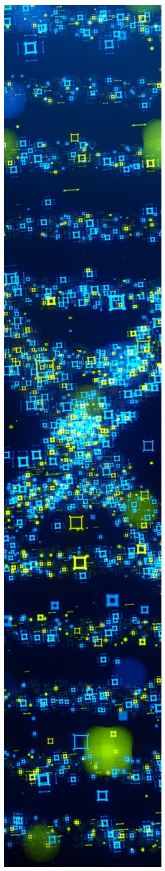
CAS BIOFINDER DISCOVERY PLATFORM™
STOP DIGGING THROUGH DATA —START MAKING DISCOVERIES
CAS BioFinder helps you find the right biological insights in seconds
Start your search
CAS
A division of the American Chemical Society

https://doi.org/10.1021/acs.inorgchem.6c01882
Inorg. Chem. XXXX, XXX, XXX−XXX

Woei Jer Ng

Relations Structure–Propriétés dans les Combustibles pour Réacteurs Rapides à Sels de Chlorures Fondus: Approche Intégrée Computationnelle et Expérimentale du Système $NaCl–MgCl_2–LaCl_3$

Cette thèse porte sur l'étude des relations structure–propriétés dans des mélanges de chlorures fondus utilisés comme combustibles pour les réacteurs rapides à sels de chlorures fondus (MCFR). La France étudie actuellement l'utilisation du mélange $NaCl–MgCl_2–PuCl_3–AmCl_3$ afin de réduire l'inventaire d'actinides contenus dans les combustibles nucléaires usés. Dans ce cadre, l'amélioration des performances de ces combustibles nécessite une compréhension approfondie de la structure locale des sels fondus, laquelle gouverne des propriétés macroscopiques telles que la viscosité et la solubilité de l'oxygène.

Au CEMHTI–CNRS, le système $NaCl–MgCl_2–LaCl_3$ a été utilisé comme combustible modèle, non radiotoxique et actif en résonance magnétique nucléaire (RMN), afin d'étudier in situ les environnements de coordination et la structure des réseaux dans les chlorures fondus. Dans cette démarche, un protocole de validation multimodal combinant la RMN à haute température (RMN HT), des simulations classiques de dynamique moléculaire (DM) et des calculs RMN obtenus à partir des premiers principes (chimie quantique) a été mis en œuvre afin d'assurer la cohérence entre les modèles structurels obtenus expérimentalement et ceux issus de la modélisation. Le couplage entre structure locale et propriétés macroscopiques a également été approfondi. Les propriétés de transport du système ternaire ont été évaluées par les calculs DM, tandis que les coefficients de diffusion calculés ont été validés pour quelques compositions par RMN à gradients de champ pulsé (RMN–PFG). La solubilité de l'oxygène a en outre été examinée à l'aide de dopants LaOCl enrichis en oxygène-17, selon le même protocole multimodal.

L'augmentation de la teneur en $MgCl_2$ accroît le nombre moyen de coordination La–Cl et perturbe les réseaux continus La–Cl–La. En conséquence, la suppression des complexes étendus et interdigités $[La_xCl_y]^{3x-y}$ contribue alors principalement à la diminution de la viscosité du sel fondu ainsi qu'à l'augmentation de la diffusivité ionique pour des sels de teneur élevée en $LaCl_3$. Par ailleurs, $MgCl_2$ favorise la solubilité de l'oxygène par la formation d'environnements de coordination mixtes, tels que $[La_2MgO]^{6+}$ et $[LaMg_2O]^{5+}$. Ces résultats montrent que l'ajout de $MgCl_2$ peut améliorer les propriétés de transport des combustibles MCFR tout en favorisant la séquestration des impuretés oxygénées, ce qui atténue les précipitations d'oxydes.

Mots-clés : Réacteurs à sels fondus, chlorures fondus, RMN à haute température, dynamique moléculaire, DFT

Structure–Property Coupling in Molten Chloride Fast Reactor Fuels: An Integrated Computational and Experimental Study of the $NaCl–MgCl_2–LaCl_3$ Surrogate System

This thesis investigates the structure–property relationships of molten chloride mixtures relevant to molten chloride fast reactor (MCFR) fuels. France is currently exploring $NaCl–MgCl_2–PuCl_3–AmCl_3$ as an MCFR fuel to reduce the actinide inventory in spent nuclear fuel. Improving the reactor fuel performance requires a robust understanding of the local structure in molten chlorides, which governs macroscopic behaviour such as viscosity and oxygen solubility.

At CEMHTI–CNRS, the $NaCl–MgCl_2–LaCl_3$ mixture is employed as a non-radiotoxic, NMR-active surrogate fuel system to probe *in situ* local coordination environment and network structure in chloride melts. In this endeavour, a multimodal verification framework—combining high-temperature nuclear magnetic resonance (HT NMR), classical molecular dynamics (MD) simulations, and first-principles NMR calculations—was employed to ensure consistency between experimentally derived and simulated structural models. The coupling between structure and macroscopic properties was further investigated: transport properties were computationally evaluated throughout the ternary composition space, with diffusivity calculations verified on selected compositions by pulsed field gradient NMR (PFG–NMR); oxygen solubility was examined using ^{17}O-enriched LaOCl dopants within a similar multimodal framework.

At fixed $LaCl_3$ concentrations, increasing the $MgCl_2$ content raises the average La–Cl coordination number and disrupts continuous La–Cl–La networks. Suppression of extended, interdigitated $[La_xCl_y]^{3x-y}$ complexes predominantly contributes to reduced melt viscosities and enhanced ion diffusivity at appreciable $LaCl_3$ concentrations. In addition, $MgCl_2$ promotes oxygen solubility through the formation of mixed coordination environments, such as $[La_2MgO]^{6+}$ and $[LaMg_2O]^{5+}$. These results indicate that $MgCl_2$ can serve as a beneficial component of MCFR fuels, improving transport behaviour while sequestering oxygen impurities to prevent oxide precipitation.

Keywords: Molten Salt Reactors, Molten Chlorides, High-temperature NMR, Molecular Dynamics, DFT

Conditions Extrêmes et Matériaux : Haute Température et Irradiation
CEMHTI UPR 3079 CNRS
1D, Avenue de la Recherche Scientifique 45071
Orléans Cedex 02